

Lecture Notes in Physics

745

Savely G. Karshenboim
Editor

Precision Physics
of Simple Atoms and
Molecules



Springer

Lecture Notes in Physics

Editorial Board

R. Beig, Wien, Austria
W. Beiglböck, Heidelberg, Germany
W. Domcke, Garching, Germany
B.-G. Englert, Singapore
U. Frisch, Nice, France
P. Hänggi, Augsburg, Germany
G. Hasinger, Garching, Germany
K. Hepp, Zürich, Switzerland
W. Hillebrandt, Garching, Germany
D. Imboden, Zürich, Switzerland
R. L. Jaffe, Cambridge, MA, USA
R. Lipowsky, Potsdam, Germany
H. v. Löhneysen, Karlsruhe, Germany
I. Ojima, Kyoto, Japan
D. Sornette, Nice, France, and Zürich, Switzerland
S. Theisen, Potsdam, Germany
W. Weise, Garching, Germany
J. Wess, München, Germany
J. Zittartz, Köln, Germany

The Lecture Notes in Physics

The series Lecture Notes in Physics (LNP), founded in 1969, reports new developments in physics research and teaching – quickly and informally, but with a high quality and the explicit aim to summarize and communicate current knowledge in an accessible way. Books published in this series are conceived as bridging material between advanced graduate textbooks and the forefront of research and to serve three purposes:

- to be a compact and modern up-to-date source of reference on a well-defined topic
- to serve as an accessible introduction to the field to postgraduate students and nonspecialist researchers from related areas
- to be a source of advanced teaching material for specialized seminars, courses and schools

Both monographs and multi-author volumes will be considered for publication. Edited volumes should, however, consist of a very limited number of contributions only. Proceedings will not be considered for LNP.

Volumes published in LNP are disseminated both in print and in electronic formats, the electronic archive being available at springerlink.com. The series content is indexed, abstracted and referenced by many abstracting and information services, bibliographic networks, subscription agencies, library networks, and consortia.

Proposals should be sent to a member of the Editorial Board, or directly to the managing editor at Springer:

Christian Caron
Springer Heidelberg
Physics Editorial Department I
Tiergartenstrasse 17
69121 Heidelberg / Germany
christian.caron@springer.com

S. G. Karshenboim

Precision Physics of Simple Atoms and Molecules

 Springer

Savely G. Karshenboim
D.I. Mendeleev Institute
for Metrology
190005 St. Petersburg
Russia
sgk@vniim.ru

and

Max-Planck-Institut für Quantenoptik Hans-Kopfermann-Str.1
D-85748 Garching, Germany
savely.karshenboim@mpq.mpg.de

S. G. Karshenboim, *Precision Physics of Simple Atoms and Molecules*, Lect. Notes Phys. 745 (Springer, Berlin Heidelberg 2008), DOI 10.1007/978-3-540-75479-4

ISBN: 978-3-540-75478-7

e-ISBN: 978-3-540-75479-4

Lecture Notes in Physics ISSN: 0075-8450

Library of Congress Control Number: 2007938317

© 2008 Springer-Verlag Berlin Heidelberg

This work is subject to copyright. All rights are reserved, whether the whole or part of the material is concerned, specifically the rights of translation, reprinting, reuse of illustrations, recitation, broadcasting, reproduction on microfilm or in any other way, and storage in data banks. Duplication of this publication or parts thereof is permitted only under the provisions of the German Copyright Law of September 9, 1965, in its current version, and permission for use must always be obtained from Springer. Violations are liable for prosecution under the German Copyright Law.

The use of general descriptive names, registered names, trademarks, etc. in this publication does not imply, even in the absence of a specific statement, that such names are exempt from the relevant protective laws and regulations and therefore free for general use.

Cover design: eStudio Calamar S.L., F. Steinen-Broo, Pau/Girona, Spain

Printed on acid-free paper

9 8 7 6 5 4 3 2 1

springer.com

Foreword

The study of simple atoms and molecules permits unique confrontations between fundamental theory and precision measurements. It has played a central role in many early discoveries that laid the foundations of quantum physics. Since computational and experimental tools are still evolving rapidly, intriguing opportunities for future research continue to emerge.

How could precision measurements uncover limits of the standard model? How can we improve the accuracy of fundamental constants? Are fundamental constants really constant? How could we detect possible differences between matter and antimatter? How can we overcome the problem of hadronic structure in precision tests of quantum electrodynamic theory? How well can QED predict the energy levels of atoms with few electrons? What new physics can be discovered in experiments with exotic atoms? How well do we understand simple molecules? These are just a few of the questions that are now moving into a new focus.

This volume collects contributions from experts at the frontier of atomic and molecular precision physics. It illustrates the current state of the art, points at future opportunities, and emphasizes an exciting frontier in atomic and molecular physics that remains as important as ever despite several other strong currents and fashions in the field.

Since I have devoted more than three decades of my career to precision laser spectroscopy of the simple hydrogen atom, I am particularly grateful to the editor, Dr Savely G. Karshenboim, for his initiative to highlight such precision studies of simple atoms and molecules.

Garching
April, 2007

Theodor W. Hänsch

Preface

Precision studies of simple atomic and molecular systems are a multidisciplinary field in modern physics. They massively involve methods and objects from very different areas of physics.

Experimental methods vary from laser spectroscopy to accelerator physics, from laboratory desktop-scale experiments to space missions. On the theoretical side they deal with methods of molecular, atomic, nuclear, and particle physics.

The specific feature of this area is that the simple atoms and molecules are not the object of the studies, but a powerful instrument to look into the deepest and most basic problems of physics. The most advanced precision measurements allow us to see various tiny effects, while the atomic simplicity provides us with the possibility of keeping the atomic details under control and looking into a substantially more fundamental level.

Simple atoms and molecules provide us with a good opportunity to measure fundamental constants, to look for possible violation of basic symmetries, to study properties of elementary particles and nuclei.

This book is based on extended review lectures from two recent international meetings on simple atoms and presents the most recent progress in the field. I am grateful to Claudio Lenz Cesar, Jochen Walz, and Theodor W. Hänsch, who were co-organizers of these meetings (Mangaratiba, 2004, and Venice, 2006) and made great efforts to make these meetings happen, and to many other colleagues, whose help in organizing the meetings was important.

St.Petersburg—Garching
April, 2007

Savely Karshenboim

Contents

Looking Through Simple Atoms and Molecules at Fundamental Physics

<i>S. G. Karshenboim</i>	1
1 Introduction	1
References	4

Part I Precision Measurements and Fundamental Constants

The Muon $g-2$: Status and Perspectives

<i>F. Jegerlehner</i>	9
1 Lepton Magnetic Moments	9
2 The BNL Muon $g - 2$ Experiment	12
3 Standard Model Prediction for a_{μ}	15
3.1 The Universal QED Contribution	16
3.2 Mass-Dependent QED Contribution	17
3.3 Weak Contributions	19
3.4 Hadronic Contributions	22
4 Theory Confronting the Experiment	28
5 Prospects	30
References	32

Guide for Atomic and Particle Physicists into CODATA's Recommended Values of the Fundamental Physical Constants

<i>S. G. Karshenboim</i>	35
1 Introduction	35
2 The Adjustment of the Fundamental Constants: A General View	36
3 The Adjustment of the Fundamental Constants: The Data	37
4 Electrical Data	38
5 Recommended Values and the 'Less Accurate' Original Results	40

6	The Fine Structure Constant α and Related Data	41
7	The Planck Constant h and Related Data	43
8	The Newtonian Constant of Gravitation	44
9	The Fundamental Constants and Their Numerical Values	45
10	Microscopic and Macroscopic Quantities	46
11	Reliability of the Input Data and the Recommended Values	47
12	Proton Properties	48
13	Muon Properties	50
14	Impact of a Redefinition of the Kilogram on Values of the Fundamental Constants	51
15	Legacy of the Adjustment of the Fundamental Constants	52
	References	53

Part II Proton Structure and Hydrogen Energy Levels

Precise Radii of Light Nuclei from Electron Scattering

<i>I. Sick</i>		57
1	Introduction	57
2	Proton Charge Radius	57
3	Radius of Magnetization Density	65
4	Zemach Moment of Proton	66
5	Effect of Two-Photon Exchange	68
6	Third Zemach Moment of Proton	69
7	Deuteron Radius	69
8	Radii of $A = 3$ Systems	71
9	Radius of ${}^4\text{He}$	72
10	Heavier Nuclei	73
11	Summary	74
	References	75

Nucleon Form Factor Measurements in Mainz: Past and Future

<i>J. C. Bernauer for the A1 collaboration</i>		79
1	Introduction	79
2	Mainz Experiments	81
	2.1 The Mainz LINAC era	81
	2.2 The MAMI B era	84
	2.3 The MAMI C era	87
3	Conclusion and Outlook	90
	References	90

Proton Structure Corrections to Hydrogen Hyperfine Splitting

C. E. Carlson 93

1 Introduction 93

2 Hyperfine Splitting Calculations 94

 2.1 Elastic Terms: The Zemach Correction 95

 2.2 Elastic Terms: Recoil Corrections 96

 2.3 Inelastic Terms: Polarizability Corrections 98

3 Re-evaluation of Δ_{po} 101

4 Comments on the Derivations of the Formulas 103

5 Conclusion 105

References 106

Part III Atoms with Few Electrons

Precision Laser Spectroscopy of Li^+ and Neutral Lithium

W. A. van Wijngaarden and G. A. Noble 111

1 Introduction 111

2 Background 112

3 $\text{Li}^+ (1s)^2 \ ^3S \rightarrow 1s2p \ ^3P$ Transition 113

4 Li D Lines 118

5 Conclusions 127

References 128

Halo Nuclei in Laser Light

G. W. F. Drake, Z.-T. Lu, W. Nörtershäuser, and Z.-C. Yan 131

1 Introduction 131

2 Theory 133

 2.1 Solution to the Nonrelativistic Schrödinger Equation for Helium 134

 2.2 Variational Basis Sets for Lithium 135

 2.3 Relativistic Corrections 136

 2.4 QED Corrections 137

3 Theoretical Isotope Shifts 138

4 ^6He Isotope Shift and Nuclear Radius 141

5 Experiments in Lithium 144

 5.1 Experimental Technique 145

 5.2 Results 147

6 Discussion and Future Work 151

References 152

Part IV Exotic Atoms and Heavy Ions

Quantum Electrodynamics in Extreme Fields: Precision Spectroscopy of High-Z H-like Systems

Th. Stöhlker, A. Gumberidze, M. Trassinelli, V. Andrianov, H. F. Beyer, S. Kraft-Bermuth, A. Bleile, P. Egelhof, and The FOCAL collaboration 157

1 The Current Status of the Experimental and Theoretical Investigations 157

2 Next Generation Spectroscopic Experiments on High-Z H-like Ions 159

3 Conclusions 162

References 162

Pionic Hydrogen

D. Gotta, F. Amaro, D. F. Anagnostopoulos, S. Biri, D. S. Covita, H. Gorke, A. Gruber, M. Hennebach, A. Hirtl, T. Ishiwatari, P. Indelicato, Th. Jensen, E.-O. Le Bigot, J. Marton, M. Nekipelov, J. M. F. dos Santos, S. Schlessler, Ph. Schmid, L. M. Simons, Th. Strauch, M. Trassinelli, J. F. C. A. Veloso, and J. Zmeskal 165

1 Introduction 165

2 Pion–Nucleon Interaction at Threshold 167

3 Scattering Lengths and Pionic Atoms 169

 3.1 Pionic Hydrogen 169

 3.2 Pionic Deuterium 169

4 Atomic Cascade in Pionic Hydrogen 171

5 Experimental Approach 173

 5.1 Set-Up at PSI 173

 5.2 Energy Calibration 175

 5.3 Response Function 177

 5.4 Muonic Hydrogen 178

6 Results 179

 6.1 Transition Energy and Hadronic Shift 179

 6.2 Line Width and Hadronic Broadening 180

 6.3 Scattering Length and Pion–Nucleon Coupling Constant 181

7 Summary and Outlook 182

References 183

Precision Spectroscopy of Antiprotonic Helium Atoms and Ions – Weighing the Antiproton

R. S. Hayano 187

1 Introduction 187

2 Antiprotonic Helium Atoms 189

3 Principle of the $\bar{p}\text{He}^+$ Laser Spectroscopy 190

4 Why Further \bar{p} Deceleration Using an “Inverse Linac” Is Needed? .. 191

5	Further Improvement Using an Optical Frequency Comb	193
6	The First Measurement of a Metastable-to-Metastable Transition Frequency	197
7	Experimental Results	198
8	Summary and Outlook	199
	References	200

Part V Simple Molecules

Precision Spectroscopy of Molecular Hydrogen Ions: Towards Frequency Metrology of Particle Masses

B. Roth, J. Koelemeij, S. Schiller, L. Hilico, J.-P. Karr, V. Korobov, and D. Bakalov

1	Introduction	205
2	Ab Initio Theory of H_2^+ and HD^+	207
2.1	Variational Expansion	208
2.2	Leading-Order Relativistic and Radiative Corrections	209
2.3	$R_\infty\alpha^4$ Order Corrections in the Nonrecoil Limit	210
2.4	Hyperfine Structure of States	211
2.5	Two-Photon Transition Probabilities	214
3	Two-Photon Spectroscopy of H_2^+	215
3.1	H_2^+ Level Structure	215
3.2	One-Photon Transitions: Photodissociation	216
3.3	Two-Photon Transitions: Choice of the Transition	217
3.4	Experimental Sequence	218
3.5	Experimental Setup	219
3.6	Two-Photon Excitation Laser Source	220
4	Cooling and Spectroscopy of HD^+	222
4.1	Preparation and Characterization of Cold MHI Ensembles	222
4.2	Spectroscopy of HD^+	224
5	Conclusion and Outlook	229
	References	230

Nuclear Magnetic Dipole Moments from NMR Spectra – Quantum Chemistry and Experiment

M. Jaszunski and K. Jackowski

1	Introduction	233
2	NMR Shielding Constants	235
2.1	NMR Effective Spin Hamiltonian	235
2.2	Ab Initio Studies of NMR Shielding Constants	236
3	Comparison of the Gas-Phase NMR Spectra with Ab Initio Results	238
3.1	Spin-Rotation Constants	239
4	NMR Experiment in the Gas Phase	240

5	Nuclear Magnetic Moments – A General Scheme for Different Nuclei	242
6	Results and Discussion	244
6.1	NMR Shielding Constants for the First- and Second-Row Atoms	244
6.2	NMR Shielding Constants for the Third-Row and Heavier Atoms	246
7	Consistency of the New Values of Nuclear Magnetic Moments	249
7.1	New Values of the Nuclear Magnetic Dipole Moments	249
7.2	Derived Shielding Constants	250
7.3	Accuracy of the Results	253
8	Conclusions	257
	References	258
The Negative Ion of Positronium: Decay Rate Measurements and Prospects for Future Experiments		
	<i>F. Fleischer</i>	261
1	Introduction	261
2	A Brief Survey of the Properties of Ps^-	262
2.1	Ground-State Binding Energy	262
2.2	Annihilation and Decay Rates	263
2.3	Excitation and Resonances	266
3	Experiments with the Negative Positronium Ion	268
3.1	Production of Ps^-	268
3.2	Measurements of the Decay Rate	269
3.3	Outlook: Current Status of the Decay Rate Measurements and Prospects for Further Experiments	276
4	Conclusion	279
	References	280
	Index	283

Looking Through Simple Atoms and Molecules at Fundamental Physics

S. G. Karshenboim

D. I. Mendeleev Institute for Metrology (VNIIM), 190005 St. Petersburg, Russia
and Max-Planck-Institut für Quantenoptik Hans-Kopfermann-Str. 1, D-85748
Garching, Germany
savely.karshenboim@mpq.mpg.de

1 Introduction

Truly fundamental effects can seldom be studied directly. To learn about fundamental laws and fundamental quantities we have to find a probe object, which we can really deal with and properties of which we can express in terms of basic physical laws and fundamental constants. One of the most attractive kinds of such objects is simple atoms and molecules.

Their structure is described by quantum mechanics and electrodynamics and can be expressed in terms of such values as the speed of light c , the Planck constant h , the elementary charge e , masses of electron and proton, etc. Some rather effective parameters than fundamental ones, such as nuclear masses, magnetic moments and charge radii, are also needed, but their values can be achieved experimentally in terms of more fundamental quantities.

Meanwhile, atoms and molecules can be studied with various effective techniques by means of optical, radio and NMR spectroscopy. The effectivity of the various optical and microwave instruments has been a result of long progress in the field.

That makes the simple atomic and molecular systems a great opportunity to successfully access the deepest physical level. This book presents a collection of lectures on progress in the field. The lectures were presented in two international meetings on precision physics of simple atomic systems (PSAS'2004 in Mangaratiba, Brazil, and PSAS'2006 in Venice, Italy) which followed PSAS'2000 (Hydrogen Atom, II, Castiglione della Pescaia, Italy) and PSAS'2002 (St. Petersburg, Russia), the review contributions of which were published in [1, 2].

Here we give the progress in the subfields already presented in two previous books and consider more broad applications of simple atoms to fundamental physics.

The simplest atom, which is available for theoretical and experimental studies is indeed the hydrogen atom and actually the odd conferences (in

2000 and 2004) were named after it (the Hydrogen Atom, II, and the Hydrogen Atom, III) in order to emphasize the importance of the hydrogen atom meeting in Pisa in 1988. The earlier conferences involved a number of lectures devoted to the hydrogen atom (see, e.g. [3, 4, 5]). Besides, a good collection of important quantum electrodynamics (QED) contributions is presented in [6]. While the QED calculations present an example of a very advanced ab initio theory, they are not complete because of effects beyond QED. Here, we present a discussion of the effects of the proton structure [7, 8, 9], which was missed in the two previous books. These effects determine the accuracy of any ab initio calculations for hydrogen. A consideration of the nuclear effects in light atoms was also presented in part in one of the two earlier books [10], but a single publication could not cover all questions crucial for hydrogenic levels. Here, we present an overview of crucial experiments and data evaluation for the determination of details of the proton structure. We also consider effects of the proton structure on the hydrogen energy levels and especially on the ground state hyperfine interval.

The hydrogen atom contains only a single electron and general success in QED theory for such atoms (see, e.g., reviews [11, 12]) turns attention to atoms with two and three electrons. Here, we present two lectures on light atoms of this kind. While in the two previous books we focused our attention on neutral helium [13], here we give extensive reviews on neutral lithium and the lithium ion (Li^+) [14] as well as of neutral helium and lithium with halo nuclei [15]. Studies of a light atom with such a nucleus, which contains few additional neutrons, present an important opportunity for applications of atomic methods to nuclear physics [15]. Such halo nuclei are unstable and atomic methods can successfully deliver accurate data even for short-lived species.

Another possibility for simple atoms, also related to short-lived and/or artificial atoms, is to stay with two-body systems, but to study some systems which are harder to create than usual hydrogen. The easiest source of hydrogen-like atoms is accelerators which allow to strip electrons from nuclei with many electrons. Heavy hydrogen-like atoms are studied in [16]. More exotic atoms involve particles which are unstable by themselves (like a pion) or may annihilate with the others (like an antiproton). Pionic hydrogen is considered in [17] and its study can provide important information on pion–nucleon interaction, while antiprotonic helium is studied in [18]. The latter is a very interesting system.

In principle, an antiproton should annihilate with the nucleus very fast. However, a number of long-living states were discovered some time ago. Their long lifetime allowed precision study and offers a possibility for comparison of theory and experiment with high accuracy. A review on such an atomic system was published in our first book [19]. Still, surprisingly for accelerator physics, impressive progress in the field was achieved in a very short time and is presented here in [18]. There are a number of very specific features in this three-body system. One of them is a need for a high- n and high- l orbit of the

antiproton, which allows to reduce the annihilation rate dramatically. Such a high orbit for so massive a particle leads to a motion much slower than that of the electron. As a result, a system with one electron and two heavy slow particles is somewhat similar to the hydrogen molecular ion.

The hydrogen molecular ion is studied in [20]. While antiprotonic helium can be used to determine the mass of an antiproton (or rather $m_{\bar{p}}/m_e$), the molecular systems H_2^+ and HD^+ may be used to study the value of m_p/m_e and in particular to search for its possible variation with time or even for its accurate determination. Another molecular ion, Ps^- , is considered in [21]. It does not have any heavy nucleus and because of that one cannot apply the Born–Oppenheimer approximation (considering heavy nuclei at rest as the first approximation). This is a pure QED system and its study provides us with an additional possibility to test QED theoretical methods. In contrast to the transparent pure QED system, one more review on molecular physics [22] is related to NRM spectroscopy of various molecules, which allows to determine nuclear magnetic moments with high accuracy, and an appropriate theory of electronic shielding of the bare nuclear moments which plays a crucial role in the interpretation of such experiments.

The determination of fundamental constants and development and tests of the QED theory was always an important part of the PSAS topics (see, e.g. [5, 11]). In this book we present a discussion on applications of fundamental constants in atomic and particle physics [23] and also an overview of the status of the muon anomalous magnetic moment study [24]. For a few recent years theory and experiment were in a certain agreement, which was not a perfect one. The theory and supportive experiments were under intensive reconsideration. The present situation and perspectives need a clarification and we hope the review presented in this book will be helpful for that.

Studies of simple atoms in their relation to fundamental theories (such as QED), fundamental constants (such as the Rydberg constant R_∞ and the fine structure α) and properties of fundamental objects (such as the proton charge radius or the muon magnetic moment) were for a while an important part of physics. Advanced experimental and theoretical methods make the competition of theory and experiment very exciting and fruitful. Intensive progress in the field in the last decade was in part acknowledged by awarding the Nobel prize in physics in 2005 to two participants of our first meeting (PSAS'2000), namely John L. Hall and Theodor W. Hänsch, for their contribution to precision frequency measurements (see their joint contribution to PSAS'2000 book [25]).

A broad variety of methods and their deep advanced development have created various gaps between different groups studying hydrogen and other simple atomic systems. To intensify exchange and collaboration between different scientists working in the field, the conferences on simple atoms (PSAS) have been organized. The series started in 2000 in Castiglione della Pescaia, Italy, and since then have taken place every 2 years: in St. Petersburg (2002),

Mangaratiba (2004), Venice (2006). The next meeting is scheduled for 2008 in Windsor, Canada.

Various materials of the conferences were published. The review lectures have been published by Springer-Verlag as *Lectures Notes in Physics* [1, 2]. The contributed papers of the first meeting were published on CD as a part of [1], while for conferences in 2002 and 2004 they were published in the conference issues of the *Canadian Journal of Physics* [26, 27] and the papers for PSAS'2006 will also be published there [28].

This book consists of extended and updated review lectures of conferences in 2004 and 2006. This book is the last in the series since the Lectures Notes are now intended for pedagogical use. We would like to thank Springer-Verlag for the long-term cooperation in publishing our material.

To complete the introduction to the book I like to express my gratitude to all contributing authors and to those colleagues who took efforts to organize the meetings, in particular to Claudio Lenz Cesar, Jochen Walz, Theodor W. Hänsch, Valery Shelyuto, Gordon Drake and many others.

References

1. S. G. Karshenboim et al. (Eds.): *Hydrogen atom: Precision physics of simple atomic systems*, Lect. Notes Phys. **570**. Springer, Heidelberg (2001). [1, 4]
2. S. G. Karshenboim and V. B. Smirnov (Eds.): *Precision physics of simple atomic systems*, Lect. Notes Phys. **627**. Springer, Heidelberg (2003). [1, 4]
3. F. Biraben, T. W. Hänsch, M. Fischer, M. Niering, R. Holzwarth, J. Reichert, Th. Udem, M. Weitz, B. de Beauvoir, C. Schwob, L. Jozefowski, L. Hilico, F. Nez, L. Julien, O. Acaf, J.-J. Zondy, A. Clairon: in [1], pp. 17–41. [2]
4. L. Willmann and D. Kleppner: *Ultracold Hydrogen*, Lect. Notes Phys. **570**, 42–56. Springer, Heidelberg (2001). [2]
5. P. J. Mohr and B. N. Taylor: *Fundamental Constants and the Hydrogen Atom*, Lect. Notes Phys. **570**, 145–156. Springer, Heidelberg (2001). pp. 145–156. [2, 3]
6. M. I. Eides, H. Grotch and V. A. Shelyuto: Phys. Rep. **342**, 63 (2001); M. I. Eides, H. Grotch and V. A. Shelyuto: *Theory of light hydrogenic bound states* (Springer, Berlin, Heidelberg, 2006). [2]
7. I. Sick: *Precise Radii of Light Nuclei from Electron Scattering*, Lect. Notes Phys. **745**, Springer, Heidelberg (2008). [57–77] [2]
8. J. C. Bernauer: *Nucleon Form Factor Measurements in Mainz: Past and Future*, Lect. Notes Phys. **745**, Springer, Heidelberg (2008). 79–91. [2]
9. C. E. Carlson: *Proton Structure Corrections to Hydrogen Hyperfine, Splitting*, Lect. Notes Phys. **745**, Springer, Heidelberg (2008). 93–106. [2]
10. J. L. Friar: *The Structure of Light Nuclei and Its Effect on Precise Atomic Measurements*, Lect. Notes Phys. **627**, (Springer, Berlin, Heidelberg, 2003), pp. 59–79. [2]
11. S. G. Karshenboim: *Simple Atoms, Quantum Electrodynamics, and Fundamental Constants*, Lect. Notes Phys. **627**, 141–162. Springer, Heidelberg (2003). [2, 3]
12. S. G. Karshenboim: Phys. Rep. **422**, 1 (2005). [2]

13. G. W. F. Drake: *Review of High, Precision Theory and Experiment for Helium*, Lect. Notes Phys. **570**, 57–78. Springer, Heidelberg (2001). [2](#)
14. W. A. van Wijngaarden and G. A. Noble: *Precision Laser Spectroscopy of Li+ and Neutral Lithium*, Lect. Notes Phys. **745**, 109–127. Springer, Heidelberg (2008). [2](#)
15. G. W. F. Drake et al.: *Halo Nuclei in Laser Light*, Lect. Notes Phys. **745**, 131–153. Springer, Heidelberg (2008). [2](#)
16. Th. Stöhlker et al.: *Quantum Electrodynamics in Extreme Fields: Precision Spectroscopy of High-Z H-like Systems*, Lect. Notes Phys. **745**, 157–163. Springer, Heidelberg (2008). [2](#)
17. D. Gotta et al.: *Pionic Hydrogen*, Lect. Notes Phys. **745**, 165–185. Springer, Heidelberg (2008). [2](#)
18. R. S. Hayano: *Precision Spectroscopy of Antiprotonic Helium Atoms and Ions – Weighing the Antiproton*, Lect. Notes Phys. **745**, 187–201. Springer, Heidelberg (2008). [2](#)
19. T. Yamazaki: *Antiprotonic Helium – An Exotic Hydrogenic Atom*, Lect. Notes Phys. **570**, 246–265. Springer, Heidelberg (2001). [2](#)
20. B. Roth et al.: *Precision Spectroscopy of Molecular Hydrogen Ions: Towards Frequency Metrology of Particle Masses*, Lect. Notes Phys. **745**, 205–232. Springer, Heidelberg (2008). [3](#)
21. F. Fleischer: *The Negative Ion of Positronium: Decay Rate Measurements and Prospects for Future Experiments*, Lect. Notes Phys. **745**, 261–281. Springer, Heidelberg (2008). [3](#)
22. M. Jaszunski and K. Jackowski: *Nuclear Magnetic Dipole Moments from NMR Spectra – Quantum Chemistry and Experiment*, Lect. Notes Phys. **745**, 233–260. Springer, Heidelberg (2008). [3](#)
23. S. G. Karshenboim: *Guide for Atomic and Particle Physicists into CODATA'S Recommended Values of the Fundamental Physical Constants*, Lect. Notes Phys. **745**, 261–281. Springer, Heidelberg (2008). [3](#)
24. F. Jegerlehner: *The Muon g-2: Status and Perspectives* **745**, 9–34. Springer, Heidelberg (2008). [3](#)
25. T. Udem et al.: *A New Type of Frequency Chain and Its Application to Fundamental Frequency Metrology*, Lect. Notes Phys. **570**, 125–144. Springer, Heidelberg (2001). [3](#)
26. Canadian Journal of Physics, **80-4**, 1187–1432 (2002): Contributed papers to Conference issue of PSAS'2002 (St. Petersburg, Russia). [4](#)
27. Canadian Journal of Physics, **83-4**, 273–474 (2005): Contributed papers to Conference issue of PSAS'2004 (Mangaratiba, Brazil). [4](#)
28. Canadian Journal of Physics, **85-5**, 403–595 (2007): Contributed papers to Conference issue of PSAS'2006 (Venice, Italy). [4](#)

Precision Measurements and Fundamental
Constants

The Muon $g - 2$: Status and Perspectives

F. Jegerlehner

Humboldt-Universität zu Berlin, Institut für Physik, Newtonstrasse 15, D-12489 Berlin, Germany and DESY, Platanenallee 6, D-15738 Zeuthen, Germany
fjeger@physik.hu-berlin.de

Abstract. The muon anomalous magnetic moment is one of the most precisely measured quantities in particle physics. Recent high-precision measurements (0.5 ppm) at Brookhaven reveal a “discrepancy” by three standard deviations from the electroweak Standard Model which could be a hint for an unknown contribution from physics beyond the Standard Model. This triggered numerous speculations about the possible origin of the “missing piece”. The remarkable 15-fold improvement of the previous CERN experiment actually animated a multitude of new theoretical efforts which led to a substantial improvement of the prediction of a_μ . The dominating uncertainty of the prediction, caused by strong interaction effects, could be reduced substantially, due to new hadronic cross-section measurements in electron–positron annihilation at low energies. After an introduction and a brief description of the principle of the experiment, I review the status of the theoretical prediction and discuss the role of the hadronic vacuum polarization effects and the hadronic light-by-light scattering contribution. Prospects for the future will be briefly discussed. As, in electroweak precision physics, the muon $g - 2$ shows the largest established deviation between theory and experiment at present, it will remain one of the hot topics in future also.

1 Lepton Magnetic Moments

The subject of our interest is the motion of a lepton in an external electromagnetic field under consideration of the full relativistic quantum behavior. The latter is controlled by the equations of motion of quantum electrodynamics (QED), which describes the interaction of charged leptons ($\ell = e, \mu, \tau$) with the photon (γ) as an Abelian $U(1)_{\text{em}}$ gauge theory. QED is a quantum field theory (QFT) which emerges as a synthesis of quantum mechanics with special relativity. In our case an external electromagnetic field is added, specifically a constant homogeneous magnetic field \mathbf{B} . For slowly varying fields the motion is essentially determined by the generalized Pauli equation, which also serves as a basis for understanding the role of the magnetic moment of a lepton on the classical level. As we will see below, in the absence of electrical fields \mathbf{E} the

quantum correction miraculously may be subsumed in a single number, the anomalous magnetic moment a_ℓ , which is the result of relativistic quantum fluctuations, usually simply called *radiative corrections*.

Charged leptons in the first place interact with photons, and photonic radiative corrections can be calculated in QED, the interaction Lagrangian density of which is given by (e the magnitude of the electron's charge)

$$\mathcal{L}_{\text{int}}^{\text{QED}}(x) = e j_{\text{em}}^\mu(x) A_\mu(x) \quad , \quad j_{\text{em}}^\mu(x) = - \sum_\ell \bar{\psi}_\ell(x) \gamma^\mu \psi_\ell(x) \quad , \quad (1)$$

where $j_{\text{em}}^\mu(x)$ is the electromagnetic current, $\psi_\ell(x)$ the Dirac field describing the lepton ℓ , γ^μ the Dirac matrices and with a photon field $A_\mu(x)$ exhibiting an external classical component A_μ^{ext} and hence $A_\mu \rightarrow A_\mu + A_\mu^{\text{ext}}$. We are thus dealing with QED exhibiting an additional external field insertion “vertex”.

Besides charge, spin, mass and lifetime, leptons have other very interesting static (classical) electromagnetic and weak properties like the magnetic and electric dipole moments. A well-known example is the circulating current, due to an orbiting particle with electric charge e and mass m , which exhibits a magnetic dipole moment $\boldsymbol{\mu}_L = \frac{1}{2c} e \mathbf{r} \times \mathbf{v}$ given by

$$\boldsymbol{\mu}_L = \frac{e}{2mc} \mathbf{L} \quad (2)$$

where $\mathbf{L} = m \mathbf{r} \times \mathbf{v}$ is the orbital angular momentum (\mathbf{r} position, \mathbf{v} velocity). As we know, leptons have spin (intrinsic angular momentum) $\frac{1}{2}$, which is directly responsible for the intrinsic magnetic moment. The fundamental relation which defines the “ g -factor” or the magnetic moment is

$$\boldsymbol{\mu} = g_\ell \frac{e\hbar}{2m_\ell c} \mathbf{s} \quad , \quad \mathbf{s} \text{ the spin vector.} \quad (3)$$

For leptons, the Dirac theory predicts $g_\ell = 2$ [1], unexpectedly, twice the value $g = 1$ known to be associated with orbital angular momentum. It took about 20 years of experimental efforts to establish that the electrons' magnetic moment actually exceeds 2 by about 0.12%, the first clear indication of the existence of an “anomalous” contribution to the magnetic moment [2]. In general, the anomalous magnetic moment of a lepton is related to the gyromagnetic ratio by

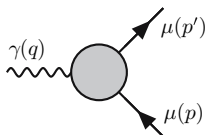
$$a_\ell = \mu_\ell / \mu_B - 1 = \frac{1}{2}(g_\ell - 2) \quad , \quad (\ell = e, \mu, \tau) \quad (4)$$

where μ_B is the Bohr magneton.

Formally, the anomalous magnetic moment is given by a form factor, defined by the matrix element

$$\langle \ell^-(p') | j_{\text{em}}^\mu(0) | \ell^-(p) \rangle$$

where $|\ell^-(p)\rangle$ is a lepton state of momentum p . The relativistically covariant decomposition of the matrix element reads



$$= (-ie) \bar{u}(p') \left[\gamma^\mu F_E(q^2) + i \frac{\sigma^{\mu\nu} q_\nu}{2m_\mu} F_M(q^2) \right] u(p)$$

with $q = p' - p$ and where $u(p)$ denotes a Dirac spinor, the relativistic wave function of a free lepton, a classical solution of the Dirac equation $(\gamma^\mu p_\mu - m) u(p) = 0$. $F_E(q^2)$ is the electric charge or Dirac form factor and $F_M(q^2)$ is the magnetic or Pauli form factor. Note that the matrix $\sigma^{\mu\nu} = \frac{i}{2} [\gamma^\mu, \gamma^\nu]$ represents the spin 1/2 angular momentum tensor. In the static (classical) limit $q^2 \rightarrow 0$ we have

$$F_E(0) = 1 \quad ; \quad F_M(0) = a_\mu \quad (5)$$

where the first relation is the charge normalization condition, which must be satisfied by the electrical form factor, while the second relation defines the anomalous magnetic moment. a_μ is a finite prediction in any renormalizable QFT: QED, the Standard Model (SM) or any renormalizable extension of it.

By the end of the 1940s the breakthrough in understanding and handling renormalization of QED had made unambiguous predictions of higher order effects possible, and in particular of the leading (one-loop diagram) contribution to the anomalous magnetic moment

$$a_\ell^{\text{QED}(1)} = \frac{\alpha}{2\pi}, \quad (\ell = e, \mu, \tau) \quad (6)$$

by Schwinger in 1948 [3]. This contribution is due to quantum fluctuations via virtual photon–lepton interactions and in QED is universal for all leptons. At higher orders, in the perturbative expansion, other effects come into play: strong interaction, weak interaction, both included in the SM, as well as yet unknown physics which would contribute to the anomalous magnetic moment.

In fact, shortly before Schwinger’s QED prediction, Kusch and Foley in 1948 established the existence of the electron “anomaly” $g_e = 2(1.00119 \pm 0.00005)$, a 1.2 per mill deviation from the value 2 predicted by Dirac in 1928.

We now turn to the muon. A muon looks like a copy of an electron, which at first sight is just much heavier $m_\mu/m_e \sim 200$; however, unlike the electron it is unstable and its lifetime is actually rather short. The decay proceeds by weak charged current interaction into an electron and two neutrinos.

The muon is very interesting for the following reason: quantum fluctuations due to heavier particles or contributions from higher energy scales are proportional to

$$\frac{\delta a_\ell}{a_\ell} \propto \frac{m_\ell^2}{M^2} \quad (M \gg m_\ell), \quad (7)$$

where M may be

- the mass of a heavier SM particle, or
- the mass of a hypothetical heavy state beyond the SM, or
- an energy scale or an ultraviolet cut-off where the SM ceases to be valid.

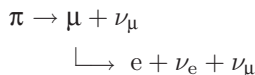
On the one hand, this means that the heavier the new state or scale the harder it is to see (it decouples as $M \rightarrow \infty$), typically the best sensitivity we have for nearby new physics, which has not yet been discovered by other experiments. On the other hand, the sensitivity to “new physics” grows quadratically with the mass of the lepton, which means that the interesting effects are magnified in a_μ relative to a_e by a factor $(m_\mu/m_e)^2 \sim 4 \times 10^4$. This is what makes the anomalous magnetic moment of the muon the predestinated “monitor for new physics” or if no deviation is found it may provide severe constraints to physics beyond the SM.

In contrast, a_e is relatively insensitive to unknown physics and can be predicted very precisely, and therefore it presently provides the most precise determination of the fine structure constant $\alpha = e^2/4\pi$.

What makes the muon so special for what concerns its anomalous magnetic moment?

- Most interesting is the enhanced high sensitivity of a_μ to all kind of interesting physics effects.
- Both experimentally and theoretically a_μ is a “clean” observable, i.e., it can be measured with high precision as well as predicted unambiguously in the SM.
- That a_μ can be measured so precisely is a kind of miracle and possible only due to the specific properties of the muon. Due to the parity violating weak (V–A) interaction property, muons can easily be polarized and perfectly transport polarization information to the electrons produced in their decay.
- There exists a magic energy (“magic γ ”) at which equations of motion take a particularly simple form. Miraculously, this energy is so high (3.1 GeV) that the μ lives 30 times longer than in its rest frame! In fact only these highly energetic muons can be collected in a muon storage ring. At much lower energies muons could not be stored long enough to measure the precession precisely!

Production and decay of the muons goes by the chain



2 The BNL Muon $g - 2$ Experiment

The first measurement of the anomalous magnetic moment of the muon became possible at the CERN cyclotron (1958–1962) [4] in 1961. Surprisingly, nothing special was observed within the 0.4% level of accuracy of the experiment. It was the first real evidence that the muon was just a heavy electron. In particular this meant that the muon is point-like and no extra short distance

effects could be seen. This latter point of course is a matter of accuracy and the challenge to go further was evident.

The idea of a muon storage ring was put forward next. A first one was successfully realized at CERN (1962–1968) [5]. It allowed to measure a_μ for both μ^+ and μ^- at the same machine. Results agreed well within errors and provided a precise verification of the CPT theorem for muons. An accuracy of 270 ppm was reached and an insignificant 1.7σ ($1\sigma = 1$ standard deviation) deviation from theory was found. Nevertheless the latter triggered a reconsideration of theory. It turned out that in the estimate of the three-loop $O(\alpha^3)$ QED contribution the leptonic light-by-light scattering part (dominated by the electron loop) was missing. Aldins et al. [6] then calculated this and after including it, perfect agreement between theory and experiment was obtained.

The CERN muon $g-2$ experiment was shut down at the end of 1976, while data analysis continued to 1979 [7]. Only a few years later, in 1984 the E821 collaboration formed, with the aim to perform a new experiment at Brookhaven National Laboratory (BNL). Data taking was between 1998 and 2001. Data analysis was completed in 2004. The E821 $g-2$ measurements achieved the remarkable precision of 0.5 ppm [8], which is a 15-fold improvement of the CERN result. The principle of the BNL muon $g-2$ experiments involves the study of the orbital and spin motion of highly polarized muons in a magnetic storage ring. This method has been applied in the last CERN experiment already. The key improvements of the BLN experiment include the very high intensity of the primary proton beam from the alternating gradient synchrotron (AGS), the injection of muons instead of pions into the storage ring and a superferroc storage ring magnet. The protons hit a target and produce pions. The pions are unstable and decay into muons plus a neutrino where the muons carry spin and thus a magnetic moment which is directed along the direction of the flight axis. The longitudinally polarized muons from pion decay are then injected into a uniform magnetic field \mathbf{B} where they travel in a circle. If one lets travel polarized muons on a circular orbit in a constant magnetic field, as illustrated in Fig. 1, then a_μ is responsible for the Larmor precession of the direction of the spin of the muon, characterized by the angular frequency ω_a . At the magic energy of about ~ 3.1 GeV, the latter is directly proportional to a_μ :

$$\omega_a = \frac{e}{m} \left[a_\mu \mathbf{B} - \left(a_\mu - \frac{1}{\gamma^2 - 1} \right) \boldsymbol{\beta} \times \mathbf{E} \right]_{\text{at "magic } \gamma}^{E \sim 3.1 \text{ GeV}} \simeq \frac{e}{m} [a_\mu \mathbf{B}]. \quad (8)$$

Electric quadrupole fields \mathbf{E} are needed for focusing the beam and they affect the precession frequency in general. $\gamma = E/m_\mu = 1/\sqrt{1-\beta^2}$ is the relativistic Lorentz factor with $\beta = v/c$, the velocity of the muon in units of the speed of light c . The magic energy $E_{\text{mag}} = \gamma_{\text{mag}} m_\mu$ is the energy E for which $\frac{1}{\gamma_{\text{mag}}^2 - 1} = a_\mu$. The existence of a solution is due to the fact that a_μ is a positive constant in competition with an energy-dependent factor of opposite sign (as $\gamma \geq 1$). The second miracle, which is crucial for the feasibility of the

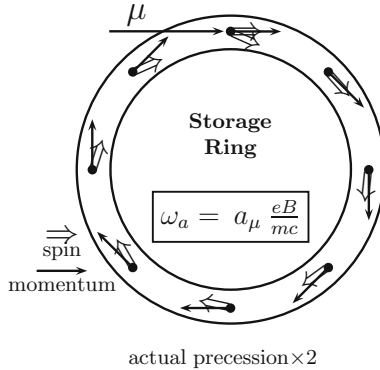


Fig. 1. Spin precession in the $g - 2$ ring ($\sim 12^\circ/\text{circle}$)

experiment, is the fact that $\gamma_{\text{mag}} = \sqrt{(1 + a_\mu)/a_\mu} \simeq 29.378$ is large enough to provide the time dilatation factor for the unstable muon boosting the life time $\tau_\mu \simeq 2.197 \times 10^{-6}$ s to $\tau_{\text{in flight}} = \gamma \tau_\mu \simeq 6.454 \times 10^{-5}$ s, which allows the muons, traveling at $v/c = 0.99942 \dots$, to be stored in a ring of reasonable size (diameter ~ 14 m). This provided the basic setup for the $g - 2$ experiments at the muon storage rings at CERN and BNL. The oscillation frequency ω_a can be measured very precisely. Also the precise tuning to the magic energy is not the major problem. The most serious challenge is to manufacture a precisely known constant magnetic field B , as the latter directly enters the experimental extraction of a_μ (8). Of course one also needs high-enough statistics to get sharp values for the oscillation frequency. The basic principle of the measurement of a_μ is a measurement of the “anomalous” frequency difference $\omega_a = |\omega_a| = \omega_s - \omega_c$, where $\omega_s = g_\mu (e\hbar/2m_\mu) B/\hbar = g_\mu/2 \cdot e/m_\mu B$ is the muon spin-flip precession frequency in the applied magnetic field and $\omega_c = e/m_\mu B$ is the muon cyclotron frequency. Instead of eliminating the magnetic field by measuring ω_c , B is determined from proton nuclear magnetic resonance (NMR) measurements. This procedure requires the value of μ_μ/μ_p to extract a_μ from the data. Fortunately, a high-precision value for this ratio is available from the measurement of the hyperfine structure in muonium. One obtains

$$a_\mu = \frac{\bar{R}}{|\mu_\mu/\mu_p| - \bar{R}}, \quad (9)$$

where $\bar{R} = \omega_a/\bar{\omega}_p$ and $\bar{\omega}_p = (e/m_\mu c) \langle B \rangle$ is the free proton NMR frequency which corresponds to the average magnetic field, seen by the muons in their orbits in the storage ring. We mention that for the electron a Penning trap is employed to measure a_e rather than a storage ring. The B field in this case can be eliminated via a measurement of the cyclotron frequency.

Since the spin precession frequency can be measured very well, the precision at which $g - 2$ can be measured is essentially determined by the possibility

to manufacture a constant homogeneous magnetic field \mathbf{B} . Important but easier to achieve is the tuning to the magic energy.

3 Standard Model Prediction for a_μ

The anomalous magnetic moment a_ℓ is a dimensionless quantity, just a number, and corresponds to an effective tensor interaction term

$$\delta\mathcal{L}_{\text{eff}}^{\text{AMM}} = -\frac{e_\ell a_\ell}{4m_\ell} \bar{\psi}(x) \sigma^{\mu\nu} \psi(x) F_{\mu\nu}(x), \quad (10)$$

which in an external magnetic field at low energy takes the well-known form of a magnetic energy (up to a sign)

$$\delta\mathcal{L}_{\text{eff}}^{\text{AMM}} = -\mathcal{H}_m \simeq -\frac{e_\ell a_\ell}{2m_\ell} \boldsymbol{\sigma} \mathbf{B}. \quad (11)$$

Such a term, if present in the fundamental Lagrangian, would spoil renormalizability of the theory and contribute to $F_M(q^2)$ at the tree level. In addition, it is not $SU(2)_L$ gauge invariant, because gauge invariance only allows minimal couplings via a covariant derivative, i.e., vector and/or axial-vector terms. The emergence of an anomalous magnetic moment term in the SM is a consequence of the symmetry breaking by the Higgs mechanism, which provides the mass to the physical particles and allows for helicity flip processes like the anomalous magnetic moment transitions. In any renormalizable theory the anomalous magnetic moment term must vanish at tree level. This means that there is no free adjustable parameter associated with it. Actually, it is a finite prediction of the theory.

The reason why it is so interesting to have such a precise measurement of a_e or a_μ of course is that it can be calculated with comparable accuracy in theory by a perturbative expansion in α of the form

$$a_\ell \simeq \sum_{n=1}^N A^{(2n)} (\alpha/\pi)^n, \quad (12)$$

with up to $N = 5$ terms under consideration at present. The recent new determination of a_e [9] allows for a very precise determination of the fine structure constant [10]:

$$\alpha^{-1}(a_e) = 137.035999070(98) [0.71 \text{ ppb}], \quad (13)$$

which we will use for the evaluation of a_μ .

At two and more loops results depend on lepton mass ratios. For the evaluation of these contributions precise values for the lepton masses are needed. We will use the following values for the muon–electron mass ratio, the muon and the tau mass [11, 12]:

$$\begin{aligned} m_\mu/m_e &= 206.768\,2838(54), & m_\mu/m_\tau &= 0.059\,4592(97) \\ m_e &= 0.510\,9989\,918(44) \text{ MeV}, & m_\mu &= 105.658\,3692(94) \text{ MeV} \\ & & m_\tau &= 1776.99(29) \text{ MeV}. \end{aligned} \quad (14)$$

3.1 The Universal QED Contribution

The leading contributions to a_ℓ can be calculated in QED. With increasing precision, higher and higher terms become relevant. At present, 4 loops are indispensable and strong interaction effects like hadronic vacuum polarization (vap) or hadronic light-by-light scattering (lbl) as well as weak effects have to be considered. Typically, analytic results for higher order terms may be expressed in terms of the Riemann zeta function:

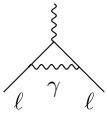
$$\zeta(n) = \sum_{k=1}^{\infty} \frac{1}{k^n} \quad (15)$$

and of the poly-logarithmic integrals

$$\text{Li}_n(x) = \frac{(-1)^{n-1}}{(n-2)!} \int_0^1 \frac{\ln^{n-2}(t) \ln(1-tx)}{t} dt = \sum_{k=1}^{\infty} \frac{x^k}{k^n}. \quad (16)$$

We first discuss the universal contributions a_ℓ where internal and external leptons are of the same type ℓ (one flavor QED): at leading order one has

- One 1-loop diagram



$$a_e = a_\mu = a_\tau = \frac{\alpha}{2\pi}$$

Schwinger 1948 [3] giving the result mentioned before.

- At 2-loops seven diagrams with one type of fermion lines



which contribute a term

$$a_\ell^{(4)} = \left[\frac{197}{144} + \frac{\pi^2}{12} - \frac{\pi^2}{2} \ln 2 + \frac{3}{4} \zeta(3) \right] \left(\frac{\alpha}{\pi} \right)^2, \quad (17)$$

obtained independently by Petermann [13] and Sommerfield [14] in 1957.

- At 3-loops, with ℓ -type fermion lines only, 72 diagrams contribute. Most remarkably, after about 25 years of hard work, Laporta and Remiddi in 1996 [15] managed to give a complete analytic result:

$$a_\ell^{(6)} = \left[\frac{28259}{5184} + \frac{17101}{810} \pi^2 - \frac{298}{9} \pi^2 \ln 2 + \frac{139}{18} \zeta(3) + \frac{100}{3} \left\{ \text{Li}_4 \left(\frac{1}{2} \right) + \frac{1}{24} \ln^4 2 - \frac{1}{24} \pi^2 \ln^2 2 \right\} - \frac{239}{2160} \pi^4 + \frac{83}{72} \pi^2 \zeta(3) - \frac{215}{24} \zeta(5) \right] \left(\frac{\alpha}{\pi} \right)^3. \quad (18)$$

It was confirming Kinoshita's earlier numerical evaluation [16]. The big advantage of the analytic result is that it allows a numerical evaluation at any desired precision. The direct numerical evaluation of the multidimensional Feynman integrals by Monte Carlo methods is always of limited precision and an improvement is always very expensive in computing power.

- At 4-loops 891 diagrams contribute to the universal term. Their evaluation is possible by numerical integration and has been performed in a heroic effort by Kinoshita [17] (reviewed in [18]) and was updated recently by Kinoshita and collaborators (2006/2007) [19, 20].

The largest uncertainty comes from 518 diagrams without fermion-loops contributing to the universal term $A_1^{(8)}$. Completely unknown is the universal 5-loop term $A_1^{(10)}$, which is leading for a_e . Some estimation discussed in [21] suggests an uncertainty of 3.8 for the 5-loop coefficient. We adopt this estimate and take into account $A_1^{(10)} = 0.0(3.8)$ (as in [19]).

Collecting the universal terms we have

$$\begin{aligned}
 a_\ell^{\text{uni}} &= 0.5 \left(\frac{\alpha}{\pi}\right) - 0.32847896557919378 \dots \left(\frac{\alpha}{\pi}\right)^2 \\
 &\quad + 1.181241456587 \dots \left(\frac{\alpha}{\pi}\right)^3 - 1.7283(35) \left(\frac{\alpha}{\pi}\right)^4 + 0.0(3.8) \left(\frac{\alpha}{\pi}\right)^5 \\
 &= 0.001\,159\,652\,176\,42(81)(10)(26) [86] \dots
 \end{aligned} \tag{19}$$

for the one-flavor QED contribution. The three errors are: the error of α , given in (13), the numerical uncertainty of the α^4 coefficient and the estimated size of the missing higher order terms, respectively.

3.2 Mass-Dependent QED Contribution

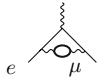
At two loops and higher, internal fermion-loops show up, where the flavor of the internal fermion differs from the one of the external lepton, in general. As all fermions have different masses, the fermion-loops give rise to mass-dependent effects, which were calculated at 2-loops in [22, 23] (see also [24, 25, 26]), and at 3-loops in [27, 28, 29, 30, 31, 32]. The leading mass-dependent effects come from photon vacuum polarization, which leads to charge screening manifest in the “running” of α . The corresponding shift in the fine structure constant comes from the leptons ($\text{lep} = e, \mu$ and τ), the five light quarks (u, b, s, c and b) and/or the corresponding hadrons (had). The running of α is governed by the renormalization group (RG).

Typical contributions are the following:

- LIGHT internal masses give rise to logs of mass ratios which become singular in the light mass to zero limit (logarithmically enhanced corrections):

$$\begin{array}{c} \text{---} \\ \diagup \quad \diagdown \\ \mu \quad \text{---} \quad e \end{array} = \left[\frac{1}{3} \ln \frac{m_\mu}{m_e} - \frac{25}{36} + O\left(\frac{m_e}{m_\mu}\right) \right] \left(\frac{\alpha}{\pi}\right)^2 .$$

- HEAVY internal masses decouple, i.e., they give no effect in the heavy mass to infinity limit:

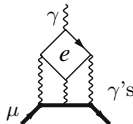


$$= \left[\frac{1}{45} \left(\frac{m_e}{m_\mu} \right)^2 + O \left(\frac{m_e^4}{m_\mu^4} \ln \frac{m_\mu}{m_e} \right) \right] \left(\frac{\alpha}{\pi} \right)^2 .$$

New physics contributions from states which are too heavy to be produced at present accelerator energies typically give this kind of contribution. Even though a_μ is 786 times less precise than a_e it is still 54 times more sensitive to new physics (NP).

Corrections due to internal e, μ - and τ -loops are different for a_e ,^[1] a_μ and a_τ .

The SM prediction of a_μ looks formally very similar to the one for a_e ; however, besides the common universal part, the mass-dependent, the hadronic and the weak effects enter with very different weight and significance. The mass-dependent QED corrections follow from the universal set of diagrams by replacing the closed internal μ -loops by e- and/or τ -loops. Typical contributions come from vacuum polarization or light-by-light scattering loops, like



$$a_\mu^{(6)}(\text{lbl}, e) = \left[\frac{2}{3} \pi^2 \ln \frac{m_\mu}{m_e} + \frac{59}{270} \pi^4 - 3 \zeta(3) - \frac{10}{3} \pi^2 + \frac{2}{3} + O \left(\frac{m_e}{m_\mu} \ln \frac{m_\mu}{m_e} \right) \right] \left(\frac{\alpha}{\pi} \right)^3 .$$

The result is given by

$$a_\mu = a_e^{\text{uni}} + a_\mu(m_\mu/m_e) + a_\mu(m_\mu/m_\tau) + a_\mu(m_\mu/m_e, m_\mu/m_\tau) \quad (22)$$

with [23, 30, 31, 32]

¹ A new extraordinary precise value

$$a_e^{\text{exp}} = 0.001\,159\,652\,180\,85(76) \quad (20)$$

for a_e has been obtained recently [9]. By comparison with the theoretical result $\alpha(a_e)$ (13) has been obtained. The result is of the form $a_e^{\text{QED}} = a_e^{\text{uni}} + a_e(\mu) + a_e(\tau) + e_e(\mu, \tau)$ with $a_e(\mu) = 5.197\,386\,70(27) \times 10^{-7} \left(\frac{\alpha}{\pi} \right)^2 - 7.373\,941\,64(29) \times 10^{-6} \left(\frac{\alpha}{\pi} \right)^3$, $a_e(\tau) = 1.83763(60) \times 10^{-9} \left(\frac{\alpha}{\pi} \right)^2 - 6.5819(19) \times 10^{-8} \left(\frac{\alpha}{\pi} \right)^3$ and $a_e(\mu, \tau) = 0.190945(62) \times 10^{-12} \left(\frac{\alpha}{\pi} \right)^3$ [23, 30, 31]. The QED part thus may be summarized in the prediction

$$a_e^{\text{QED}} = \frac{\alpha}{2\pi} - 0.328\,478\,444\,002\,90(60) \left(\frac{\alpha}{\pi} \right)^2 + 1.181\,234\,016\,828(19) \left(\frac{\alpha}{\pi} \right)^3 - 1.9144(35) \left(\frac{\alpha}{\pi} \right)^4 + 0.0(3.8) \left(\frac{\alpha}{\pi} \right)^5 + 1.706(30) \times 10^{-12} . \quad (21)$$

The last term includes the small hadronic and weak contributions: $a_e^{\text{had}} = 1.67(3) \times 10^{-12}$ and $a_e^{\text{weak}} = 0.036 \times 10^{-12}$, respectively. Therefore a_e is almost a pure QED object and therefore an excellent observable for extracting α_{QED} based on the SM prediction.

$$\begin{aligned}
 a_\mu(m_\mu/m_e) &= 1.094\,258\,311\,1\,(84) \left(\frac{\alpha}{\pi}\right)^2 + 22.868\,380\,02\,(20) \left(\frac{\alpha}{\pi}\right)^3 \\
 &\quad + 132.682\,3\,(72) \left(\frac{\alpha}{\pi}\right)^4, \\
 a_\mu(m_\mu/m_\tau) &= 7.8064\,(25) \times 10^{-5} \left(\frac{\alpha}{\pi}\right)^2 + 36.051\,(21) \times 10^{-5} \left(\frac{\alpha}{\pi}\right)^3 \\
 &\quad + 0.005\,(3) \left(\frac{\alpha}{\pi}\right)^4, \\
 a_\mu(m_\mu/m_e, m_\mu/m_\tau) &= 52.766\,(17) \times 10^{-5} \left(\frac{\alpha}{\pi}\right)^3 + 0.037\,594\,(83) \left(\frac{\alpha}{\pi}\right)^4;
 \end{aligned}$$

except for the last term, which has been worked out as a series expansion in the mass ratios [33, 34], all contributions are known analytically in exact form [30, 31]² up to 3 loops. At 4 loops only a few terms are known analytically [36]. Again the relevant 4-loop contributions have been evaluated by numerical integration methods by Kinoshita and Nio [37]. The 5-loop term has been estimated to be $A_2^{(10)}(m_\mu/m_e) = 663(20)$ in [38, 39, 40].

Our knowledge of the QED result for a_μ may be summarized by

$$\begin{aligned}
 a_\mu^{\text{QED}} &= \frac{\alpha}{2\pi} + 0.765\,857\,410(26) \left(\frac{\alpha}{\pi}\right)^2 \\
 &\quad + 24.050\,509\,65(46) \left(\frac{\alpha}{\pi}\right)^3 + 130.8105(85) \left(\frac{\alpha}{\pi}\right)^4 + 663(20) \left(\frac{\alpha}{\pi}\right)^5. \quad (23)
 \end{aligned}$$

We thus arrive at a QED prediction of a_μ given by

$$a_\mu^{\text{QED}} = 116\,584\,718.113(.082)(.014)(.025)(.137)[.162] \times 10^{-11} \quad (24)$$

where the first error is the uncertainty of α in (13), the second one combines in quadrature the uncertainties due to the errors in the mass ratios, the third is due to the numerical uncertainty and the last stands for the missing $O(\alpha^5)$ terms. With the new value of $\alpha[a_e]$ the combined error is dominated by our limited knowledge of the 5-loop term.

3.3 Weak Contributions

The electroweak SM is a non-Abelian gauge theory with gauge group $SU(2)_L \otimes U(1)_Y \rightarrow U(1)_{\text{QED}}$, which is broken down to the electromagnetic Abelian subgroup $U(1)_{\text{QED}}$ by the Higgs mechanism, which requires a scalar Higgs field H which receives a vacuum expectation value v . The latter fixes the experimentally well-known Fermi constant $G_\mu = 1/(\sqrt{2}v^2)$ and induces the masses of the heavy gauge bosons M_W and M_Z ³ as well as all fermion masses

² Explicitly, the papers only present expansions in the mass ratios; some result have been extended in [32] and cross-checked against the full analytic result in [35].

³ $M_Z = 91.1876 \pm 0.0021$ GeV, $M_W = 80.403 \pm 0.026$ GeV, also $m_H > 115$ GeV.

m_f . Other physical constants which we will need later for evaluating the weak contributions are the Fermi constant and the weak mixing parameter:

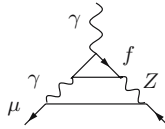
$$G_\mu = 1.16637(1) \times 10^{-5} \text{ GeV}^{-2}, \quad \sin^2 \Theta_W = 0.2225(5). \quad (25)$$

The weak interaction contributions to a_μ are due to the exchange of the heavy gauge bosons, the charged W^\pm and the neutral Z , which mixes with the photon via a rotation by the weak mixing angle Θ_W and which defines the weak mixing parameter $\sin^2 \Theta_W = 1 - M_W^2/M_Z^2$. What is most interesting is the occurrence of the first diagram of Fig. 2, which exhibits a non-Abelian triple gauge vertex and the corresponding contribution provides a test of the Yang–Mills structure involved. It is of course not surprising that the photon couples to the charged W boson the way it is dictated by electromagnetic gauge invariance. The gauge boson contributions up to negligible terms of order $O(\frac{m_\mu^2}{M_{W,Z}^2})$ are given by (the Higgs contribution is negligible)

$$a_\mu^{(2)\text{EW}} = [5 + (-1 + 4 \sin^2 \Theta_W)^2] \frac{\sqrt{2}G_\mu m_\mu^2}{48\pi^2} \simeq 194.82(2) \times 10^{-11}. \quad (26)$$

The error comes from the uncertainty in $\sin^2 \Theta_W$ given above.

The electroweak 2-loop corrections have to be taken into account as well. In fact triangle fermion-loops may give rise to unexpectedly large radiative corrections. The diagrams which yield the leading corrections are those including a VVA triangular fermion-loops ($VVA \neq 0$ while $VVV = 0$) associated with a Z boson exchange



which exhibits a parity violating axial coupling (A). A fermion of flavor f yields a contribution

$$a_\mu^{(4)\text{EW}}([f]) \simeq \frac{\sqrt{2}G_\mu m_\mu^2}{16\pi^2} \frac{\alpha}{\pi} 2T_{3f} N_{\text{cf}} Q_f^2 \left[3 \ln \frac{M_Z^2}{m_{f'}^2} + C_f \right] \quad (27)$$

where T_{3f} is the third component of the weak isospin, Q_f the charge and N_{cf} the color factor, 1 for leptons, 3 for quarks. The mass $m_{f'}$ is m_μ if $m_f < m_\mu$

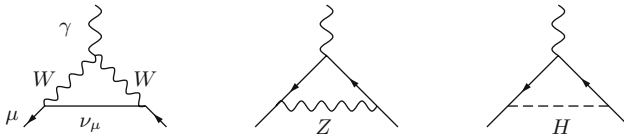


Fig. 2. The leading weak contributions to a_ℓ ; diagrams in the physical unitary gauge

and m_f if $m_f > m_\mu$, and $C_e = 5/2$, $C_\mu = 11/6 - 8/9 \pi^2$, $C_\tau = -6$ [41]. However, in the SM the consideration of individual fermions makes no sense and a separation of quarks and leptons is not possible. Mathematical consistency of the SM requires complete VVA anomaly cancellation between lepton and quark and actually $\sum_f N_{cf} Q_f^2 T_{3f} = 0$ holds for each of the three known lepton–quark families separately. Indeed, the $\sim \ln M_Z$ terms cancel if quarks are treated as free fermions [42]. However, strong interaction effects must be included as well.

In fact, low-energy QCD is characterized in the *chiral limit* of massless light quarks u,d,s, by *spontaneous chiral symmetry breaking* ($S\chi SB$) of the chiral group $SU(3)_V \otimes SU(3)_A$, which in particular implies the existence of the pseudo-scalar octet of pions and kaons as Goldstone bosons. The light quark condensates are essential features in this situation and lead to non-perturbative effects completely absent in a perturbative approach. Thus low-energy QCD effects are intrinsically non-perturbative and controlled by chiral perturbation theory (CHPT), the systematic QCD low-energy expansion, which accounts for the $S\chi SB$ and the chiral symmetry breaking by quark masses in a systematic manner. The low-energy effective theory describing the hadronic contributions related to the light quarks u,d,s requires the calculation of the diagrams of the type shown in Fig. 3. The leading effect for the first plus second family takes the form [43]

$$\begin{aligned}
 a_\mu^{(4)\text{EW}} \left(\begin{array}{c} [e, u, d] \\ [\mu, c, s] \end{array} \right)_{\text{CHPT}} &= \frac{\sqrt{2} G_\mu m_\mu^2}{16\pi^2} \frac{\alpha}{\pi} \left[-\frac{14}{3} \ln \frac{M_\Lambda^2}{m_\mu^2} + 4 \ln \frac{M_\Lambda^2}{m_c^2} - \frac{35}{3} + \frac{8}{9} \pi^2 \right] \\
 &\simeq -\frac{\sqrt{2} G_\mu m_\mu^2}{16\pi^2} \frac{\alpha}{\pi} \times 26.2(5) \simeq -7.09(13) \times 10^{-11}. \quad (28)
 \end{aligned}$$

The error comes from varying the cut-off M_Λ between 1 and 2 GeV. Below 1 GeV CHPT can be trusted above 2 GeV we can trust pQCD. Fortunately the result is not very sensitive to the choice of the cut-off. For more sophisticated analyses we refer to [42, 43, 44] which was corrected and refined in [45, 46]. Thereby, a new kind of non-renormalization theorems played a key role [47, 48, 49]. Including subleading effects yields -5.0×10^{-11} for the first two families. The third family of fermions including the heavy top quark can be treated in perturbation theory and was worked out to

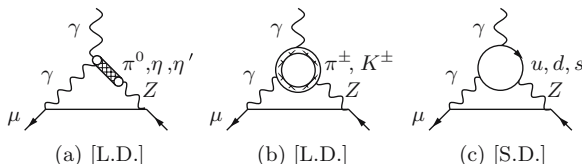


Fig. 3. The two leading CHPT diagrams (L.D.) and the QPM diagram (S.D.). The charged pion loop is sub-leading and is actually discarded. Diagrams with permuted $\gamma \leftrightarrow Z$ on the μ -line have to be included

be -8.2×10^{-11} in [50]. Subleading fermion-loops contribute -5.3×10^{-11} . There are many more diagrams contributing, in particular the calculation of the bosonic contributions (1678 diagrams) is a formidable task and has been performed by Czarnecki, Krause and Marciano (1996) as an expansion in $(m_\mu/M_V)^2$ and $(M_V/m_H)^2$ [51]. Later complete calculations, valid also for lighter Higgs masses, were performed [52, 53], which confirmed the previous result -22.3×10^{-11} .

The complete weak contribution may be summarized by [46]

$$\begin{aligned} a_\mu^{\text{EW}} &= \frac{\sqrt{2}G_\mu m_\mu^2}{16\pi^2} \left\{ \frac{5}{3} + \frac{1}{3} (1 - 4 \sin^2 \Theta_W)^2 - \frac{\alpha}{\pi} [155.5(4)(2)] \right\} \\ &= (154 \pm 1[\text{had}] \pm 2[m_H, m_t, \text{3-loop}]) \times 10^{-11} \end{aligned} \quad (29)$$

with errors from triangle quark-loops and from variation of the Higgs mass in the range $m_H = 150_{-40}^{+100}$ GeV. The 3-loop effect has been estimated to be negligible [45, 46].

3.4 Hadronic Contributions

So far when we were talking about fermion-loops we only considered the lepton loops. Besides the leptons the strongly interacting quarks also have to be taken into account. The problem is that strong interactions at low energy are non-perturbative and straightforward first principle calculations become very difficult and often impossible.

Fortunately the leading hadronic effects are vacuum polarization type corrections, which can be safely evaluated by exploiting causality (analyticity) and unitarity (optical theorem) together with experimental low-energy data. The imaginary part of the photon self-energy function $\Pi_\gamma(s)$ is determined via the optical theorem by the total cross-section of hadron production in electron-positron annihilation:

$$\sigma(s)_{e^+e^- \rightarrow \gamma^* \rightarrow \text{hadrons}} = \frac{4\pi^2\alpha}{s} \frac{1}{\pi} \text{Im} \Pi_\gamma(s). \quad (30)$$

The leading hadronic contribution is represented by Fig. 4, which has a representation as a dispersion integral

$$a_\mu = \frac{\alpha}{\pi} \int_0^\infty \frac{ds}{s} \frac{1}{\pi} \text{Im} \Pi_\gamma(s) K(s), \quad K(s) \equiv \int_0^1 dx \frac{x^2(1-x)}{x^2 + \frac{s}{m_\mu^2}(1-x)}. \quad (31)$$

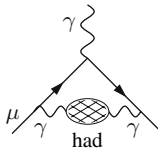


Fig. 4. The leading order (LO) hadronic vacuum polarization diagram

As a result the leading non-perturbative hadronic contributions a_μ^{had} can be obtained in terms of $R_\gamma(s) \equiv \sigma^{(0)}(e^+e^- \rightarrow \gamma^* \rightarrow \text{hadrons})/\frac{4\pi\alpha^2}{3s}$ data via the dispersion integral:

$$a_\mu^{\text{had}} = \left(\frac{\alpha m_\mu}{3\pi}\right)^2 \left(\int_{4m_\pi^2}^{E_{\text{cut}}^2} ds \frac{R_\gamma^{\text{data}}(s) \hat{K}(s)}{s^2} + \int_{E_{\text{cut}}^2}^{\infty} ds \frac{R_\gamma^{\text{pQCD}}(s) \hat{K}(s)}{s^2} \right). \quad (32)$$

The rescaled kernel function $\hat{K}(s) = 3s/m_\mu^2 K(s)$ is a smooth bounded function, increasing from 0.63... at $s = 4m_\pi^2$ to 1 as $s \rightarrow \infty$. The $1/s^2$ enhancement at low energy implies that the $\rho \rightarrow \pi^+\pi^-$ resonance is dominating the dispersion integral ($\sim 75\%$). Data can be used up to energies where $\gamma - Z$ mixing comes into play at about 40 GeV. However, by virtue of asymptotic freedom, perturbative quantum chromodynamics (pQCD) becomes more reliable the higher the energy and in fact may be used safely in regions away from the flavor thresholds where the non-perturbative resonances show up: ρ , ω , ϕ , the J/ψ series and the Υ series. We thus use perturbative QCD [54, 55] from 5.2 to 9.6 GeV and for the high-energy tail above 13 GeV, as recommended in [54, 55].

Hadronic cross-section measurements $e^+e^- \rightarrow \text{hadrons}$ at electron-positron storage rings started in the early 1960s and continued up to date. Since our analysis [56] in 1995 data from MD1 [57], BES-II [58] and from CMD-2 [59] have led to a substantial reduction in the hadronic uncertainties on a_μ^{had} . More recently, KLOE [60], SND [61] and CMD-2 [62] published new measurements in the region below 1.4 GeV. My up-to-date evaluation of the leading order hadronic VP yields [63]

$$a_\mu^{\text{had}(1)} = (692.1 \pm 5.6) \times 10^{-10}. \quad (33)$$

Some other recent evaluations are collected in Table I. Differences in errors come about mainly by utilizing more “theory-driven” concepts : use of selected

Table 1. Some recent evaluations of $a_\mu^{\text{had}(1)}$

$a_\mu^{\text{had}(1)} \times 10^{10}$	data	Reference
696.3[7.2]	e^+e^-	[64]
711.0[5.8]	$e^+e^- + \tau$	[64]
694.8[8.6]	e^+e^-	[65]
684.6[6.4]	e^+e^- TH	[66]
699.6[8.9]	e^+e^-	[67]
692.4[6.4]	e^+e^-	[68]
693.5[5.9]	e^+e^-	[69]
701.8[5.8]	$e^+e^- + \tau$	[69]
690.9[4.4]	$e^+e^-^{**}$	[70]
692.1[5.6]	$e^+e^-^{**}$	[63]

data sets only, extended use of perturbative QCD in place of data [assuming local quark-hadron duality], sum rule methods, low-energy effective methods. Only the last two (**) results include the most recent data from SND, CMD-2 and BaBar.

In principle, the $I = 1$ iso-vector part of $e^+e^- \rightarrow$ hadrons can be obtained in an alternative way by using the precise vector spectral functions from hadronic τ -decays $\tau \rightarrow \nu_\tau +$ hadrons which are related by an isospin rotation [71]. After isospin violating corrections, due to photon radiation and the mass splitting $m_d - m_u \neq 0$, have been applied, there remains an unexpectedly large discrepancy between the e^+e^- - and the τ -based determinations of a_μ [64], as may be seen in Table 1. Possible explanations are so far unaccounted isospin breaking [65] or experimental problems with the data. Since the e^+e^- - data are more directly related to what is required in the dispersion integral, one usually advocates to use the e^+e^- data only.

At order $O(\alpha^3)$ diagrams of the type shown in Fig. 5 have to be calculated, where the first diagram stands for a class of higher order hadronic contributions obtained if one replaces one internal photon line by a dressed one in any of the 6-two loop diagrams which do not exhibit a fermion loop. The relevant kernels for the corresponding dispersion integrals have been calculated analytically in [72] and appropriate series expansions were given in [73] (for earlier estimates see [74, 75]). Based on my recent compilation of the e^+e^- data [63] I obtain

$$a_\mu^{\text{had}(2)} = (-100.3 \pm 2.2) \times 10^{-11}, \quad (34)$$

in accord with previous evaluations [75, 73, 71, 68].

We encounter much more serious problems with non-perturbative hadronic effect with the hadronic light-by-light (LbL) contribution at $O(\alpha^3)$ depicted in Fig. 6. Experimentally, we know that $\gamma\gamma \rightarrow$ hadrons $\rightarrow \gamma\gamma$ is dominated by the hadrons π^0 , η , η' , \dots , i.e., single pseudo-scalar meson spikes, and that $\pi^0 \rightarrow \gamma\gamma$, etc., is governed by the parity odd Wess-Zumino-Witten (WZW) effective Lagrangian

$$\mathcal{L}^{(4)} = -\frac{\alpha N_c}{12 \pi f_0} \varepsilon_{\mu\nu\rho\sigma} F^{\mu\nu} A^\rho \partial^\sigma \pi^0 + \dots \quad (35)$$

which reproduces the Adler-Bell-Jackiw triangle anomaly and which helps in estimating the leading hadronic LbL contribution. f_0 denotes the pion decay constant f_π in the chiral limit of massless light quarks. Again, in a low-energy

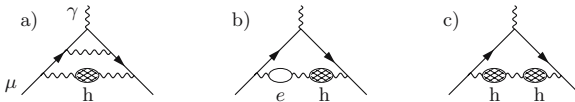


Fig. 5. Higher order (HO) vacuum polarization contributions

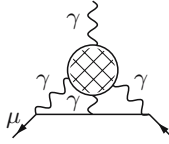


Fig. 6. Hadronic light-by-light scattering in $g-2$

effective description, the quasi Goldstone bosons, the pions and kaons play an important role, and the relevant diagrams are displayed in Fig. 7.

However, as we know from the hadronic VP discussion, the ρ meson is expected to play an important role in the game. It looks natural to apply a vector-meson dominance (VMD) like model. Electromagnetic interactions of pions treated as point-particles would be described by scalar QED in a first step. However, due to hadronic interactions the photon mixes with hadronic vector-mesons like the ρ^0 , which is properly accommodated by the Resonance Lagrangian Approach (RLA) [76] or versions of it, an extended version of CHPT which incorporates vector-mesons in accordance with the basic symmetries.

Based on such effective field theory (EFT) models, two major efforts in evaluating the full a_μ^{LbL} contribution were made by Hayakawa, Kinoshita and Sanda (HKS 1995) [77], Bijnens, Pallante and Prades (BPP 1995) [78] and Hayakawa and Kinoshita (HK 1998) [79] (see also Kinoshita, Nizic and Okamoto (KNO 1985) [75]). Although the details of the calculations are quite different, which results in a different splitting of various contributions, the results are in good agreement and essentially given by the π^0 -pole contribution, which was taken with the wrong sign, however. In order to eliminate the cut-off dependence in separating L.D. and S.D. physics, more recently it became favorable to use quark-hadron duality, as it holds in the large N_c limit of QCD, for modeling of the hadronic amplitudes [80]. The infinite series of narrow vector states known to show up in the large N_c limit is then approximated by a suitable lowest meson dominance (LMD+V) Ansatz [81], assumed to be saturated by known low-lying physical states of appropriate quantum numbers. This approach was adopted in a reanalysis by Knecht and Nyfeler (KN 2001) [82, 83, 84] in 2001, in which they discovered a sign mistake

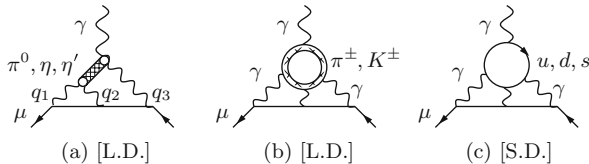


Fig. 7. Leading hadronic light-by-light scattering diagrams: the two leading CHPT diagrams (L.D.) and the QPM diagram (S.D.). The charged pion loop is sub-leading only, actually. Diagrams with permuted γ s on the μ -line have to be included. γ -hadron/quark vertices at $q^2 \neq 0$ are dressed (VMD)

in the dominant π^0, η, η' exchange contribution, which changed the central value by $+167 \times 10^{-11}$, a 2.8σ shift, and which reduces a larger discrepancy between theory and experiment. More recently, Melnikov and Vainshtein (MV 2004) [85] found additional problems in previous calculations, this time in the short distance constraints (QCD/OPE) used in matching the high-energy behavior of the effective models used for the π^0, η, η' exchange contribution.

The most important pion-pole term, Fig. 7(a), exhibits the non-perturbative aspects in a product of two essentially unknown $\pi^0\gamma\gamma$ form factors (FF) like $\mathcal{F}_{\pi^*\gamma^*\gamma^*}(q_2^2, q_1^2, q_3^2) \cdot \mathcal{F}_{\pi^*\gamma^*\gamma^*}(q_2^2, q_2^2, 0)$ where the photon momenta q_1 and q_2 are the loop momenta to be integrated over.

A new quality of the problem encountered here is the fact that the integrand depends on three invariants q_1^2, q_2^2, q_3^2 with $q_3 = -(q_1 + q_2)$, while hadronic VP correlators or the VVA triangle with an external zero momentum vertex only depends on a single invariant q^2 . In the latter case the invariant amplitudes (form factors) may be separated into a low-energy part $q^2 \leq \Lambda^2$ (soft) where the low-energy effective description applies and a high-energy part $q^2 > \Lambda^2$ (hard) where pQCD works. In multi-scale problems, however, there are mixed soft–hard regions where no answer is available in general, unless we have data to constrain the amplitudes in such regions. In our case, only the soft region $q_1^2, q_2^2, q_3^2 \leq \Lambda^2$ and the hard region $q_1^2, q_2^2, q_3^2 > \Lambda^2$ are under control of either the low-energy EFT or pQCD, respectively. In the mixed soft–hard domains operator product expansions and/or soft versus hard factorization “theorems” may apply. Actually, one more approximation is usually made: the *pion-pole approximation*, i.e., the pion-momentum square (first argument of the \mathcal{F}) is set equal to m_π^2 , as the main contribution is expected to come from the pole. Knecht and Nyffeler modeled $\mathcal{F}_{\pi\gamma^*\gamma^*}(m_\pi^2, q_1^2, q_2^2)$ in the spirit of the large N_c expansion as a “LMD+V” form factor:

$$\mathcal{F}_{\pi\gamma^*\gamma^*}(m_\pi^2, q_1^2, q_2^2) = \frac{f_\pi}{3} \frac{q_1^2 q_2^2 (q_1^2 + q_2^2) + h_1 (q_1^2 + q_2^2)^2 + h_2 q_1^2 q_2^2 + h_5 (q_1^2 + q_2^2) + h_7}{(q_1^2 - M_1^2)(q_1^2 - M_2^2)(q_2^2 - M_1^2)(q_2^2 - M_2^2)}, \quad (36)$$

with $h_7 = -(N_c M_1^4 M_2^4 / 4\pi^2 f_\pi^2)$, $f_\pi \simeq 92.4$ MeV. An important constraint comes from the pion-pole form factor $\mathcal{F}_{\pi\gamma^*\gamma}(m_\pi^2, -Q^2, 0)$, which has been measured by CELLO [86] and CLEO [87]. Experiments are in fair agreement with the Brodsky–Lepage [88] form

$$\mathcal{F}_{\pi\gamma^*\gamma}(m_\pi^2, -Q^2, 0) \simeq -\frac{N_c}{12\pi^2 f_\pi} \frac{1}{1 + (Q^2/8\pi^2 f_\pi^2)} \quad (37)$$

which interpolates between a $1/Q^2$ asymptotic behavior and the constraint from π^0 decay at $Q^2 = 0$. This behavior requires $h_1 = 0$. Identifying the resonances with $M_1 = M_\rho = 769$ MeV, $M_2 = M_{\rho'} = 1465$ MeV, the phenomenological constraint fixes $h_5 = 6.93$ GeV⁴. h_2 will be fixed by later. As the previous analyses, Knecht and Nyffeler apply the above VMD-type form factor on both ends of the pion line. In fact at the vertex attached to the external zero momentum photon, this type of pion-pole form factor cannot

apply for kinematical reasons: when $q_{\text{ext}}^\mu = 0$ not $\mathcal{F}_{\pi\gamma^*\gamma}(m_\pi^2, -Q^2, 0)$ but $\mathcal{F}_{\pi^*\gamma^*\gamma}(q_2^2, q_2^2, 0)$ is the relevant object to be used, where q_2 is to be integrated over. However, for large q_2^2 the pion must be far off-shell, in which case the pion exchange effective representation becomes obsolete. Melnikov and Vainshtein reanalyzed the problem by performing an operator product expansion (OPE) for $q_1^2 \simeq q_2^2 \gg (q_1 + q_2)^2 \sim m_\pi^2$. In the chiral limit this analysis reveals that the external vertex is determined by the exactly known ABJ anomaly $\mathcal{F}_{\pi\gamma\gamma}(m_\pi^2, 0, 0) = -1/(4\pi^2 f_\pi)$. This means that in the chiral limit there is no VMD-like damping at high energies at the external vertex. However, the absence of a damping in the chiral limit does not prove that there is no damping in the real world with non-vanishing quark masses. In fact, the quark triangle-loop in this case provides a representation of the $\pi^{0*}\gamma^*\gamma^*$ amplitude given by $F_{\pi^{0*}\gamma^*\gamma^*}^{\text{CQM}}(q^2, p_1^2, p_2^2) \equiv (-4\pi^2 f_\pi) \mathcal{F}_{\pi^*\gamma^*\gamma^*}(q^2, p_1^2, p_2^2) = 2m_q^2 C_0(m_q; q^2, p_1^2, p_2^2)$, where C_0 is a well-known scalar 3-point function and m_q is a quark mass ($q=u,d,s$). For $p_1^2 = p_2^2 = q^2 = 0$ we obtain $F_{\pi^{0*}\gamma^*\gamma^*}^{\text{CQM}}(0, 0, 0) = 1$, which is the proper ABJ anomaly. For large p_1^2 at $p_2^2 \sim 0$, $q^2 \sim 0$ or $p_1^2 \sim p_2^2$ at $q^2 \sim 0$ the asymptotic behavior is given by

$$F_{\pi^{0*}\gamma^*\gamma}^{\text{CQM}}(0, p_1^2, 0) \sim r \ln^2 r, \quad F_{\pi^{0*}\gamma^*\gamma^*}^{\text{CQM}}(0, p_1^2, p_1^2) \sim 2r \ln r, \quad (38)$$

where $r = \frac{m_q^2}{-p_1^2}$. As C_0 is permutation symmetric the same power behavior $\sim 1/p_i^2$ modulo logarithms holds in all channels. Thus at high energies the anomaly gets screened by chiral symmetry breaking effects.

We therefore advocate to use consistently dressed form factors as inferred by the resonance Lagrangian approach. However, other effects which were first considered in [85] must be taken into account:

- 1) The constraint on the twist four ($1/q^4$)-term in the OPE requires $h_2 = -10 \text{ GeV}^2$ in the Knecht–Nyffeler form factor [36]: $\delta a_\mu \simeq +5 \pm 0$.
- 2) The contributions from the f_1 and f_1' isoscalar axial-vector mesons: $\delta a_\mu \simeq +10 \pm 4$ (using dressed photons).
- 3) For the remaining effects: scalars (f_0) + dressed π^\pm, K^\pm loops + dressed quark loops: $\delta a_\mu \simeq -5 \pm 13$.

Note that the remaining terms have been evaluated in [77, 78] only. The splitting into the different terms is model dependent and only the sum should be considered: the results read -5 ± 13 (BPP) and 5.2 ± 13.7 (HKS) and hence the contribution remains unclear⁴.

Results are overviewed in Table 2. The last column gives my estimates based on [77, 78, 82, 85]. The “no FF” column shows results for undressed photons (no form factor). The constant WZW form factor yields a divergent

⁴ We adopt the value estimated in [78], because the sign of the scalar contribution, which dominates in the sum, has to be negative in any case (see [84]).

Table 2. LbL: Summary of most recent results for $a_\mu \times 10^{11}$

	no FF	BPP	HKS	KN	MV	FJ
π^0, η, η'	$+\infty$	85 ± 13	82.7 ± 6.4	83 ± 12	114 ± 10	88 ± 12
axial-vector		2.5 ± 1.0	1.7 ± 0.0		22 ± 5	10 ± 4
scalar		-6.8 ± 2.0	–	–	–	-7 ± 2
π, K loops	-49.8	-19 ± 13	-4.5 ± 8.1		0 ± 10	-19 ± 13
quark loops	$62(3)$	21 ± 3	9.7 ± 11.1	–	–	21 ± 3
total		83 ± 32	89.6 ± 15.4	80 ± 40	136 ± 25	93 ± 34

result; applying a cut-off Λ one obtains [83] $(\alpha/\pi)^3 \mathcal{C} \ln^2 \Lambda$, with an universal coefficient $\mathcal{C} = N_c^2 m_\mu^2 / (48\pi^2 f_\pi^2)$; in the VMD dressed cases M_V represents the cut-off $\Lambda \rightarrow M_V$ if $M_V \rightarrow \infty$.

4 Theory Confronting the Experiment

The following Table 3 collects the typical contributions to a_μ evaluated in terms of α determined via a_e (13). The world average experimental muon magnetic anomaly, dominated by the very precise BNL result, now is [8]

$$a_\mu^{\text{exp}} = 1.16592080(60) \times 10^{-3} \quad (39)$$

(relative uncertainty 5.3×10^{-7}), which confronts with the SM prediction

$$a_\mu^{\text{the}} = 1.16591793(68) \times 10^{-3} . \quad (40)$$

Figure 8 illustrates the improvement achieved by the BNL experiment. The theoretical predictions mainly differ by the L.O. hadronic effects, which also dominate the theoretical error. A deviation between theory and experiment

Table 3. The various types of contributions to a_μ in units 10^{-6} , ordered according to their size (L.O. lowest order, H.O. higher order, LbL. light-by-light)

L.O. universal	1161.409 73	(0)
e -loops	6.194 57	(0)
H.O. universal	-1.757 55	(0)
L.O. hadronic	0.069 20	(56)
L.O. weak	0.001 95	(0)
H.O. hadronic	-0.001 00	(2)
LbL. hadronic	0.001 00	(39)
τ -loops	0.000 43	(0)
H.O. weak	-0.000 41	(2)
$e+\tau$ -loops	0.000 01	(0)
theory	1165.917 93	(68)
experiment	1165.920 80	(60)

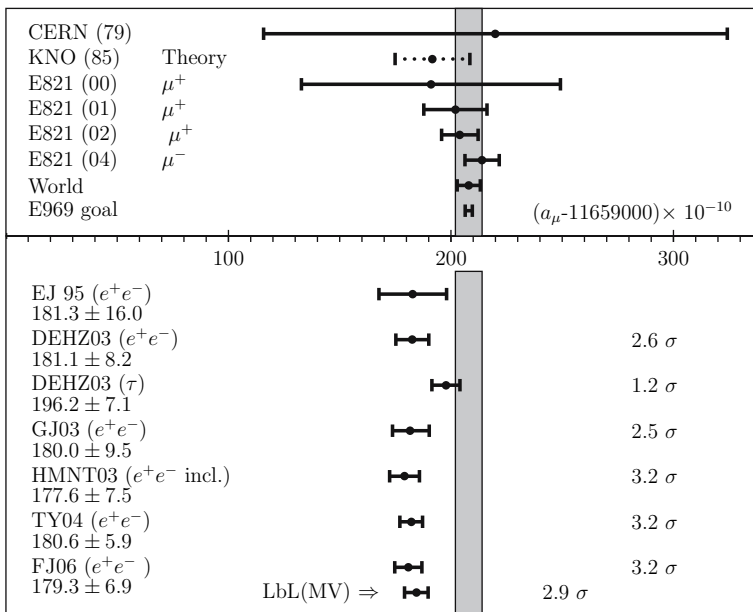


Fig. 8. Comparison between theory and experiment. Results differ by different L.O. hadronic vacuum polarizations, except for the last point which includes the Melnikov-Vainshtein estimate of the LbL contribution. EJ95 vs. FJ06 illustrates the improvement of the e^+e^- -data between 1995 and now (see also Table [II](#))

of about 3 σ was persisting since the first precise BNL results came out, in spite of progress in theory and experiment since.

At present the deviation between theory and experiment is

$$\delta a_\mu = a_\mu^{\text{exp}} - a_\mu^{\text{the}} = 287 \pm 91 \times 10^{-11}, \quad (41)$$

which is a 3.2 σ effect. We note that the theory error is somewhat larger than the experimental one. It is fully dominated by the uncertainty of the hadronic low-energy cross-section data, which determine the hadronic vacuum polarization and, partially, form the uncertainty of the hadronic light-by-light scattering contribution.

As we notice, the enhanced sensitivity to “heavy” physics is somehow good news and bad news at the same time: the sensitivity to “New Physics” we are always hunting for at the end is enhanced due to

$$a_\ell^{\text{NP}} \sim \left(\frac{m_\ell}{M_{\text{NP}}} \right)^2$$

by the mentioned mass ratio square, but at the same time also scale-dependent SM effects are dramatically enhanced, and the hadronic ones are not easy to estimate with the desired precision.

5 Prospects

The BNL muon $g-2$ experiment has determined a_μ (39), reaching the impressive precision of 0.54 ppm, a 14-fold improvement over the CERN experiment from 1976. Herewith, a new quality has been achieved in testing the SM and in limiting physics beyond it. The main achievements and problems are

- a first confirmation of the fairly small weak contribution at the 2–3 σ level,
- a substantial improvement in testing CPT $a_{\mu^+} = a_{\mu^-}$ for muons,
- the hadronic vacuum polarization contribution, obtained via experimental e^+e^- annihilation data, limits the theoretical precision at the 1 σ level,
- now and for the future the hadronic light-by-light scattering contribution, which amounts to about 2σ , is not far from being as important as the weak contribution; present calculations are model-dependent and may become the limiting factor for future progress.

At present a 3.2σ deviation between theory and experiment is observed⁵ and the “missing piece” (41) could hint to new physics, but at the same time rules out big effects predicted by many possible extensions of the SM.

Usually, new physics (NP) contributions due to not yet seen heavy states via virtual corrections are expected to produce contributions proportional to m_μ^2/M_{NP}^2 and thus are expected to be suppressed by $M_{\text{W}}^2/M_{\text{NP}}^2$ relative to the weak contribution.

The most promising theoretical scenarios are super symmetric (SUSY) extensions of the SM, in particular the minimal MSSM. Typical super-symmetric contributions to a_μ stem from smuon–neutralino and sneutrino–chargino loops Fig. 9. Some contributions are enhanced by the parameter $\tan\beta$ which may be large (in some cases of order $m_t/m_b \approx 40$). One obtains [89] (for the extension to 2-loops see [90])

$$a_\mu^{\text{SUSY}} \simeq \text{sign}(\mu) \frac{\alpha(M_Z)}{8\pi \sin^2 \Theta_W} \frac{m_\mu^2}{\tilde{m}^2} \tan\beta \left(1 - \frac{4\alpha}{\pi} \ln \frac{\tilde{m}}{m_\mu} \right), \quad (42)$$

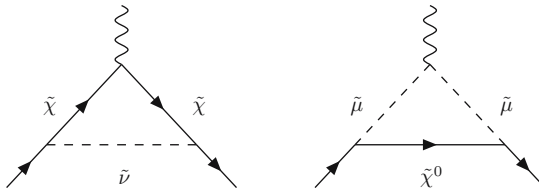


Fig. 9. Physics beyond the SM: leading SUSY contributions to $g-2$ in super-symmetric extension of the SM

⁵ It is the largest established deviation between theory and experiment in electroweak precision physics at present.

$\tilde{m} = m_{\text{SUSY}}$ a typical SUSY loop mass and μ is the Higgsino mass term. In view of (41) negative μ models give the opposite sign contribution to a_μ and are strongly disfavored. For $\tan\beta$ in the range 3–40 one obtains

$$\tilde{m} \simeq 110\text{--}430 \text{ GeV}, \quad (43)$$

precisely the range where SUSY particles are often expected. For a variety of non-SUSY extensions of the SM typically $|a_\mu(\text{NP})| \simeq \mathcal{C} m_\mu^2/M^2$ where $\mathcal{C} = O(1)$ [or $O(\alpha/\pi)$ if radiatively induced]. The current constraint suggests $M \simeq 1.5\text{--}2.5\text{TeV}$ [$M \simeq 80\text{--}120\text{GeV}$]. Note that $\mathcal{C} = O(1)$ could be in conflict with the requirement that no tree level contribution is allowed. For a more elaborate discussion and further references I refer to [91].

Plans for a new $g-2$ experiment exist [92]. In fact, the impressive 0.5 ppm precision measurement by the E821 collaboration at Brookhaven was still limited by statistical errors rather than by systematic ones. Therefore an upgrade of the experiment at Brookhaven or J-PARC (Japan) is supposed to be able to reach a precision of 0.2 ppm (Brookhaven) or 0.1 ppm (J-PARC).

For the theory this poses a new challenge. It is clear that on the theory side, a reduction of the leading hadronic uncertainty is required, which actually represents a big experimental challenge: one has to attempt cross-section measurements at the 1% level up to $J/\psi[\Upsilon]$ energies (5[10] GeV). Such measurements would be crucial for the muon $g-2$ as well as for a more precise determination of the running fine structure constant $\alpha_{\text{QED}}(E)$. In particular, e^+e^- low-energy cross-section measurements in the region between 1 and 2.5 GeV [93, 94] are able to substantially improve the accuracy of $a_\mu^{\text{had}(1)}$ and $\alpha_{\text{QED}}(M_Z)$ [63].

New ideas are required to get less model-dependent estimations of the hadronic LbL contribution.

In any case the muon $g-2$ story is a beautiful example which illustrates the experience that the closer we look the more there is to see, but also the more difficult it gets to predict and interpret what we see. Even facing problems to pin down precisely the hadronic effects, the achievements in the muon $g-2$ is a big triumph of science. Here all kinds of physics meet in one number which is the result of a truly ingenious experiment. Only getting all details in all aspects correct makes this number a key quantity for testing our present theoretical framework in full depth. It is the result of tremendous efforts in theory and experiment and on the theory side has triggered the development of new methods and tools such as computer algebra as well as high-precision numerical methods which are indispensable to handle the complexity of hundreds to thousands of high-dimensional integrals over singular integrands suffering from huge cancellations of huge numbers of terms. Astonishing that all this really works!

Acknowledgments

It is a pleasure to thank the organizers of PSAS 2006 and in particular to Savely Karshenboim for the kind invitation to this stimulating meeting. Thanks also to Oleg Tarsov and Rainer Sommer for helpful discussions and for carefully reading the manuscript. This work was supported in part by EC-Contracts HPRN-CT-2002-00311 (EURIDICE) and RII3-CT-2004-506078 (TARI).

References

1. P. A. M. Dirac: Proc. Roy. Soc. A **117**, 610 (1928); A **118**, 351 (1928). [10](#)
2. P. Kusch, H. M. Foley: Phys. Rev. **73**, 421 (1948); Phys. Rev. **74**, 250 (1948). [10](#)
3. J. S. Schwinger: Phys. Rev. **73**, 416 (1948). [11](#)
4. G. Charpak et al.: Phys. Lett. **1**, 16 (1962). [12](#)
5. J. Bailey et al.: Nuovo Cimento A **9**, 369 (1972). [13](#)
6. J. Aldins et al.: Phys. Rev. Lett. **23**, 441 (1969); Phys. Rev. D **1**, 2378 (1970). [13](#)
7. J. Bailey et al.: Nucl. Phys. B **150**, 1 (1979). [13](#)
8. R. M. Carey et al.: Phys. Rev. Lett. **82**, 1632 (1999); H. N. Brown et al.: Phys. Rev. D **62**, 091101 (2000); Phys. Rev. Lett. **86**, 2227 (2001); G. W. Bennett et al.: Phys. Rev. Lett. **89**, 101804 (2002)[Erratum: Phys. Rev. Lett. **89**, 129903 (2002)]; Phys. Rev. Lett. **92**, 161802 (2004). [13](#), [28](#)
9. B. Odom et al.: Phys. Rev. Lett. **97**, 030801 (2006). [15](#), [18](#)
10. G. Gabrielse et al.: Phys. Rev. Lett. **97**, 030802 (2006) [Erratum-ibid. **99**, 039902 (2007)]. [15](#)
11. S. Eidelman et al.: [Particle Data Group], Phys. Lett. B **592**, 1 (2004). [15](#)
12. P. J. Mohr, B. N. Taylor, Rev. Mod. Phys. **72**, 351 (2000); **77**, 1 (2005). [15](#)
13. A. Petermann: Helv. Phys. Acta **30**, 407 (1957); Nucl. Phys. **5**, 677 (1958). [16](#)
14. C. M. Sommerfield: Phys. Rev. **107**, 328 (1957); Ann. Phys. (N.Y.) **5**, 26 (1958). [16](#)
15. S. Laporta, E. Remiddi: Phys. Lett. B **379**, 283 (1996). [16](#)
16. T. Kinoshita: Phys. Rev. Lett., **75**, 4728 (1995). [17](#)
17. T. Kinoshita, W. B. Lindquist: Phys. Rev. D **27**, 867 (1983); **27**, 877 (1983); **27**, 886 (1983); **39**, 2407 (1989); **42**, 636 (1990). [17](#)
18. V. W. Hughes, T. Kinoshita: Rev. Mod. Phys. **71**, S133 (1999). [17](#)
19. T. Kinoshita, M. Nio: Phys. Rev. D **73**, 013003 (2006). [17](#)
20. T. Aoyama, M. Hayakawa, T. Kinoshita, M. Nio, Phys. Rev. Lett. **99**, 110406 (2007). [17](#)
21. P. J. Mohr, B. N. Taylor: Rev. Mod. Phys. **77**, 1 (2005). [17](#)
22. H. Suura, E. Wichmann: Phys. Rev., **105**, 1930 (1957); A. Petermann: Phys. Rev. **105**, 1931 (1957). [17](#)
23. H. H. Elend: Phys. Lett. **20**, 682 (1966) [Erratum: Phys. Lett. **21**, 720 (1966)]. [17](#), [18](#)
24. B. E. Lautrup, E. De Rafael: Nuovo Cim. A **64**, 322 (1969). [17](#)
25. B. Lautrup: Phys. Lett. B **69**, 109 (1977). [17](#)
26. G. Li, R. Mendel, M. A. Samuel: Phys. Rev. D **47**, 1723 (1993). [17](#)
27. T. Kinoshita: Nuovo Cim. B **51**, 140 (1967). [17](#)
28. B. E. Lautrup, E. De Rafael: Phys. Rev. **174**, 1835 (1968); B. E. Lautrup, M. A. Samuel: Phys. Lett. B **72**, 114 (1977). [17](#)

29. M. A. Samuel, G. Li: Phys. Rev. D **44**, 3935 (1991) [Errata: Phys. Rev. D **46**, 4782 (1992); D **48**, 1879 (1993)]. [17](#)
30. S. Laporta: Nuovo Cim. A **106**, 675 (1993). [17](#) [18](#) [19](#)
31. S. Laporta, E. Remiddi: Phys. Lett. B **301**, 440 (1993). [17](#) [18](#) [19](#)
32. J. H. Kühn et al.: Phys. Rev. D **68**, 033018 (2003). [17](#) [18](#) [19](#)
33. A. Czarnecki, M. Skrzypek: Phys. Lett. B **449**, 354 (1999). [19](#)
34. S. Friot, D. Greynat, E. De Rafael: Phys. Lett. B **628**, 73 (2005). [19](#)
35. M. Passera: J. Phys. G **31**, R75 (2005); Phys. Rev. D **75**, 013002 (2007). [19](#)
36. M. Caffo, S. Turrini, E. Remiddi: Phys. Rev. D **30**, 483 (1984); E. Remiddi, S. P. Sorella: Lett. Nuovo Cim. **44**, 231 (1985); D. J. Broadhurst, A. L. Kataev, O. V. Tarasov: Phys. Lett. B **298**, 445 (1993); S. Laporta: Phys. Lett. B **312**, 495 (1993); P. A. Baikov, D. J. Broadhurst: hep-ph/9504398. [19](#)
37. T. Kinoshita, M. Nio: Phys. Rev. Lett. **90**, 021803 (2003); Phys. Rev. D **70**, 113001 (2004). [19](#)
38. S. G. Karshenboim: Phys. Atom. Nucl. **56**, 857 (1993). [19](#)
39. T. Kinoshita, M. Nio: Phys. Rev. D **73**, 053007 (2006). [19](#)
40. A. L. Kataev: Nucl. Phys. Proc. Suppl. **155**, 369 (2006); hep-ph/0602098; Phys. Rev. D **74**, 073011 (2006). [19](#)
41. E. A. Kuraev, T. V. Kukhto, A. Schiller: Sov. J. Nucl. Phys. **51**, 1031 (1990); T. V. Kukhto et al.: Nucl. Phys. **B 371**, 567 (1992). [21](#)
42. A. Czarnecki, B. Krause, W. Marciano: Phys. Rev. D **52**, R2619 (1995). [21](#)
43. S. Peris, M. Perrottet, E. de Rafael: Phys. Lett. B **355**, 523 (1995). [21](#)
44. M. Knecht, S. Peris, M. Perrottet, E. de Rafael: JHEP **0211**, 003 (2002). [21](#)
45. G. Degrassi, G. F. Giudice: Phys. Rev. **58D**, 053007 (1998). [21](#) [22](#)
46. A. Czarnecki, W. J. Marciano, A. Vainshtein: Phys. Rev. D **67**, 073006 (2003). [21](#) [22](#)
47. A. Vainshtein: Phys. Lett. B **569**, 187 (2003). [21](#)
48. M. Knecht, S. Peris, M. Perrottet, E. de Rafael: JHEP **0403**, 035 (2004). [21](#)
49. F. Jegerlehner, O. V. Tarasov: Phys. Lett. B **639**, 299 (2006). [21](#)
50. E. D'Hoker: Phys. Rev. Lett. **69**, 1316 (1992). [22](#)
51. A. Czarnecki, B. Krause, W. J. Marciano: Phys. Rev. Lett. **76**, 3267 (1996). [22](#)
52. S. Heinemeyer, D. Stöckinger, G. Weiglein: Nucl. Phys. B **699**, 103 (2004). [22](#)
53. T. Gribouk, A. Czarnecki: Phys. Rev. D **72**, 053016 (2005). [22](#)
54. S. G. Gorishnii, A. L. Kataev, S. A. Larin: Phys. Lett. B **259**, 144 (1991); L. R. Surguladze, M. A. Samuel: Phys. Rev. Lett. **66**, 560 (1991) [Erratum: Phys. Rev. Lett. **66**, 2416 (1991)]; K. G. Chetyrkin: Phys. Lett. B **391**, 402 (1997). [23](#)
55. K. G. Chetyrkin, J. H. Kühn: Phys. Lett. B **342**, 356 (1995); K. G. Chetyrkin, R. V. Harlander, J. H. Kühn: Nucl. Phys. B **586**, 56 (2000) [Erratum: Nucl. Phys. B **634**, 413 (2002)]. [23](#)
56. S. Eidelman, F. Jegerlehner: Z. Phys. C **67**, 585 (1995). [23](#)
57. A. E. Blinov et al. [MD-1]: Z. Phys. C **70**, 31 (1996). [23](#)
58. J. Z. Bai et al. [BES]: Phys. Rev. Lett. **84**, 594 (2000); Phys. Rev. Lett. **88**, 101802 (2002). [23](#)
59. R. R. Akhmetshin et al. [CMD-2]: Phys. Lett. B **578**, 285 (2004); Phys. Lett. B **527**, 161 (2002). [23](#)
60. A. Aloisio et al. [KLOE]: Phys. Lett. B **606**, 12 (2005). [23](#)
61. M. N. Achasov et al. [SND]: J. Exp. Theor. Phys. **103**, 380 (2006). [23](#)

62. V. M. Aulchenko et al. [CMD-2]: JETP Lett. **82**, 743 (2005); R. R. Akhmetshin et al.: JETP Lett. **84**, 413 (2006) [Pisma Zh. Eksp. Teor. Fiz. **84**, 491 (2006)]; Phys. [23](#)
63. F. Jegerlehner: Nucl. Phys. Proc. Suppl. **162**, 22 (2006) [hep-ph/0608329]. [23](#), [24](#), [31](#)
64. M. Davier et al.: Eur. Phys. J. C **27**, 497 (2003); Eur. Phys. J. C **31**, 503 (2003). [23](#), [24](#)
65. F. Jegerlehner: J. Phys. G **29**, 101 (2003); S. Ghozzi, F. Jegerlehner: Phys. Lett. B **583**, 222 (2004). [23](#), [24](#)
66. S. Narison: Phys. Lett. B **568**, 231 (2003) [23](#)
67. V. V. Ezhela, S. B. Lugovsky, O. V. Zenin: hep-ph/0312114. [23](#)
68. K. Hagiwara et al.: Phys. Rev. D **69**, 093003 (2004). [23](#), [24](#)
69. J. F. de Troconiz, F. J. Yndurain: Phys. Rev. D **71**, 073008 (2005). [23](#)
70. S. Eidelman et al.: ICHEP 2006 Moscow, (preliminary). [23](#)
71. R. Alemany, M. Davier, A. Höcker: Eur. Phys. J. C **2**, 123 (1998). [24](#)
72. R. Barbieri, E. Remiddi: Phys. Lett. B **49**, 468 (1974); Nucl. Phys. B **90**, 233 (1975). [24](#)
73. B. Krause: Phys. Lett. B **390**, 392 (1997). [24](#)
74. J. Calmet, S. Narison, M. Perrottet, E. de Rafael: Phys. Lett. B **61**, 283 (1976). [24](#)
75. T. Kinoshita, B. Nizic, Y. Okamoto: Phys. Rev. D **31**, 2108 (1985). [24](#), [25](#)
76. G. Ecker, J. Gasser, A. Pich, E. de Rafael: Nucl. Phys. B **321**, 311 (1989); G. Ecker et al.: Phys. Lett. B **223**, 425 (1989). [25](#)
77. M. Hayakawa, T. Kinoshita, A. I. Sanda: Phys. Rev. Lett. **75**, 790 (1995); Phys. Rev. D **54**, 3137 (1996). [25](#), [27](#)
78. J. Bijnens, E. Pallante, J. Prades: Phys. Rev. Lett. **75**, 1447 (1995) [Erratum: Phys. Rev. Lett. **75**, 3781 (1995)]; Nucl. Phys. B **474**, 379 (1996); [Erratum: Nucl. Phys. **626**, 410 (2002)]. [25](#), [27](#)
79. M. Hayakawa, T. Kinoshita: Phys. Rev. D **57**, 465 (1998) [Erratum: Phys. Rev. D **66**, 019902 (2002)]. [25](#)
80. E. de Rafael: Phys. Lett. B **322**, 239 (1994). [25](#)
81. S. Peris, M. Perrottet, E. de Rafael: JHEP **9805**, 011 (1998); M. Knecht, S. Peris, M. Perrottet, E. de Rafael: Phys. Rev. Lett. **83**, 5230 (1999); M. Knecht, A. Nyffeler: Eur. Phys. J. C **21**, 659 (2001). [25](#)
82. M. Knecht, A. Nyffeler: Phys. Rev. D **65**, 073034 (2002). [25](#), [27](#)
83. M. Knecht, A. Nyffeler, M. Perrottet, E. De Rafael: Phys. Rev. Lett. **88**, 071802 (2002). [25](#), [28](#)
84. I. Blokland, A. Czarnecki, K. Melnikov: Phys. Rev. Lett. **88**, 071803 (2002). [25](#), [27](#)
85. K. Melnikov, A. Vainshtein: Phys. Rev. D **70**, 113006 (2004). [26](#), [27](#)
86. H. J. Behrend et al. [CELLO Collaboration]: Z. Phys. C **49**, 401 (1991). [26](#)
87. J. Gronberg et al. [CLEO Collaboration]: Phys. Rev. D **57**, 33 (1998). [26](#)
88. S. J. Brodsky, G. P. Lepage: Phys. Rev. D **24**, 1808 (1981). [26](#)
89. T. Moroi: Phys. Rev. D **53**, 6565 (1996) [Erratum: Phys. Rev. D **56**, 4424 (1997)]. [30](#)
90. S. Heinemeyer, D. Stöckinger, G. Weiglein: Nucl. Phys. B **690**, 62 (2004). [30](#)
91. A. Czarnecki, W. J. Marciano: Phys. Rev. D **64**, 013014 (2001). [31](#)
92. B. L. Roberts: Nucl. Phys. B (Proc. Suppl.) **131**, 157 (2004); R. M. Carey et al.: Proposal of the BNL Experiment E969, 2004; J-PARC Letter of Intent L17. [31](#)
93. S. Eidelman, Physics at VEPP-2000, Nucl. Phys. Proc. Suppl. **162**, 323 (2006). [31](#)
94. F. Ambrosino et al.: Prospects for e^+e^- physics at Frascati between the Φ and the ψ , Eur. Phys. J. C **50**, 729 (2007); G. Venanzoni, Nucl. Phys. Proc. Suppl. **162**. [31](#)

Guide for Atomic and Particle Physicists to CODATA's Recommended Values of the Fundamental Physical Constants

S. G. Karshenboim

D. I. Mendeleev Institute for Metrology (VNIIM), 190005 St. Petersburg, Russia,
and Max-Planck-Institut für Quantenoptik, 85748 Garching, Germany
savely.karshenboim@mpq.mpg.de

Abstract. The CODATA recommended values of the fundamental constants are widely applied in particle, nuclear and atomic physics. They are a result of a complicated evaluation (adjustment) of numerous correlated data of different natures. Their application is often rather mechanical and as a result is not free of various confusions which are discussed in this note.

1 Introduction

Precision physics deals with numbers rather than with functions, but any theoretical prediction in numerical terms can appear only after one applies certain values of input parameters, the most important of which are the fundamental physical constants. The most popular are recommended values published by CODATA¹. Working for a while for precision physics of simple atoms, which is based on quantum electrodynamics (QED) calculations, and for fundamental constants, I have witnessed a certain number of confusions in applications of the CODATA values. This chapter aims to serve as a guide to fundamental constants with a hope to avoid such confusions in future. One can consider it as a kind of 'fundamental constants for non-experts' or 'frequently necessary but not asked questions'.

Some applications of the values of certain fundamental constants to precision studies are sensitive to a choice of the values for the constant to be used. For such a case it is incorrect to apply any value of the constant blindly. The real option is to look for the origin of the result, checking what kind of measurements and calculations have been done to obtain it, what suggestions were

¹ CODATA is the Committee on Data for Science and Technology, an interdisciplinary Scientific Committee of the International Council for Science (ICSU). The CODATA recommended values are published under the auspices of the CODATA Task Group on Fundamental Constants.

made if any. Before any application of a particular result on the fundamental constant, one has to realize whether this application is in line with the actions done to derive the constant.

The CODATA papers [1, 2] represent a very specific kind of papers, namely, reference papers. They contain very important information, which can be found on demand, but most of the users are aware only about the tables of the recommended values of the fundamental constants, and even most of them do not read the papers, but access the values through the Internet (via, e.g., the NIST web site [3]) or through other compilations, such as the Review of Particle Properties [4]. In such a case they do not even have a chance to see any details of the original CODATA evaluation.

We consider this note as a supplementary paper to [1] and intentionally do not provide any references which can be found there. We also intentionally do not present any progress since the adjustment-2002 [1]. In particular, there have been a number of remarkable results improving accuracy in determination of the fine structure constant α and the Planck constant h , as well as substantial progress in understanding the muon anomalous magnetic moment.

Our purpose is not to discuss the most accurate data for a particular time period, since the data are continuously improving, but to explain how to deal with the CODATA recommendations, which may be applied to any CODATA recommendations, current and future.

Most of the physicists consider CODATA as a kind of brand for publication of the list of the best values of the constants. However, the main objective of the CODATA task group on the fundamental constants is to study the precision data, their accuracy, reliability and overall consistency. Its papers present a very detailed critical review of the experimental data which serve as input data of the adjustments.

2 The Adjustment of the Fundamental Constants: A General View

What is the adjustment? Normally, when one performs an experiment, the final result is an average of various measurements, or a result of a simple fitting, if we cannot measure the needed values directly, but only their combinations. For instance, we can measure certain cross-sections as a function of the momentum transfer, and the slope of specifically normalized cross-section (as a function of the momentum transfer squared, q^2) gives us a charge radius.

In the case of the fundamental constants the ‘topology’ of correlation links between data is cumbersome. It may be possible to measure e , h , e/h , e^2/h , e/m_e , h/m_e , etc. In contrast to the mentioned scattering experiment, the accuracy of different results is high, but quite different, and the data themselves may also have substantial experimental or computational correlations in uncertainties. The adjustment is such a procedure which attempts to find the most plausible result for the output parameters.

It involves a least-square method as a technical part; however, a crucial issue is a careful reconsideration of each inconsistency between and inside various portions of the input data. It depends on the physics of whether we have to treat them symmetrically or asymmetrically. A symmetric treatment may suggest, e.g., either multiplying their uncertainties by the same factor in order to reach a reasonable χ^2 value or, in contrast, assigning to all the data equal uncertainties despite the fact that they have been claimed to be very different. An example of an asymmetric treatment is the very removal of certain doubtful data as an ultimate choice.

3 The Adjustment of the Fundamental Constants: The Data

All the input data can be subdivided into a few groups as shown in Table I (see, e.g., [5, 6] for more detail). Two 'big blocks' involve substantially correlated data of various kinds (see below). Evaluation of data of these two big blocks is the main part of the procedure of *the adjustment of the values of the fundamental constants*.

Data which are known with a higher accuracy can be found separately before the main adjustment of these two blocks. Those most accurate data are

Table 1. The recommended values of some fundamental constants [1] and their subdivision into the adjustment blocks. Here, u_r is the relative standard uncertainty. Comments: * – fixed by the current definition of the SI units; ** – measured and adjusted; † – derived from the adjusted data; ‡ – e is not measured directly, but its various combinations with h and N_A

Constant	Value	u_r	Comment
c	299 792 458 m/s	0	exact*
μ_0	$4\pi \times 10^{-7}$ N/A ²	0	exact*
R_∞	10 973 731.568 525(73) m ⁻¹	$[6.6 \times 10^{-12}]$	auxiliary**
m_p/m_e	1 836.152 672 61(85)	$[4.6 \times 10^{-10}]$	auxiliary**
m_e	$5.485 799 094 5(24) \times 10^{-4}$ u	$[4.4 \times 10^{-10}]$	auxiliary**
α^{-1}	137.035 999 11(46)	$[3.3 \times 10^{-9}]$	α -block**
$\lambda_C = \hbar/(m_e c)$	$386.159 267 8(26) \times 10^{-15}$ m	$[6.7 \times 10^{-9}]$	α -block†
$h N_A$	$3.990 312 716(27) \times 10^{-10}$ J s/mol ⁻¹	$[6.7 \times 10^{-9}]$	α -block†
$R_K = h/e^2$	25 812.807 449(86) Ω	$[3.3 \times 10^{-9}]$	α -block**
e	$1.602 176 53(14) \times 10^{-19}$ C	$[8.5 \times 10^{-8}]$	h -block‡
h	$6.626 069 3(11) \times 10^{-34}$ J s	$[1.7 \times 10^{-7}]$	h -block**
N_A	$6.022 141 5(10) \times 10^{23}$ mol ⁻¹	$[1.7 \times 10^{-7}]$	h -block**
m_e	0.510 998 918(44) Mev/c ²	$[8.6 \times 10^{-8}]$	h -block†
m_e	$9.109 382 6(16) \times 10^{-31}$ kg	$[1.7 \times 10^{-7}]$	h -block†
$K_J = 2e/h$	$483 597.879(41) \times 10^9$ Hz V ⁻¹	$[8.5 \times 10^{-8}]$	h -block**
G	$6.674 2(10) \times 10^{-11}$ m ³ kg ⁻¹ s ⁻²	$[1.5 \times 10^{-4}]$	independent

referred to as *auxiliary*. An example of such data is the data on the Rydberg constant R_∞ and various mass ratios like m_e/m_p (we have to mention also a few constants such as the speed of light c whose numerical values are fixed in the SI by definition).

Data which are less accurate can be in principle ignored. The related constants are to be derived afterwards from the results of the adjustment. An example is a value of $h/(m_e c)$, which is in principle correlated with a value of the fine structure constant α (see below); it cannot be directly measured with high accuracy but can be extracted from adjusted data on R_∞ , α , etc. Such data are related to blocks, but only as their output results.

There are also certain data which are completely *uncorrelated* with the two big blocks as, e.g., the results for the Newtonian constant of gravitation G .

The first block is formed by the data related to the fine structure constant α . It also includes the so-called molar Planck constant hN_A and various results for the particle and atomic masses in the frequency units (i.e., in the result for the value Mc^2/h related to the mass M). The results in the frequency units are related to α because of the equation

$$\begin{aligned} R_\infty &= \frac{\alpha^2 m_e c}{2h} \\ &= \frac{1}{2c} \alpha^2 \frac{Mc^2}{2h} \frac{m_e}{M}, \end{aligned} \quad (1)$$

where M is related to the mass of the particle or atom measured in an experiment in the frequency units and we remind that the Rydberg constant and a number of important mass ratios m_e/M are known with higher accuracy.

The molar Planck constant hN_A enters this block as a conversion factor between two units in which microscopic masses can be measured with a very high accuracy, namely, the unified atomic mass units and frequency units.

The other block is formed by somewhat less accurate data related to the electron charge e , the Planck constant h and the Avogadro constant N_A . Because of the high accuracy obtained for the fine structure constant

$$\alpha = \frac{e^2}{4\pi\epsilon_0\hbar c} \quad (2)$$

and the molar Avogadro constant hN_A , the final results for these three constants are strongly correlated.

4 Electrical Data

An important feature of these two blocks is a substantial involvement of electric data related to standards and to some other macroscopic measurements. Two fundamental constants of quantum macroscopic effects play an important role there: the von Klitzing constant

$$R_K = \frac{h}{e^2} = \frac{\mu_0 c}{2\alpha}, \quad (3)$$

which describes the quantized resistance in the quantum Hall effect, and the Josephson constant

$$K_J = \frac{2e}{h}. \quad (4)$$

The related data are often refereed in a very confusing way. For instance, in the so-called measurement of the von Klitzing constant R_K the crucial part is not the measurement proper, but a construction of a reference resistance, which should have a known value in the SI units. The only opportunity for such a resistance, or rather for an impedance, is based on a so-called calculable capacitor. Surprising for devices based on classical physics, the value of the capacitance of certain symmetric configurations can be set with high accuracy. That is because of the special topological Thompson–Lampard theorem. Realizations of this theorem have recently provided us with classical-physics standards of the SI farad and ohm for a long period. At present a realization of the Thompson–Lampard capacitor is the only way to determine a value of R_K directly.

The watt-balance experiments do not involve any balance which deals with the power. They deal with a special kind of ampere balance which can be run in the dynamic and static regimes. The static regime involves an electric current, while the dynamic one deals with an induced potential. Combining the two measurements we arrive at a new quantity, power, as their product with an unknown geometric factor completely vanishing in the final equation.

A number of electric measurements deal with the gyromagnetic ratio or the Faraday constant. In practice, they do that in a very specific way. We have been numerously told from the high school time that we have to use the International System of Units, the SI (despite certain resistance from the physical community). And that is under control of the International Committee on Weights and Measures, CIPM. However, the CIPM has sanctioned a departure from the SI system in precision electric measurements, for which the so-called practical units were recommended in 1990 [7]. The latter, ohm-90 and volt-90, are based on certain fixed values of R_K and K_J [7] and all accurate electric measurements have been performed in these units.

If one declares a measurement of a certain electric quantity A (e.g., the gyromagnetic ratio of a proton in water), in practice the value actually measured in the SI units is somewhat more complicated:

$$AR_K^n K_J^m,$$

where n and m are certain integer numbers ($0, \pm 1, \pm 2$) which depend on the experiment.

This issue is so non-trivial that on measuring the same quantity, e.g., the gyromagnetic ratio of a proton, by different methods, ‘in a low magnetic

field’ and ‘in a high magnetic field’, we arrive at very different results: a determination of α in former case and of h in the latter, because of difference in values of n and m . That is a kind of a metrological joke because even the units of the gyromagnetic ratio are different because of involvement of factors such as V_{90}/V . Such factors appear because in certain situations we cannot avoid applying the SI since the value of the magnetic constant μ_0 is known exactly in the SI units and we also have to deal with the practical units as long as a real measurement is concerned.

One more confusing example is a measurement of the Compton wavelength of a neutron $h/(m_n c)$. The experiment consisted of two important measurements: one is related to the de Broglie wavelength $\lambda_v = h/(m_n v)$ and the other to the velocity v . They were measured in a sense in quite different units. The velocity was determined in the proper SI units directly. Meanwhile the wavelength λ_v was compared with the lattice spacing of a certain crystal. This crystal was indirectly compared with a so-called perfect crystal, basically used for the Avogadro project. Because of that the h/m_n result is strongly correlated with a certain block of the data related to N_A and it is not just an isolated result related to a neutron.

Unfortunately, this customary practice with labelling the results is very confusing and for a non-expert it is hard to understand what was really measured and which data are correlated.

5 Recommended Values and the ‘Less Accurate’ Original Results

Now, we can describe the adjustment. In the first approximation, we have to evaluate the most accurate data only (i.e., the auxiliary data), next to deal with the results from the α -block and afterwards to adjust the h -block. That should give a good approximate result.

In reality, the less accurate data can still affect more accurate data, often marginally, but not always. The adjustment is very similar in a sense to a simple least-square procedure, where the statistical weight of data drops down with increase of their uncertainty. However, the less accurate data are still very important. If they agree with the main part of the data, then that increases the final reliability of the evaluation, which is not just a question of the χ^2 test. We always want confirmations, even not very accurate, but independent. However, with such a large amount of data some may disagree. In such a case the less accurate data can have very important impact on the final results.

The data are strongly correlated and one may wonder what should be done by a user if certain input data are inconsistent as it actually happens from time to time. If the accuracy of the application is really sensitive to what value of the constant to take, one should avoid using the CODATA tables and use instead the CODATA analysis of the input data. If accuracy is not

important, it is better to use the same data all over the world, i.e., the data from the CODATA tables, and it should not matter whether they are well consistent or not.

6 The Fine Structure Constant α and Related Data

Let us consider a situation with the fine structure constant as an example. The CODATA's result

$$\alpha^{-1} = 137.035\,999\,11(46), \quad [3.3 \times 10^{-9}], \quad (5)$$

is based mainly on a datum from the anomalous magnetic moment of an electron a_e . All the related contributions are shown in Fig. [1](#).

The fine structure constant α plays a crucial role in quantum electrodynamics (QED) and because of that a few questions may arise.

- Could we use the CODATA's value to test QED theory? The answer is negative. Comparisons of theory and experiment, which are the most sensitive to a choice of α , have already been included in the deduction of the result [\(5\)](#). If we like to check a particular QED effect we should apply a value of α obtained without any use of the effects under question. The CODATA adjusted value includes in principle all QED effects, for a precision test of which we need an accurate value of α .
- Which value of α can we use then? The answer depends on what kind of a test we would like to perform. If we would like to test QED 'absolutely',

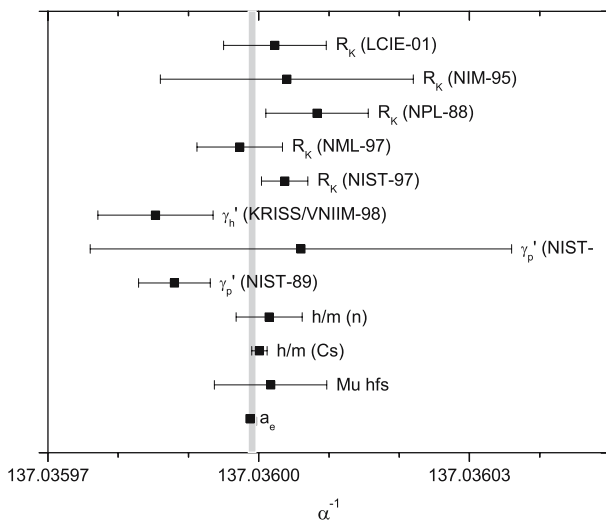


Fig. 1. The fine structure constant α . The vertical strip is related to the CODATA recommended values. The original results are explained in [\[1\]](#)

we should take the best non-QED value which is

$$\alpha^{-1}(\text{Cs}) = 137.036\,000\,1(11), \quad [7.7 \times 10^{-9}], \quad (6)$$

a result derived from the Rahman spectroscopy of the caesium atom. If we like to check the consistency of QED, we can take one of QED-related values such as

$$\alpha^{-1}(a_e) = 137.035\,998\,80(52), \quad [3.8 \times 10^{-9}], \quad (7)$$

and use it for a calculation of other QED effects, such as the hyperfine interval in the muonium atom.

- If we calculate a value which is very sensitive to a choice of α among known values, what have we to do? The best choice is to reverse the situation, i.e., determine α and put it into Fig. 1. In this case we can see whether it agrees with various values. Sometimes the data are not in good agreement and a new value can completely change the situation.
- If we like to determine α , what is the crucial level of accuracy? Let us assume for a moment that the data are perfectly consistent. In such a case the crucial accuracy is that of the second value in the row, which is (6). This value is vital for the reliability of the CODATA result. We remind that the dominant contribution to (5) comes from the anomalous magnetic moment and the result (7) has not been confirmed either experimentally or theoretically.
- That is not an unusual situation. The most advanced experiments and calculations are hard to repeat or confirm. Meanwhile, they have entered ‘terra incognita’ and despite high quality of the research teams they are most vulnerable because of lack of experience or rather a wrong ‘experience’ based on trusted unimportance of various phenomena which may become important. For instance, for recommendation of conservative committees of CIPM they sometimes introduce a kind of factor or reliability for accurate measurements, which may increase the uncertainty tenfold (8).
- Have we to trust all data for α ? That is not exactly the case since there is no appropriate theory for the quantum Hall effect which provides us with five data points.
- However, the agreement is good, but not perfect. We note that two values with the gyromagnetic ratio of a proton are within certain disagreement with the most accurate value. From a purely scientific point of view we have a rather good general agreement (cf. with the situation on h and G below). Nevertheless, there is an application which deals with a practical unit of resistance by CIPM (9). They conservatively estimate an uncertainty as a part in 10^7 . The related value of the fine structure constant is

$$\alpha^{-1}(\text{CIPM}) = 137.035\,997(14), \quad [1 \times 10^{-7}].$$

We should mention, however, that CIPM is overconservative because their results may have legal consequences and their examinations are for this reason not just a kind of scientific research (see (6) for further discussion).

Actually, that is a strange story how we deal with, e.g., 3σ -off points. When they are a part of a large statistics set of similar measurements, we are satisfied by the χ^2 criterium. Meanwhile, when the data are different such as for the adjustment of the fundamental constants or QED tests with different systems, we sometimes pay special attention to such 'bad' points trying to understand what is wrong in their particular cases.

A comparison of α , extracted from a particular QED value, let us say, the muonium hyperfine interval, after a certain improvement of theory, with other α s has a number of additional reasons (in respect to a comparison with the CODATA recommended value only):

- The muonium datum has already been used for determination of α in [5]. Despite the fact that it has a marginal effect, it is not appropriate to compare a certain improvement of α (Muhfs) with an average value, which includes an earlier version of α (Muhfs). The new and old values are based on the same experiment and the very appearance of the new value means that the old value is out of date.
- If we have a contradiction, we can clearly see whether the new value contradicts to one or two most accurate data but agrees with most of the rest or so, or it disagrees with all.
- Known data experience corrections from time to time. Using a set of original data, one can introduce the proper corrections. However, there is no way to correct the CODATA value, except indeed redoing the adjustment.

The latter is a result of a complicated procedure which includes re-examination of accuracy of various data and test of their accuracy. It is not possible to update the list of recommended values very often. Because of that a substantial delay may take place. For instance, the most recent CODATA paper was published in 2005 and we can expect a new one in 2008. The deadline for the input data in [1] was the end of 2002. That means that any evaluation including data obtained since 2003 will not be available until 2008. Because of that it may be important in certain cases to consider original results reviewed in the recent CODATA paper [1] and add the new results, available since recently, if any.

7 The Planck Constant h and Related Data

Determination of the fine structure constant has demonstrated a rather good agreement. The situation is not always so good. As an important example of a substantially worse agreement we present data related to the Planck constant h in Fig. 2.

The data are not in good agreement. In particular, a result related to N_A contradicts to the most accurate data obtained from the watt-balance

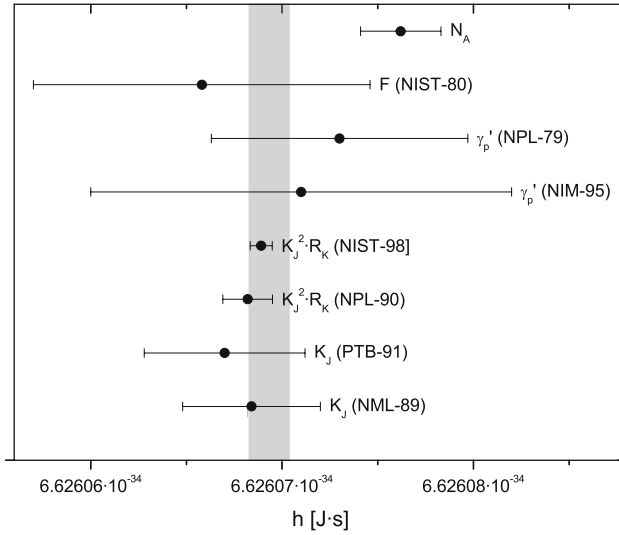


Fig. 2. The Planck constant. The vertical strip is related to the CODATA recommended values. The original results are explained in [11]

experiments. We will return to this result later. We need to mention that CIPM recommended a value of the Josephson constant $K_J = 2e/h$ with a conservative uncertainty of 2 parts in 10^7 while their conservative value of $R_K = h/e^2$ has uncertainty of a part in 10^7 . The related value for the Planck constant is

$$h(\text{CIPM}) = 6.626\,068\,9(53) \times 10^{-34} \text{ J s} , \quad [8.1 \times 10^{-7}] .$$

8 The Newtonian Constant of Gravitation

The results on the Newtonian constant of gravitation G show an even much worse situation with a scatter superseding the uncertainty by many times (see Fig. 3).

Despite the gravitation constant being without any doubt one of the most fundamental constants, its accuracy does not have great importance. Fundamentality of G shows itself first of all in the application to quantum gravity where the obtained results are rather qualitative than quantitative. Another important application is due to general relativity. Precision tests of general relativity involve much higher accuracy than the one in the determination of the Newtonian constant. For actual problems, the most important constant is a product of a gravitating mass (of Sun or Earth) and G and such products have been known much more accurately than G and from completely different kind of data.

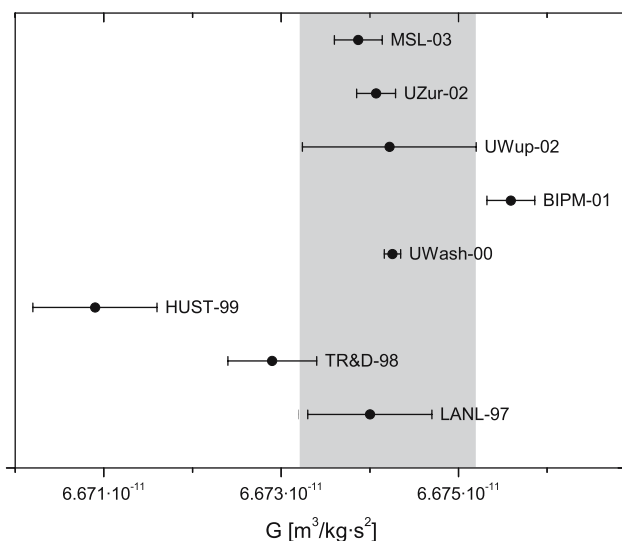


Fig. 3. The Newtonian constant of gravitation. The vertical strip is related to the CODATA recommended values. The original results are explained in [11]

Still there is a kind of experiments of fundamental nature which are in part similar to measurements of G , namely, studies of equivalence principle in laboratory distance scale. However, such experiments are differential, and the essential part of uncertainty should cancel out.

As a result, we note that the determination of G is indeed an ambitious and important problem, but it is somewhat separated from both the rest of the precision data and applications of fundamental physics.

9 The Fundamental Constants and Their Numerical Values

The discussion above raises a more general question on fundamental constants and their values. The numerical value of a dimensional fundamental constant involves the units and thus a certain kind of phenomena which are used to determine units. Such an involvement can change the physical meaning when going from the constant to its value drastically.

While the constants, such as the speed of light or the Planck constant, are determined by Nature, their numerical values can be treated with a certain room for arbitrariness. We can, e.g., adopt certain numerical values by definition.

In the case of variability of the constants, the interpretation of possible changes of the constants and their numerical values is quite different (see, e.g., [9]).

Two constants, discussed above, h and G , are truly fundamental, but they are not very often needed for accurate calculations. Below we consider certain values more closely related to atomic and particle physics or, in more general terms, to microscopic physics.

10 Microscopic and Macroscopic Quantities

In microscopic physics nobody intends to apply any macroscopic unit such as a kilogram. However, the nature of the units is not a trivial issue. We should distinguish between their rough values and their definition. Rough values of various units have been determined historically. For most of the SI units they are macroscopic, such as for a kilogram or a second. Meanwhile, the SI kilogram is defined as a macroscopic unit, but the SI second at present is defined as a kind of atomic unit via the hyperfine interval in caesium-133 atom.

The only SI unit which has a clear historic microscopic sense is the volt. To proceed with potentials one dealt with breaking atomic or molecular bonds. A characteristic ionization potential is of a few volts and, in particular, in hydrogen it is about 13.6 V. A popular non-SI unit, the electron-volt possesses a clear atomic sense in a rough consideration. Because of this ionization issue, an energy related to R_∞ is, indeed, 13.6 eV. However, if we look at the definition of the volt in a practical way, we find that the volt of the SI is defined via the ampere and the watt. The latter are defined via the kilogram, the metre, the second and a fixed value of the magnetic constant of vacuum μ_0 . Because of the presence of the kilogram, the volt and the electron-volt have macroscopic meaning from the point of view of measurements.

Measuring microscopic values in terms of macroscopic units is always a complicated problem, which introduces serious unnecessary uncertainties. Meanwhile, the very use of the electron-volt in the atomic, nuclear and particle physics is an issue completely based on a custom and never related to real matter. It is a kind of illusion. However, for missing a difference between reality and illusion, one has to pay. The price is an unnecessary uncertainty in various data, expressed in the electron-volts, and a correlation between uncertainties of various data.

The electron-volt is widely used in microscopic physics. In particular, it is customarily applied to characterize the X-ray and gamma-ray transitions by their energy and to present particle masses in units of GeV/c^2 . We have to emphasize that nobody performs any precision measurement in these units in practice. The transitions are measured in relative units. To measure them absolutely one has to apply X-ray optical interferometry and either compare an X-ray and an optical wavelength or calibrate a lattice parameter in a certain crystal in terms of an optical wavelength. This means that in actual precision measurements one really deals with the wavelength (or related frequency) and not with the energy of the transition.

The most accurate relative measurements of hard radiation are in fact more accurate than the conversion factor between the frequency and the energy, namely, e/h (if the energy is measured in the electron-volts). The uncertainty of this coefficient is presently 8.5×10^{-8} [4]. We strongly recommend for transition frequencies measured more accurately than 1 ppm to present results in frequency units and for results in the electron-volts to present separately two uncertainties: of the measurement and of the conversion into electron-volts. It would also be helpful to specify explicitly the value of the conversion factor used.

If one even tries to measure energy in electron-volts ‘by definition’, the electron-volts proper are still not the best choice. CIPM recommended a practical unit, volt-90, in terms of which the Josephson constant K_J has an exactly fixed value [7]. In such a case, the result would be expressed in terms of eV_{90} , rather than in eVs. The uncertainty of the conversion factor e/h in practical units is zero.

MeVs and GeVs are also widely used for the masses of particles and for the energy excess in nuclear physics. From the point of view of accuracy, such units are not better than kilograms. The best choice is to apply direct results of relative measurements (mass ratios), when available, or to express the masses in terms of either of the two adequate microscopic units. One of the latter is the unified atomic mass unit, u , and the other corresponds to the frequency related to mc^2/h . In these two units elementary masses are known with the highest accuracy.

11 Reliability of the Input Data and the Recommended Values

The easiest part of the evaluation is their mutual evaluation. Two most important questions are related to the data.

1. Not all available data are included as input data and not all input data are exactly equal to the originally published data. The question to decide prior to the evaluation is how to treat each piece of data? Should we accept them ‘as they are’ or assign them a corrected uncertainty or even dismiss some of them prior to any evaluation procedure? That should be decided on the basis of quality of the data.
2. After initial probe mutual least-square evaluations are done, we used to see that some pieces are not in perfect agreement with the rest of the data. That cannot be avoided once we have many pieces of data. That opens another important question, to be decided at the initial stage of the evaluation. How should we treat the data when they are combined together? In other words, should we do anything with the data due to their inconsistency if any? At this stage the decision is partly based on their consistency, partly on their correlations and partly still on their initial properties.

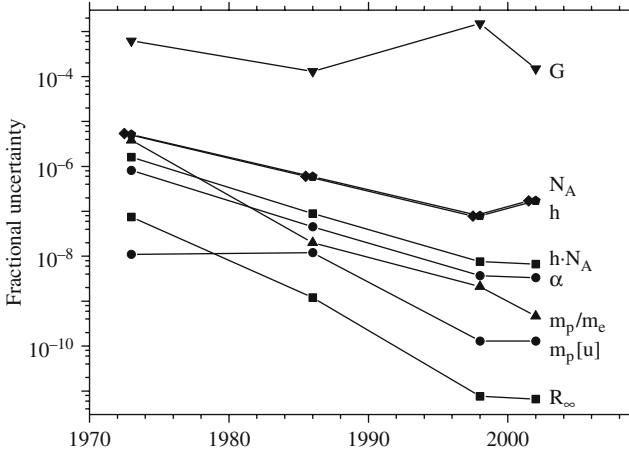


Fig. 4. Progress in determination of fundamental constants by the CODATA task group (see [1, 2] and references to earlier results therein)

These questions are to be decided not on the basis of statistics (like when in an easy case of a number of data points for the same quantity one drops the smallest and the largest results) but first of all on the basis of their origin, their experimental and theoretical background.

The CODATA's recommended values are the best ones, but in principle that does not mean all of them are really good. They are the best because the authors perform the best possible evaluation of existing data. If data are not good enough, the result of any evaluation cannot be good. The CODATA task group are not magicians. That is why it is essential to have independent results for each important quantity. Below we consider a question of the reliability of data important in atomic and particle physics.

The conservative policy of CIPM and discrepancy in the input data (see Fig. 2) show that direct use of the CODATA result is not a single option to be considered. The CIPM treatment of the data does not contradict the CODATA approach, because CIPM applies the CODATA analysis; however, it prefers to derive a more conservative result from the CODATA's consideration.

An important illustration of reliability of the recommended values is presented in Fig. 4. While for most of them progress with time reduced the uncertainty, sometimes (e.g., for h or G) better understanding meant appearance of a discrepancy.

12 Proton Properties

Among the particles listed in CODATA tables [1] two, a proton and muon, are of particular interest. The most confusing datum on a proton is its charge radius, R_p . The CODATA paper recommends the result

$$R_p(\text{CODATA}) = 0.8750(68) \text{ fm} , \quad (8)$$

which, in principle, is based on all available data including electron scattering and hydrogen spectroscopy. Nevertheless, we would not recommend to apply this result blindly to any sensitive issue. The dominant contribution comes from spectroscopy of hydrogen and deuterium and the related theory. The spectroscopic data included various experiments, which partly confirm each other. However, a substantial progress made in the theory (the Lamb shift) is related to surprisingly large higher-order two-loop terms [10], which are neither understood qualitatively nor independently confirmed quantitatively. I would not consider the theoretical expressions at the moment as a reliable result until their proper confirmation or understanding. Such a need for an independent confirmation is a characteristic issue for any breakthrough in either theory or experiment.

The second (in terms of accuracy) result mentioned in [11]

$$R_p(\text{Sick}) = 0.895(18) \text{ fm} \quad (9)$$

is the one obtained by Sick [11] from the examination of world scattering data. This piece of CODATA input data is very specific. CODATA very seldom accepts any evaluation of world data without performing a critical re-consideration. A crucial feature of the CODATA treatment of the world data is reconsideration of accuracy on experimental and theoretical results. The most important scattering results were obtained long time ago. They dealt with QED scattering corrections obtained a few decades ago. At present, the QED corrections are known better, but there is no simple way to re-evaluate the existing scattering data. The Sick's examination is the most competent I have ever seen. But it is an evaluation of the data 'as they were published'.

The problem of correcting the experimental data because of a possibly inappropriate treatment of higher-order radiative corrections by the original authors was not addressed in his evaluations. I would rather consider the central value of this evaluation as a valid one but would somewhat increase the uncertainty (see discussion in [12]) achieving

$$R_p = 0.895(30) \text{ fm} . \quad (10)$$

It is hard to be more precise with the uncertainty. If such a re-evaluation were done in the CODATA paper, the problem should be addressed. But it was not done in [1]. A reason not to do that is twofold.

First, it is an obvious fear that the job could not be done properly because of lack of necessary information for experiments done long time ago. Next, the proton size from the scattering plays rather minor role in the adjustment. The evaluation of the auxiliary block with the Rydberg constant is sensitive to the theory of a so-called state-dependent part of the Lamb shift of the n states and to theory of states with a non-zero orbital moment. Both depend on a value of the proton size marginally. This means that CODATA evaluation of

the Rydberg constant needs only a very rough value of the proton size and we can accept any result for R_p for such an evaluation.

The recommended value of the proton charge radius is actually determined by the same spectroscopic study. The rest of the data can rather produce a marginal effect on the value of R_p . In particular, the second value of the radius, obtained from the scattering, is rather out of interest of the CODATA evaluation and they do not care about it. The re-evaluation of the world scattering data from the CODATA side looks like an unnecessary overcomplicated problem with unclear reliability of the outcome.

One more proton property of interest is its magnetic moment or rather electron-to-proton ratio of the magnetic moments:

$$\frac{\mu_e}{\mu_p} = 658.210\,6860(66), \quad [1 \times 10^{-8}]. \quad (11)$$

The result is completely based on an MIT experiment performed long time ago [13]. While for the most important for constants such as α and h one can easily find all sources for particular results in [1], it is hard to see what result is the second in accuracy. While details of the analysis will be published elsewhere, here we conclude that the data may be obtained from a study of the muonium magnetic moment and the most accurate partial result

$$\frac{\mu_e}{\mu_p} = 658.210\,70(15), \quad [2.3 \times 10^{-7}] \quad (12)$$

is much less accurate than the MIT value.

13 Muon Properties

The muon data include the muon magnetic moment, mass and a_μ , the anomalous magnetic moment. The latter should not be used at all for any sensitive issue. The CODATA can make a reasonable prediction only after the situation is settled, while for a_μ it is not. Speaking more generally, CODATA is a brand for the best constants, but not all products with this brand are equally good. Critical examination of input data can improve their reliability and reduce their scatter. I would say that is the most competent evaluation of world data on the fundamental constants. Nevertheless, there is no magic in the CODATA adjustment and the result cannot be better than the input data. Before trusting any particular CODATA result one has to take a look into the data analysis.

The result for a_μ has contributions from experiment and theoretical evaluations based on e^+e^- and τ data. To consider physics we should not average these partial results but re-examine and compare them.

The mass and magnetic moment have been used numerously in a quite confusing way. The experiment, most sensitive to their values, has been included

in the evaluation. For instance, one can apply a value of m_e/m_μ (or μ_μ/μ_p) to the hyperfine interval in muonium, either assuming QED to determine α or accepting a certain value of α to verify QED. However, the CODATA results

$$\begin{aligned}\frac{m_\mu}{m_e} &= 206.768\,283\,8(54), & [2.6 \times 10^{-8}], \\ \frac{\mu_\mu}{\mu_p} &= 3.183\,345\,118(89), & [2.6 \times 10^{-8}],\end{aligned}\tag{13}$$

are dominated by a value extracted from the muonium hyperfine interval assuming a certain value of α and validity of QED. The second best set

$$\begin{aligned}\frac{m_\mu}{m_e} &= 206.768\,276(24), & [1.2 \times 10^{-7}], \\ \frac{\mu_\mu}{\mu_p} &= 3.183\,345\,24(37), & [1.2 \times 10^{-7}],\end{aligned}\tag{14}$$

comes from separate data and may be used to either determine α or test QED.

We emphasize that all this information is contained in the CODATA papers [1, 2]; however, since ‘simple users’ are more interested just in the tables they usually miss it.

We remind that there is a number of compilations of various kinds of data around the world and even reading carefully most of the compilations, there is no chance to find details of input data. Sentences such as ‘the uncertainty does not include systematic error’ or so are often missing when a datum came from the original paper to a compilation. The CODATA paper is one of the very few exceptions; however, a way of reader’s treatment of the CODATA papers sometimes does not make use of this advantage.

14 Impact of a Redefinition of the Kilogram on Values of the Fundamental Constants

To conclude the paper, we would like to discuss two issues. One is rather technical and related to a possible redefinition of the kilogram and the ampere in terms of fixed values of h and e [14]. It is most likely that this redefinition will be adopted, but it is unclear when. The numerical values of the fundamental constants play two roles. One is that they represent in a numerical way certain experimental data. Redefining the kilogram, obviously the experimental results would not change and the information would not be added. Still, certain pieces of the information and related uncertainty can be removed from some data. After redefinition of units, certain experiments done with a relatively low accuracy could be isolated from the fundamental constants (e.g., any direct study of the prototype of the kilogram would have no relation to basic physical quantities anymore). The other role of the numerical values is that they are reference data. As we mentioned above, it is customary to use, without any

experimental or theoretical reasons, the electron-volts. The redefinition of the kilogram and the ampere would establish them as microscopic units (and the volt as well). The conversion factor e/h would be known exactly. This means that all values in electron-volts would have adequate accuracy.

15 Legacy of the Adjustment of the Fundamental Constants

The last question to discuss here is a conceptual one. Doing precision physics, we cannot ignore the very fact that we accept a large number of physical laws. Sometimes they are proved with a certain accuracy, sometimes they are not.

For instance, there is no accepted theory which demands that the electron charge and the proton charge be of the same value. We have various direct experimental tests, but those are always limited by their accuracy. The conceptual evidence should come from a new theory, which is confirmed experimentally. We strongly expect a certain unification theory, but no evidence has been available up-to-date.

We expect that the fundamental constants are really constant, but we do not understand their origin and we (or most of us) believe that during the inflation epoch of the universe some constants such as m_e/m_p changed. So, the constancy of the constants is merely an experimental fact. What is even more important is that certain physical laws are put into the very base of our system of units, the SI, and if they would occur incorrect, one may wonder whether that is detectable. The answer is positive. If we adopt a set of assumptions, either with an internal inconsistency or inconsistent with Nature, we should be able to see either an inconsistency in the interpretation of the results (e.g., a contradiction within two determinations of the same quantity) or a discrepancy between the trusted assumption and the observed reality.

To test any particular law, one has to rely on specific experiments sensitive to such a violation. The CODATA examination is mainly based on the assumption that we can follow the known physical laws. We know that any particular physical theory is an approximation. Combining the data from different fields we check the consistency of the overall picture (both the laws and the approximations) and the result obtained is satisfactory, up to now.

Acknowledgment

I am grateful to Simon Eidelman for useful discussions. This work was supported in part by the RFBR grant # 06-02-16156 and DFG grant GZ 436 RUS 113/769/0.

References

1. P. J. Mohr and B. N. Taylor: Rev. Mod. Phys. **77**, 1 (2005). [36](#), [37](#), [41](#), [43](#), [44](#), [45](#), [47](#), [48](#), [49](#).
2. P. J. Mohr and B. N. Taylor: Rev. Mod. Phys. **72**, 351 (2000). [36](#), [48](#), [51](#)
3. <http://physics.nist.gov/cuu/Constants/index.html>. [36](#)
4. S. Eidelman et al.: *The Review of Particle Physics*, Phys. Lett. B**592**, 1 (2004). [36](#)
5. P. J. Mohr and B. N. Taylor: Phys. Today (August 2000) BG6; (March 2001) 29. [37](#)
6. S. G. Karshenboim: Physics-Uspekhi **48**, 255 (2005). [37](#), [42](#)
7. T. J. Quinn: Metrologia **26**, 69 (1989) (see p. 70);
T. J. Quinn: Metrologia **38**, 89 (2001) (see p. 91);
T. J. Quinn: Metrologia **26**, 69 (1989) (see p. 69). [39](#), [42](#), [47](#)
8. T. J. Quinn: Metrologia **40**, 103 (2003). [42](#)
9. S. G. Karshenboim: Can. J. Phys. **83**, 767 (2005). [45](#)
10. K. Pachucki: Phys. Rev. A**63**, 042503 (2001);
K. Pachucki and U. D. Jentschura: Phys. Rev. Lett. **91**, 113005 (2003). [49](#)
11. I. Sick: Phys. Lett. B**576**, 62 (2003). See also contributions on the proton charge radius in this book (S. G. Karshenboim (Ed.): *Precision Physics of Simple Atoms and Molecules*, Lect. Notes Phys. **XXX**. Springer, Heidelberg (2007)):
by I. Sick (pp. [57](#)-[77](#)) and by J. C. Bernauer (pp. [79](#)-[91](#)). [49](#)
12. S. G. Karshenboim: Phys. Rep. **422**, 1 (2005). [49](#)
13. P. F. Winkler, D. Kleppner, T. Myint and F. G. Walther: Phys. Rev. A**5**, 83 (1972). [50](#)
14. I. M. Mills, P. J. Mohr, T. J. Quinn, B. N. Taylor and E. R. Williams: Metrologia **42**, 71 (2005); *Metrologia* **43**, 227 (2006). [51](#)

Proton Structure and Hydrogen Energy Levels

Precise Radii of Light Nuclei from Electron Scattering

I. Sick

Departement für Physik und Astronomie, Universität Basel, Basel, Switzerland
ingo.sick@unibas.ch

Abstract. We summarize various analyses of the *world* data on elastic electron scattering for the determination of the most precise *rms*-radii of light nuclei. We also present the Zemach moments needed for the interpretation of atomic hyperfine structure and μ -X-ray experiments.

1 Introduction

The root-mean-square (rms) radii of light nuclei are quantities of great interest for the understanding of these nuclei. They describe the most integral property concerning their size. The most precise radii are needed for the interpretation of modern data on atomic transitions, measurements performed in connection with determinations of fundamental constants and QED tests. These measurements recently have reached extreme precisions with, e.g., the 2p–1s energy difference and the hyperfine splitting (HFS) in hydrogen determined to 14 and 12 significant digits, respectively [1, 2]. The interpretation of such data is now entirely limited by the knowledge on the nuclear radii.

In this contribution we discuss the use of the *world* data on electron–nucleus elastic scattering for the determination of the most accurate radii. For the proton charge radius in particular we find significantly larger values than past studies and understand the reason for the dispersion of previous results. We also address the quantity — the Zemach moment — required to calculate the atomic HFS.

2 Proton Charge Radius

Elastic electron scattering from the proton has received extensive attention and the data [3, 4, 5, 6, 7, 8, 9, 10, 11, 12, 13, 14, 15, 16, 17, 18, 19] today cover a very large range of momentum transfer. In several cases, these data

are very precise (systematic errors below 1%) with the consequence that electron–proton scattering often served as cross-section reference.

Due to the spin $I=1/2$ nature of the proton, the elastic cross-section is determined by two independent form factors, the electric (Sachs) form factor $G_{\text{ep}}(q)$ and the magnetic form factor $G_{\text{mp}}(q)$, depending on the (four) momentum transfer q . In plane wave Born approximation (PWBA) the cross-sections can be written as

$$\frac{d\sigma}{d\Omega} = \sigma_{\text{Mott}} f_{\text{recoil}} [(G_{\text{ep}}^2 + \tau G_{\text{mp}}^2)/(1 + \tau) + 2\tau G_{\text{mp}}^2 \text{tg}^2(\theta/2)]$$

with $\tau = q^2/4m^2$, m being the mass of the proton. In order to separate G_{ep} and G_{mp} a so-called Rosenbluth separation has to be done. Measurements at the same momentum transfer q but different angles (hence different electron energies) allow one to separate G_{ep} and G_{mp} . For the low momentum transfers of interest here $(1 + \tau) \sim 1$ and the [...] bracket in the above equation reads

$$G_{\text{ep}}^2 + 2G_{\text{mp}}^2 \tau (1/2 + \text{tg}^2(\theta/2)).$$

A plot of [...] as a function of $1/2 + \text{tg}^2(\theta/2)$ yields a straight line with slope proportional to G_{mp}^2 and intercept given by G_{ep}^2 . For a precise determination of the G s, measurements covering the largest possible range in scattering angle are desirable. The standard procedure in the past was to use data from individual experiments to produce the G s, of which thus many independent sets are available in the literature.

In order to extract the proton *rms*-radii of the charge and magnetization densities, one can start from the low- q expansion of $G(q)$:

$$G(q) = 1 - q^2 \langle r^2 \rangle / 6 + q^4 \langle r^4 \rangle / 120 - \dots$$

Most of the radii in the literature have been obtained using this model-independent expansion. Some of the earlier radii have been determined by fitting $G(q)$ with a suitable model-parameterization, G_{mod} , and determining the *rms*-radius by the $q^2 = 0$ slope of $(1 - G(q))$. Some of the radii given in the literature have been obtained by fitting the data using parameterizations derived in terms of the vector dominance model (VDM) which starts from the assumption that the photon–nucleon coupling proceeds via the various vector mesons.

A selection of results for the proton charge *rms*-radius is shown in Fig. [11](#). The CODATA value was, before the publication of the proton radius discussed below, the “recommended” value. It was obtained by averaging two of the determinations (Mainz MI, VDM) that were considered to be particularly reliable. The error bar was basically a guess.

Figure [11](#) shows that the results for the proton *rms*-radius have a large amount of scatter; this scatter is actually considerably larger than one could expect from the high-quality database available. Particularly worrisome is the high value of the Mainz 2-pole fit, which used a database that was very similar

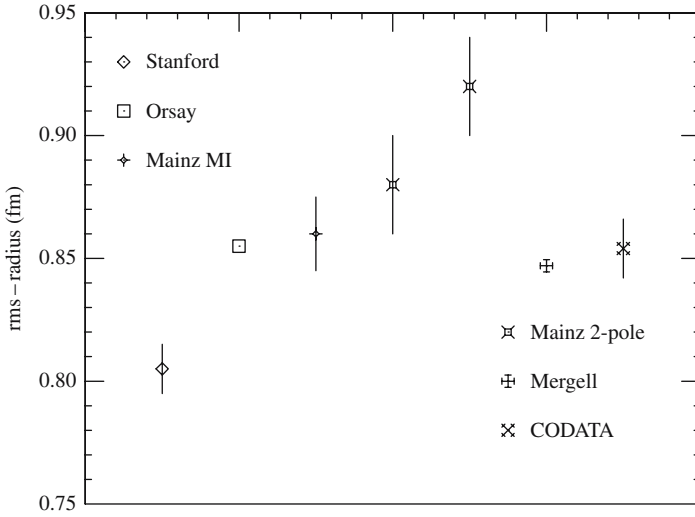


Fig. 1. Published values for the charge *rms*-radii of the proton [5, 7, 20, 21, 22, 23]

to the one employed in the Mainz MI fit. The low value from the very early Stanford data is not much of a concern; the data set did not contain cross-sections at low enough a momentum transfer to really be sensitive to the *rms*-radius.

This situation on the charge *rms*-radius was clearly very unsatisfactory. Moreover, the CODATA value disagreed with the radius 0.89 ± 0.014 fm determined using the hydrogen Lamb shift data [24].

The past determinations of the radius suffer from a number of shortcomings which we will discuss below.

- The cross-sections have always been analyzed in terms of PWBA, which treats the electron waves as *plane* waves and thus neglects Coulomb distortion. This was done because $Z\alpha$, the parameter which governs Coulomb distortion, is small for $Z = 1$. The Coulomb distortion was neglected because the difference between q and $q_{\text{eff}} \sim q(1 + 4Z\alpha/(3RE))$ appeared to be small. q_{eff} does more or less correctly account for the shift of diffraction minima due to Coulomb distortion. However, the shift ($q - q_{\text{eff}}$) is *not* the main Coulomb effect at low q . There, Feshbach and McKinley [25] showed, in second Born approximation and for a point nucleus, that the dominant effect is a multiplicative change of the Mott cross-section:

$$\tilde{\sigma}_{\text{Mott}} = \left(\frac{Ze^2}{2E} \right)^2 \frac{\cos^2(\theta/2)}{\sin^4(\theta/2)} \left[1 + \frac{\pi Z}{137} \frac{\sin(\theta/2)(1 - \sin(\theta/2))}{\cos^2(\theta/2)} \right].$$

The consequences of the terms in the [...] are by no means negligible. This is shown in Fig. 2 which displays both the effect of Coulomb distortion (exchange of one additional soft photon) and the exchange of an additional

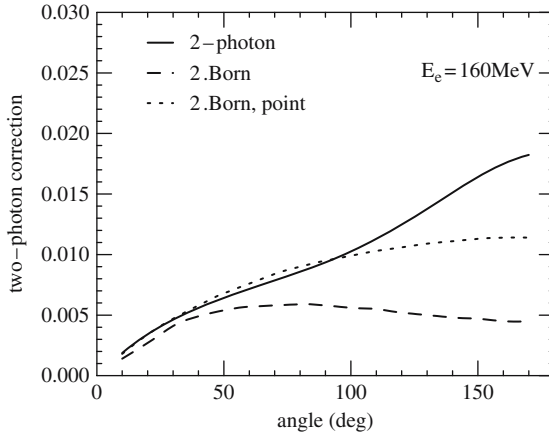


Fig. 2. Relative contribution of two-photon exchange to elastic e-p scattering at $E_e=160$ MeV. The results in second Born approximation account for the Coulomb distortion (exchange of second soft photon) only

(soft or hard) photon to be discussed later. If one is interested in determining radii with accuracies in the %-region, the Coulomb effect obviously must be accounted for.

Convenient expressions for the Coulomb distortion for nuclei of finite size have been derived in [26]. For $Z = 1, 2$ these expressions are much easier to use than the full (numerical) solution of the Dirac equation standard for the heavier nuclei; the second Born approximation used is accurate enough as the neglected terms are of the order $(Z\alpha)^2 \sim 10^{-4}$.

• A second problem concerns the usage of the “model-independent” power expansion of $G(q)$ which at first sight appears to be more reliable than the uses of G_{mod} or G_{VDM} . In order to make the “model-independent” approach practical, one wants to reduce the importance of the higher moments. One could hope that the $q^4\langle r^4 \rangle$ and higher-order terms can be made sufficiently small by going to low q . This is true in principle, but very hard in practice. At small momentum transfer also the $q^2\langle r^2 \rangle/6$ is small and very difficult to extract from data that have finite (statistical or systematic) errors. The measured cross-section is proportional to $(1 - q^2\langle r^2 \rangle/6)^2$, so very small errors in the cross-section lead to large errors in $q^2\langle r^2 \rangle/6$. One therefore in practice has to include data at not-so-low q , and these are also sensitive to the higher moments. This is particularly problematic for the proton, which has a density that can be reasonably approximated by an exponential function. For such a density, the higher moments are rapidly increasing with order, i.e., $\langle r^4 \rangle = 2.5 \langle r^2 \rangle^2$, $\langle r^6 \rangle = 11.6 \langle r^2 \rangle^3$, etc., and give a large contribution to $G(q)$.

As a consequence, there is no region of q where the $\langle r^2 \rangle$ -term dominates the finite size effect to $>98\%$ and the finite size effect is sufficiently large to get an accurate *rms*-radius with say $<2\%$ error bar. There is also no region where, in

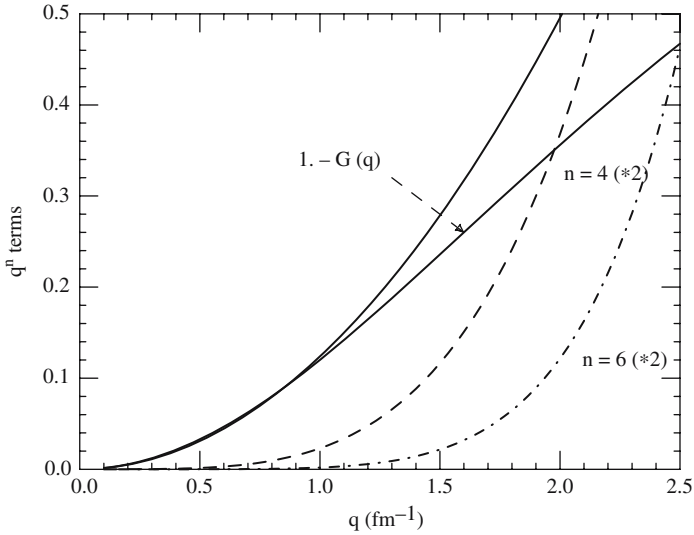


Fig. 3. The figure shows the contribution of the q^n terms to the finite size effect, calculated using the moments from the CF parameterization. The full curve labeled $1 - G(q)$ gives the total finite size effect

a fit with $\langle r^2 \rangle$ and $\langle r^4 \rangle$, one does not get into trouble with the $\langle r^6 \rangle$ term. This is illustrated in Fig. 3. Towards larger q the model-independent expansion is anyway seriously limited by the low convergence radius of $q \sim 1.4 \text{ fm}^{-1}$.

Padé approximants have been invented to solve the “problem of moments” and deal optimally with the reconstruction of a function from its moments $\langle z^n \rangle$. These approximants also accelerate the convergence of poorly converging (even diverging) series [27] and have a much larger convergence radius. For the fit of the proton form factor, we use a special subclass of Padé approximants, which can be rewritten as a continued fraction (CF) expression:

$$G(q) = \frac{1}{1 + \frac{q^2 b_1}{1 + \frac{q^2 b_2}{1 + \dots}}}$$

The CF expansion is also the natural parameterization for form factors obtained in the VDM, where the nearest (dominating) pole gives a contribution like $1/(1 + q^2 b_1)$.

- A third problem relates to the fact that in most of the fits of $G(q)$ -data the overall normalization of the cross-sections has been floated in order to minimize the χ^2 . This procedure unfortunately reduces the sensitivity of the data to the *rms*-radius considerably. It also means that one disregards a large fraction of the effort (typically 1/2) that went into the experiment. “Elimination” of potential normalization errors by floating the data makes

the normalization-determining (implicit) extrapolation to $q = 0$ very sensitive to q -dependent systematic errors. These errors are never discussed in the publications describing the experiment, and thus always ignored.

For the determination of the proton radii not subject to the above shortcomings we have used the *world* data [28]. In these fits we use the primary cross-sections and *not* the form factors extracted in PWBA. This allows us to apply the Coulomb corrections, which depend on energy and angle. When parameterizing both G_{ep} and G_{mp} and then fitting the data, the separation of G_{ep} and G_{mp} is automatically performed. This separation is of much superior quality as compared to the standard one, since for the L/T-separation all the *world* data in the considered q -range are employed, and not only those of a given individual experiment.

This approach has another fundamental advantage: when fitting the data with their random uncertainties, one obtains the error matrix which allows one to calculate the random errors of all derived quantities, and this error includes all the correlations that result from the fact that the cross-section depends on a combination of G_{ep} and G_{mp} .

At the same time, this approach allows for a consistent inclusion of the systematic errors of the data (mainly normalization uncertainties). When using published form factors, the correct treatment of statistical and systematic errors is virtually impossible. In the approach used here, the systematic errors are included by changing each data set individually by its quoted systematic error, re-fitting and adding quadratically all the resulting changes for the derived quantities (radii, form factors, ...). The systematic errors are quadratically added to the random ones; this should be fine given the large number of data sets employed. The treatment of the systematic errors in particular is most conservative, i.e., produces uncertainties that are *larger* than what is found using other approaches described in the literature.

In order to use the CF expansions, two quantities have to be fixed: the number of terms $b_n, n = 1, N$ and the maximum momentum transfer q_{\max} of the data employed. In order to explore possible ambiguities resulting from a particular choice, we have tested the dependence on N and q_{\max} using pseudo-data. These data were generated using parameterized expressions for the form factors (dipole form or the dispersion relation parameterization of Hoehler et al. [29]). The pseudo-data were generated at the energies and angles of the experimental data and with the error bars of the experimental data. In the fits, the pseudo-data were used as calculated from the parameterization or with random fluctuations calculated from the experimental error bars superimposed.

When using the q -region $1 \text{ fm}^{-1} < q_{\max} < 5 \text{ fm}^{-1}$ and when using 2–5 terms in the CF expansion, we find a scatter of the fitted *rms*-radius of $\pm 0.010 \text{ fm}$ around the true (input) value. This scatter then is representative of the uncertainty due to the choice of N and q_{\max} ; it covers at the same time the statistical errors (which for pseudo- and real data are the same by construction).

With respect to the range of momentum transfer it is of interest to explore the region of q which contributes most to the determination of the *rms*-radius. It is by no means obvious, for example, that the very low q data are the most important. The cross-sections measure $(1 - q^2 \langle r^2 \rangle / 6)^2$; if the data on the cross-sections have uncertainties (statistical or systematic), then the finite size effect $q^2 \langle r^2 \rangle / 6$ has a much larger uncertainty.

In order to explore the importance of real data for the determination of the *rms*-radii, we have carried out the following “notch test”. The cross-sections in a given q -region of $q_0 \pm 0.1 \text{ fm}^{-1}$ have all been increased by 1%, the total data set then has been re-fitted and the change of the *rms*-radii plotted as a function of q_0 . Figure 4 shows the result. For the determination of both the charge- and the magnetic radii, the q -region of $0.85 \pm 0.3 \text{ fm}^{-1}$ is the most important one.

In Fig. 5 we show the ratio of the experimental data and the fit cross-sections. No systematic deviation is visible, and no (arbitrary but) χ^2 -improving renormalization of some data set is called for.

Although the data have been taken over a long time-span and at different facilities the quality of the fits is very good. The χ^2 is 512 for 310 data points. The main data set yielding a χ^2 per degree of freedom > 1 is the very early one from Stanford, which has data points that scatter too much; omitting this set or adding 3% to the error bars reduces the χ^2 to close to 1 per d.o.f., but changes the resulting radius by $< 0.1\%$ only. The charge-*rms*-radius from the above analysis is 0.895 fm. The uncertainty due to N , q_{max} and statistics is ± 0.010 fm, the systematic uncertainty 0.013 fm. This yields as the final result for the charge radius of the proton $r_{\text{rms}}^e = 0.895 \pm 0.018$ fm.

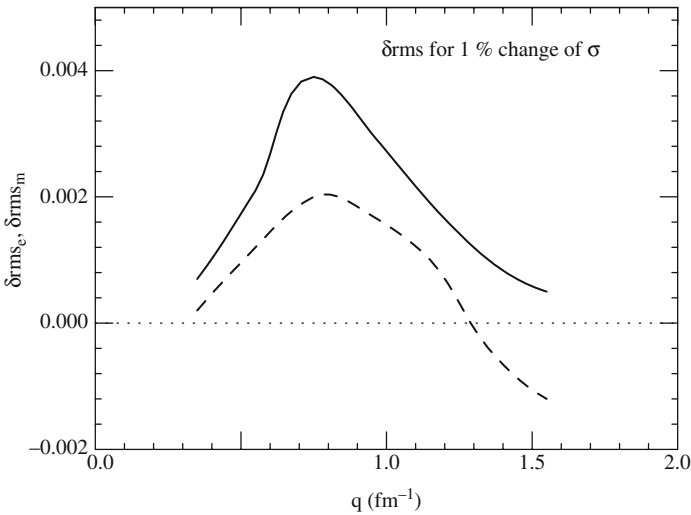


Fig. 4. The figure shows the results of the “notch test” used to explore the sensitivity of the radii (solid: charge) to different q -regions

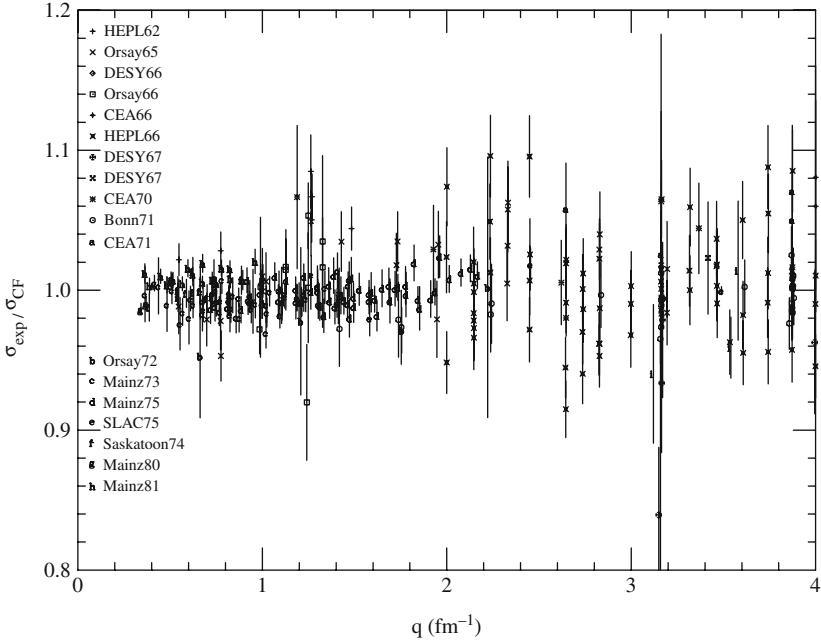


Fig. 5. Ratio of experimental and fit cross-sections for the CF parameterization

The charge *rms*-radius we find is significantly larger than the values cited in the literature. Although we use the *world* data, the error bar has not really decreased; this is a consequence of the fact that we treat the systematic errors in a very conservative way. It is satisfactory to observe that our radius agrees with the one determined from atomic transitions [24] 0.890 ± 0.014 fm.

This re-determination of the radius would not be complete without an understanding of the differences to previous analyses. We here discuss the two which were considered to be perhaps the most reliable ones. Simon et al. [7], who found $r_{\text{rms}} = 0.862$ fm, used the polynomial expansion up to q^4 and $q_{\text{max}} = 1.2 \text{ fm}^{-1}$. They quote a value for the $\langle r^4 \rangle$ -moment that turns out to be a factor of 10 smaller than given by fits that explain the proton data at higher q ; this difference comes from very small systematic problems in the data and the fact that the normalization has been floated, which enhances small q -dependent errors. When repeating their fit with a value of $\langle r^4 \rangle$ that explains the data at larger q , one finds a radius that agrees with the one we obtain.

The *rms*-radius coming from the analysis of the data using dispersion relations and the VDM also often has been considered as the most reliable. The VDM provides a strong constraint to the fit, partly because of the desire to fit all four nucleon form factors simultaneously. When looking at the ratio of experimental and VDM cross-sections with the resolution used in Fig. 5

one immediately observes a systematic difference reaching 2% as q increases from 0 to 1 fm^{-1} . This difference fully explains the low VDM-radius.

We have also looked at all other determinations of the radii. In all cases, we understand the origin of the differences, resulting either from misfit of the data, use of PWBA and/or use of the “model-independent” expansion.

3 Radius of Magnetization Density

The fit described above yields both G_{ep} and G_{mp} , hence also the magnetic *rms*-radius. G_{mp} at low q is harder to extract as the magnetic contribution to the cross-section comes with an additional q^2 -factor. As a consequence, much of the *world* data at low q is dominated by the G_{ep} -contribution as shown by Fig. 6 where we plot the ratio of contributions $r = (\text{charge})/(\text{magnetic}+\text{charge})$ for all cross-section data. There are, however, some accurate 180° data in the q -region of interest (points at $r = 0$) and these are totally dominated by G_{mp}^2 .

Our fit to the *world* data, performed in the manner described above, gives $r_{\text{rms}}^{\text{m}} = 0.855 \pm 0.035 \text{ fm}$ for the radius of the magnetization density; the error bar again includes statistics, systematics and model dependence.

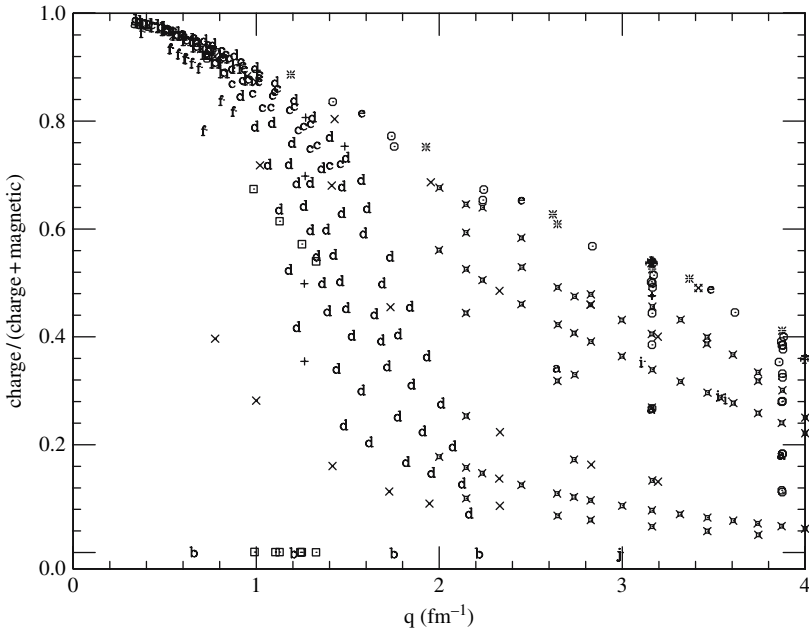


Fig. 6. Ratio of charge to total contribution to e-p cross-section for various experiments

4 Zemach Moment of Proton

For the calculation of the atomic hyperfine structure HFS one obviously needs information on the radial distribution of the magnetization in the proton. The situation is, however, more complex than for the Lamb shift, which depends only on the charge *rms*-radius. The electron–nucleus magnetic interaction in the H-atom is very short-ranged and confined to the vicinity of the nucleus. In this region the electron wave function is also affected by the radial distribution of the nucleon charge. The HFS thus depends simultaneously on the proton charge- and magnetization densities.

Zemach [30] has derived the finite size effect on HFS a long time ago and has shown that it depends on a convolution of the charge- and magnetization densities:

$$\Delta E_{\text{Zemach}} = -2 Z \alpha m \langle r \rangle_{(2)} E_{\text{F}} ,$$

$$\langle r \rangle_{(2)} = \int d^3 r r \int d^3 r' \rho_e(|\mathbf{r} - \mathbf{r}'|) \rho_m(r') .$$

The folding integral can be, by partial integration, re-expressed recognizing that the G s are Fourier transforms of the ρ s:

$$\langle r \rangle_{(2)} = \int_0^\infty \frac{dq}{q^2} (G_e(q^2) G_m(q^2) - 1) .$$

Above, E_{F} is the Fermi hyperfine splitting, m is the electron mass, Z is the nuclear charge, α is the fine-structure constant. The latter expression for $\langle r \rangle_{(2)}$ is obviously easier to exploit.

From the above equation, it would appear that, due to the $1/q^2$ factor, the Zemach integral would depend on data at very low q , lower than relevant for the *rms*-radii. This conclusion would, however, be incorrect. At $q = 0$ the term $G_e G_m$ compensates the “1” in the integrand, and the next higher term is proportional to q^4 , thus leading to a *small* contribution of the low- q data. We have, as described for the *rms*-radii, used the “notch test” to explore the range of sensitivity in q for the Zemach moment. We find that the data for $0.8 < q < 2.6 \text{ fm}^{-1}$ are the most important ones.

This Zemach moment has been extracted from the CF parameterizations obtained as discussed above [31]. Our procedure has the important feature that we have fitted the charge and magnetic form factors *simultaneously* to the available cross-sections. The error matrix of the fit therefore contains all the correlations between the two form factors, resulting from the fact that the cross-sections depend on a linear combination of charge and magnetic form factors squared. These correlations obviously are important when computing the uncertainty in the Zemach integral. The separation of charge and magnetic form factors leads to an *anticorrelation* between G_{ep} and G_{mp} since the cross-sections depend on $G_{\text{ep}}^2 + \dots + G_{\text{mp}}^2$. As the Zemach moment depends on

$G_{\text{ep}} \cdot G_{\text{mp}}$, where part of this anticorrelation compensates, the Zemach moment interestingly can be determined more accurately than quantities depending on G_{ep} or G_{mp} alone such as, e.g., the *rms*-radii.

The systematic uncertainties of the data are also affecting the uncertainty of the Zemach moment. We have determined this uncertainty again in the most conservative way, by changing the individual data sets by their quoted systematic uncertainty, re-fitting the form factors and adding quadratically the resulting changes of the Zemach moments.

We have found that the Zemach moment is quite sensitive to the exact shape of the densities (the q -dependence of the G s). The values used previously in the literature, all calculated using too simple-minded model-densities (model- G s) thus should no longer be employed.

The Zemach moment for the proton is 1.086 ± 0.012 fm [31]. The anticorrelation mentioned above and the fact that the Zemach moment depends on data at large q where the finite size effect in $G(q)$ is larger lead to the smaller error as compared to the *rms*-radii.

J. Friar has used our value of the Zemach moment to calculate the atomic HFS [31] based on the available CODATA evaluation [23] and the QED and recoil corrections listed in [2]. In calculating the HFS, a complication arises from the contribution of two-photon exchange (the same effect discussed below for electron scattering). This contribution is difficult to evaluate as it depends on the excitation of the proton to all conceivable intermediary (continuum) states. Faustov and Martynenko [32] has calculated this contribution using the knowledge on the spin structure functions then available. This correction brings calculated and experimental value of the HFS closer to each other, but a difference of 1.8 ± 0.8 ppm remains [33]. This difference at present is not understood.

The polarization correction calculated by Faustov et al. depends strongly on the nucleon spin structure functions at low q and large Bjorken- x (low electron energy loss). Nazaryan et al. [34] have recently done a new analysis by including the recent data on the spin structure functions from CLAS. Their result is similar to the Faustov result, but has a smaller error bar. This therefore does not resolve the HFS discrepancy. The usage of a subtracted dispersion relation does, however, introduce an ambiguity [35], the consequences of which should be clarified.

One might, of course, also suspect the QED calculations as a source for the HFS discrepancy. This, however, is very unlikely. Brodsky et al. [36] have shown that many terms for the HFS calculation occur similarly in positronium, where experiment and QED calculation perfectly agree.

In the hope to find alternative G s that could explain the HFS-puzzle, Brodsky et al. have looked at some 10 (combinations of) parameterizations of G_{ep} and G_{mp} . From the resulting values of $\langle r \rangle_{(2)}$ one finds that there is quite a strict linear correlation with the charge *rms*-radius, see Fig. 7. Our fit also agrees with this correlation line, while the point from the hydrogen atom with and without nuclear polarization correction disagrees [33]. While

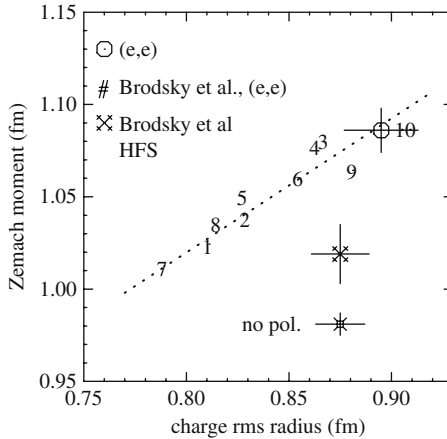


Fig. 7. Correlation between *rms*-radii and Zemach moments; the parameterizations used by Brodsky et al. are labeled by # and are fit by the dashed line

the correlation is an interesting one, one should not forget that all points numbered # in Fig. 7, except number 10, correspond to form factors that give unacceptably large χ^2 to the low- q (e,e) data, as pointed out in [33].

5 Effect of Two-Photon Exchange

Recent measurements of G_{ep} at very large q have revealed a pronounced discrepancy: measurements using polarization transfer such as $p(\mathbf{e}, e)\mathbf{p}$ give much smaller values than found via Rosenbluth separation. At large qs (several GeV/c) the contribution of G_{ep}^2 to the cross-section becomes very small (a few %) so any small correction to the cross-section can have a large effect on G_{ep} . It has been shown that even at the large electron energies used to get large q the small Coulomb corrections have a significant effect [37].

The main cause presently held responsible for the G_{ep} -discrepancy is the presence of two-photon exchange. While Coulomb distortion corresponds to the exchange of a second soft photon, the exchange of a second *hard* photon is also possible. This process has been calculated by two groups [38, 39] and they find that two-photon exchange can explain about half of the discrepancy. Both calculations are incomplete, though, as one includes as intermediary state only the proton in its ground state, while the other includes only the deep-inelastic continuum.

In the present context the question is: does this exchange of a second hard photon affect the *rms*-radius and Zemach moment discussed above? We have investigated this problem [40] using the two-photon corrections as calculated by P. Blunden [39]. In Fig. 2 we have already shown the effect of the exchange of a second hard photon — the difference between solid and dashed lines.

We have found that the effect on the moments is rather small. When including the correction, the charge *rms*-radius increases by 0.0015 fm, and the Zemach moment increases by 0.0052 fm. These changes are small, and go in the wrong direction to explain the HFS discrepancy.

6 Third Zemach Moment of Proton

At PSI, a group is in the process of measuring the Lamb shift in muonic hydrogen. Such a measurement could potentially improve the precision on the charge *rms*-radius by an order of magnitude relative to what can be achieved using electron scattering.

Such a muonic hydrogen experiment of course also requires a high-precision calculation based on QED. In order to calculate the terms of order $(Z\alpha)^5$ one requires another moment that can be determined via (e,e), the third Zemach moment given by

$$\langle r^3 \rangle_2 = \frac{48}{\pi} \int_0^\infty \frac{dq}{q^4} (G_e^2(q^2) - 1 + q^2 \langle r^2 \rangle_e / 3).$$

Very different values are found in the literature, as the subtraction of the dominant term $(-1 + q^2 \langle r^2 \rangle / 3)$ makes the integrand very sensitive to small changes in the q -dependence of G_{ep} .

We have extracted the third Zemach moment from the fit to the *world* proton data described above. We find $\langle r^3 \rangle_2 = 2.71(13) \text{ fm}^3$, where the error bar includes both random and systematic errors of the data. The two-photon corrections again have a very minor effect, they would increase the moment by 0.02 fm^3 .

7 Deuteron Radius

For a number of applications in atomic physics, the charge radius of the deuteron is of interest. We discuss below the determination of this radius from the *world* set of e-d scattering data.

The deuteron on the one hand presents an additional complication due to its spin $I=1$ nature. It has *three* form factors, with multipolarity $C0$ (charge monopole), $M1$ (magnetic dipole) and $C2$ (charge quadrupole). These in turn determine the two structure functions $A(q)$ and $B(q)$:

$$\sigma(E, \theta)^{\text{PWIA}} = \sigma_{\text{Mott}}(E, \theta) [A(q) + B(q) \text{tg}^2(\theta/2)],$$

where σ_{Mott} includes the recoil factor, with

$$A(q) = F_{C0}^2(q) + (M_d^2 Q)^2 \frac{8}{9} \tau^2 F_{C2}^2(q) + \left(\frac{M_d}{M_p} \mu \right)^2 \frac{2}{3} \tau (1 + \tau) F_{M1}^2(q),$$

$$B(q) = \left(\frac{M_d}{M_p} \mu \right)^2 \frac{4}{3} \tau (1 + \tau) F_{M1}^2(q) \quad \text{with} \quad \tau = q^2 / (4M_d^2).$$

In the above equations, M are the masses, μ the deuteron magnetic moment in units of magnetons, Q the quadrupole moment and q is the four momentum transfer (>0). While the structure functions $A(q)$ and $B(q)$ can be separated using the standard Rosenbluth approach, the charge monopole and charge-quadrupole form factors can only be separated when including the tensor polarization data in the analysis, in particular T_{20} :

$$T_{20} \quad \sqrt{2} \left(A + B \text{tg}^2 \frac{\theta}{2} \right) = - \left(\frac{8}{3} \tau F_{C0} F_{C2} Q M_d^2 + \frac{8}{9} \tau^2 F_{C2}^2 Q^2 M_d^4 \right. \\ \left. + \tau \left(\frac{1}{3} + \frac{2}{3} (1 + \tau) \text{tg}^2 \frac{\theta}{2} \right) F_{M1}^2 \left(\frac{M_d}{M_p} \mu \right)^2 \right).$$

The data on T_{20} are not very extensive nor very precise, leading potentially to a larger uncertainty of the radius.

On the other hand, the deuteron radius is strongly influenced by the large-radius tail of the proton wave function, as a consequence of the small deuteron binding energy. The *shape* of this tail outside the range of the N–N interaction is well known, a Hankel function, and can be used as a constraint during the analysis of the data. This additional knowledge largely compensates the potential increase of the uncertainty cited above.

We have analyzed the world data for e–d scattering [41, 42, 43, 44, 45, 46, 47, 48, 49, 50, 51, 52, 53, 54, 55, 56, 14, 57, 58, 59, 60, 61, 62, 19, 63, 64] in the analogous way as described above for the proton [65] (see Fig. 8). The major difference is the use of the SOG parameterization, which allows one to write the density in r -space as needed when employing the shape of $\rho(r)$ as a constraint.

The analysis of the *world* data on electron–deuteron scattering yields 2.130 ± 0.010 fm for the deuteron charge *rms*-radius. This value agrees with the one derived from optical isotope shifts [66] and from the low-energy properties of the deuteron as measured by N–N scattering (scattering length and asymptotic normalizations) [67]. The long-standing discrepancy with the latter value had been removed when realizing that for scattering from $Z=1$ nuclei also Coulomb corrections are important [65].

As a consequence of the disagreement in the past of deuteron *rms*-radii coming from different sources as mentioned above, various correction terms have been studied. Dispersive effects — corresponding to a two-step scattering process with excitation of the deuteron in the intermediate state — can give a small correction to the cross-sections. This correction has been studied by Herrmann and Rosenfelder [68] who take into account the Coulomb excitation only and use an S-wave separable potential (Yamaguchi) to calculate the deuteron wave function. When analyzing the data of Simon et al. [19], they find a change of the *rms*-radius of -0.003 fm when correcting the data for the

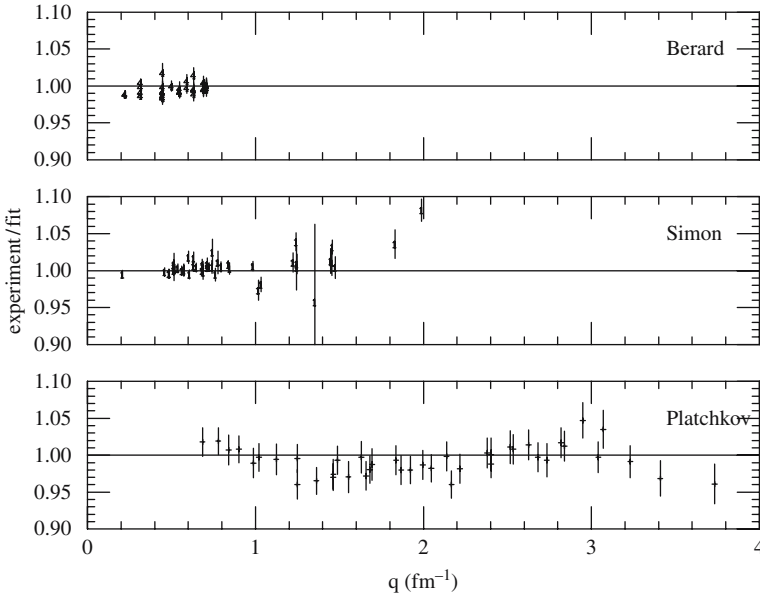


Fig. 8. Ratio of data and fit for the most precise sets of data at low q [26]

dispersive effects. This calculation gives a significantly smaller effect than a previous estimate [69], but is much more reliable. When using their parameterized dispersion corrections with the full set of data, we find, in agreement with their result, a change of -0.0024 fm.

Another correction to the electron scattering data results from the contribution of non-nucleonic degrees of freedom. The effects of meson exchange currents (MEC) have been studied in great detail by Buchmann et al. [70]. When correcting the experimental data for the mesonic effects, these authors find a change of the *rms*-radius of -0.005 fm, with a fluctuation of 0.001 fm depending on the approach used. The estimate for the contribution of 6-quark components is much smaller, and presumably also much more uncertain.

These corrections are quite small and have considerable uncertainties. We prefer at the present time to not apply these as corrections to the *rms*-radii extracted from the DWBA analyses.

The Zemach moment of the deuteron is another quantity that can be derived from the fits: it amounts to 2.593 ± 0.016 fm, where the error bar includes both random and systematic errors of the data.

8 Radii of $A = 3$ Systems

The *world* data on electron scattering from ${}^3\text{H}$ and ${}^3\text{He}$ [71, 72, 73, 74, 75, 76, 77, 78, 79, 80] have been analyzed in [81]. The resulting *rms*-radii are

Table 1. The *rms* nuclear radii of $A = 3$ systems

nucleus	type	<i>rms</i> -radius
^3H	charge	1.755 ± 0.087 fm
^3H	magnetic	1.840 ± 0.182 fm
^3He	charge	1.959 ± 0.034 fm
^3He	magnetic	1.965 ± 0.154 fm

less precise than for $A=1,2,4$, as a consequence of the less extensive and less precise database at low q . The ^3H and ^3He nuclei, present particular challenges for the experimentalist. For both nuclei, targets of adequate and well-known thickness are difficult to produce and use, particularly of course for the radioactive ^3H .

Table 1 gives the radii together with their errors, covering both random and systematic uncertainties of the data.

For ^3He the isotope shift to ^4He has been determined in [82]. In combination with the ^4He radius discussed below, this yields a ^3He -radius which agrees with the one given in Table 1, but is more precise.

9 Radius of ^4He

The nucleus ^4He may be of interest to ongoing and future studies of high-precision atomic spectroscopy, as witnessed by several contributions to this volume. We therefore discuss ^4He as well.

The ^4He nucleus presents an especially simple case: due to its spin $I = 0$ nature there is only one form factor, so no error-magnifying L/T-separation is necessary. The electron scattering database is also very good [83, 78, 84, 75, 80], in particular there is one very accurate data set [75] in the q -region of interest for the radius determination (see Fig. 9).

For ^4He there is another aspect that helps the determination of a very precise radius: at large radii not only the *shape* of the proton radial wave function is known (a Whittaker function depending on the proton separation energy) but also the *absolute value* of the large- r wave function. The study of the *world* proton- ^4He elastic scattering data in terms of forward dispersion relations (FDR) [85] has provided an accurate value of the residuum of the proton-exchange pole, which translates into the asymptotic normalization of the large- r proton wave function. This quantity can be included in the analysis of the (e,e) data. Knowledge of the large-radius density greatly benefits the accuracy of the radius one can deduce.

We have recently updated the analysis described originally in [86] by including the data from [75] not yet available at the time. The ^4He charge

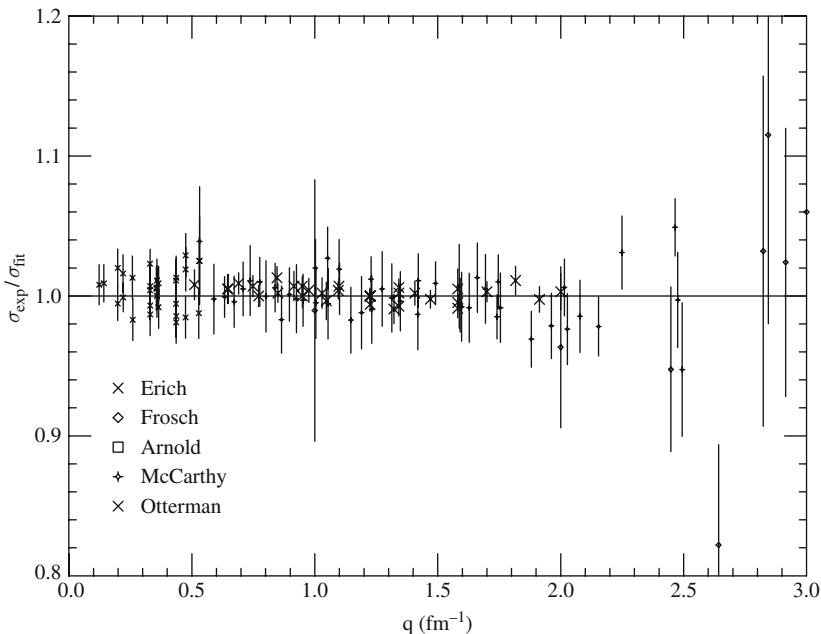


Fig. 9. Ratio of experimental cross-sections to fit for ^4He

rms-radius resulting from this analysis is 1.680 ± 0.005 fm, where the error bar covers both random and systematic errors of the data. This radius of ^4He is actually the most precise *rms*-radius determined from electron scattering data for any nucleus.

The above radius agrees with the (apparently) more precise value determined from the $2p-2s$ transition in muonic Helium [87] of $1.673 \pm .003$ fm. There are, however, serious doubts about this value. Subsequent experiments on muonic helium [88, 89] never could detect the $2s$ -state with sufficiently long lifetime to allow for a $2p-2s$ transition measurement.

10 Heavier Nuclei

The accuracy of *rms*-radii that can be obtained from electron scattering experiments is typically in the $\pm 1\%$ region. For exceptional cases such as, e.g., ^{12}C [86], which has received much attention as it is often used as an absolute cross-section reference, a higher accuracy can be achieved. The $\pm 1\%$ accuracy may suffice for the interpretation of most atomic-physics experiments, particularly for the ones involving many-electron systems where the uncertainties of the electronic structure come in. For selected systems, such as one-electron systems of large- Z nuclei, however, more accurate *rms*-radii might be desirable. We briefly mention below how one might get such radii from published data.

Very accurate information on nuclear sizes is available from muonic X-ray experiments. For $A > 20$ these experiments typically provide more accurate radii than electron scattering. The radii measured by μ -X-ray experiments are, however, not *rms*-radii but moments of the type $\langle r^k e^{-\alpha r} \rangle$, where k depends on the transition studied (2p-1s, ..) and α is derived from the calculated muon wave functions and chosen such as to make the moment $\langle r^k e^{-\alpha r} \rangle$ essentially model-independent, i.e., within reasonable bounds not depend on the particular shape of the nuclear charge density $\rho(r)$ (this would not be the case for the *rms*-radius). For some of the heavier nuclei, more than one of these so-called Barrett moments have been determined.

For nuclei where both (e,e) data and precise Barrett moments are available, the two can be combined to determine precise *rms*-radii. The usually very detailed information on the *shape* of the nuclear charge density from (e,e) allows one to go from the precisely known Barrett moment to $\langle r^2 \rangle$ with little ambiguity.

The feasibility of this approach obviously depends on the quality of the available (e,e) and μ -X-ray data for the specific nucleus of interest. It may be useful, however, to remember that the approach outlined above at least in principle provides a viable means to get precise *rms*-radii for the heavier nuclei as well.

11 Summary

From the *world* data on electron-nucleus scattering one can extract rather precise values of the *rms*-charge radii and Zemach moments. One finds consistently good fits to the data, somewhat surprisingly given the fact that the database has been accumulated over some 30 years.

For the determination of precise radii it is important to account for the Coulomb distortion of the e-waves. This in the past systematically has been neglected for $Z = 1$, assuming that the distortion effect is small. This, however, is not the case. Surprisingly, the distortion effects not only are important for the low-energy (low- q) data of interest to the determination of radii. Coulomb distortion also is non-negligible at large q , where the contribution to the cross-section of G_{ep}^2 becomes small as compared to the one of G_{mp}^2 in which case small (Coulomb) corrections to the G_{mp} -dependent term have significant effects upon the value of G_{ep} extracted in a Rosenbluth separation [37].

In order to extract reliable values, it is important to use adequate parameterizations of the form factors; the standard low- q expansion of the form factors in terms of $\langle r^{2n} q^{2n} \rangle$ moments is seriously affected by problems with the higher moments, particularly for the proton which has a density with unusually large higher moments.

It is also important to analyze the cross-sections, and not the form factors determined from individual experiments. The separation of charge- and

magnetic form factors can be done with much superior quality when starting from the cross-sections and fitting the full data set simultaneously with parameterized charge- and magnetic form factors.

Potential corrections to the standard interpretation of (e,e) involve the effect of two-photon exchange which, at very large momentum transfer, has been shown to have an appreciable effect for the proton. For the low qs of interest to determinations of *rms*-radii their effect is found to be small.

The radii for the light nuclei given above are not likely to be superseded in any foreseeable future by more accurate values from electron scattering. For more precise radii, one presumably will have to turn to muonic X-ray experiments, particularly for the proton which is of special interest to atomic physics.

References

1. M. Niering et al.: Phys. Rev. Lett. **84**, 5496 (2000). [57](#)
2. M.I. Eides, H. Grotch, and V.A. Shelyuto: Phys. Rep. **342**, 63 (2001). [57](#) [67](#)
3. F.A. Bumiller et al.: Phys. Rev. **124**, 1623 (1961). [57](#)
4. T. Janssens et al.: Phys. Rev. **142**:922, 1966. [57](#)
5. F. Borkowski et al.: Nucl. Phys. **A222**, 269 (1974). [57](#) [59](#)
6. F. Borkowski et al.: Nucl. Phys. **B93**, 461 (1975). [57](#)
7. G.G. Simon et.al. Nucl. Phys. **A333**, 381 (1980). [57](#) [59](#) [64](#)
8. W. Albrecht et al.: Phys. Rev. Lett. **17**, 1192 (1966). [57](#)
9. W. Bartel et al.: Phys. Rev. Lett. **17**, 608 (1966). [57](#)
10. D. Frerejacque, D. Benaksas, and D. Drickey: Phys. Rev. **141**, 1308 (1966). [57](#)
11. W. Albrecht et al.: Phys. Rev. Lett. **18**, 1014 (1967). [57](#)
12. W. Bartel et al.: Phys.Lett. **25B**, 236 (1967). [57](#)
13. W. Bartel et al.: Nucl. Phys. **B58**, 429 (1973). [57](#)
14. D. Ganichot, B. Grossetête, and D.B. Isabelle: Nucl. Phys. **A178**, 545 (1972). [57](#) [70](#)
15. P.N. Kirk et al.: Phys. Rev. **D8**, 63 (1973). [57](#)
16. J.J. Murphy II, Y.M. Shin, and D.M. Skopik: Phys. Rev. **C9**, 2125 (1974). [57](#)
17. Ch. Berger et al.: Phys.Lett. **35B**, 87 (1971). [57](#)
18. W. Bartel et al.: Phys. Rev. Let. **33**, 245 (1970). [57](#)
19. G.G. Simon, Ch. Schmitt, and V.H. Walther: Nucl. Phys. **A364**, 285 (1981). [57](#) [70](#)
20. P. Mergell, U.-G. Meissner, and D. Drechsel: Nucl. Phys. **A596**, 367 (1996). [59](#)
21. D. Lehmann, R. Taylor, and R. Wilson: Phys. Rev. **126**, 1183 (1962). [59](#)
22. L. Hand, D.I. Miller, and R. Wilson: Rev. Mod. Phys. **35**, 335 (1963). [59](#)
23. P. Mohr and B. Taylor: Rev. Mod. Phys. **72**, 351 (2000). [59](#) [67](#)
24. T. Udem et al.: Phys. Rev. Lett. **79**, 2646 (1997). [59](#) [64](#)
25. W.A. McKinley and H. Feshbach: Phys. Rev. **74**, 1759 (1948). [59](#)
26. I. Sick and D. Trautmann: Nucl. Phys. **A637**, 559 (1998). [60](#) [71](#)
27. P. Hänggi, F. Roesel, and D. Trautmann: J. Comp. Phys. **37**, 242 (1980). [61](#)
28. I. Sick: Phys. Lett. **B576**, 62 (2003). [62](#)
29. G. Hoehler et al.: Nucl. Phys. **B114**, 505 (1976). [62](#)
30. C. Zemach: Phys. Rev. **104**, 1771 (1956). [66](#)
31. J.L. Friar and I. Sick: Phys. Lett. **B579**, 285 (2004). [66](#) [67](#)
32. R.N. Faustov and A.P. Martynenko: Eur. Phys. **C24**, 281 (2002). [67](#)

33. J.L. Friar and I. Sick: Phys. Rev. Lett. **95**, 49101 (2005). [67](#), [68](#)
34. V. Nazaryan, C.E. Carlson, and K. Griffioen: Phys. Rev. Lett. **96**, 163001 (2006). [67](#)
35. C. Carlson: priv. com. [67](#)
36. S.J. Brodsky et al.: Phys. Rev. Lett., **94**, 22001 (2005). [67](#)
37. J. Arrington and I. Sick: Phys. Rev. **C70**, 028203 (2004). [68](#), [74](#)
38. A. Afanasev et al.: Phys. Rev. **D72**, 13008 (2005). [68](#)
39. P.G. Blunden, W. Melnitchouk, and J.A. Tjon: Phys. Rev. Lett. **91**, 142304 (2003). [68](#)
40. P.G. Blunden and I. Sick: Phys. Rev. **C72**, 57601 (2005). [68](#)
41. D. Abbott et al.: Phys. Rev. Lett. **82**, 1379 (1999). [70](#)
42. L.C. Alexa et al.: Phys. Rev. Lett. **82**, 1374 (1999). [70](#)
43. Yu.K. Akimov et al.: Sov. J. Nucl. Phys. **29**, 335 (1979). [70](#)
44. R.G. Arnold et al.: Phys. Rev. Lett. **35**, 776 (1975). [70](#)
45. R.G. Arnold et al.: Phys. Rev. Lett. **58**, 1723 (1987). [70](#)
46. S. Auffret et al.: Phys. Rev. Lett. **54**, 649 (1985). [70](#)
47. D. Benaksas, D. Drickey, and D. Frerejacque: Phys. Rev. **148**, 1327 (1966). [70](#)
48. R.W. Berard et al.: Phys. Lett. **B47**, 355 (1973). [70](#)
49. P.E. Bosted et al.: Phys. Rev. **C42**, 38 (1990). [70](#)
50. F.A. Bumiller et al.: Phys. Rev. Lett. **25**, 1774 (1970). [70](#)
51. C.D. Buchanan and M.R. Yearian: Phys. Rev. Lett. **15**, 303 (1965). [70](#)
52. R. Cramer et al.: Z. Phys. **C29**, 513 (1985). [70](#)
53. D. Drickey and L.N. Hand: Phys. Rev. Lett. **9**, 521 (1962). [70](#)
54. J.E. Elias et al.: Phys. Rev. **177**, 2075 (1969). [70](#)
55. J.I. Friedman, H.W. Kendall, and P.A.M. Gram: Phys. Rev. **120**, 992 (1960). [70](#)
56. S. Galster et al.: Nucl. Phys. **B32**, 221 (1971). [70](#)
57. J. Goldemberg and C. Schaerf: Phys. Rev. Lett. **12**, 298 (1964). [70](#)
58. A. Honegger: Thesis, Univ. of Basel, (1999). [70](#)
59. B. Grossetête, D. Drickey, and P. Lehmann: Phys. Rev. **141**, 1425 (1966). [70](#)
60. F. Martin et al.: Phys. Rev. Lett. **38**, 1320 (1977). [70](#)
61. S. Platchkov et al.: Nucl. Phys. **A510**, 740 (1990). [70](#)
62. R.E. Rand et al.: Phys. Rev. Lett. **18**, 469 (1967). [70](#)
63. P. Stein et al.: Phys. Rev. Lett. **16**, 592 (1966). [70](#)
64. B.B. Voitsekhovskii et al.: Pis'ma Zh. Eksp. Teor. Fiz. **43**, 567 (1986). [70](#)
65. I. Sick and D. Trautmann: Phys. Lett. **B375**, 16 (1996). [70](#)
66. K. Pachucki et al.: J. Phys. **B29**, 177 (1996). [70](#)
67. S. Klarsfeld et al.: Nucl. Phys. **A456**, 373 (1986). [70](#)
68. T. Herrmann and R. Rosenfelder: Eur. Phys. J. **A2**, 29 (1998). [70](#)
69. A. Bottino and G. Ciochetti: Nucl. Phys. **A178**, 593 (1972). [71](#)
70. A. Buchmann, H. Henning, and P.U. Sauer: Few Body Syst. **21**, 149 (1996). [71](#)
71. H. Collard et al.: Phys. Rev. **C15**, 57 (1965). [71](#)
72. D. Beck et al.: Phys. Rev. Lett. **59**, 1537 (1987). [71](#)
73. F.P. Juster et al.: Phys. Rev. Lett. **55**, 2261 (1985). [71](#)
74. A. Amroun et al.: Nucl. Phys. **A579**, 596 (1994). [71](#)
75. C.R. Ottermann et al.: Nucl. Phys. **A435**, 688 (1985). [71](#), [72](#)
76. Z.M. Szalata et al.: Phys. Rev. **C15**, 1200 (1977). [71](#)
77. J.S. McCarthy et al.: Phys. Rev. Lett. **25**, 884 (1970). [71](#)
78. J.S. McCarthy, I. Sick, and R.R. Whitney: Phys. Rev. **C15**, 1396 (1977). [71](#), [72](#)
79. J.M. Cavedon et al.: Phys. Rev. Lett. **49**, 978 (1982). [71](#)

80. R.G. Arnold et al.: Phys. Rev. Lett. **40**, 1429 (1978). [71](#), [72](#)
81. I. Sick: Prog. Nucl. Part. Phys. **47**, 245 (2001). [71](#)
82. D. Shiner, R. Dixson, and V. Vedantham: Phys. Rev. Lett. **74**, 3553 (1995). [72](#)
83. R. Frosch et al.: Phys. Rev. **160**, 874 (1967). [72](#)
84. U. Erich et al.: Z. Phys. **209**, 208 (1968). [72](#)
85. G.R. Plattner and R.D. Viollier: Nucl. Phys. A**365**, 8 (1981). [72](#)
86. I. Sick: Phys. Lett. B**116**, 212 (1982). [72](#), [73](#)
87. G. Carboni et al.: Nucl. Phys. A**278**, 381 (1977). [73](#)
88. P. Hauser et al.: Phys. Rev. A**46**, 2363 (1992). [73](#)
89. M. Eckhause et al.: Phys. Rev. A**33**, 1743 (1986). [73](#)

Nucleon Form Factor Measurements in Mainz: Past and Future

J. C. Bernauer for the A1 collaboration

Institut für Kernphysik, Johannes Gutenberg-Universität Mainz, Germany
bernauer@kph.uni-mainz.de

Abstract. The form factors of proton and neutron provide a natural and direct insight into their internal structure. They were a main research goal in the nuclear physics program of the Universität Mainz, which led to some of the most precise measurements to date. This article gives an overview, starting from the very first experiments at the now obsolete linear accelerator and ending at the exhaustive experiments currently underway at the Mainz Microtron (MAMI) facilities.

1 Introduction

Form factors encode unique information about the internal structure of the scatterer. Provided they are sufficiently precisely known over a sufficiently large range of momentum transfer, the Fourier transformation gives the spatial distribution of the “charge” associated with the interaction between scatterer and projectile, e.g., mass, electrical charge or magnetization. This leads to insights into aspects of the internal structure like the presence of constituents and their interaction. Therefore, the measurement of the form factors constitute a significant test of any model of the scatterer.

In an elastic electron nucleon scattering experiment, the electric and magnetic form factors, G_E and G_M , are determined, as can be seen from the cross-section for the unpolarized case, given in the one photon exchange picture by the well-known Rosenbluth formula [1],

$$\frac{d\sigma}{d\Omega} = \left(\frac{d\sigma}{d\Omega} \right)_{\text{Mott}} \cdot \frac{1}{\epsilon(1+\tau)} (\tau G_M^2(Q^2) + \epsilon G_E^2(Q^2)) , \quad (1)$$

where Q^2 is the negative transferred four-momentum squared and $\tau = Q^2/4m_N^2$, where m_N is the nucleon mass. In this picture, the exchanged virtual photon has a longitudinal polarization given by

$$\epsilon = \left(1 + 2(1 + \tau) \tan^2 \frac{\theta}{2} \right)^{-1} . \quad (2)$$

The measurement of this cross-section for different angles and incident beam energies allows the disentanglement of the form factors; in the case of measurements at constant momentum transfer Q and different ϵ , this can be done without any model dependency by means of the Rosenbluth separation. In general, either a projection to constant Q^2 using a local model or a fit using a global model has to be employed to determine the form factors.

To get the distribution of the charge in r -space, the form factors have to be Fourier transformed. While an exact result is only achievable with complete knowledge of the Q^2 -dependence of the form factors, some special quantities are accessible more easily. The root mean square radius of the nucleon is directly related to the slope of the form factors at $Q^2 = 0$

$$\langle r_{E,M}^2 \rangle = -6 \left. \frac{d(G_{E,M}/G_{E,M}(0))}{dQ^2} \right|_{Q^2=0}. \quad (3)$$

While the form factors are interesting quantities in their own right, the radii are a link between nuclear physics and atomic physics. For the Lamb shift, the first order correction due to the finite size of the proton depends quadratically on the radius

$$\Delta E(nl) = \frac{2}{3} \frac{(Z\alpha)^4}{n^3} m^3 \langle r_E^2 \rangle \delta_{l0}. \quad (4)$$

Interpreting a comparison between the theoretical Lamb shift and the experimental value not as a test for bound state QED but as a determination of the proton charge radius, Karshenboim [2] found $\langle r_E^2 \rangle^{\frac{1}{2}} = 0.89 \pm 0.02$ fm. This value agrees with the Mainz result of Simon et al. presented below. On the other hand, the Stanford value of [3] disagrees with both the Mainz and the spectroscopy result. To facilitate the Lamb shift as a test of theory, the uncertainty in the proton radius has to be reduced further.

A common, but (as will be shown below) not very accurate, phenomenological parameterization of the form factors is the so-called dipole form factor, introduced by Hofstadter [4]

$$G_{EP} = G_{MP}/\mu_P = G_{MN}/\mu_N = G_{\text{dipole}} = \left(1 + \frac{Q^2}{0.71 \left(\frac{\text{GeV}}{c} \right)^2} \right)^{-2}. \quad (5)$$

Here, P/N refers to the proton/neutron and $\mu_{P/N}$ is the proton/neutron magnetic moment in units of the nuclear magneton. This parameterization is compatible with the Stanford value for the radius.

The form factors were in the focus of many institutes, so the number of scattering experiments to measure the form factors is quite extensive. For any detailed review, one has to confine oneself to a certain subset of these experiments. For the low Q^2 -region, which is of special interest not just in the context of the radii as will be seen below, no experiment rivals the accuracy of the Mainz proton data. Thus, the following review is limited to the experiments conducted in Mainz.

2 Mainz Experiments

The history of the experiments in Mainz can be divided into three parts:

- The LINAC era
- The MAMI B era
- The MAMI C era

2.1 The Mainz LINAC era

In 1965 the first accelerator in Mainz was commissioned. It was a normal conducting commercial linear accelerator (CSF, France) with a maximum energy of 400 MeV at the end of its operating life in 1983. In contrast to other linear accelerators of its time, the Mainz setup used a chicane and a rf-section positioned after the linac to reduce the energy spread considerably. The principle of operation is shown in Fig. 1. In essence, the same effect is intrinsically used in modern accelerators like MAMI or ELSA as longitudinal beam stabilization.

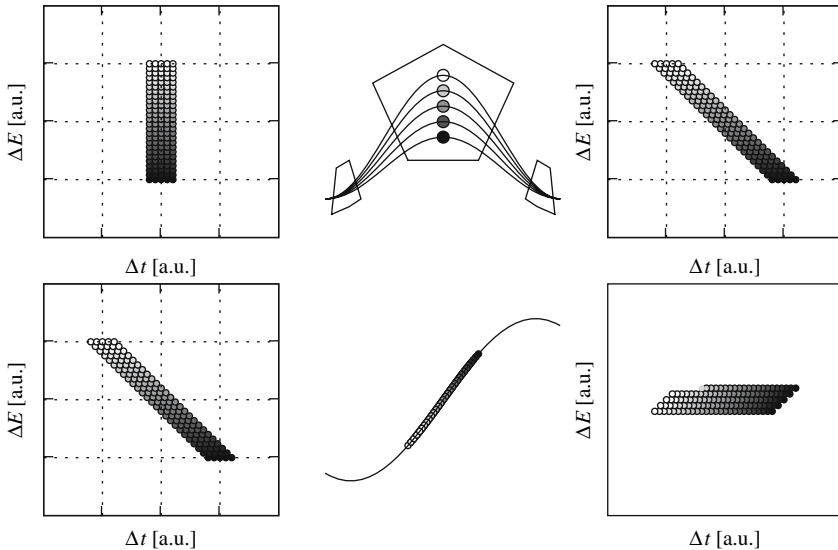


Fig. 1. The principal function of the energy compressing system of the Mainz linac: The ensemble of electrons in a bunch has a small spread in time and a big spread in energy, as shown in the top left phase space diagram (color coded according to the energy after the accelerator line). Electrons with higher energy are less deflected in the magnetic fields of a chicane. Thus, the path length varies according to initial energy (middle of top row), and the phase space after the chicane exhibits a correlation between relative time and relative energy (top right, bottom left). The phase of the rf-wave in the following small accelerator section is chosen such that the earlier electrons (those with higher energy) are decelerated, the later ones (with lower energy) accelerated. This results in a compression of the energy spread, as depicted in the phase diagram on the bottom right

In this era, two measurements of the electron–proton cross-section were performed. Both used the experimental setup available in the experimental hall 2 of the Institut für Kernphysik. The main detector was a 180° spectrometer which could be rotated around the fixed target. An additional spectrometer was at a fixed angle of about 30° . It was used mainly as a luminosity monitor.

The First Experiment: Borkowski et al.

The first measurement was performed by Borkowski et al. [5]. A liquid hydrogen target was used to measure the cross-section for several incident beam energies between 150 and 275 MeV and scattering angles between 28° and 75° . The measured data points cover the Q^2 -region from 0.005 to $0.083 \text{ (GeV}/c)^2$. Figure 2 depicts the measured cross-sections normalized to the dipole cross-section. With increasing Q^2 , the measured values fall below this model.

For a fit, the form factors were parameterized as a sum of monopoles,

$$G(q^2) = \sum_{i=1}^4 \frac{a_i}{(1 + q^2/m_i^2)}; \quad \sum a_i = 1, \quad (6)$$

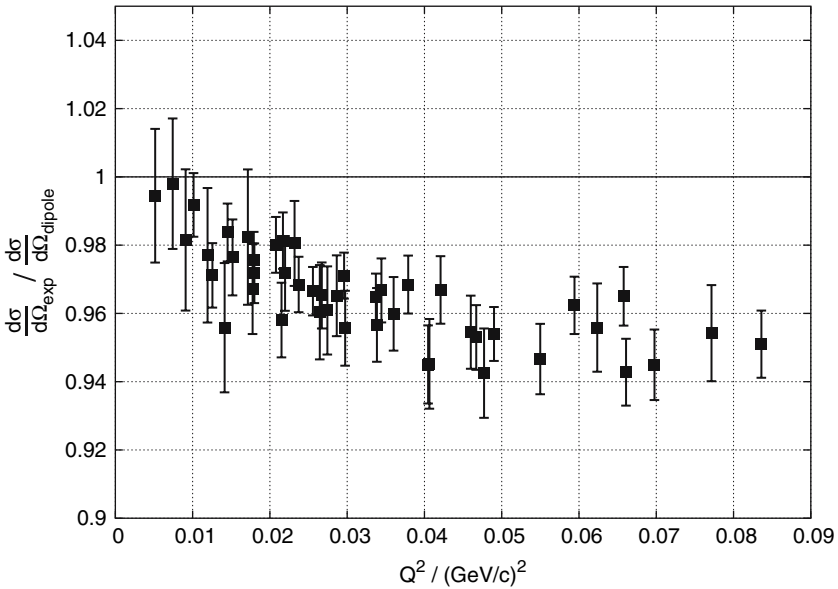


Fig. 2. The experimental cross-section of Borkowski et al. [5], normalized to the dipole prediction

with two of the parameters m_i fixed to the masses of the ρ and ρ' mesons. From the slope of the parameterization, they found a charge rms radius $\langle r_E^2 \rangle^{\frac{1}{2}} = 0.92 \pm 0.03$ fm and a magnetic rms radius $\langle r_M^2 \rangle^{\frac{1}{2}} = 0.83 \pm 0.07$ fm.

A Better Target: Simon et al.

In 1979, the experiment done by Simon et al. [6] was a more sophisticated version of the Borkowski experiment. A lot of care was taken to eliminate or at least reduce the systematic errors resulting from uncertainties in the luminosity, target thickness and beam position, etc. The main improvement was the new target, a high-pressure cell, filled with great care at the TH Darmstadt by the group of Prof. Frank with 10 bar of hydrogen gas. This reduced the uncertainty of the target thickness to 0.05%. The data, measured in the Q^2 -range from 0.005 to 0.054 $(\text{GeV}/c)^2$, were analyzed using the scaling relation

$$G_E = \frac{G_M}{\mu}, \quad (7)$$

which is believed to be (sufficiently) true at least for very small Q^2 and allows the pointwise disentanglement of the form factors for each measured cross-section. The extracted values for G_E are shown in Fig. 3 again normalized to the dipole. As before, the data deviate from the dipole prediction as in the

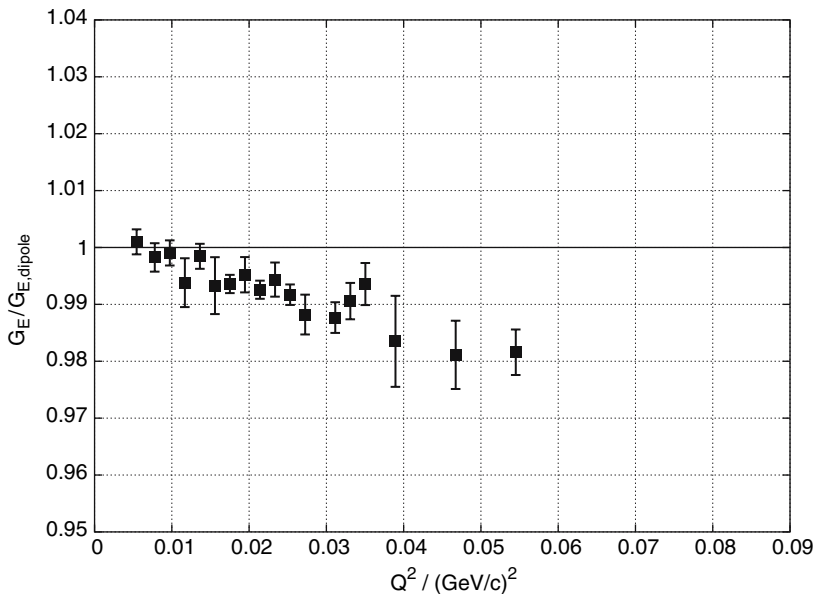


Fig. 3. The electric form factor G_{EP} , as extracted from the measurements of Simon et al. [6], normalized to the dipole prediction

Borkowski experiment (note that Fig. 3 shows the form factor while Fig. 2 shows the cross-section, which depends quadratically on the former).

Together with data from other laboratories (Dudelzak [7], Orsay and Murphy [8], Saskatoon), the data were fitted using

$$G(q^2) = a_0 \left(1 + q^2 \frac{a_1}{a_0} + q^4 \frac{a_2}{a_0} \right) \quad (8)$$

with adjustable parameters a_0, a_1, a_2 . The normalization parameter a_0 was allowed to be different for the data sets of the different laboratories. From the fit there resulted the rms radius $\langle r_E^2 \rangle^{\frac{1}{2}} = 0.862 \pm 0.012$ fm.

2.2 The MAMI B era

Because linear accelerators are a very ineffective design – most of the electric power is needed to generate the accelerating field – a new design was called for. The racetrack design, i.e., the repeated use of an accelerator segment by circulating the beam back many times, was the key for the design of the high-performance Mainz Microtron. The principle is realized in three cascaded RTMs (Racetrack Microtrons) with increasing output energy. While the two RTMs of MAMI A yield a fixed output energy of 180 MeV, the beam can be extracted from every other recirculation line of the third RTM (MAMI B), allowing to vary the beam energy in 15 MeV steps from 180 to 855 MeV. A complete energy shift can be realized in less than 6 h, allowing a very flexible design of experiments. Two electron sources are installed: A thermic electron gun generates an unpolarized electron beam with currents up to $100 \mu\text{A}$, the second source uses a crystal and a laser to produce a highly polarized beam ($>80\%$ polarization) up to $30 \mu\text{A}$. The accelerator provides an excellent cw-beam with an energy spread of 30 keV (FWHM), a horizontal emittance of 13π mm mrad (1σ) and a vertical emittance of 1.7π mm mrad (1σ) (measured at 855 MeV, $100 \mu\text{A}$). In 1991, the productive phase of the Mainz Microtron MAMI began. The form factor experiments were done in the hall of the three-spectrometer facility [9]. With the advancement of the accelerator and experimental capabilities, the objective shifted.

A Polarization Experiment: Pospischil et al.

While the main focus was on the neutron, there was one form factor experiment on the proton. It was meant as a test for the new proton polarimeter installed in the focal plane of one of the three spectrometers. Via polarization transfer in the reaction $p(\vec{e}, e' \vec{p}')$, one measures the ratio $\frac{G_E}{G_M/\mu}$ [10, 11]. As seen in Fig. 4, the Q^2 -region where the data were taken by Pospischil et al. [12] is much higher than in the previous Mainz experiments with the linac.

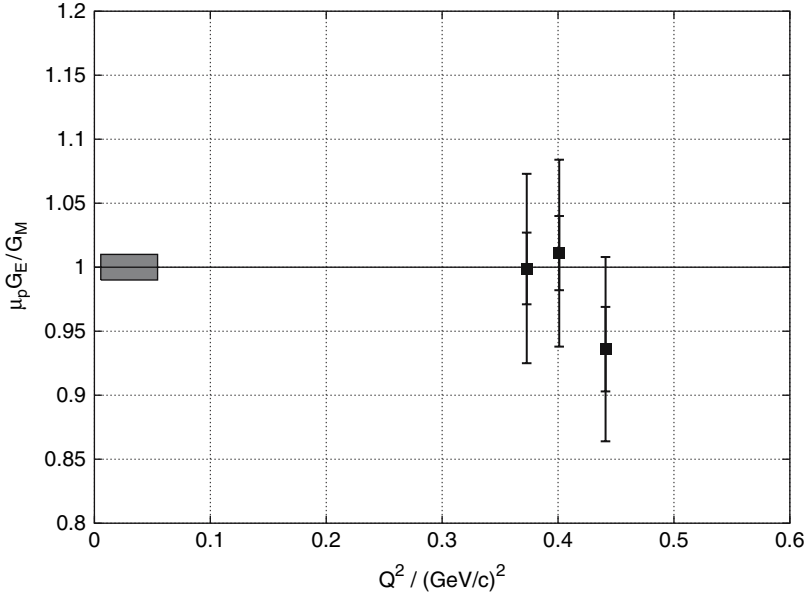


Fig. 4. The ratio $\frac{G_E}{G_M/\mu}$ extracted from the Pospischil et al. [12] polarization-transfer experiment. The gray box represents the Q^2 -range in the Simon et al. experiment

G_{MN} Experiments: Anklin et al., Kubon et al.

The neutron form factors were in the main focus of the experimental work. While hydrogen is a readily available (free) proton target, there is no free neutron target, so one has to resort to simple systems of proton and neutron, like the deuteron or ^3He .

Anklin [13] and Kubon [14] measured the neutron magnetic form factor via the branching ratio of the deuteron breakup channels

$$R = \frac{d\sigma [D(e, e'n)p]}{d\Omega} / \frac{d\sigma [D(e, e'p)n]}{d\Omega} \tag{9}$$

in the Q^2 -region from 0.071 to 0.89 $(\text{GeV}/c)^2$. Since the cross-sections of both channels were measured simultaneously, the ratio is independent of the luminosity. The result is shown in Fig. 5, again normalized to the dipole. As for the proton form factor, the measured data fall below the dipole form factor for lower Q^2 , while, for higher values, the data lie above this canonical fit.

G_{EN} Experiments

The neutron has no net charge and the electric form factor is quite small. Therefore, it needs a lot of effort to measure it with high precision. In 1999, Rohe et al. [15] and Becker et al. [16, 17] used a polarized target to measure the

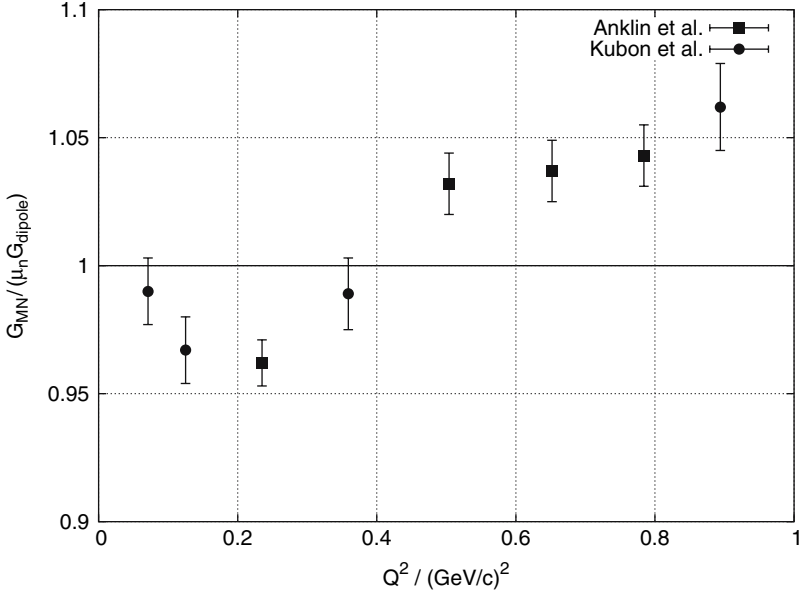


Fig. 5. The neutron magnetic form factor measured by Anklin et al. [13] and Kubon et al. [14], normalized to the dipole fit

electric form factor of the neutron in the reaction ${}^3\text{H}\vec{e}(\vec{e}, e'n)$ for Q^2 -values of 0.67 and 0.385 $(\text{GeV}/c)^2$. In 2003 Bermuth et al. [18] performed an updated experiment with the same kinematics as Rohe et al. to reduce the statistical error. The asymmetry in double polarization experiments is determined as

$$A(\theta, \phi) = \frac{1}{P_e P_t} \frac{N^+ - N^-}{N^+ + N^-} \quad (10)$$

where θ, ϕ are the polar and the azimuthal angles of the target-spin direction with respect to the three momentum transfer, P_e, P_t the polarization of beam and target and N^+ (N^-) the normalized ${}^3\text{H}\vec{e}(\vec{e}, e'n)$ events for positive (negative) electron helicity. With the target-spin orientation parallel and perpendicular to \mathbf{q} , two independent asymmetries $A_{\parallel} = A(0^\circ, 0^\circ)$ and $A_{\perp} = A(90^\circ, 0^\circ)$ can be measured. In PWIA, G_{EN} can be determined via

$$G_{\text{EN}}^{\text{PWIA}} \propto G_{\text{MN}} \frac{(P_e P_t V)_{\parallel} A_{\perp}}{(P_e P_t V)_{\perp} A_{\parallel}}, \quad (11)$$

with V accounting for a possible dilution due to contributions of vanishing asymmetry.

In 1999 Herberg et al. [19] and Ostrick et al. [20] measured G_{EN} at two Q^2 -values via the reaction $\text{D}(\vec{e}, e'\vec{n})p$, i.e., using the deuteron as a target and measuring the polarization of the outgoing neutron. In 2005, an experiment

done by Glazier et al. [21] added three additional data points using the same reaction. For a free neutron target, with the z -axis parallel to momentum transfer and the x -axis in the scattering plane, the ratio of the neutron polarization along these axes is related to the form factors as

$$\frac{P_x^N}{P_z^N} = \frac{-\sqrt{2\epsilon}}{\sqrt{\tau(1+\epsilon)}} \times \frac{G_{EN}}{G_{MN}}. \quad (12)$$

For a neutron bound in the deuteron, the model dependence of the extracted form factors, which occurs via the dependence of the neutron wave function on the nuclear potential, cancels in leading order.

The complete Mainz data set is shown in Fig. 6 together with the Galster parameterization, which is in agreement with the dataset.

2.3 The MAMI C era

With the almost completed MAMI C, the third stage of the MAMI accelerator, the maximum energy will be boosted to 1.5 GeV. In contrast to MAMI A and B, the third stage is a harmonic, double-sided microtron (HDSM), with two accelerator segments, one operating at the base frequency, the other at the first harmonic. The higher incident beam energy allows to do new kinds of experiments, like kaon production; but it also allows to extend the Q^2 -range for the determination of the elastic form factors. For the near future, two experiments have been conceived and accepted by the program advisory committee.

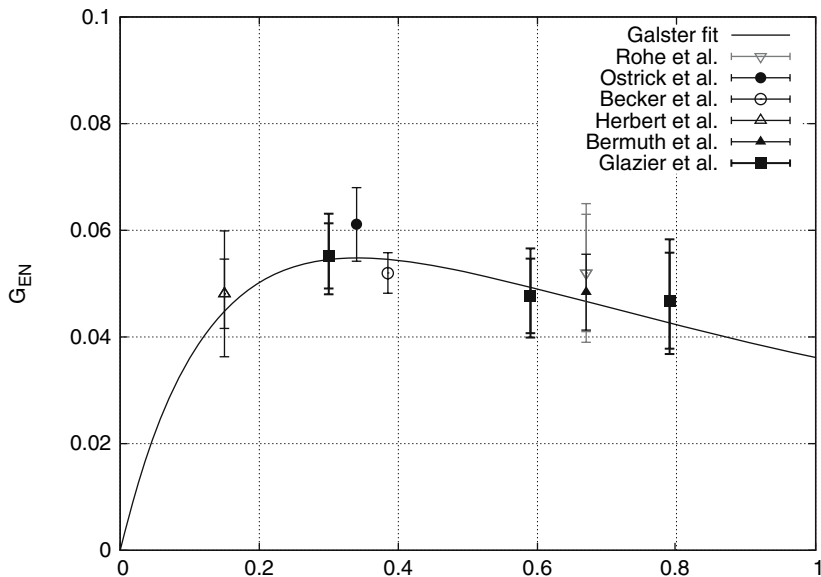


Fig. 6. The complete Mainz data set for G_{EN}

A High-Precision Proton Experiment: Bernauer et al.

When Friedrich and Walcher, triggered by the publication of new, high-precision G_{EN} data, reanalyzed the world data for the nucleon form factors [22], they found in all four form factors a very interesting anomaly, a bump/dip-structure around $0.2(\text{GeV}/c)^2$. They used the superposition of two dipoles,

$$G_s(q^2) = \frac{a_1}{(1 + Q^2/a_2)} + \frac{a_3}{(1 + Q^2/a_4)}, \quad (13)$$

to describe the smooth part of the form factors and a bump term,

$$G_b(q^2) = \exp\left(-\frac{1}{2}\left(\frac{Q - Q_a}{\sigma_b}\right)^2\right) + \exp\left(-\frac{1}{2}\left(\frac{Q + Q_a}{\sigma_b}\right)^2\right), \quad (14)$$

to describe the bump structure. To attribute the full normalization to the dominating smooth part, i.e., $G(Q^2 = 0) = G_s(Q^2 = 0)$, G_b is multiplied by Q^2 , so that the full parameterization is

$$G(Q^2) = G_s(Q^2) + a_b \cdot Q^2 G_b(Q^2). \quad (15)$$

Inspecting the top plot in Fig. 7, it is obvious that the dipole prediction completely fails for the higher Q^2 -regime where the data from polarization-transfer experiments are taken into account [23, 24]. The bottom plot shows the contribution of the bump term to the full parameterization. While the data sets, measured over decades all around the globe, agree surprisingly well, there is not one complete data set completely overlapping the dip structure. Since the global normalization is always problematic, it is possible but unlikely that this structure is an artifact. To establish the existence of such a structure and its shape, a new and comprehensive data set is called for. Luckily, the complete region is accessible by the MAMI facility.

The experimental program is designed to achieve an overall error in the range of 0.5%, which, for the time being, is only possible for the proton. While the original experiment [25] was planned to focus on the bump region, input from the atomic community widened the focus to include the very low Q^2 -region to determine the root mean square radii of the proton. The Q^2 -range from 0.002 to $2(\text{GeV}/c)^2$ will be covered with more than 250 kinematical setups. The first data have been taken by now.

G_{EN} for Higher Q^2 : Rohe et al.

Rohe et al. [26] are planning to redo their original experiment for a higher Q^2 -value of $1.5(\text{GeV}/c)^2$ in order to get good overlap with the data from the Jefferson laboratory [27, 28]. This will become possible with the higher beam

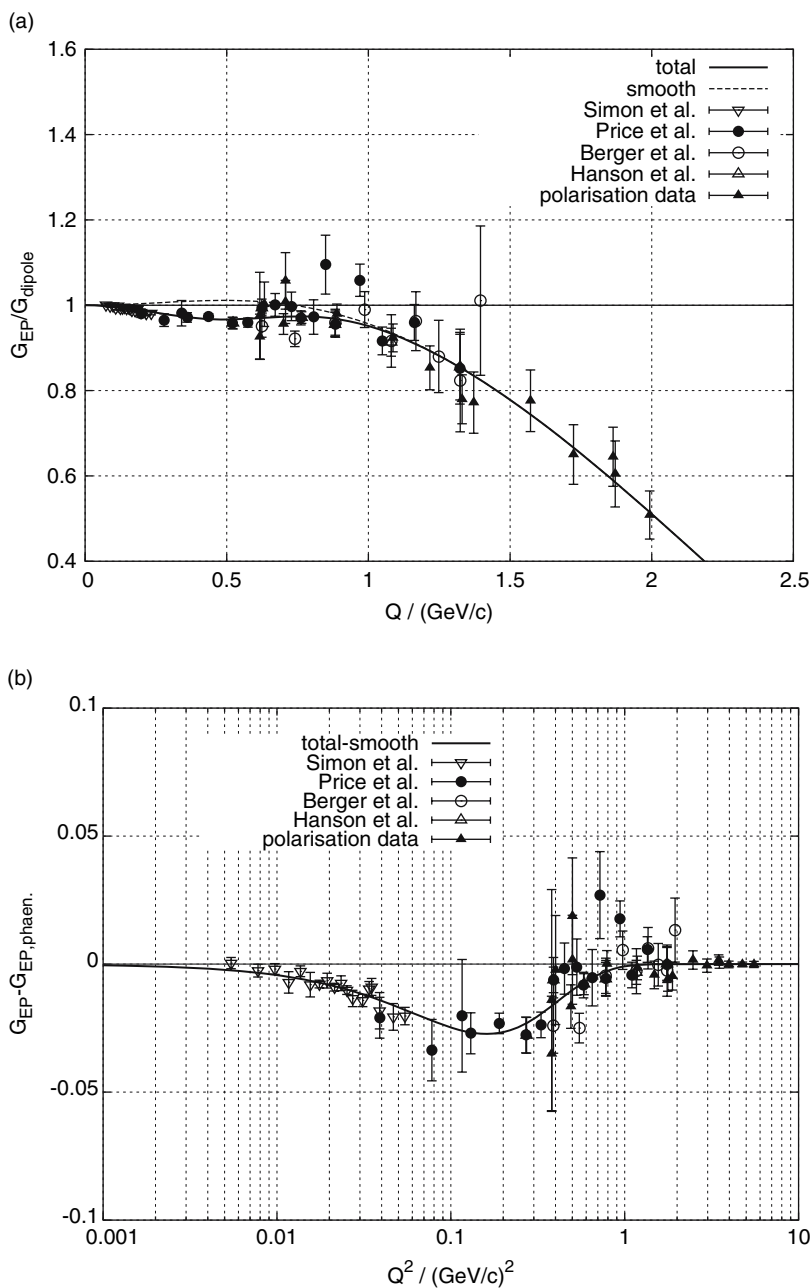


Fig. 7. The compilation of the world data for G_{EP} by Friedrich and Walcher [22] and their phenomenological fit. **Top:** normalized to the dipole form factor; **bottom:** only the bump contribution

energies provided by MAMI C. As an improvement over the original experiment, the scintillator volume of the neutron detector will be doubled. The construction of this new detector is already in progress and will be completed by the end of the year.

3 Conclusion and Outlook

As shown, not only the Mainz data for the standard nucleon form factors but the world data as well disagree with the dipole parameterization. There exist many better models and parameterizations of the form factors, phenomenological one and those with physical footing.

Upcoming experiments will clarify the situation concerning the dip in the proton form factors; also, additional data points for the neutron will become available in the near future.

Acknowledgment

The author wants to thank the many people who planned and performed the experiments. Special acknowledgments go to those involved in providing the excellent beam of the accelerators, to name a few: K. Aulenbacher, H. Euteneuer, H. Herminghaus, K.H. Kaiser. The successful completion of any experiment would not be possible without the construction and maintenance work done by the different workshops of the institute.

References

1. M.N. Rosenbluth: Phys. Rev. **79**, 615 (1950). [79](#)
2. S.G. Karshenboim: Can. J. Phys. **77**, 241 (1999). [80](#)
3. L. Hand et al.: Rev. Mod. Phys. **35**, 335 (1963). [80](#)
4. R. Hofstadter et al.: Rev. Mod. Phys. **30**, 482 (1958). [80](#)
5. F. Borkowski et al.: Nucl. Phys. A**222**, 269 (1974). [82](#)
6. G.G. Simon et al.: Nucl. Phys. A**333**, 381 (1980). [83](#)
7. B. Dudelzak: Thèse, Université de Paris, (1965). [84](#)
8. J. J. Murphy, II et al.: Phys. Rev. C**9**, 2125 (1974). [84](#)
9. K.I. Blomqvist et al.: Nucl. Instr. and Meth. A **403**, 263 (1998). [84](#)
10. A.I. Akhiezer et al.: Sov. J. Part. Nucl. **3**, 277 (1974). [84](#)
11. R. G. Arnold et al.: Phys. Rev. C **23**, 363 (1981). [84](#)
12. Th. Pospischil et al.: Eur. Phys. J. A **12**, 125 (2001). [84](#), [85](#)
13. H. Anklin et al.: Phys. Lett. B **428**, 248 (1998). [85](#), [86](#)
14. G. Kubon et al.: Phys. Lett. B **524**, 26 (2002). [85](#), [86](#)
15. D. Rohe et al.: Phys. Rev. Lett. **83**, 4257 (1999). [85](#)
16. J. Becker et al.: Eur. Phys. J. A **6**, 329 (1999). [85](#)
17. J. Golak et al.: Phys. Rev. C**63**, 034006 (2001). [85](#)

18. J. Bermuth et al.: Phys. Lett. B **564**, 199 (2003). [86](#)
19. C. Herberg et al.: Eur. Phys. J. A **5**, 132 (1999). [86](#)
20. M. Ostrick et al.: Phys. Rev. Lett. **83**, 276 (1999). [86](#)
21. D.I. Glazier et al.: Eur. Phys. J. A **24**, 101 (2005). [87](#)
22. J. Friedrich and Th. Walcher: Eur. Phys. J. A **17**, 607 (2003) and the references therein. [88](#), [89](#)
23. M. K. Jones et al.: Phys. Rev. Lett **84**, 1398 (2000). [88](#)
24. O. Gayou et al.: Phys. Rev. Lett. **88**, 092301 (2002). [88](#)
25. A1 Collaboration, Proposal A1-2/05, Institut für Kernphysik, Univ. Mainz. [88](#)
26. A1 Collaboration, Proposal A1-1/05, Institut für Kernphysik, Univ. Mainz. [88](#)
27. A. Lung et al.: Phys. Rev. Lett. **70**, 718 (1993). [88](#)
28. B. Plaster et al.: Phys. Rev. C **73**, 025205 (2006). [88](#)

Proton Structure Corrections to Hydrogen Hyperfine Splitting

C. E. Carlson

Physics Department, The College of William and Mary,
Williamsburg, VA 23187-8795, USA
carlson@physics.wm.edu

Abstract. The largest uncertainty in calculations of hydrogen ground-state hyperfine splitting comes from corrections due to proton structure. We review these corrections, with special mention of the inelastic, or polarizability, corrections which have been recently re-evaluated. Summing up the arguably best current values for the calculated corrections leaves us 1–2 ppm short of the experimental data. We speculate how one may explain this shortfall, and along the way broadly outline the derivations of the relevant formulas, attempting to explain how certain terms come to appear and commenting on the use of unsubtracted dispersion relations.

1 Introduction

Hyperfine splitting (hfs) in the hydrogen ground state is measured to 13 significant figures in frequency units [1],

$$E_{\text{hfs}}(e^-p) = 1\,420.405\,751\,766\,7(9) \text{ MHz}. \quad (1)$$

Theory is far from this level of accuracy, and theorists are hopeful of obtaining calculations accurate to a part per million (ppm) or so. We are close to reaching this goal, but some improvement is still needed and there currently seems to be a few ppm discrepancy between the best calculations and the data.

The main uncertainty in calculating the hfs in hydrogen comes from the hadronic, or proton structure, corrections. One can contrast this to the case of muonium, where the “nucleus” is a point particle, so that calculations are almost purely QED, and agreement between theory and experiment is about 0.1 ppm [2].

For ordinary hydrogen, as we have said, one must consider the proton structure, and find that it contributes about 40 ppm to the hfs. Working out these contributions theoretically requires knowing details about proton structure that cannot be obtained currently from ab initio calculation. Instead, one has to measure information about proton structure in other experiments,

particularly experiments on elastic and inelastic electron–proton scattering. Then calculations are done to relate the scattering information to the bound state energy. Recent new results have been driven by improvement in the data, including both new data for polarized inelastic scattering in kinematic regions of interest to hfs calculators and new analyses of the elastic scattering data. These will be outlined below.

Historically, the elastic and inelastic contributions, the latter also called polarizability corrections, have often been treated separately, with the elastic corrections further divided into a non-relativistic Zemach term and relativistic recoil corrections. From a modern viewpoint, the elastic and inelastic corrections should be treated as a unit since the sum lacks certain ambiguities that exist in the individual terms. The present discussion will focus on the polarizability contributions, but following the last remark, discussion of the Zemach and recoil corrections will not be omitted.

2 Hyperfine Splitting Calculations

The calculated hyperfine splitting in hydrogen is [1, 2, 3]

$$E_{\text{hfs}}(e^-p) = (1 + \Delta_{\text{QED}} + \Delta_{\text{weak}}^{\text{P}} + \Delta_{\text{Str}}) E_{\text{F}}^{\text{P}}, \quad (2)$$

where the Fermi energy is

$$E_{\text{F}}^{\text{P}} = \frac{8\alpha^3 m_{\text{r}}^3}{3\pi} \mu_{\text{B}} \mu_{\text{p}} = \frac{8\alpha^4 m_{\text{r}}^3}{3m_{\text{e}} m_{\text{p}}} (1 + \kappa_{\text{p}}), \quad (3)$$

with $m_{\text{r}} = m_{\text{e}} m_{\text{p}} / (m_{\text{p}} + m_{\text{e}})$ being the reduced mass (and there are hadronic and muonic vacuum polarization terms [2] which are included as higher order corrections to the Zemach term below). The QED terms are accurately calculated and well known. They will not be discussed, except to mention that they could be obtained without calculation. The QED corrections are the same as for muonium, so it is possible to obtain them to an accuracy more than adequate for the present purpose using muonium hfs data and a judicious subtraction [4, 5]. The weak interaction corrections [6] also will not be discussed, and are in any case quite small. We will discuss the proton structure dependent corrections,

$$\Delta_{\text{Str}} = \Delta_{\text{el}} + \Delta_{\text{inel}} = \Delta_{\text{Z}} + \Delta_{\text{R}}^{\text{P}} + \Delta_{\text{pol}}, \quad (4)$$

where the terms on the right-hand-side are the Zemach, recoil and polarizability corrections.

Generically, the proton structure corrections come from two-photon exchange, as diagrammed in Fig. 1. The diagram can be seen as Compton scattering of off-shell photons from an electron knit together with similar Compton scattering from the proton. (We are neglecting the characteristic momentum

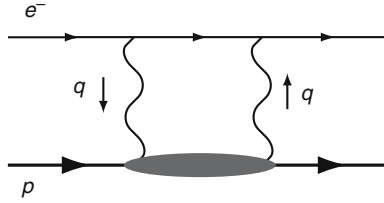


Fig. 1. Generic two-photon exchange diagrams, giving proton-structure corrections to hyperfine splitting

of the bound electron. This allows a noticeably simpler two-photon calculation than for a scattering process [7]. One can show that keeping the characteristic momentum would give corrections of $\mathcal{O}(\alpha m_e/m_p)$ smaller than terms that are kept [8].)

2.1 Elastic Terms: The Zemach Correction

In this author’s opinion, the best calculation of the box diagram uses dispersion relations, even though there are questions about using dispersion relations in their unsubtracted form. In a dispersive calculation, it is easy to consider the elastic and inelastic intermediate states simultaneously. This one should do because the full calculation is well defined, even though historically terms have been shuttled between the “elastic” and “inelastic” contributions.

At the outset, however, we will present results from a direct calculation of the elastic contributions, without dispersion theory. The results have been obtained by a number of authors [9, 10], and follow after assuming a certain photon–proton–proton vertex which is plausible but which cannot be defended perfectly.

The “elastic” contributions are those where the hadronic intermediate state, the blob in Fig. 1, is just a proton. The diagram specializes to Fig. 2. The photon–electron vertex is known, and we use [9, 10]

$$\Gamma_\mu = \gamma_\mu F_1(q^2) + \frac{i}{2m_p} \sigma_{\mu\nu} q^\nu F_2(q^2) \quad (5)$$

for the photon–proton vertex with incoming photon momentum q . Functions F_1 and F_2 are the Dirac and Pauli form factors of the proton, which are

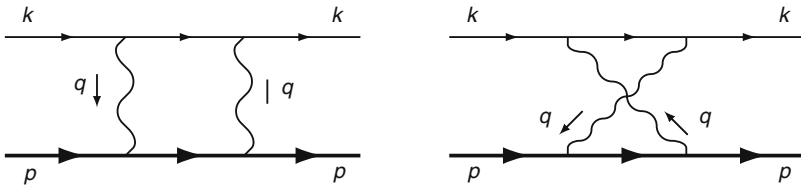


Fig. 2. Two-photon exchange diagrams for the elastic proton structure corrections to hyperfine splitting

measured in elastic electron–proton scattering. The normalization is $F_1(0) = 1$ and $F_2(0) = \kappa_p$, where κ_p is the proton’s anomalous magnetic moment measured in proton magnetons.

The above photon–proton vertex is complete and correct only if the protons entering and exiting the vertex have physical, on-shell, momenta. In a loop diagram, the intermediate proton is on-shell only at special values of momenta out of a continuum of momenta. Hence one may feel some hesitation in using the results that follow. However, there is also the (coming) dispersive calculation which only needs the vertices when all protons are on-shell, and so (again modulo questions surrounding dispersion relations with no subtraction) gives a reliable result. Any terms in the “elastic” calculations that appear to require modification can be fixed by adding or subtracting terms in other parts of the quoted result.

The elastic contributions are separated as

$$\left. \frac{E_{2\gamma}}{E_F} \right|_{\text{el}} = \Delta_Z + \Delta_R^p. \quad (6)$$

The separation is into non-relativistic and relativistic terms—“Zemach” and “recoil.” Non-relativistic means the limit $m_p \rightarrow \infty$ with m_e held fixed and with the proton size held fixed; proton size information is embedded in the form factors F_1 and F_2 .

The Zemach correction was worked out by Zemach in 1956 [11]; in modern form it is

$$\Delta_Z = \frac{8\alpha m_r}{\pi} \int_0^\infty \frac{dQ}{Q^2} \left[G_E(-Q^2) \frac{G_M(-Q^2)}{1 + \kappa_p} - 1 \right] = -2\alpha m_r r_Z, \quad (7)$$

where the last equality defines the Zemach radius r_Z and we have used $Q^2 = -q^2$. The charge and magnetic form factors are linear combinations of F_1 and F_2 ,

$$\begin{aligned} G_M &= F_1 + F_2, \\ G_E &= F_1 - \frac{Q^2}{4m_p^2} F_2. \end{aligned} \quad (8)$$

Table 1 gives the evaluated Zemach radius r_Z and correction Δ_Z for two modern form factor fits, and for the dipole fit, which is out of date and included only because it is a common benchmark. We believe the Ingo Sick fit is best for the purpose at hand, because the Zemach integrals depend mainly on the form factors at low Q^2 , and Sick’s fit concentrates on the low Q^2 scattering data.

2.2 Elastic Terms: Recoil Corrections

The relativistic elastic corrections Δ_R^p are known as recoil corrections. They depend on the form factors and hence are part of the proton structure corrections. However, evaluating Δ_R^p with different form factor representations

Table 1. Values of the Zemach radius and the Zemach corrections for selected fits to proton elastic form factors (The Zemach term Δ_Z includes a 1.53% correction from higher order electronic contributions [12], as well as a +0.07 ppm correction from muonic vacuum polarization and a +0.01 ppm correction from hadronic vacuum polarization [2])

form factor	r_Z (fm)	Δ_Z (ppm)
Kelly [13]	1.069(13)	-40.93(49)
Sick [13]	1.086(12)	-41.59(46)
dipole	1.025	-39.24

based on fits to the scattering data reveals that its numerical value is fairly stable (to about ± 0.15 ppm) by present standards.

The full result is

$$\begin{aligned}
 \Delta_R^p &= \frac{\alpha m_e m_p}{2(1 + \kappa_p)\pi(m_p^2 - m_e^2)} \times \\
 &\times \left\{ \int_0^\infty \frac{dQ^2}{Q^2} \left(\frac{\beta_1(\tau_p) - 4\sqrt{\tau_p}}{\tau_p} - \frac{\beta_1(\tau_e) - 4\sqrt{\tau_e}}{\tau_e} \right) F_1(-Q^2) G_M(-Q^2) \right. \\
 &+ 3 \int_0^\infty \frac{dQ^2}{Q^2} \left(\beta_2(\tau_p) - \beta_2(\tau_e) \right) F_2(-Q^2) G_M(-Q^2) \left. \right\} \\
 &+ \frac{2\alpha m_r}{\pi m_p^2} \int_0^\infty dQ F_2(-Q^2) \frac{G_M(-Q^2)}{1 + \kappa_p} \\
 &- \frac{\alpha m_e}{2(1 + \kappa_p)\pi m_p} \int_0^\infty \frac{dQ^2}{Q^2} \beta_1(\tau_e) F_2^2(-Q^2), \tag{9}
 \end{aligned}$$

where $\beta_{1,2}$ are auxiliary functions that were first found useful in discussing the inelastic terms [14, 15, 16, 17, 18, 19],

$$\begin{aligned}
 \beta_1(\tau) &= -3\tau + 2\tau^2 + 2(2 - \tau)\sqrt{\tau(\tau + 1)} = \frac{9}{4}\beta(\tau), \\
 \beta_2(\tau) &= 1 + 2\tau - 2\sqrt{\tau(\tau + 1)}. \tag{10}
 \end{aligned}$$

These are used with the notation,

$$\tau_p \equiv \frac{Q^2}{4m_p^2}, \quad \tau_e \equiv \frac{Q^2}{4m_e^2}. \tag{11}$$

The reasons for showing the whole formula for the recoil corrections is partly to show it is not so long (it sometimes appears more forbidding, cf. [9]), to explicitly see the form factor dependence, and to display the F_2^2 term in

the last line. The F_2^2 term is noteworthy because it is absent in a dispersive calculation, in contrast to all the other terms, which come forth unchanged.

All the integrals are finite, although some require the form factors to prevent ultraviolet divergence, and some would be infrared divergent if $m_e \rightarrow 0$. Of minor interest, the penultimate line could be subsumed into the Zemach correction, if the Zemach correction were to be written in terms of $F_1 G_M$ rather than $G_E G_M$.

2.3 Inelastic Terms: Polarizability Corrections

When the blob in Fig. 1 is not a lone proton, we obtain inelastic contributions or polarizability contributions [14, 15, 16, 17, 18, 19]. The inelastic contributions are not calculable ab initio. Instead, one relates them to the amplitude for forward Compton scattering of off-shell photons off protons, given in terms of the matrix element

$$T_{\mu\nu}(q, p, S) = \frac{i}{2\pi m_p} \int d^4\xi e^{iq\cdot\xi} \langle pS | j_\mu(\xi) j_\nu(0) | pS \rangle, \quad (12)$$

where j_μ is the electromagnetic current and the states are proton states of momentum p and spin 4-vector S . The spin dependence is in the antisymmetric part

$$T_{\mu\nu}^A = \frac{i}{m_p\nu} \epsilon_{\mu\nu\alpha\beta} q^\alpha \left[(H_1(\nu, q^2) + H_2(\nu, q^2)) S^\beta - H_2(\nu, q^2) \frac{S\cdot q p^\beta}{p\cdot q} \right]. \quad (13)$$

There are two structure functions H_1 and H_2 which depend on q^2 and on the photon energy ν , defined in the lab frame so that $m_p\nu = p\cdot q$.

There is an optical theorem that relates the imaginary part of the forward Compton amplitude to the cross-section for inelastic scattering of off-shell photons from protons. The relations precisely are

$$\text{Im } H_1(\nu, q^2) = \frac{1}{\nu} g_1(\nu, q^2) \quad \text{and} \quad \text{Im } H_2(\nu, q^2) = \frac{m_p}{\nu^2} g_2(\nu, q^2), \quad (14)$$

where g_1 and g_2 are functions appearing in the cross-section and are measured [20, 21, 22, 23, 24] at SLAC, HERMES, JLab and elsewhere.

Using the Compton amplitude in terms of H_1 and H_2 , (13), in evaluating the inelastic part of the two-photon loops gives

$$\begin{aligned} \Delta_{\text{pol}} = \frac{E_{2\gamma}}{E_F} \Big|_{\text{inel}} &= \frac{2\alpha m_e}{(1 + \kappa_p)\pi^3 m_p} \int \frac{d^4Q}{(Q^4 + 4m_e^2 Q_0^2)Q^2} \times \\ &\times \left\{ (2Q^2 + Q_0^2) H_1^{\text{inel}}(iQ_0, -Q^2) - 3Q^2 Q_0^2 H_2^{\text{inel}}(iQ_0, -Q^2) \right\}, \end{aligned} \quad (15)$$

where we have Wick rotated the integral so that $Q_0 = -i\nu$, $\mathbf{Q} = \mathbf{q}$ and $Q^2 \equiv Q_0^2 + \mathbf{Q}^2$. Since $H_{1,2}$ are not measured, we obtain them from a dispersion

relation, which will be discussed in a subsequent section. Assuming no subtraction,

$$H_1^{\text{inel}}(\nu_1, q^2) = \frac{1}{\pi} \int_{\nu_{\text{th}}}^{\infty} d\nu \frac{\text{Im} H_1(\nu, q^2)}{\nu^2 - \nu_1^2}, \quad (16)$$

where the integral is only over the inelastic region ($\nu_{\text{th}} = m_\pi + (m_\pi^2 + Q^2)/(2m_p)$), and similarly for H_2 .

Putting things together, neglecting m_e inside the integral and integrating what can be integrated, one obtains the expression

$$\Delta_{\text{pol}} = \frac{\alpha m_e}{2(1 + \kappa_p)\pi m_p} (\Delta_1 + \Delta_2), \quad (17)$$

where, with $\tau = \nu^2/Q^2$,

$$\begin{aligned} \Delta_1 &= \frac{9}{4} \int_0^\infty \frac{dQ^2}{Q^2} \left\{ F_2^2(-Q^2) + 4m_p \int_{\nu_{\text{th}}}^\infty \frac{d\nu}{\nu^2} \beta(\tau) g_1(\nu, -Q^2) \right\}, \quad (18) \\ \Delta_2 &= -12m_p \int_0^\infty \frac{dQ^2}{Q^2} \int_{\nu_{\text{th}}}^\infty \frac{d\nu}{\nu^2} \beta_2(\tau) g_2(\nu, -Q^2). \end{aligned}$$

The integral for Δ_1 is touchy. Only the second term comes from the procedure just outlined. The first arises when one applies the dispersive calculation also to the elastic corrections, and discovers that the F_2^2 term pointed out earlier in (9) is absent. It was then thought convenient to add the first term as seen above, and then subtract the same term from the recoil contributions. This leaves the elastic corrections exactly as already shown. This stratagem also allows the electron mass to be taken to zero in Δ_1 . The individual dQ^2 integrals in Δ_1 diverge (they would not had the electron mass been kept), but the whole is finite because of the Gerasimov–Drell–Hearn (GDH) sum rule [25, 26],

$$4m_p \int_{\nu_{\text{th}}}^\infty \frac{d\nu}{\nu^2} g_1(\nu, 0) = -\kappa_p^2, \quad (19)$$

coupled with the observation that the auxiliary function $\beta(\tau)$ becomes unity as we approach the real photon point.

The polarizability expressions have some history. A short version is that considerations of Δ_{pol} were begun by Iddings in 1965 [14], improved by Drell and Sullivan in 1966 [15] and given in present notation by de Rafael in 1971 [16]. But no sufficient spin-dependent data existed, so it was several decades before the formula could be evaluated to a result incompatible with zero. In 2002, Faustov and Martynenko became the first to use $g_{1,2}$ data to obtain results inconsistent with zero [18]. Their 2002 result was

$$\Delta_{\text{pol}} = (1.4 \pm 0.6) \text{ ppm} \quad (20)$$

However, they only used SLAC data and Δ_1 and Δ_2 are sensitive to the behavior of the structure functions at low Q^2 . Also in 2002 there appeared analytic expressions for $g_{1,2}$ fit to data by Simula, Osipenko, Ricco, and Taiuti [27], which included JLab as well as SLAC data. They did not at that time integrate their results to obtain Δ_{pol} . Had they done so, they would have obtained $\Delta_{\text{pol}} = (0.4 \pm 0.6)$ ppm [19].

We now have enough information to discover a bit of trouble. Table 2 summarizes how things stood before the 2005/2006 re-evaluations of Δ_{pol} . The sum of all corrections is 1.59 ± 0.77 ppm short of what would be desired by experimental data. Using the Simula et al. value for Δ_{pol} would make the deficit greater. Using other proton form factor fits (limiting ourselves to modern ones that fit the data well) in evaluating Δ_Z can reduce the deficit somewhat, but not enough to ameliorate the problem [19].

The discrepancy is not large, measured in standard deviations. On the other hand, the problem is clearly not in statistical fluctuations of the hfs measurement one is trying to explain, so one would like to do better. As listed in the table, the largest uncertainty in the corrections comes from Δ_{pol} . Further, the polarizability corrections require knowledge of g_1 and g_2 at relatively low Q^2 , and good data pressing farther into the required kinematic regime has relatively recently become available from JLab (the Thomas Jefferson National Accelerator Laboratory, in Newport News, VA, USA). Accordingly, we shall present a state-of-the-art evaluation of the polarizability correction for electronic hydrogen. To give away our results [19] at the outset, we essentially confirm (remarkably, given the improvements in data) the 2002 results of Faustov and Martynenko.

Table 2. Corrections to hydrogenic hyperfine structure, as they could have been given in 2004. The first line with numbers gives the “target value” based on the experimental data and the best evaluation of the Fermi energy (eight figures) based on known physical constants. The corrections are listed next. (The Zemach term includes a 1.53% correction from higher order electronic contributions [12], as well as a +0.07 ppm correction from muonic vacuum polarization and a +0.01 ppm correction from hadronic vacuum polarization [2].) The total of all corrections is 1.59 ± 0.77 ppm short of the experimental value

quantity	value (ppm)	uncertainty (ppm)
$(E_{\text{hfs}}(e^-p)/E_F^p) - 1$	1 103.49	0.01
Δ_{QED}	1 136.19	0.00
Δ_Z (using Friar and Sick [28])	-41.59	0.46
Δ_R^p	5.84	0.15
Δ_{pol} (from Faustov and Martynenko, 2002 [18])	1.40	0.60
Δ_{weak}^p	0.06	
total	1101.90	0.77
deficit	1.59	0.77

3 Re-evaluation of Δ_{pol}

Data for $g_1(\nu, q^2)$ has improved due to the EG1 experiment at JLab, which had a data run in 2000–2001. Some data based on preliminary analysis became available in 2005 [24]; final data are anticipated in late 2006. A sample of the new data is shown in Fig. 3. Since a function of two variables can be complicated to show, what is shown is the integral

$$I(Q^2) \equiv 4m_p \int_{\nu_{\text{th}}}^{\infty} \frac{d\nu}{\nu^2} g_1(\nu, -Q^2), \quad (21)$$

which differs from an integral appearing in Δ_1 in lacking the auxiliary function. The integration was done by the experimenters themselves. We remind the reader that this integral is expected to reach the Gerasimov–Drell–Hearn value $-\kappa_p^2$ at the real photon point, and that because of cancellations the difference of this integral from $-\kappa_p^2$ is more relevant to the final answer for Δ_{pol} than its absolute value.

All the data shown are new; there was no polarized electron–proton scattering data available below $Q^2 = 0.3 \text{ GeV}^2$ when Simula et al. and Faustov and Martynenko did their earlier fits. A curve obtained by integrating Simula et al.’s fit for g_1 is also shown in the figure; we do not have enough information to produce a similar curve for Faustov and Martynenko’s fit.

Integration in the region $Q^2 > 0.05 \text{ GeV}^2$ is done using analytic fits to actual data for g_1 . For Q^2 below 0.05 GeV^2 , where there is no data, we do an interpolation based on a low Q^2 expansion within the integral to get (with $Q_1^2 \rightarrow 0.05 \text{ GeV}^2$),

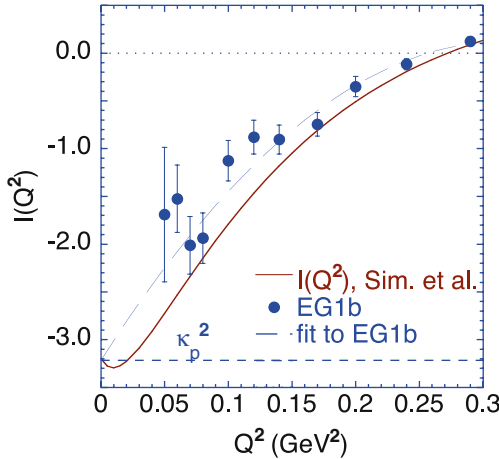


Fig. 3. Data for (an integral over) the spin-dependent structure function $g_1(\nu, q^2)$. The data is from the EG1 experiment at Jefferson Lab and from the year 2005. The Simula et al. curve is from a fit published in 2002

$$\begin{aligned} \Delta_1[0, Q_1^2] &\equiv \frac{9}{4} \int_0^{Q_1^2} \frac{dQ^2}{Q^2} \left\{ F_2^2(-Q^2) + 4m_p \int_{\nu_{\text{th}}}^{\infty} \frac{d\nu}{\nu^2} \beta(\tau) g_1(\nu, -Q^2) \right\} \\ &= \left[-\frac{3}{4} r_p^2 \kappa_p^2 + 18m_p^2 c_1 - \frac{5m_p^2}{4\alpha} \gamma_0 \right] Q_1^2 + \mathcal{O}(Q_1^4). \end{aligned} \quad (22)$$

Here r_p is from the expansion of the Pauli form factor

$$F_2(-Q^2) = \kappa_p^2 (1 - r_p^2 Q^2/6 + \dots),$$

and the ‘‘forward spin polarizability’’ γ_0 has been evaluated from data for other purposes [29],

$$\gamma_0 \equiv \frac{2\alpha}{m_p} \int_{\nu_{\text{th}}}^{\infty} \frac{d\nu}{\nu^4} g_1(\nu, 0) = [-1.01 \pm 0.08 \pm 0.10] \times 10^{-4} \text{ fm}^4. \quad (23)$$

The parameter c_1 is defined from the slope at low Q^2 of the integral shown in Fig. 3.

$$I(Q^2) = 4m_p \int_{\nu_{\text{th}}}^{\infty} \frac{d\nu}{\nu^2} g_1(\nu, -Q^2) = -\kappa_p^2 + 8m_p^2 c_1 Q^2 + \mathcal{O}(Q^4); \quad (24)$$

we find and use $c_1 = 2.95 \pm 0.11 \text{ GeV}^{-4}$ [19].

We need to comment that for Δ_2 , we need g_2 , and there is almost no data for g_2 on the proton. One estimates g_2 by relating it to g_1 using the Wandzura–Wilczek relation [30], which we shall not detail here. Fortunately, the auxiliary function $\beta_2(\tau)$ is small over the region where we need to do the integrals, so that even when we assigned 100% error bars to the contribution from g_2 , the effect on the final answer was not great.

Our overall result is [19]

$$\Delta_{\text{pol}} = 1.3 \pm 0.3 \text{ ppm}, \quad (25)$$

which is similar to the 2002 Faustov–Martynenko result. This result means that the polarizability corrections no longer give the largest uncertainty in Table 2. It also means that the theory deficit outlined in Table 2 still remains, even becoming modestly larger with a smaller uncertainty limit, at $(1.69 \pm 0.57) \text{ ppm}$.

Faustov, Gorbacheva, and Martynenko [31] quite recently published a new analysis and result for Δ_{pol} , obtaining the somewhat larger value

$$\Delta_{\text{pol}} = 2.2 \pm 0.8 \text{ ppm}. \quad (26)$$

We still believe our published result [19] is the best one for now because the Jefferson Lab EG1b data, which goes to lower Q^2 than other data sets, have been used to constrain and validate the fits that we use to do the integrals. Faustov et al. used only higher Q^2 data from other laboratories. It is, of course, possible that the final EG1b data will lead to some change.

4 Comments on the Derivations of the Formulas

The polarizability corrections depend on theoretical results that are obtained using unsubtracted dispersion relations. This has been alluded to before in this text, and this section will attempt to explain how a dispersion calculation works and what an unsubtracted dispersion relation is. Also, given that there may be a small discrepancy between calculation and data, one would like to assess the validity of unsubtracted dispersion relations.

Also, the hyperfine splitting in muonic hydrogen may be measured soon. The polarizability corrections have been calculated for this case also [32], albeit only with older fits to the structure function data and the relevant formulas, with non-zero lepton mass everywhere, are available [32] from a single source, so one would like to verify these formulas. It turns out that keeping the lepton mass does not greatly increase calculational effort or the length of the formulas, so we can do the groundwork for the muonic hfs case simultaneously with the assessment of the ordinary hydrogen hfs calculation, although we shall not display here the formulas for non-zero lepton mass.

The calculation begins by writing out the loop calculation using the known electron vertices and the definition of the Compton scattering amplitudes involving H_1 and H_2 as given in (13). One can and should use this formalism for all the hadronic intermediate states, including the single proton intermediate states. The single proton intermediate states give contributions to H_1 and H_2 that can be (more-or-less) easily calculated given a photon–proton–proton vertex such as (5). For reference, we give the result for H_1 ,

$$H_1^{\text{el}} = -\frac{2m_p}{\pi} \left(\frac{q^2 F_1(q^2) G_M(q^2)}{(q^2 + i\epsilon)^2 - 4m_p^2 \nu^2} + \frac{F_2^2(q^2)}{4m_p^2} \right). \quad (27)$$

The criticism of the proton vertex used to obtain the above result is that it is not demonstrably valid when the intermediate proton is off shell, so the above expression may or may not be correct overall. However, it is correct at the proton pole.

One may do a unified calculation of the elastic and inelastic contributions. Since we do not have a direct calculation of the H_i for the inelastic case, we have to obtain them using dispersion relations. Also obtaining the elastic terms from the dispersion relation is no problem [14, 15]. One just needs the imaginary parts of H_i^{el} ; these are easy to obtain, and contain Dirac delta-functions that ensure the elastic scattering condition $\nu = \pm Q^2/(2m_p)$ and hence depends only on the reliable part of (27).

Dispersion relations involve imagining one of the real variables to be a complex one and then using the Cauchy integral formula to find the functions H_i at a particular point in terms of an integral around the boundary of some region. In the present case we “disperse” in ν , treating q^2 as a constant while we do so. Three things are needed to make the dispersion calculation work:

- The Cauchy formula and knowing the analytic structure of the desired amplitudes.

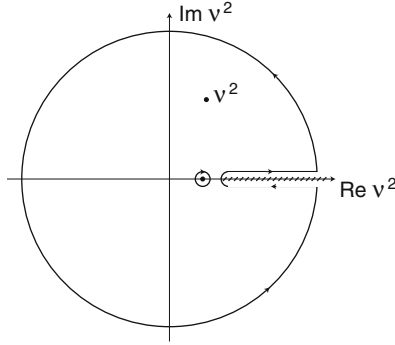


Fig. 4. Contour in complex ν^2 plane for applying Cauchy identity to H_1 or H_2

- The optical theorem, to relate the forward Compton $\text{Im } H_i$ to inelastic scattering cross-sections.
- Legitimately discarding contributions from some ∞ contour, if the dispersion relation is to be “unsubtracted.”

The first two are not in question.

For the present case, the contour of integration is illustrated in Fig. 4, where one should imagine the outside circle having infinite radius. The result for H_1 begins its existence as

$$\begin{aligned}
 H_1(\nu, q^2) = & \frac{\text{Res } H_1(\nu, q^2)|_{\text{el}}}{\nu_{\text{el}}^2 - \nu^2} \\
 & + \frac{1}{\pi} \int_{\text{cut}} \frac{\text{Im } H_1(\nu', q^2)}{\nu'^2 - \nu^2} d\nu'^2 + \frac{1}{2\pi i} \int_{|\nu'|=\infty} \frac{H_1(\nu', q^2)}{\nu'^2 - \nu^2} d\nu'^2.
 \end{aligned}
 \tag{28}$$

The numerator of the first term is the residue (Res) from the poles in ν for the elastic part of H_1 , as from (27). Note that the F_2^2 term in H_1^{el} , (27), is constant in ν , certainly lacking a pole in ν . Hence this term never enters the dispersion relation, and no F_2^2 term arises from the elastic contribution, as calculated this way.

The second term leads to the g_1 term in the quantity Δ_1 given earlier, after using the optical theorem to relate $\text{Im } H_i$ to g_1 .

The third term is the integral over the part of the contour which is the infinite radius circle. The commonly quoted results for Δ_{pol} , which appear in this chapter, depend on dropping this term. The term is zero, if H_1 falls to zero at infinite $|\nu|$. Assuming this is true, however, appears to be a dramatic assumption. It fails for H_1^{el} alone. Hence, for the assumption to succeed requires an exact cancellation between elastic and inelastic contributions (or a failure of (27) on the big contour). On the positive side are several considerations. One is that nearly the same derivation gives the GDH sum rule, which is checked experimentally and works, within current experimental uncertainty

(8%) [33]. Also, the GDH sum rule is checkable theoretically in QED, where lowest order and next-to-lowest order perturbation theory calculations can be done, and the GDH sum rule appears to work [34, 35]. Finally, Regge theory suggests the full Compton amplitude does fall to zero with energy [36], as one would like, although Regge theory famously gave wrong high ν behavior for spin-independent analogs of g_1 and g_2 [37]. Hence there are indications, though not decisive proof, supporting the unsubtracted dispersion relation.

The derivation finishes, as noted earlier, by subtracting a term involving F_2^2 from the relativistic recoil term, so as to obtain exactly the elastic corrections $\Delta_{\text{el}} = \Delta_Z + \Delta_R^p$ that were obtained (say) by Bodwin and Yennie for a calculation of the elastic terms only, using (5) at the photon–proton vertices and no dispersion theory [9]. After adding the same term to the polarizability corrections in Δ_1 , one obtains the commonly quoted result for Δ_1 [15, 16, 18]. Beyond the historical connection, if one is comfortable with the unsubtracted dispersion relation, the use of the dispersion theory gives a more secure result because it uses only the pole part of the photon–proton–proton vertex, so that the combined elastic and inelastic result does not depend on the general validity of whatever photon–proton–proton vertex one uses.

5 Conclusion

The evaluation of the polarizability contributions to hydrogen hyperfine structure, Δ_{pol} , based on latest proton structure function data is $\Delta_{\text{pol}} = 1.3 \pm 0.3$ ppm [19]. This is quite similar to the Faustov–Martynenko 2002 result, which we think is remarkable given the improvement in the data upon which it is based. Most of the calculated Δ_{pol} comes from integration regions where the photon four-momentum squared is small, $Q^2 < 1$ GeV².

There is still a modest discrepancy between the hydrogen hfs calculation and experiment, on the order of 2 ppm. Optimistically, one can hope for a rapid reconciliation between data and calculation. It surely has not been missed that using the Kelly form factor [13] value of the Zemach radius and the new Faustov–Gorbacheva–Martynenko value for Δ_{pol} [31] give excellent agreement between theory and data. Nonetheless, one can argue that other choices are currently better. The integrals that give Δ_Z and Δ_{pol} emphasize the low- Q^2 region. The Sick form factors are the only modern ones that are tuned to fit best at low Q^2 , and the determination of Δ_{pol} in [19] is the only one that has explicitly used the lower Q^2 Jefferson Lab inelastic data.

An interplay between the fields of atomic and nuclear or particle physics may be relevant to sorting out problem. For one example, the best values of the proton charge radius currently come from small corrections accurately measured in atomic Lamb shift [38]. Sick’s value of the charge radius [13], from the analysis of scattering data, is somewhat larger. The precision of the atomic measurement of the proton charge radius can increase markedly if the Lamb shift is measured in muonic hydrogen [39], which could happen in 2007, if the

Paul Scherrer Institute accelerator schedule holds. In the present context, the charge radius is noticed by its effect on determinations of the Zemach radius.

For ourselves, we look forward to a high-accuracy resolution of the proton structure corrections to hydrogen hfs, and also to finishing a clear continuation of the present program by the evaluation of the muonic hydrogen ground-state hfs. We have formulas with all lepton masses in place, and are currently waiting until the final EG1 data is released, which we think will be rather soon, before proceeding and publishing a numerical evaluation.

Acknowledgement

My contributions to this subject have all been made in collaboration with Vahagn Nazaryan and Keith Griffioen. I thank them for the pleasure I have had working with them. In addition, we thank José Goity, Savely Karshenboim, Ingo Sick, Silvano Simula, and Marc Vanderhaeghen for helpful discussions and information. This work was supported by the National Science Foundation under grants PHY-0245056 and PHY-0555600 (C.E.C.); PHY-0400332 (V.N.); and by the Department of Energy under contract DE-FG02-96ER41003 (K.A.G.).

References

1. S. G. Karshenboim: Phys. Rep. **422**, 1 (2005) [arXiv:hep-ph/0509010]. [93](#), [94](#)
2. A. V. Volotka, V. M. Shabaev, G. Plunien and G. Soff: Eur. Phys. J. D **33**, 23 (2005). [94](#), [97](#), [100](#)
3. A. Dupays, A. Beswick, B. Lepetit, C. Rizzo, and D. Bakalov: Phys. Rev. A **68**, 052503 (2003). [94](#)
4. S. J. Brodsky, C. E. Carlson, J. R. Hiller and D. S. Hwang: Phys. Rev. Lett. **94**, 022001 (2005); Phys. Rev. Lett. **94**, 169902 (E) (2005) [arXiv:hep-ph/0408131]. See also [5](#). [94](#)
5. J. L. Friar and I. Sick: Phys. Rev. Lett. **95**, 049101 (2005) [arXiv:nucl-th/0503020] and S. J. Brodsky, C. E. Carlson, J. R. Hiller and D. S. Hwang: Phys. Rev. Lett. **95**, 049102 (2005). [94](#), [106](#)
6. M. I. Eides: Phys. Rev. A **53**, 2953 (1996). [94](#)
7. P. G. Blunden, W. Melnitchouk and J. A. Tjon: Phys. Rev. Lett. **91**, 142304 (2003) [arXiv:nucl-th/0306076]; Y. C. Chen, A. Afanasev, S. J. Brodsky, C. E. Carlson and M. Vanderhaeghen: Phys. Rev. Lett. **93**, 122301 (2004) [arXiv:hep-ph/0403058]; A. V. Afanasev, S. J. Brodsky, C. E. Carlson, Y. C. Chen and M. Vanderhaeghen: Phys. Rev. D **72**, 013008 (2005) [arXiv:hep-ph/0502013]; J. Arrington: Phys. Rev. C **71**, 015202 (2005) [arXiv:hep-ph/0408261]. [95](#)
8. C. K. Iddings and P. M. Platzman: Phys. Rev. **113**, 192 (1959). [95](#)
9. G. T. Bodwin and D. R. Yennie: Phys. Rev. D **37**, 498 (1988). [95](#), [97](#), [105](#)
10. A. P. Martynenko: Phys. Rev. A **71**, 022506 (2005) [arXiv:hep-ph/0409107]. [95](#)
11. A. C. Zemach: Phys. Rev. **104**, 1771 (1956). [96](#)

12. S. G. Karshenboim: Phys. Lett. **225A**, 97 (1997). [97](#) [100](#)
13. I. Sick: Phys. Lett. B **576**, 62 (2003) [arXiv:nucl-ex/0310008]; J. J. Kelly: Phys. Rev. C **70**, 068202 (2004). [97](#) [105](#)
14. C. K. Iddings: Phys. Rev. **138**, B446 (1965). [97](#) [98](#) [99](#) [103](#)
15. S. D. Drell and J. D. Sullivan: Phys. Rev. **154**, 1477 (1967). [97](#) [98](#) [99](#) [103](#) [105](#)
16. E. De Rafael: Phys. Lett. B **37**, 201 (1971). [97](#) [98](#) [99](#) [105](#)
17. P. Gnädig and J. Kuti: Phys. Lett. B **42**, 241 (1972). [97](#) [98](#)
18. R. N. Faustov and A. P. Martynenko: Eur. Phys. J. C **24**, 281 (2002); R. N. Faustov and A. P. Martynenko: Phys. Atom. Nucl. **65**, 265 (2002) [Yad. Fiz. **65**, 291 (2002)]. [97](#) [98](#) [99](#) [100](#) [105](#)
19. V. Nazaryan, C. E. Carlson and K. A. Griffioen: Phys. Rev. Lett. **96**, 163001 (2006) [arXiv:hep-ph/0512108]. [97](#) [98](#) [100](#) [102](#) [105](#)
20. P. L. Anthony et al. [E155 Collaboration]: Phys. Lett. B **493**, 19 (2000) [arXiv:hep-ph/0007248]. [98](#)
21. P. L. Anthony et al. [E155 Collaboration]: Phys. Lett. B **553**, 18 (2003) [arXiv:hep-ex/0204028]. [98](#)
22. R. Fatemi et al. [CLAS Collaboration]: Phys. Rev. Lett. **91**, 222002 (2003) [arXiv:nucl-ex/0306019]. [98](#)
23. J. Yun et al.: Phys. Rev. C **67** 055204, (2003); S. Kuhn: private communication. [98](#)
24. A. Deur: arXiv:nucl-ex/0507022. [98](#) [101](#)
25. S. B. Gerasimov: Sov. J. Nucl. Phys. **2**, 430 (1966) [Yad. Fiz. **2**, 598 (1966)]. [99](#)
26. S. D. Drell and A. C. Hearn: Phys. Rev. Lett. **16**, 908 (1966). [99](#)
27. S. Simula, M. Osipenko, G. Ricco and M. Taiuti: Phys. Rev. D **65**, 034017 (2002) [arXiv:hep-ph/0107036]. Silvano Simula provided us with an updated version of the code, including error estimates. [100](#)
28. J. L. Friar and I. Sick: Phys. Lett. B **579**, 285 (2004). [100](#)
29. D. Drechsel, B. Pasquini and M. Vanderhaeghen: Phys. Rept. **378**, 99 (2003) [arXiv:hep-ph/0212124]. [102](#)
30. S. Wandzura and F. Wilczek: Phys. Lett. B **72**, 195 (1977). [102](#)
31. R. N. Faustov, I. V. Gorbacheva and A. P. Martynenko: “Proton polarizability effect in the hyperfine splitting of the hydrogen atom,” arXiv:hep-ph/0610332. [102](#) [105](#)
32. R. N. Faustov, E. V. Cherednikova and A. P. Martynenko: Nucl. Phys. A **703**, 365 (2002) [arXiv:hep-ph/0108044]. [103](#)
33. P. Pedroni [GDH and A2 Collaborations]: AIP Conf. Proc. **814**, 374 (2006); H. Dutz et al. [GDH Collaboration]: Phys. Rev. Lett. **94**, 162001 (2005). [105](#)
34. D. A. Dicus and R. Vega: Phys. Lett. B **501**, 44 (2001) [arXiv:hep-ph/0011212]. [105](#)
35. G. Altarelli, N. Cabibbo and L. Maiani: Phys. Lett. B **40**, 415 (1972). [105](#)
36. H. D. I. Abarbanel and S. Nussinov: Phys. Rev. **158**, 1462 (1967). [105](#)
37. M. Damashek and F. J. Gilman: Phys. Rev. D **1**, 1319 (1970); C. A. Dominguez, C. Ferro Fontan and R. Suaya: Phys. Lett. B **31**, 365 (1970). [105](#)
38. P. J. Mohr and B. N. Taylor: Rev. Mod. Phys. **72**, 351 (2000); and Rev. Mod. Phys. **77**, 1 (2005) [2002 CODATA]; cf., the electron scattering value of I. Sick: Phys. Lett. B **576**, 62 (2003) [arXiv:nucl-ex/0310008] or the spread from Sick’s value to that of J. J. Kelly: Phys. Rev. C **70**, 068202 (2004). [105](#)
39. A. Antognini et al.: AIP Conf. Proc. **796**, 253 (2005). [105](#)

Atoms with Few Electrons

Precision Laser Spectroscopy of Li^+ and Neutral Lithium

W. A. van Wijngaarden and G. A. Noble

Physics Department, York University, Toronto, ON, M3J 1P3, Canada
waww@yorku.ca

Abstract. Lithium has a number of properties that make it useful for both experimental and theoretical study. Precise spectroscopic measurements of optical transitions in both Li^+ and neutral Li are reviewed. Experiments have yielded hyperfine and fine structure splittings that test QED as well as isotope shifts that determine the relative nuclear charge radius between isotopes to an accuracy of 2×10^{-17} m. Experimental and theoretical results agree very well for Li^+ and a measurement of the fine structure of the $1s2p\ ^3P_{0,1,2}$ levels is of interest to determine the fine structure constant. For neutral lithium, additional theoretical work is needed to match the experimental accuracy for the 2P fine structure splitting.

1 Introduction

Lithium is the lightest naturally occurring solid element in the periodic table. It has a number of properties that make it a preferred atom to study for experimentalists including a relatively low melting point of 180°C that facilitates the generation of an atomic beam and most importantly for the application of precise spectroscopic techniques, transitions at visible wavelengths where continuous wave lasers readily operate. These transitions include the Li^+ $1s2s\ ^3S_1 \rightarrow 1s2p\ ^3P_{0,1,2}$ at 548 nm and the D lines in neutral lithium at 670 nm. Lithium has a number of isotopes, two of which are stable, as shown in Table [1](#). This is important when doing precise experiments where nuclear effects are comparable or exceed the measurement accuracy. The experiment can then be repeated using different isotopes whose nuclear size differ markedly. This is especially important for ^7Li which has been found to have halo neutrons [2](#).

Lithium is a multielectron system that precludes a simple analytic solution to the Schrödinger equation. Theoretical progress remained limited until about 15 years ago when G. W. F. Drake and collaborators began applying the so-called Hylleraas variational method to initially model two-electron and more recently three-electron systems [3](#). Extensive computations using thousands of carefully constructed basis functions to represent the wavefunction have

Table 1. Lithium isotopes

Isotope	Natural Abundance	Nuclear Spin	Lifetime (msec)
${}^6\text{Li}$	7.5%	1	
${}^7\text{Li}$	92.5%	3/2	
${}^8\text{Li}$		2	836 ± 6 [2]
${}^9\text{Li}$		3/2	178.3 ± 0.4 [2]
${}^{11}\text{Li}$		3/2	8.59 ± 0.14 [3]

enabled the non-relativistic eigenenergies for helium states to be found with an accuracy of one part in 10^{16} [5]. These wavefunctions have in turn been used to perturbatively evaluate relativistic, hyperfine and QED terms to high accuracy. Comparison of theoretical energy estimates to measured isotope shifts has permitted the determination of the nuclear charge radius with an order of magnitude higher accuracy than is possible in electron scattering experiments [6, 7].

Several review articles give detailed descriptions of the various experimental techniques used to measure isotope shifts, fine and hyperfine splittings in neutral and singly ionized lithium [8, 9]. This article presents the results of the most accurate experiments and emphasizes recent work that has yielded improved values of the relative charge radii for the various lithium isotopes [6, 7, 10].

This paper is organized as follows. First, Sect. 2 gives a brief background of the theoretical and experimental techniques used in the most recent work. Next in Sect. 3, experimental data for the hyperfine and fine structure splittings found for the Li^+ $1s2s$ 3S_1 and $1s2p$ ${}^3P_{0,1,2}$ states are presented and compared to theory. The possibility of determining the fine structure constant from an improved measurement of the $1s2p$ ${}^3P_{0,1,2}$ fine structure splittings is examined. Section 4 presents results for the 2P fine structure as well as the D1 and D2 isotope shifts. The latter allow the determination of the relative nuclear charge radii of the various lithium isotopes. Finally, conclusions regarding the status of the work are made.

2 Background

The energy of an atom or ion having a nucleus with charge Z can be expressed as

$$E = E_{\text{NR}} + Z^2\alpha^2 E_{\text{Rel}} + Z^4\alpha^3 E_{\text{QED}} + E_{\text{Hyp}} + E_{\text{Nuc}} . \quad (1)$$

Here, E_{NR} is the sum of the kinetic energy of the electrons and the Coulomb interaction of the electrons with each other and with the nucleus. For light atoms such as lithium, E_{NR} is about 10^4 times larger than the relativistic

correction term $Z^2\alpha^2 E_{\text{Rel}}$ where α is the fine structure constant. E_{QED} represents the QED corrections whose largest term is the Lamb shift while E_{HYP} is the hyperfine interaction. The finite size of the nucleus is described by [11]

$$E_{\text{Nuc}} = \frac{2\pi Z e^2 r_c^2}{3} \langle \Sigma_i \delta(\mathbf{r}_i) \rangle, \quad (2)$$

where r_c is the nuclear charge radius, e is the charge of the proton and the summation term equals the expectation value of the electron density at the nucleus where i is summed over all the electrons.

E_{Rel} , E_{QED} , E_{HYP} and E_{Nuc} can be evaluated if highly accurate wavefunctions corresponding to the non-relativistic energy E_{NR} are known. These wavefunctions have been found using a so-called Hylleraas basis set [4]. The required computational time increases rapidly with the electron number. Hence, Li^+ is much easier to model than neutral lithium. Precisely measured hyperfine and fine structure intervals provide a stringent test of the theoretical calculations. The computed wavefunctions can also be used in conjunction with measured isotope shifts to determine the nuclear charge radius r_c .

A common technique to determine a frequency interval is to use a narrow linewidth laser to excite the transitions to the two energy levels. One then measures the absolute laser frequency to high accuracy for each transition. In practice, two separate lasers are commonly used. Each laser is locked to one of the transitions and the frequency difference of the two lasers is found by focussing part of each laser beam onto a fast photodiode and measuring the beat frequency [12]. Large frequency intervals can be found by locking one laser beam to an iodine reference transition [13]. Recently, the femtosecond frequency comb has simplified absolute frequency measurements [14]. However, accurately locking a laser to a line center may not be possible for transitions to various hyperfine levels and/or different isotopes that overlap. In that case, it is essential to examine the entire spectrum.

3 $\text{Li}^+ (1s)^2 \ ^3\text{S} \rightarrow 1s2p \ ^3\text{P}$ Transition

Our group has developed a method to measure frequency intervals whereby an electro-optically modulated laser beam excites either an ion (LIBEO) or neutral atomic beam (LABEO) that is illustrated in Fig. 1 [15, 16]. It requires only a single laser having frequency ν that is passed through either an acousto or electro-optic modulator (EOM). The modulation frequency is conveniently specified by a frequency synthesizer to one part in 10^7 . The output laser beam then has frequencies ν , $\nu \pm n\nu_{\text{mod}}$ where n is an integer. Fluorescence, generated by the radiative decay of the excited state, is detected by a photomultiplier (PMT) as the laser is scanned across the resonance. Each transition therefore generates multiple peaks in the spectrum that are separated by the modulation frequency which in turn permits calibration of the

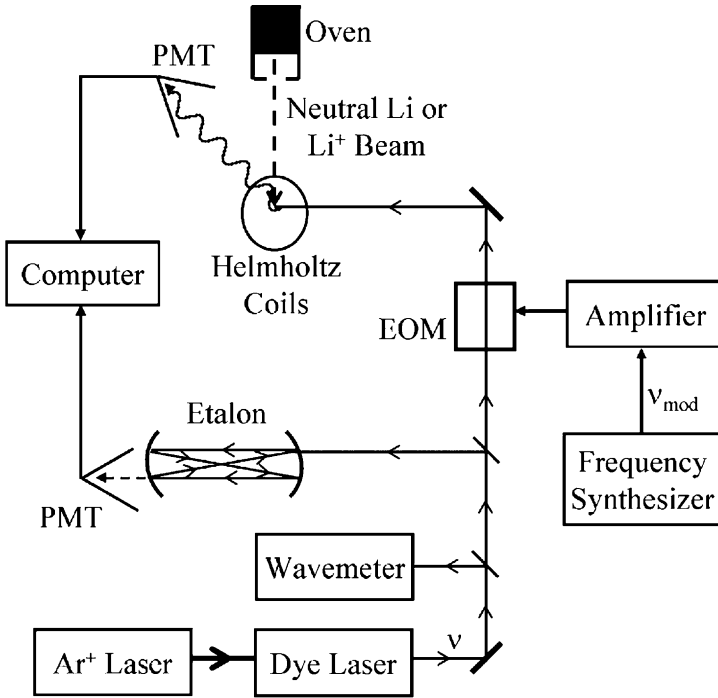


Fig. 1. Apparatus. See text for a description. For the case of a neutral atomic beam, Helmholtz coils surround the region where the laser and atomic beams intersect to cancel the Earth's magnetic field

frequency scan. The linearity of the laser scan is checked by monitoring the transmission of part of the laser beam through a Fabry–Perot etalon.

This technique was used to study the $\text{Li}^+ 1s2s \ ^3S_1 \rightarrow 1s2p \ ^3P_{0,1,2}$ transition [17]. The various hyperfine levels corresponding to this transition are shown in Fig. 2 for ${}^{6,7}\text{Li}^+$. The $\text{Li}^+ 1s2s \ ^3S_1$ state is 59 eV above the ground state and has a lifetime of 59 sec. It was produced by colliding an electron beam with a neutral Li beam. The ions were then passed through a Wien filter. A Faraday cup measured a Li^+ current of 250 nA. An argon ion laser pumped a ring dye laser that had a linewidth of 0.5 MHz. The dye laser beam was directed nearly collinearly to the ion beam. A wavemeter was used to coarsely tune the dye laser wavelength in order to locate the resonance. Fluorescence was detected by a liquid nitrogen cooled photomultiplier.

Figure 3 shows a sample signal obtained when a dye laser beam electro-optically modulated at 9.200000 GHz excited the transition. The peaks generated by the laser beam frequency shifted by ν_{mod} , have a smaller amplitude as most of the laser power was not frequency shifted. The fluorescent peaks have an asymmetric shape because of the non-Gaussian distribution of ion velocities. The etalon transmission peaks occurred nearly every 300 MHz

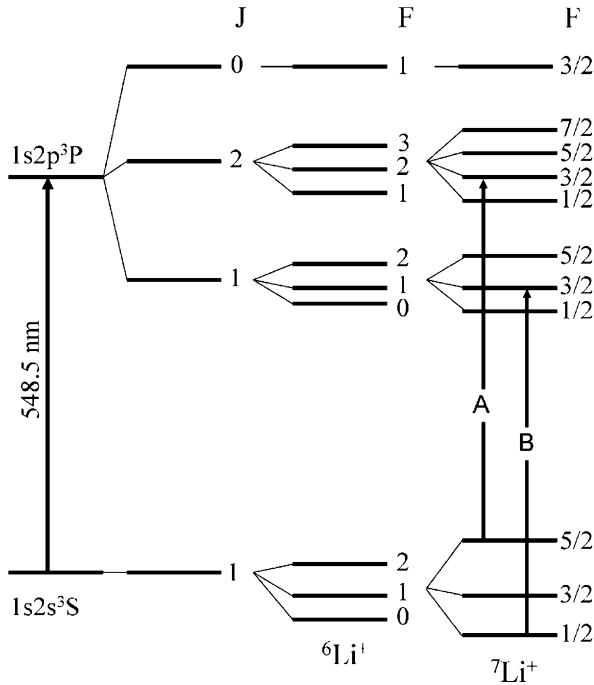


Fig. 2. Fine and hyperfine levels involved in the $\text{Li}^+ 1s2s^3S_1 \rightarrow 1s2p^3P_{0,1,2}$ transition. The vertical axis is not drawn to scale

corresponding to the free spectral range of the Fabry–Perot etalon. The free spectral range of the confocal etalon was monitored for each laser scan using the electro-optic modulation frequency to account for any change of the etalon length caused by temperature or pressure fluctuations. The laser scan was found to be linear to better than one part in 10^3 . The position of each fluorescence peak relative to the nearest Fabry–Perot peak was determined using a fifth-order polynomial to interpolate between the six nearest Fabry–Perot peak centers to account for any non-linearity of the laser frequency scan.

The measured hyperfine splittings are shown in Table 2. There is excellent agreement with the results for the $1s2s^3S_1$ hyperfine splittings obtained by a so-called laser microwave (LM) experiment [18]. The latter method used a laser to excite the ions before they passed through a microwave region. The laser excitation depleted one hyperfine level of the metastable $1s2s^3S_1$ state which was in turn repopulated if the microwaves were in resonance with a transition between the metastable state hyperfine levels. A second laser beam then probed the ions after the microwave region. The data from both experiments is in excellent agreement with the calculated values [12].

Our experiment determined the $1s2p^3P_{1,2}$ fine structure splitting by measuring the frequency difference between transitions A and B shown in Fig. 2 and using the appropriate hyperfine splittings. Table 3 shows our result agrees

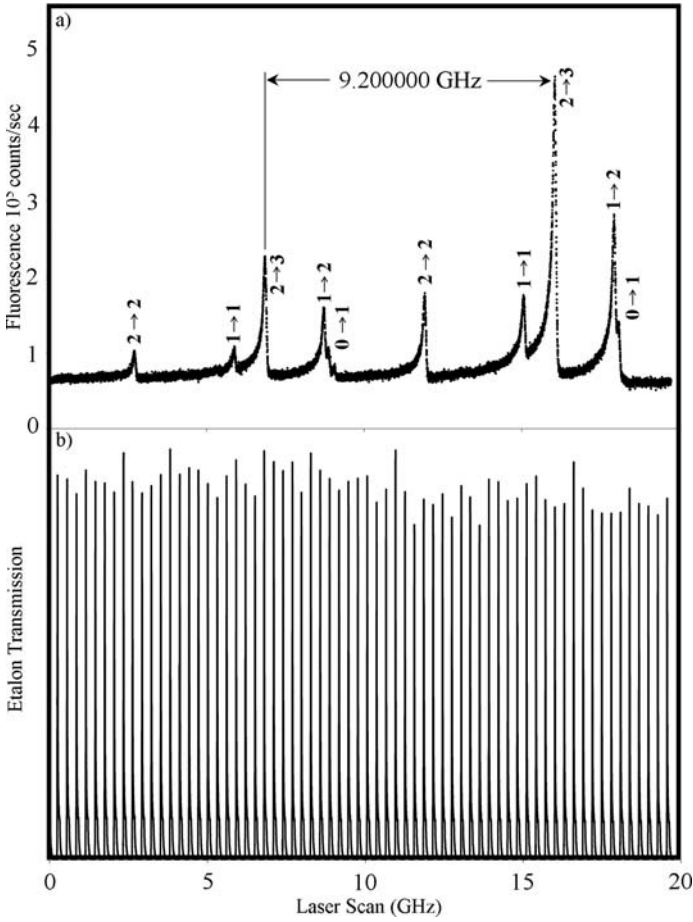


Fig. 3. (a) Fluorescent signal recorded as laser frequency modulated at 9.200000 GHz was scanned across Li^+ transitions labeled between hyperfine levels $F \rightarrow F'$. (b) Transmission of dye laser beam through etalon

very well with that found by Riis et al. [12] who precisely measured absolute laser frequencies for transitions to the various fine structures levels using a fast ion beam (LIB). Both of these experiments differ sharply with the result found by Rong et al. [13] who performed a laser heterodyne (LH) experiment using two frequency-locked dye lasers. One laser was locked to the Li^+ transition while the second laser was locked to an iodine transition. A portion of each laser beam was then focussed onto a fast photodiode that was connected to a frequency counter that measured the beat frequency. The results of Rong et al. also disagree with the Hylleraas variational calculation [12] for both the $1s2p\ ^3P_{1-2}$ and $^3P_{0-1}$ fine structure intervals.

Table 2. Hyperfine splittings of ${}^6,7\text{Li}^+$ $1s2s$ ${}^3\text{S}_1$ and $1s2p$ ${}^3\text{P}_{1,2}$ states

Isotope	State	Interval	LIBEO [17] (MHz)	MW [18] (MHz)	Theory [12] (MHz)
${}^6\text{Li}$	$1s2s$ ${}^3\text{S}_1$	2-1	6003.66 ± 0.51	6003.600 ± 0.050	6003.614 ± 0.024
		1-0	3001.83 ± 0.51	3001.780 ± 0.050	3001.765 ± 0.038
	$1s2p$ ${}^3\text{P}_1$	2-1	2888.98 ± 0.59		2888.327 ± 0.029
		1-0	1316.06 ± 0.59		1317.649 ± 0.046
${}^7\text{Li}$	$1s2p$ ${}^3\text{P}_2$	3-2	4127.16 ± 0.76		4127.882 ± 0.043
		2-1	2857.00 ± 0.72		2858.002 ± 0.060
	$1s2s$ ${}^3\text{S}_1$	5/2-3/2	19817.90 ± 0.73	19817.673 ± 0.040	19817.680 ± 0.025
${}^6\text{Li}$	$1s2p$ ${}^3\text{P}_1$	3/2-1/2	11891.22 ± 0.60	11890.018 ± 0.040	11890.013 ± 0.038
		5/2-3/2	9966.30 ± 0.69	9965.2 ± 0.6	9966.14 ± 0.13
	$1s2p$ ${}^3\text{P}_2$	3/2-1/2	4239.11 ± 0.54		4238.86 ± 0.20
${}^7\text{Li}$	$1s2p$ ${}^3\text{P}_2$	7/2-5/2	11774.04 ± 0.94	11775.8 ± 0.5	11773.05 ± 0.18
		5/2-3/2	9608.90 ± 0.49		9608.12 ± 0.15
		3/2-1/2	6204.52 ± 0.80	6203.6 ± 0.5	6203.27 ± 0.30

Table 3. Li^+ $1s2p$ ^3P fine structure splittings

Interval	Experiment (MHz)	Technique	Theory [19] (MHz)
$^3\text{P}_{1-2}$	62667.4 ± 2.0	LH [13]	62679.4 ± 0.5
	62678.41 ± 0.65	LIB [12]	
	62679.46 ± 0.98	LIBEO [17]	
$^3\text{P}_{0-1}$	155709.0 ± 2	LH [13]	155703.4 ± 1.5
	155704.27 ± 0.66	LIB [12]	

Our experimental uncertainty arises from the asymmetric lineshape of the fluorescent peaks. The full width at half maximum (FWHM) natural linewidth estimated using the 44 ns radiative lifetime of the $1s2p$ ^3P state is 3.7 MHz. Hence, an experiment that determined the line center to 0.1% as is done in other careful spectroscopic work has the potential to determine the $1s2p$ $^3\text{P}_{0-1}$ interval to one part in 4×10^8 . Such an experiment could be done using a single ion in a trap or a so-called optical double resonance experiment [8]. It would be interesting if theory could calculate the fine structure to a few kHz as this would then enable the determination of the fine structure constant. Work is underway to evaluate higher order QED effects [19]. It would be of interest to compare such a result for α with the recent value as determined by the electron $g-2$ experiment [20, 21].

4 Li D Lines

The lithium D lines have been studied by a number of different experimental techniques [8, 22]. The advantage of our method using an electro-optically modulated laser to excite an atomic beam is that one single experiment yields information about the hyperfine intervals of both the ground and excited states, the 2P fine structure splitting as well as the D1 and D2 isotope shifts [10]. A stringent test is to check that the result for the ground state hyperfine splitting agrees with the value obtained using the atomic beam magnetic resonance method which is known to one part in 10^9 [23]. Our measured $2\text{S}_{1/2}$ hyperfine splittings are within 40 kHz of the accepted values for both $^6,^7\text{Li}$.

Figure 4 illustrates the 12 lines comprising the D lines. The experiment used a neutral atomic beam of lithium that was orthogonally intersected by a laser beam to eliminate the first-order Doppler shift. Electro-optic modulators operating at 6.8 and 9.2 GHz were used to avoid overlapping peaks. Data were taken separately using ^6Li and natural lithium as shown in Figs. 5 and 6, respectively. Data were recorded by a fast digital storage oscilloscope such that each point corresponded to a frequency interval of 12 kHz. The fluorescence peak positions were found by fitting a sum of Lorentzian functions to the

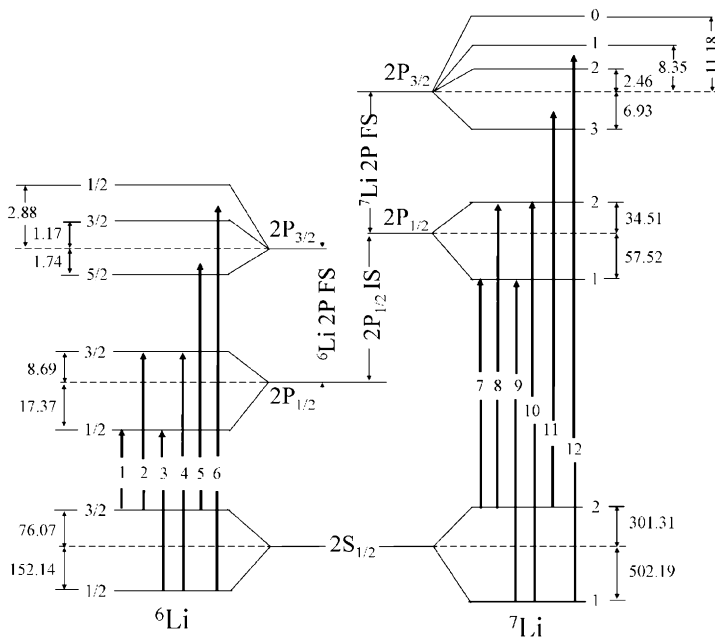


Fig. 4. Neutral lithium energy levels involved in D line transitions. The vertical energy axis is not drawn to scale. The positions of the various hyperfine levels are indicated relative to the center of gravity energy of a state $E_{\text{cg}} = \Sigma_F(2F + 1)E_F / \Sigma_F(2F + 1)$. All units are in MHz

spectrum using MATLAB 7.0. Each fluorescence peak position was found using the same procedure as described previously for the Li^+ work.

A complication arises in analyzing peaks 11 and 12 because the 5.8 MHz fullwidth at half maximum (FWHM) natural linewidth of the $2S$ – $2P$ transition is comparable to the ${}^7\text{Li}$ $2P_{3/2}$ hyperfine splittings as shown in Fig. 4. This causes the observed peaks to have an asymmetric shape as shown in Figs. 7 and 8. Peaks 11 and 12 were fit using three Lorentzian functions. The relative center frequencies of the three peaks were set equal to the $2P_{3/2}$ hyperfine intervals that were previously determined [24]. The red fitted curve appearing in each of Figs. 7 and 8 was found by varying the center frequency of the first peak appearing in the laser scan as well the amplitudes and widths of all three Lorentzian functions to obtain the optimum fit to the data.

For peak 11, the fluorescence is dominated by the radiative decay of the $F = 3$ hyperfine level of the $2P_{3/2}$ state. The linearly polarized laser beam preferentially excites more atoms from the $2S_{1/2}$ $F = 2$ level to the $F = 3$ level than to the $F = 2$ and $F = 1$ levels of the $2P_{3/2}$ state. Moreover, selection rules only allow the $2P_{3/2}$ $F = 3$ level to radiatively decay to the $F = 2$ ground state level from which it can be re-excited by the laser. In contrast,

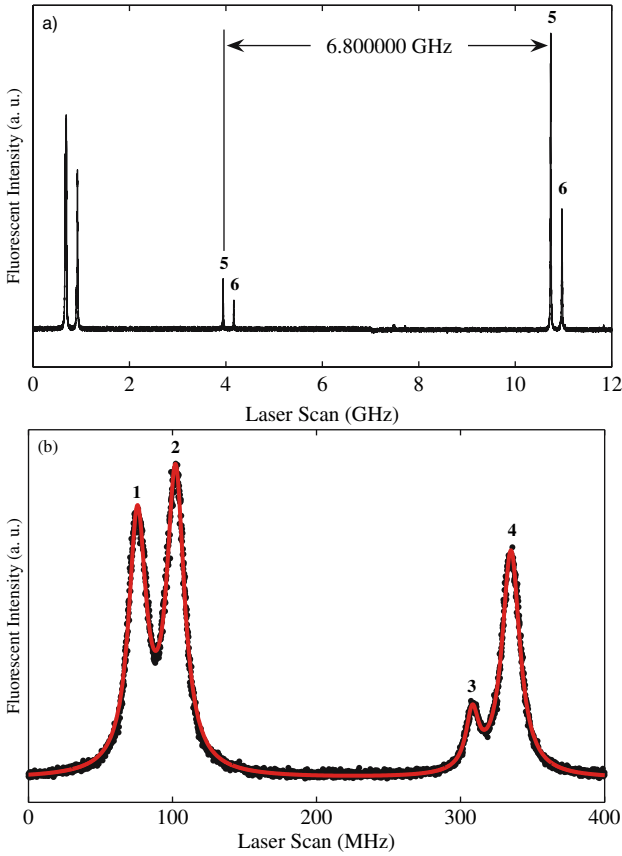


Fig. 5. Excitation of ${}^6\text{Li}$. (a) shows a scan where the laser-excited transitions 1–6 illustrated are in Fig. 4. The first four peaks are shown in (b) along with the red curve fitted to the data as is discussed in the text

the $2P_{3/2}$ $F = 1$ and 2 levels can also decay to the $F = 1$ ground state level which is not in resonance with the laser beam.

For peak 12, no one $2P_{3/2}$ hyperfine level has a dominant contribution to the fluorescent signal. This can be understood by modeling the effect of repeated excitation and radiative decay as an atom passes through the linearly polarized laser beam. An atom, initially entering the laser beam, was assumed to have all of its ground state hyperfine sublevels equally populated. A computer program modeled changes of the sublevel populations caused by the repeated laser excitation and radiative decay. The fluorescence contributions to peak 12 from the $2P_{3/2}$ $F = 0, 1$ and 2 hyperfine levels were predicted to be 28%, 36% and 36%, respectively. This compares very closely with the averaged fitted peak amplitude values of 29%, 34% and 37%.

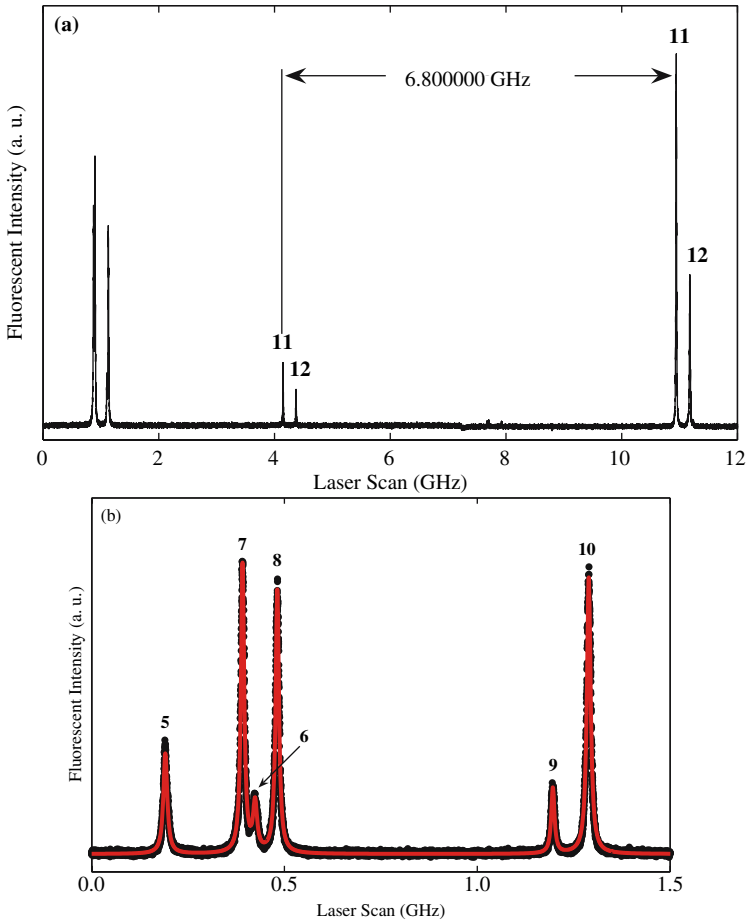


Fig. 6. Excitation of natural lithium. (a) shows a scan where transitions 5 and 6 of ^6Li and transitions 7–12 of ^7Li , as illustrated in Fig. 4, were excited. (b) shows the first six peaks where the gray curve is fitted to the data as is discussed in the text

The 2P fine structure splittings were found by measuring the frequency difference between the D2 and D1 transitions illustrated in Fig. 4. For ^7Li , the 2P fine structure splitting was found by determining the frequency separating peaks 11 and 12 from peaks 7 to 10 and using the appropriate hyperfine splittings. Our hyperfine splittings of the $2\text{P}_{1/2}$ state agreed with the most accurate measurements in the literature [22]. The 2P fine structure splittings using peaks 11 and 12 were found to be 10053.116 ± 0.079 and 10053.123 ± 0.086 MHz, respectively. These two values were averaged to give the result listed in Table 4.

The ^6Li 2P fine structure was found as follows. The repeated excitation of the $2\text{S}_{1/2}$ $F = 1/2$ level to the $2\text{P}_{3/2}$ $F = 1/2$ and $3/2$ levels and their

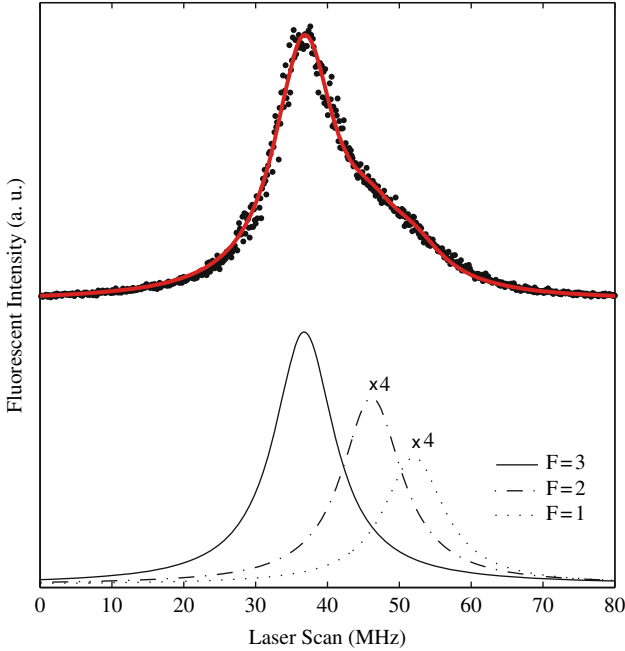


Fig. 7. Analysis of peak 11. The red fitted curve is comprised of three peaks to the $2P_{3/2}$ state hyperfine levels $F = 1, 2, 3$ as discussed in the text. The fluorescence contributions from the $2P_{3/2}$ $F = 1, 2$ hyperfine levels are magnified by a factor of 4

subsequent radiative decay do not affect the relative populations of the $2S_{1/2}$ $F = 1/2$ $m_F = \pm 1/2$ hyperfine sublevels. The fluorescence contributions from the $2P_{3/2}$ $F = 1/2$ and $3/2$ levels were calculated to be 47.8% and 52.2%, respectively. Hence, using the $2P_{3/2}$ hyperfine splitting, peak 6 is shifted 1.987 MHz above the $2P_{3/2}$ center of gravity as indicated in Fig. 4. The shift of peak 5 below the $2P_{3/2}$ center of gravity is found by measuring the frequency interval separating peaks 5 and 6 and subtracting the aforementioned shift of peak 6 and the hyperfine splitting of the ${}^6\text{Li}$ ground state which is known to very high accuracy [23]. The shifts of peaks 5 and 6 relative to the $2P_{3/2}$ center of gravity were comparable in magnitude but opposite in sign. Hence, the effect of these shifts was minimized by determining the ${}^6\text{Li}$ 2P fine structure by averaging the values obtained using peaks 5 and 6 relative to peaks 1–4 giving the result listed in Table 4.

The D1 isotope shift can be found by measuring the frequency intervals separating the ${}^6\text{Li}$ D1 transition peaks 1–4 from the corresponding ${}^7\text{Li}$ D1 peaks 7–10 and using the hyperfine splittings of the $2S_{1/2}$ and $2P_{1/2}$ states. Ideally, data would be taken using a lithium sample consisting of equal amounts of the two isotopes ${}^6,7\text{Li}$. This was not done as increasing the amount of ${}^6\text{Li}$ enhances the amplitude of peak 6 which overlaps with peaks 7 and 8.

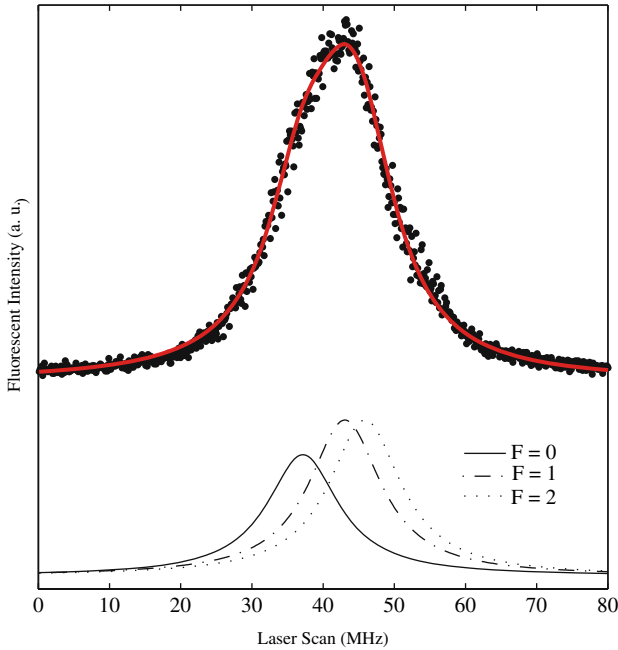


Fig. 8. Analysis of peak 12. The red fitted curve is comprised of three peaks to the $2P_{3/2}$ state hyperfine levels indicated as discussed in the text

The isotope shift was therefore found by first finding the separation of peaks 7–10 relative to peak 5 for scans obtained using natural lithium as shown in Fig. 6. The frequency interval separating peak 5 from peaks 1 to 4 was then found from laser scans using ^6Li as shown in Fig. 5.

Table 4. Neutral lithium 2P fine structure (FS) and D1 isotope shift

Quantity	Experiment (MHz)	Technique	Theory ^[25] (MHz)
^6Li 2P FS	10052.76 ± 0.22	LC ^[26]	10050.846 ± 0.012
	10051.62 ± 0.20	LAB ^[27]	
	10052.964 ± 0.050	LABEO ^[10]	
^7Li 2P FS	10053.24 ± 0.22	LC ^[26]	10051.214 ± 0.012
	10053.184 ± 0.058	ODR ^[28]	
	10053.4 ± 0.2	LAB ^[27]	
	10053.119 ± 0.058	LABEO ^[10]	
D1 Isotope Shift	10534.3 ± 0.3	LAB ^[29]	10534.12 ± 0.07
	10533.13 ± 0.15	LAB ^[27]	
	10533.160 ± 0.068	LAB ^[30]	
	10534.039 ± 0.070	LABEO ^[10]	

Table 4 lists the most accurate published 2P fine structure splittings. Our measurements agree very well with the results of level crossing spectroscopy (LC) [26] as well as an optical double resonance experiment (ODR) [28] for both ${}^6,{}^7\text{Li}$. There is only disagreement with the result for the ${}^6\text{Li}$ 2P fine structure interval as found by a laser atomic beam (LAB) measurement [27]. The latter experiment uses a Fabry–Perot etalon to monitor the change of the laser frequency during a scan. Unfortunately, it is difficult to maintain proper calibration of the etalon as its length can be affected by pressure and temperature fluctuations that have caused errors in previous work [31]. All of the experiments obtain values for the fine structure that are several MHz greater than the theoretical value [25]. The uncertainty listed for the theoretical value in Table 4 is the computational uncertainty. It does not consider the effect of QED correction terms proportional to α^4 times the Rydberg energy which for helium contribute several MHz to the fine structure splitting [32].

Table 4 also lists the most accurate published results for the D1 isotope shifts. Our value agrees with an earlier laser atomic beam measurement [29] and also is very close to the theoretical estimate [25] but disagrees with the two other measurements. Further insight into these isotope shifts can be obtained by determining the nuclear charge radius using [4]

$$\Delta r_c^2 = r_c^2({}^6\text{Li}) - r_c^2({}^7\text{Li}) = (\delta\nu_{jk} - \delta E_{jk})/C_{jk}. \quad (3)$$

Here, $\delta\nu_{jk}$ is the measured isotope shift for the transition between states j and k , δE_{jk} is the calculated isotope shift difference for the two states excluding the nuclear size correction E_{Nuc} and C_{jk} is proportional to the square of the electron wavefunction at the nucleus.

Table 5 lists the results for a number of experiments that studied various transitions in Li^+ and neutral Li. The data listed for the ${}^6\text{Li}$ nuclear charge radius r_c were found using the measured value for ${}^7\text{Li}$ of 2.39 ± 0.03 fm obtained in an electron scattering experiment [33]. Our result for the D2 isotope shift listed in Table 5 was obtained by adding the ${}^7\text{Li}$ 2P fine structure splitting to the D1 isotope shift and subtracting the ${}^6\text{Li}$ 2P fine structure splitting. An important test of each experiment is to check whether the results obtained for different transitions give consistent results. All three results for the Li^+ transitions made by Riis et al. [12] agree well with each other as do our results [10]. The two results for Δr_c^2 found by Scherf et al. [27] disagree by nearly 10 times the stated uncertainty. The remaining isotope shifts found for the Li $2\ 2S_{1/2} \rightarrow 3\ 2S_{1/2}$ transition and one value for the D1 isotope shift were all found by the same group. For the two photon $2S_{1/2} \rightarrow 3S_{1/2}$ transition, the atoms passed through an optical cavity that enhanced the power of the dye laser tuned at 610 nm. The uncertainty of their first measurement [30] apparently did not adequately take into account the ac Stark shift which was estimated in their later experiment to increase the uncertainty by 110 kHz [6, 7]. Both isotope shifts of their initial experiment yield results for Δr_c^2 which are lower than the results of our work, Riis et al. and an electron scattering experiment [33] as well as the results predicted by the nuclear theory [34].

Table 5. Determination of ${}^6\text{Li}$ nuclear charge radius. The measured isotope shifts are given by $\delta\nu_{jk}$, while δE_{jk} and C_{jk} were obtained by a Hylleraas variational calculation given in [4]. The first and second error bars in the columns for Δr_c^2 and r_c (${}^6\text{Li}$) are the total and experimental (bracketed) uncertainties

Transition	ν_{jk} (MHz)	δE_{jk} (MHz)	C_{jk}	Δr_c^2 (fm ²)	$r_c({}^6\text{Li})$ (fm)
$\text{Li}^+ (2\ ^3\text{S}_1 - 2\ ^3\text{P}_0)$	34747.73 ± 0.55 [12]	34740.17 ± 0.03	9.705	$0.779 \pm 0.057(0.057)$	$2.548 \pm 0.031(0.011)$
$\text{Li}^+ (2\ ^3\text{S}_1 - 2\ ^3\text{P}_1)$	34747.46 ± 0.67 [12]	34739.87 ± 0.03		$0.782 \pm 0.069(0.069)$	$2.548 \pm 0.032(0.014)$
$\text{Li}^+ (2\ ^3\text{S}_1 - 2\ ^3\text{P}_2)$	34748.91 ± 0.62 [12]	34742.71 ± 0.03		$0.639 \pm 0.064(0.064)$	$2.520 \pm 0.031(0.031)$
$\text{Li} (2\ ^2\text{S}_{1/2} - 3\ ^2\text{S}_{1/2})$	11453.95 ± 0.13 [7]	11453.01 ± 0.06	1.566	$0.600 \pm 0.091(0.083)$	$2.512 \pm 0.033(0.018)$
	11453.734 ± 0.030 [30]			$0.462 \pm 0.042(0.019)$	$2.485 \pm 0.030(0.009)$
$\text{Li} (2\ ^2\text{S}_{1/2} - 2\ ^2\text{P}_{1/2})$	10533.160 ± 0.068 [30]	10532.17 ± 0.07	2.457	$0.403 \pm 0.040(0.028)$	$2.473 \pm 0.030(0.008)$
	10533.13 ± 0.15 [27]			$0.391 \pm 0.067(0.061)$	$2.470 \pm 0.032(0.014)$
	10534.039 ± 0.070 [10]			$0.761 \pm 0.040(0.028)$	$2.544 \pm 0.030(0.006)$
$\text{Li} (2\ ^2\text{S}_{1/2} - 2\ ^2\text{P}_{3/2})$	10534.93 ± 0.15 [27]	10532.57 ± 0.07	2.457	$0.961 \pm 0.067(0.061)$	$2.592 \pm 0.032(0.014)$
	10534.194 ± 0.104 [10]			$0.661 \pm 0.050(0.042)$	$2.524 \pm 0.030(0.009)$
e-nuclear scattering [33]				0.842	2.56 ± 0.05
Nuclear theory [34]				0.740	2.54 ± 0.01

The value of Δr_c^2 obtained by averaging the results of the Riis experiment [12] that studied the $\text{Li}^+ 2^3\text{S}_1 \rightarrow 3^3\text{P}_{0,1,2}$ transitions and the Ewald experiment [6] that examined the $\text{Li } 2^3\text{S}_{1/2} \rightarrow 3^2\text{S}_{1/2}$ transition is 0.700 fm^2 . This is in excellent agreement with the average value of our two measured values of 0.704 fm^2 . However, the uncertainty of our results is due about equally to experimental and theoretical uncertainties whereas it is dominated by experimental effects in the other experiments. The uncertainties listed in Table 5 for $r_c(^6\text{Li})$ are dominated by the accuracy of $r_c(^7\text{Li})$. The average value of the ^6Li charge radius obtained by averaging the results of the experiments by Riis et al., Ewald et al. and our work is 2.53 fm which is listed in Table 6.

The charge radii of the radioactive lithium isotopes were found using the accelerator at the GSI facility in Darmstadt, Germany [6, 7]. The $^8,^9\text{Li}$ nuclei were generated using a 11.4 MeV/u beam of ^{12}C incident on a tungsten target. The reaction products were then ionized and passed through a magnetic mass separator before being stopped by a graphite foil. The graphite was heated to $1800 - 1900^\circ\text{C}$ using a 4 W CO_2 laser to enable the lithium to diffuse out of the foil. The lithium atoms were then laser ionized and detected after passing through a quadrupole mass spectrometer. $^8,^9\text{Li}$ beams of 2×10^5 and 1×10^5 atoms/sec were obtained. The atoms were laser ionized when they passed through an optical cavity. For the case of the two-photon $2\text{S}_{1/2} \rightarrow 3\text{S}_{1/2}$ transition, a dye laser operating at 610 nm was tuned to maximize the production of Li^+ . Part of this laser was focussed onto a fast photodiode along with a diode laser locked to an iodine reference line. The isotope shift was then found by measuring the beat frequency.

Table 6. Lithium charge and mass radii

Isotope	Δr_c^2 (fm) ²	Charge Radius (fm)	Mass Radius [1] (fm)
^6Li	0.636 ± 0.051	2.53 ± 0.03	2.35 ± 0.03
^7Li		2.39 ± 0.03 [33]	2.35 ± 0.03
^8Li	-0.43 ± 0.11	2.30 ± 0.04 [7]	2.38 ± 0.02
^9Li	-0.72 ± 0.14	2.24 ± 0.04 [7]	2.32 ± 0.02
^{11}Li			3.10 ± 0.17

Table 6 lists values for the charge and mass radii for the lithium isotopes. It is not surprising that the mass and charge radii differ as the quark constituents of the nuclei do not have equal charge. The mass radii of the radioactive lithium isotopes was determined by scattering an accelerator-generated beam of these nuclei from a target nucleus and measuring the interaction cross-section given by [1]:

$$\sigma_{\text{I}} = \pi[R_{\text{I}}^2 + R_{\text{T}}^2]. \quad (4)$$

Various targets composed of Be, C and Al were used in order to separately determine the radii of the target R_T and incoming nuclei R_I . The root mean square mass radius of the nucleon distribution was then deduced from R_I using a variety of nuclear models. Values for the mass radii found using the so-called Gaussian and harmonic oscillator nucleon distributions differed by less than the experimental uncertainties [35, 36]. The mass radius remains nearly constant for ${}^6,7,8,9\text{Li}$ while a small decrease is evident for the charge radius. It will be interesting to compare the mass and charge radii of ${}^{11}\text{Li}$ to determine whether the charge radius is also significantly perturbed by the halo neutrons as is the mass radius [37].

5 Conclusions

Important advances in both theory and experiment have been made in recent years in both Li^+ and neutral lithium. For the case of Li^+ it will be interesting to improve both the theory and measurement to reduce the uncertainty of the $1s2p\ 2\ ^3P$ fine and hyperfine structure splittings to 1 kHz. Future experiments with this level of accuracy would not only test QED but also enable the fine structure constant α to be determined with an accuracy competitive with other techniques that yield conflicting results [20, 21]. For the case of the neutral lithium D lines, the 2P fine structure as measured using a variety of techniques by a number of experimental groups, all agree. The theoretical result is significantly lower than the measured value. It is interesting that the variational calculations yield a D1 isotope shift that agrees much better with the experimental value than is the case with the fine structure. The reason is that various QED terms are mass independent and cancel in the calculation of an isotope shift but cannot be neglected when evaluating the fine structure [4]. Hence, further theoretical work to improve the estimate of the lithium 2P fine structure is needed.

Optically measured isotope shifts have permitted the nuclear charge radii of the various lithium isotopes to be found with an experimental uncertainty of ≤ 0.02 fm. It is remarkable that these experiments yield more accurate results than is obtained using electron scattering. Ironically, one now has a better understanding of how an electron in the lithium atom interacts with the nucleus than of how a macroscopic electron beam scatters from a Li nucleus. This underscores the incredible advances made in both atomic theory and experiment and motivates future work in both Li^+ and neutral lithium.

Acknowledgment

The authors would like to thank the Natural Science and Engineering Research Council of Canada for financial support.

References

1. I. Tanihata, T. Kobayashi, O. Yamakawa, S. Shimoura, K. Ekuni, K. Sugimoto, N. Takahashi, T. Shimoda and H. Sato: *Phys. Lett. B* **206**, 592 (1988). [111](#), [126](#)
2. Handbook of Chemistry and Physics 69th Edition, edited by R. C. Weast, (CRC Press, Boca Raton, 1988). [112](#)
3. F. Schmitt, A. Dax, R. Kirchner, H. J. Kluge, T. Kühl, I. Tanihata, M. Wakasugi, H. Wang and C. Zimmermann: *Hyp. Inter.* **127**, 111 (2000). [112](#)
4. G. W. F. Drake, W. Nörtershäuser and Z. C. Yan: *Can. J. Phys.* **83**, 311 (2005). [111](#), [113](#), [124](#), [125](#), [127](#)
5. G. W. F. Drake: *Atomic, Molecular and Optical Physics Handbook*, edited by G. W. F. Drake (AIP, New York, 1996). [112](#)
6. G. Ewald, W. Nörtershäuser, A. Dax, S. Götte, R. Kirchner, H. J. Kluge, T. Kühl, R. Sanchez, A. Wojtaszek, B. A. Bushaw, G. W. F. Drake, Z. C. Yan and C. Zimmerman: *Phys. Rev. Lett.* **93**, 113002 (2004). [112](#), [124](#), [126](#)
7. G. Ewald, W. Nörtershäuser, A. Dax, S. Götte, R. Kirchner, H. J. Kluge, T. Kühl, R. Sanchez, A. Wojtaszek, B. A. Bushaw, G. W. F. Drake, Z. C. Yan and C. Zimmerman: *Phys. Rev. Lett.* **94**, 039901 (2005). [112](#), [124](#), [125](#), [126](#)
8. W. A. van Wijngaarden: *Can. J. Phys.* **83**, 327 (2005). [112](#), [118](#)
9. J. J. Clarke and W. A. van Wijngaarden: *Recent Res. Dev. Phys.* **3**, 347 (2002). [112](#)
10. G. A. Noble, B. E. Schultz, H. Ming and W. A. van Wijngaarden: *Phys. Rev. A* **74**, 012502 (2006). [112](#), [118](#), [123](#), [124](#), [125](#)
11. J. D. Morgan II and J. S. Cohen: *Atomic, Molecular and Optical Physics Handbook*, edited by G. W. F. Drake (AIP, New York, 1996). [113](#)
12. E. Riis, A. G. Sinclair, O. Poulsen, G. W. f. Drake, W. R. C. Rowley and A. P. Levick: *Phys. Rev. A* **49**, 207 (1994). [113](#), [115](#), [116](#), [117](#), [118](#), [124](#), [125](#), [126](#)
13. H. Rong, S. Grafström, J. Kowalski, G. zu Putlitz, W. Jastrzebski and R. Neumann: *Z. Phys. D* **25**, 337 (1993). [113](#), [116](#), [118](#)
14. T. Udem, J. Reichert, R. Holzwarth and T. W. Hänsch: *Opt. Lett.* **24**, 881 (1999). [113](#)
15. W. A. van Wijngaarden: *Adv., At., Mol., Opt. Phys.* **36**, 141 (1996). [113](#)
16. W. A. van Wijngaarden: *Proc. of Int. Conf. on Atomic Phys.* **16**, 305 (1999). [113](#)
17. J. J. Clarke and W. A. van Wijngaarden: *Phys. Rev. A* **67**, 012506 (2003). [114](#), [117](#), [118](#)
18. J. Kowalski, R. Neumann, S. Noelte, K. Scheffzek, H. Suhr and G. zu Putlitz: *Hyp. Int.* **15/16**, 15 (1983). [115](#), [117](#)
19. T. Zhang, Z. C. Yan and G. W. F. Drake: *Phys. Rev. Lett.* **77**, 1715 (1996). [118](#)
20. G. Gabrielse, D. Hanneke, T. Kinoshita, M. Nio and B. Odom: *Phys. Rev. Lett.* **97**, 030802 (2006). [118](#), [127](#)
21. G. W. F. Drake: *Can. J. Phys.* **80**, 1195 (2002). [118](#), [127](#)
22. J. Walls, R. Ashby, J. J. Clarke, B. Lu and W. A. van Wijngaarden: *Eur. Phys. J. D* **22**, 159 (2003). [118](#), [121](#)
23. A. Beckmann, K. D. Böklen and D. Elke: *Z. Phys.* **270**, 173 (1974). [118](#), [122](#)
24. E. Arimondo, M. Inguscio and P. Violino: *Rev. Mod. Phys.* **49**, 31 (1977). [119](#)
25. Z. C. Yan and G. W. F. Drake: *Phys. Rev. A* **66**, 042504 (2002). [123](#), [124](#)
26. K. C. Brog, T. G. Eck and H. Wieder: *Phys. Rev.* **153**, 91 (1967). [123](#), [124](#)
27. W. Scherf, O. Khait, H. Jäger and L. Windholz: *Z. Phys. D: At. and Mol. Clusters* **36**, 31 (1996). [123](#), [124](#), [125](#)
28. H. Orth, H. Ackermann and E. W. Otten: *Z. Phys. A* **273**, 221 (1975). [123](#), [124](#)

29. L. Windholz, H. Jäger, M. Musso and G. Zerza: *Z. Phys. D: At., Mol. Clusters* **16**, 41 (1990). [123](#), [124](#)
30. B. A. Bushaw, W. Nörtershäuser, G. Ewald, A. Dax and G. W. F. Drake: *Phys. Rev. Lett.* **91**, 043004 (2003). [123](#), [124](#), [125](#)
31. C. Umfer, L. Windholz and M. Musso: *Z. Phys. D: At., Mol. Clusters* **25**, 23 (1992). [124](#)
32. G. W. F. Drake, I. B. Khriplovich, A. I. Milstein and A. S. Yelkhovsky: *Phys. Rev. A* **48**, R15 (1993). [124](#)
33. C. W. de Jager, H. de Vries and C. de Vries: *At. Nucl. Data Tables* **36**, 495 (1987). [124](#), [125](#), [126](#)
34. S. C. Pieper, V. R. Pandharipande, R. B. Wiringa and J. Carlson: *Phys. Rev. C* **64**, 014001 (2001). [124](#), [125](#)
35. I. Tanihata, H. Hamagaki, O. Hashimoto, Y. Shida, N. Yoshikawa, K. Sugimoto, O. Yamakawa, T. Kobayashi and N. Takahashi: *Phys. Rev. Lett.* **55**, 2676 (1985). [127](#)
36. R. B. Elton: *Nuclear Sizes* (Oxford Univ. Press, Oxford, 1961). [127](#)
37. W. Nörtershäuser, A. Dax, G. Ewald, I. Katayama, R. Kirchner, H. J. Kluge, T. Kühl, R. Sanchez, I. Tanihata, M. Tomaselli, H. Wang and C. Zimmermann: *Nucl. Instr. and Methods in Phys. Res. B* **204** 644 (2003). [127](#)

Halo Nuclei in Laser Light

G. W. F. Drake¹, Z.-T. Lu², W. Nörtershäuser³, and Z.-C. Yan⁴

¹ Department of Physics, University of Windsor, Windsor, Ontario N9B 3P4
Canada

GDrake@uwindsor.ca

² Physics Division, Argonne National Laboratory, Argonne, Illinois 60439
lu@anl.gov

³ Gesellschaft für Schwerionenforschung, D-64291 Darmstadt, Germany
W.Noertershaeuser@gsi.de

⁴ Department of Physics, University of New Brunswick, Fredericton, New
Brunswick E3B 5A3 Canada
zyan@unb.ca

1 Introduction

The purpose of this paper is to summarize recent progress in the use of high-precision atomic theory and spectroscopy to develop a new tool to probe the properties of the nucleus. Of particular interest will be the so-called halo nuclei first discovered more than 20 years ago by I. Tanihata et al. [1, 2]. They observed that some isotopes of the lightest elements close to the neutron dripline have nuclear matter radii that by far exceed those of their neighbors. At that time, it was possible to extract the matter (mass) radii from interaction cross-section measurements, with the results shown in Fig. 1. It soon became evident that these large radii reflect the presence of weakly bound neutrons whose wavefunctions extend far into the classically forbidden region far from the more tightly bound nuclear core. Hansen and Jonson [3] first used the term “halo nucleus” to describe such systems. As reviewed by Tanihata [4], the halo structure reveals itself most clearly as a difference between the nuclear mass radius and the nuclear charge radius. Since the neutrons are massive but uncharged, one expects the mass radius to be larger than the charge radius. Moreover, the change in the charge radius relative to the corresponding isotope without the halo neutrons provides a sensitive probe of the core structure, and the effective low-energy nucleon–nucleon interaction potential.

This new form of nuclear matter has been extensively investigated using various techniques from nuclear and atomic physics (for review see, e.g., [4]) and many properties were determined. However, a nuclear-model-free direct measurement of the nuclear charge radius was not possible until recently. Based on new and very specialized techniques two groups succeeded

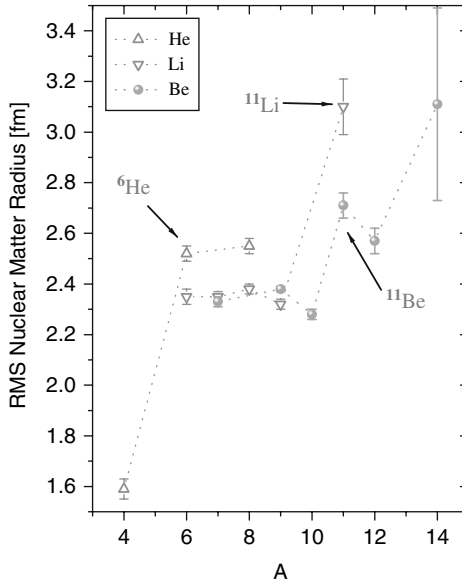


Fig. 1. Comparison of nuclear matter radii of helium, lithium and beryllium isotopes from Tanihata et al. [1, 2, 5]

in measuring for the first time isotope shifts of radioactive very light nuclei with a precision that is sufficient to extract nuclear charge radii. At Argonne National Lab the charge radius of ${}^6\text{He}$ was obtained from laser spectroscopy on helium atoms in a magneto-optical trap, while a collaboration from GSI Darmstadt and the University of Tübingen developed a method for high-resolution resonance ionization spectroscopy and measured the charge radii of ${}^{8,9}\text{Li}$ at GSI [6] and of ${}^{11}\text{Li}$ [7] at the ISAC mass separator at TRIUMF. To determine the charge radius from the isotope shift it is necessary to calculate the mass-dependent part of the isotope shift with high accuracy. While this was possible for one- and two-electron systems already since the 1980s, as first suggested by Drake for helium [8], for lithium-like three-electron systems the breakthrough came in 2000 when Yan and Drake succeeded in calculating the mass effect in transitions of neutral lithium with a relative accuracy of better than 5×10^{-6} [9]. These calculations were the foundations of the lithium experiment and similar calculations are in progress for the singly charged beryllium ion. ${}^{11}\text{Be}$ is the archetype of a one-neutron halo and has been the subject of many investigations [4, 5 W. Geithner et al., PRL 83, 3792 (1999)]. After the charge radii determinations of borromean two-neutron halo systems of first (${}^{11}\text{Li}$) and second kind (${}^6\text{He}$), this would be the first measurement of a nuclear-model-independent charge radius of a one-neutron halo nucleus. Hence, it should provide information that is complementary to that obtained in the other cases.

There is now a large body of related work where the isotope shift method has been used to measure other known nuclear radii as reviewed by Drake et al. [10]. The good agreement obtained in these cases gives confidence that the isotope shift method can indeed be used to determine the size of light nuclei. There are also other high-precision measurements for absolute transition frequencies, as reviewed by Morton et al. [11] and Drake and Martin [12]. The comparison between theory and experiment provides significant tests of the relativistic and QED corrections that are also needed for the analysis of isotope shift measurements.

The remainder of this chapter is organized as follows. The next two sections give a brief overview of the theory needed to calculate the atomic isotope shift to sufficient accuracy so that a value for the nuclear charge radius can be extracted from the measured isotope shift. The following two sections then describe the experiments that have been performed for the cases of ${}^6\text{He}$ and ${}^{11}\text{Li}$, including a brief discussion of the significance of the results for theories of nuclear structure. This is followed by a concluding section that discusses prospects for future work in this area, including the determination of nuclear charge radii directly from absolute transition frequency measurements.

2 Theory

Table 1 summarizes the various contributions to the energy, expressed as a double expansion in powers of $\alpha \simeq 1/137.036$ and the electron reduced mass ratio $\mu/M \simeq 10^{-4}$. Since all the lower-order terms can now be calculated to very high precision, including the QED terms of order $\alpha^3 \text{Ry}$, the dominant source of uncertainty comes from the QED corrections of order $\alpha^4 \text{Ry}$ or higher. For the isotope shift, the QED terms independent of μ/M cancel out, and so it is only the radiative recoil terms of order $\alpha^4 \mu/M \simeq$

Table 1. Contributions to the energy and their orders of magnitude in terms of Z , $\mu/M \simeq 10^{-4}$, and $\alpha^2 = 0.532\,513\,5450 \times 10^{-4}$

Contribution	Magnitude
Nonrelativistic energy	Z^2
Mass polarization	$Z^2 \mu/M$
Second-order mass polarization	$Z^2 (\mu/M)^2$
Relativistic corrections	$Z^4 \alpha^2$
Relativistic recoil	$Z^4 \alpha^2 \mu/M$
Anomalous magnetic moment	$Z^4 \alpha^3$
Hyperfine structure	$Z^3 g_I \mu_0^2$
Lamb shift	$Z^4 \alpha^3 \ln \alpha + \dots$
Radiative recoil	$Z^4 \alpha^3 (\ln \alpha) \mu/M$
Finite nuclear size	$Z^4 \langle \bar{r}_c / a_0 \rangle^2$

10^{-12}Ry (~ 10 kHz) that contribute to the uncertainty. Since this is much less than the finite nuclear size correction of about 1 MHz, the comparison between theory and experiment clearly provides a means to determine the nuclear size.

2.1 Solution to the Nonrelativistic Schrödinger Equation for Helium

The starting point for the calculation is to find accurate solutions to the Schrödinger equation for helium. Considering first the case of infinite nuclear mass, the equation in atomic units is given by

$$\left(-\frac{1}{2}\nabla_1^2 - \frac{1}{2}\nabla_2^2 - \frac{Z}{r_1} - \frac{Z}{r_2} + \frac{1}{r_{12}}\right)\Psi(\mathbf{r}_1, \mathbf{r}_2) = E\Psi(\mathbf{r}_1, \mathbf{r}_2). \quad (1)$$

The usual methods of theoretical atomic physics, such as the Hartree–Fock approximation or configuration interaction methods, are not capable of yielding results of spectroscopic accuracy. For this reason, specialized methods have been developed. As long ago as 1929, Hylleraas suggested expanding the wavefunction in an explicitly correlated variational basis set of the form

$$\Psi(\mathbf{r}_1, \mathbf{r}_2) = \sum_{i,j,k} a_{ijk} r_1^i r_2^j r_{12}^k e^{-\alpha r_1 - \beta r_2} \mathcal{Y}_{l_1 l_2 L}^M(\hat{\mathbf{r}}_1, \hat{\mathbf{r}}_2), \quad (2)$$

where $r_{12} = |\mathbf{r}_1 - \mathbf{r}_2|$ is the interelectronic separation, and $\mathcal{Y}_{l_1 l_2 L}^M$ is a vector-coupled product of spherical harmonics to form a state of total angular momentum L and component M .

The coefficients a_{ijk} are linear variational parameters, and α and β are nonlinear variational coefficients that set the distance scale for the wavefunction. The usual strategy is to include all powers such that $i + j + k \leq \Omega$ (a so-called Pekeris shell), where Ω is an integer. In addition, the nonlinear parameters α and β are separately optimized for each set of angular momentum terms and, as discussed in [8, 13, 14], it is desirable further to “double” the basis set so that each set of powers $\{i, j, k\}$ is included two (or more [15]) times with different values of α and β . Finally, a complete optimization is performed with respect to variations in the α s and β s so as to minimize the energy. For sufficiently large basis sets, the doubling is very important because it helps to preserve the numerical stability of the wavefunction, gives improved accuracy for a given total size of basis set, and avoids the disastrous loss of accuracy that normally sets in for variational calculations involving the higher-lying Rydberg states [8, 13, 14].

For high-precision calculations, and especially for the isotope shift, it is necessary to also include the motion of the nucleus in the center-of-mass (CM) frame. A transformation to CM plus relative coordinates yields the additional $-(\mu/M)\nabla_1 \cdot \nabla_2$ mass polarization term in the modified Hamiltonian:

$$H = -\frac{1}{2}\nabla_1^2 - \frac{1}{2}\nabla_2^2 - \frac{Z}{r_1} - \frac{Z}{r_2} + \frac{1}{r_{12}} - \frac{\mu}{M}\nabla_1 \cdot \nabla_2 \quad (3)$$

in reduced mass atomic units e^2/a_μ , where $a_\mu = (m/\mu)a_0$ is the reduced mass Bohr radius, and $\mu = mM/(m + M)$ is the electron reduced mass, M is the nuclear mass, and $a_0 = \hbar^2/me^2$ is the Bohr radius. The mass polarization term can be treated by including it explicitly in the Hamiltonian, and the coefficient of the second-order term extracted by differencing [13, 14].

As an example, Table 2 shows a convergence study for the very well studied case of the ground state of helium [15]. The quantity R in the last column is the ratio of successive differences between the energies. A constant or slowly changing value of R indicates smooth convergence and allows a reliable extrapolation to $\Omega \rightarrow \infty$. The results clearly indicate that convergence to 20 or more figures can be readily obtained, using conventional quadruple precision (32 decimal digit) arithmetic in FORTRAN. The very large calculation by Schwartz [17], using 104-digit arithmetic, provides a benchmark for comparison.

2.2 Variational Basis Sets for Lithium

The same variational techniques can be applied to lithium and other three-electron atomic systems. In this case, the terms in the Hylleraas correlated basis set have the form

Table 2. Convergence study for the ground state of helium (infinite nuclear mass case) [15]. N is the number of terms in the “triple” basis set

Ω	N	$E(\Omega)$	$R(\Omega)$
8	269	-2.903 724 377 029 560 058 400	
9	347	-2.903 724 377 033 543 320 480	
10	443	-2.903 724 377 034 047 783 838	7.90
11	549	-2.903 724 377 034 104 634 696	8.87
12	676	-2.903 724 377 034 116 928 328	4.62
13	814	-2.903 724 377 034 119 224 401	5.35
14	976	-2.903 724 377 034 119 539 797	7.28
15	1150	-2.903 724 377 034 119 585 888	6.84
16	1351	-2.903 724 377 034 119 596 137	4.50
17	1565	-2.903 724 377 034 119 597 856	5.96
18	1809	-2.903 724 377 034 119 598 206	4.90
19	2067	-2.903 724 377 034 119 598 286	4.44
20	2358	-2.903 724 377 034 119 598 305	4.02
Extrapolation	∞	-2.903 724 377 034 119 598 311(1)	
Korobov [16]	5200	-2.903 724 377 034 119 598 311 158 7	
Korobov extrap.	∞	-2.903 724 377 034 119 598 311 159 4(4)	
Schwartz [17]	10259	-2.903 724 377 034 119 598 311 159 245 194 404 4400	
Schwartz extrap.	∞	-2.903 724 377 034 119 598 311 159 245 194 404 446	
Goldman [18]	8066	-2.903 724 377 034 119 593 82	
Bürgers et al. [19]	24 497	-2.903 724 377 034 119 589(5)	
Baker et al. [20]	476	-2.903 724 377 034 118 4	

$$r_1^{j_1} r_2^{j_2} r_3^{j_3} r_{12}^{j_{12}} r_{23}^{j_{23}} r_{31}^{j_{31}} e^{-\alpha r_1 - \beta r_2 - \gamma r_3} \mathcal{Y}_{(\ell_1 \ell_2) \ell_{12}, \ell_3}^{LM}(\mathbf{r}_1, \mathbf{r}_2, \mathbf{r}_3) \chi_1, \quad (4)$$

where $\mathcal{Y}_{(l_1 l_2) l_{12}, l_3}^{LM}$ is again a vector-coupled product of spherical harmonics, and χ_1 is a spin function with spin angular momentum 1/2. As for helium, the usual strategy is to include all terms from (4) such that

$$j_1 + j_2 + j_3 + j_{12} + j_{23} + j_{31} \leq \Omega \quad (5)$$

and study the eigenvalue convergence as Ω is progressively increased. The lithium problem is much more difficult than helium both because the integrals over fully correlated wavefunctions are more difficult, and because the basis set grows much more rapidly with increasing Ω . Nevertheless, there has been important progress in recent years [9, 21, 22, 23, 24], and results of spectroscopic accuracy can be obtained for the low-lying states.

2.3 Relativistic Corrections

This section briefly summarizes the lowest-order relativistic corrections of order $\alpha^2 \text{Ry}$ and the relativistic recoil corrections of order $\alpha^2 \mu/M \text{Ry}$. The well-known terms in the Breit interaction [25] (including for convenience the anomalous magnetic moment terms of order $\alpha^3 \text{Ry}$) give rise to the first-order perturbation correction

$$\Delta E_{\text{rel}} = \langle \Psi_J | H_{\text{rel}} | \Psi_J \rangle, \quad (6)$$

where Ψ_J is a nonrelativistic wavefunction for total angular momentum $\mathbf{J} = \mathbf{L} + \mathbf{S}$ and H_{rel} is defined by (in atomic units)

$$H_{\text{rel}} = \left(\frac{\mu}{m_e} \right)^4 B_1 + \left(\frac{\mu}{m_e} \right)^3 \left[B_2 + B_4 + B_{\text{so}} + B_{\text{soo}} + B_{\text{ss}} + \frac{m_e}{M} (\tilde{\Delta}_2 + \tilde{\Delta}_{\text{so}}) \right. \\ \left. + \gamma \left(2B_{\text{so}} + \frac{4}{3} B_{\text{soo}} + \frac{2}{3} B_{3e}^{(1)} + 2B_5 \right) + \gamma \frac{m_e}{M} \tilde{\Delta}_{\text{so}} \right] \quad (7)$$

with $\gamma = \alpha/(2\pi)$. The factors of $(\mu/m_e)^4 = (1 - \mu/M)^4$ and $(\mu/m_e)^3 = (1 - \mu/M)^3$ arise from the mass scaling of each term in the Breit interaction, while the terms $\tilde{\Delta}_2$ and $\tilde{\Delta}_{\text{so}}$ are dynamical corrections arising from the transformation of the Breit interaction to CM plus relative coordinates [26]. These latter terms are often not included in atomic structure calculations, but they make an important contribution to the isotope shift. As usual, B_1 denotes the p^4 relativistic variation of mass with velocity, B_2 is the orbit-orbit interaction, B_4 contains the Dirac delta-function terms, and B_{so} , B_{soo} , and B_{ss} represent the spin-orbit, spin-other-orbit and spin-spin interactions, respectively. The relativistic recoil ‘‘Stone’’ terms are [26]

$$\tilde{\Delta}_2 = -\frac{Z\alpha^2}{2} \left\{ \frac{1}{r_1} (\mathbf{p}_1 + \mathbf{p}_2) \cdot \mathbf{p}_1 + \frac{1}{r_1^3} \mathbf{r}_1 \cdot [\mathbf{r}_1 \cdot (\mathbf{p}_1 + \mathbf{p}_2)] \mathbf{p}_1 \right. \\ \left. + \frac{1}{r_2} (\mathbf{p}_1 + \mathbf{p}_2) \cdot \mathbf{p}_2 + \frac{1}{r_2^3} \mathbf{r}_2 \cdot [\mathbf{r}_2 \cdot (\mathbf{p}_1 + \mathbf{p}_2)] \mathbf{p}_2 \right\}, \quad (8)$$

$$\tilde{\Delta}_{\text{so}} = \frac{Z\alpha^2}{2} \left(\frac{1}{r_1^3} \mathbf{r}_1 \times \mathbf{p}_2 \cdot \boldsymbol{\sigma}_1 + \frac{1}{r_2^3} \mathbf{r}_2 \times \mathbf{p}_1 \cdot \boldsymbol{\sigma}_2 \right). \quad (9)$$

It is then a relatively straightforward matter to calculate accurate expectation values for these operators. Also, asymptotic expansions have been derived for the matrix elements and compared with the direct variational calculations, as discussed in [14].

2.4 QED Corrections

For a many-electron atom, the total QED shift of order $\alpha^3 \text{Ry}$ consists of two parts—an electron-nucleus part $E_{L,1}$ (the Kabir-Salpeter term [27]) and an electron–electron term $E_{L,2}$ originally obtained by Araki [28] and Sucher [29]. The $E_{L,2}$ term is relatively small and straightforward to calculate. The principal computational challenges come from the $E_{L,1}$ term given by (in atomic units)

$$E_{L,1} = \frac{4}{3} Z\alpha^3 \langle \delta(\mathbf{r}_1) + \delta(\mathbf{r}_2) \rangle \left[\ln \alpha^{-2} - \beta(1sn\ell) + \frac{19}{30} \right], \quad (10)$$

where $\beta(1sn\ell)$ is the two-electron Bethe logarithm arising from the emission and re-absorption of a virtual photon (see Fig. 2). It is the logarithmic remainder after mass renormalization and is defined by

$$\beta(1sn\ell) = \frac{\mathcal{N}}{\mathcal{D}} = \frac{\sum_i |\langle \Psi_0 | \mathbf{p}_1 + \mathbf{p}_2 | i \rangle|^2 (E_i - E_0) \ln |E_i - E_0|}{\sum_i |\langle \Psi_0 | \mathbf{p}_1 + \mathbf{p}_2 | i \rangle|^2 (E_i - E_0)}. \quad (11)$$

The foregoing equations are virtually identical to the corresponding one-electron (hydrogenic) case, except that there the δ -function matrix elements can be replaced by their hydrogenic value $\langle \delta(\mathbf{r}_1) + \delta(\mathbf{r}_2) \rangle \rightarrow Z^3 / (\pi n^3)$.

The accurate calculation of $\beta(1sn\ell)$ has been a long-standing problem in atomic physics. The problem has recently been solved by use of a discrete variational representation of the continuum in terms of pseudostates [30]. The key idea is to define a variational basis set containing a huge range of distance scales through multiple sets of exponential scale factors α and β that

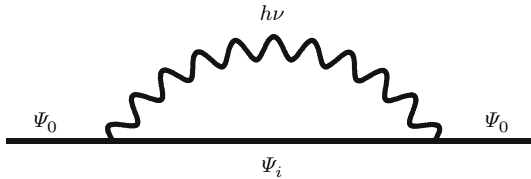


Fig. 2. Feynman diagram for the electron self energy

themselves span many orders of magnitude. the Bethe logarithm comes almost entirely from virtual excitations of the inner $1s$ electron to p -states lying high in the photoionization continuum, and so the basis set must be extended to very short distances for this particle. The outer electrons are to a good approximation just spectators to these virtual excitations.

Results for the low-lying states of helium and the He-like ions are listed in Table 3 (see also Korobov [31]). In order to make the connection with the hydrogenic Bethe logarithm more obvious, the quantity tabulated is $\ln(k_0/Z^2 Ry)$. The effect of dividing by a factor of Z^2 is to reduce all the Bethe logarithms to approximately the same number $\beta(1s) = 2.984\,128\,556$ for the ground state of hydrogen.

Table 4 compares the Bethe logarithms for the two lowest S-states of lithium with those for the Li-like ions $\text{Li}^+(1s^2\ ^1\text{S})$ and $\text{Li}^{2+}(1s\ ^2\text{S})$. The comparison emphasizes again that the Bethe logarithm is determined almost entirely by the hydrogenic value for the $1s$ electron and is almost independent of the state of excitation of the outer electrons or the degree of ionization.

3 Theoretical Isotope Shifts

The various contributions to the isotope shift are listed in Table 5 for ^6He relative to ^4He and Table 6 for ^{11}Li relative to ^7Li . The results are expressed as contributions to the isotope shift for the ionization energy of each state

Table 3. Bethe logarithms $\ln(k_0/Z^2 Ry)$ for He-like atoms, from [30] (see also [31])

State	$Z = 2$	$Z = 3$	$Z = 4$	$Z = 5$
$1\ ^1\text{S}$	2.983 865 9(1)	2.982 624 558(1)	2.982 503 05(4)	2.982 591 383(7)
$2\ ^1\text{S}$	2.980 118 275(4)	2.976 363 09(2)	2.973 976 98(4)	2.972 388 16(3)
$2\ ^3\text{S}$	2.977 742 36(1)	2.973 851 679(2)	2.971 735 560(4)	2.970 424 952(5)
$2\ ^1\text{P}$	2.983 803 49(3)	2.983 186 10(2)	2.982 698 29(1)	2.982 340 18(7)
$2\ ^3\text{P}$	2.983 690 84(2)	2.982 958 68(7)	2.982 443 5(1)	2.982 089 5(1)
$3\ ^1\text{S}$	2.982 870 512(3)	2.981 436 5(3)	2.980 455 81(7)	2.979 778 086(4)
$3\ ^3\text{S}$	2.982 372 554(8)	2.980 849 595(7)	2.979 904 876(3)	2.979 282 037
$3\ ^1\text{P}$	2.984 001 37(2)	2.983 768 943(8)	2.983 584 906(6)	2.983 449 763(6)
$3\ ^3\text{P}$	2.983 939 8(3)	2.983 666 36(4)	2.983 479 30(2)	2.983 350 844(8)
$4\ ^1\text{S}$	2.983 596 31(1)	2.982 944 6(3)	2.982 486 3(1)	2.982 166 154(3)
$4\ ^3\text{S}$	2.983 429 12(5)	2.982 740 35(4)	2.982 291 37(7)	2.981 988 21(2)
$4\ ^1\text{P}$	2.984 068 766(9)	2.983 961 0(2)	2.983 875 8(1)	2.983 813 2(1)
$4\ ^3\text{P}$	2.984 039 84(5)	2.983 913 45(9)	2.983 828 9(1)	2.983 770 1(2)
$5\ ^1\text{S}$	2.983 857 4(1)	2.983 513 01(2)	2.983 267 901(6)	2.983 094 85(5)
$5\ ^3\text{S}$	2.983 784 02(8)	2.983 422 50(2)	2.983 180 677(6)	2.983 015 17(3)
$5\ ^1\text{P}$	2.984 096 174(9)	2.984 038 03(5)	2.983 992 23(1)	2.983 958 67(5)
$5\ ^3\text{P}$	2.984 080 3(2)	2.984 014 4(4)	2.983 968 9(4)	2.983 937 2(4)

Table 4. Comparison of Bethe Logarithms for lithium and its ions

Atom	Li($1s^2 2s$)	Li($1s^2 3s$)	Li ⁺ ($1s^2$)	Li ²⁺ ($1s$)
$\ln(k_0/Z^2 Ry)$	2.981 06(1)	2.982 36(6)	2.982 624	2.984 128

so that the isotope shift for the transition is obtained by subtracting the entries for the corresponding initial and final states. The terms are classified according to their dependence on μ/M and the fine structure constant α . The various contributions are as follows. The term labeled μ/M contains the sum of the reduced mass scaling of the nonrelativistic ionization energy and the first-order mass polarization correction. For example, the mass-scaling term is $2R_\infty[2 - E_{\text{NR}}(\infty)][(\mu/M)_{^6\text{He}} - (\mu/M)_{^4\text{He}}]$, where $E_{\text{NR}}(\infty)$ is the nonrelativistic energy for infinite nuclear mass (in atomic units), and R_∞ is the corresponding Rydberg. The term of order $(\mu/M)^2$ comes from second-order mass polarization. The relativistic recoil terms of order $\alpha^2\mu/M$ come from mass scaling, mass polarization, and the Stone terms as expressed by (7) and (8). The radiative recoil terms similarly come from a combination of mass scaling, mass polarization, and higher-order recoil corrections, as discussed by Pachucki and co-workers [24, 32, 33] and Yan and Drake [21, 22, 23]. In addition, Puchalski et al. [24] have calculated the nuclear polarizability correction to the isotope shift and found that it makes a significant contribution for the case of the isotope shift for ^{11}Li . The correction is an additional contribution of 39 ± 4 kHz to the (positive) $3^2\text{S}_{1/2} - 2^2\text{S}_{1/2}$ isotope shift for ^{11}Li . The correction is negligibly small for the other isotopes.

Concerning the accuracy, for helium the uncertainty is completely dominated by the nuclear mass uncertainty for ^6He , as listed in Table 7. This is also largely the case for lithium, where the largest source of uncertainty is the nuclear mass for ^{11}Li . The one exception for Li is the relativistic recoil term of order $\alpha^2\mu/M$. Because of severe numerical cancellation among the

Table 5. Contributions to the isotope shifts in the ionization energies of ^6He relative to ^4He . Units are MHz

Term	2^3S_1	2^3P_2	3^3P_2
μ/M ^a	55 195.526(19)	20 730.146(7)	12 000.673(4)
$(\mu/M)^2$	-3.964	-14.132	-4.847
$\alpha^2\mu/M$	1.435	3.285	0.724
$\alpha^3\mu/M$	-0.280	-0.206	-0.036
Total	55 192.717(19)	20 719.093(7)	11 996.515(4)
Nuc. vol. ^b	-1.315	0.401	0.115

^aUncertainties for this line are dominated by the nuclear mass uncertainty for ^6He .

^bNuclear volume correction, assuming $r_p(^6\text{He}) = 2.056$ fm and $r_p(^4\text{He}) = 1.676$ fm.

Table 6. Contributions to the isotope shifts in the ionization energies of ^{11}Li relative to ^7Li . Units are MHz

Term	$2\ ^2\text{S}_{1/2}$	$3\ ^2\text{S}_{1/2}$
μ/M ^a	39 602.308(34)	14 497.818(12)
$(\mu/M)^2$	-5.647	-2.679
$\alpha^2\mu/M$	-0.097(1)	-0.119(11)
$\alpha^3\mu/M$	-0.154(4)	-0.036
Total	39 596.410(19)	14 494.984(7)
Nuc. vol. ^b	-0.257	-0.060

^aUncertainties for this line are dominated by the nuclear mass uncertainty for ^{11}Li .

^bNuclear volume correction, assuming $r_p(^7\text{Li}) = 2.39$ fm and $r_p(^{11}\text{Li}) = 2.42$ fm.

reduced mass, mass polarization, and Stone terms, the final numerical value is small and the percentage uncertainty is correspondingly large. Our numerical value is 0.022(11) MHz (from the column difference in Table 6), as compared with 0.038 MHz obtained by Puchalski et al. [24]. Further calculations are in progress to improve the accuracy of this term. Since the value from [24] appears to be more accurate, we will adopt it for the present work.

Finally, the correction for the finite nuclear size is given in lowest order by

$$\Delta E_{\text{nuc}} = \frac{2\pi Z e^2 r_c^2}{3} \left\langle \sum_i \delta^3(\mathbf{r}_i) \right\rangle. \quad (12)$$

The contributions to the isotope shift shown in Tables 5 and 6 correspond to the adjusted value of r_c to bring theory and experiment into agreement, as discussed in the following sections. For convenience, the theoretical results relating the measured isotope shift $\delta\nu$ to the nuclear radii are as follows:

Table 7. Table of nuclear masses used in the calculations. Units are atomic mass units

Isotope	Mass
^3He	3.016029310(1)
^4He	4.002603250(1)
^6He	6.0188881(11)
^6Li	6.015122794(16)
^7Li	7.0160034256(45)
^8Li	8.02248736(10)
^9Li	9.0267895(21)
^{11}Li	11.0437157(54)

$$\delta\nu(2^3S_1-2^3P_2) = 34\,473.625(13) + 1.210 [r_c^2(^4\text{He}) - r_c^2(^3\text{He})] , \quad (13)$$

$$\delta\nu(2^3S_1-3^3P_2) = 43\,196.202(16) + 1.008 [r_c^2(^4\text{He}) - r_c^2(^3\text{He})] , \quad (14)$$

$$\delta\nu(2^2S_{1/2}-3^3S_{1/2}) = 25\,101.474(22) + 1.566 [r_c^2(^7\text{Li}) - r_c^2(^6\text{Li})] . \quad (15)$$

The last line for Li includes the nuclear polarization correction and the adjusted relativistic recoil term of Puchalski et al. [24]. These results are compared with experiment in the following two sections.

4 ^6He Isotope Shift and Nuclear Radius

The principal challenge in measuring the isotope shift for ^6He is the high sensitivity needed to probe the small number of ^6He atoms available and their short half-life of 0.8 s. To overcome these difficulties, laser spectroscopy was performed on single atoms prepared in a magneto-optical trap (MOT) [34]. The experiment was made even more difficult by the fact that there are no suitable transitions from the $1s^2\ ^1S$ ground state that can be used for trapping the helium atoms, and for subsequent isotope shift measurements. For example, the $1\ ^1S_0-2\ ^3P_1$ resonance transition lies at 58.4 nm in the far vacuum ultraviolet. For this reason, the atoms must first be excited to the $2\ ^3S_1$ metastable state in a discharge via electron impact excitation. From the metastable state, the $2\ ^3S_1-2\ ^3P_2$ transition can be used for cooling and trapping and the $2\ ^3S_1-3\ ^3P_J$ transition at 389 nm used for fluorescence detection of single atoms and isotope shift measurements.

The details of the experiment are as follows [35]. The ^6He nuclei were produced by aiming a 60 MeV beam of ^7Li from the ATLAS accelerator onto a

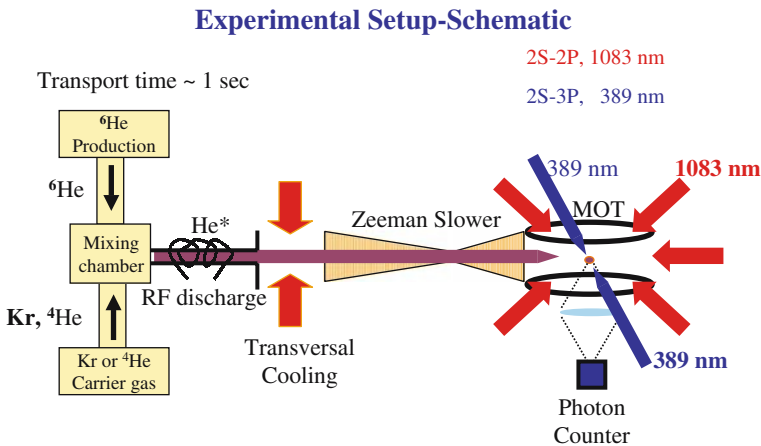


Fig. 3. Schematic diagram of the apparatus of the ^6He experiment

hot (750°) graphite target and extracting the products of the $^{12}\text{C}(^7\text{Li},^6\text{He})^{13}\text{N}$ reaction. The neutral ^6He atoms diffused out of the target at the rate of about 10^6 s^{-1} and into the nearby atomic beam assembly (see [36] for further details, and Fig. 3). The atomic transition $2\ ^3\text{S}_1-2\ ^3\text{P}_2$ was excited by laser beams at 1083 nm produced by a diode laser and a fiber amplifier to trap the small fraction ($\sim 10^{-5}$) of ^6He atoms that were successfully excited to the $2\ ^3\text{S}_1$ metastable state. The excitation was accomplished by mixing the atoms with a krypton carrier gas and sending them through an RF discharge. The metastable helium atoms were then transversely cooled and decelerated by the Zeeman slowing technique before entering the MOT. The ^6He atoms remained trapped in the MOT for an average of only 0.4 s due to collisional losses and nuclear β decays. The overall capture rate was about 100 h^{-1} , with a total capture efficiency of 2×10^{-8} . A single trapped atom emitted fluorescence photons at the rate of 10^6 s^{-1} , and fluorescence from a single atom induced a photon count rate of $7 \times 10^2\text{ s}^{-1}$, compared with a background count rate of $2 \times 10^2\text{ s}^{-1}$.

The experiment itself consisted of two modes: a capture mode and a spectroscopy mode. Because of the low capture rate, the capture mode was spent mostly waiting for a ^6He atom to arrive at the MOT. During this phase, the trapping laser beams at 1083 nm were constantly on, with their intensity (10 mW/cm^2) and frequency detuning (-20 MHz) tuned to maximize the capture probability. The probing laser beams at 389 nm were also constantly on in order to detect the arrival of a trapped ^6He metastable atom. Within 0.1 s of its arrival, the system switched to the spectroscopy mode in which the intensity of the trapping beams was lowered (0.8 mW/cm^2) and the detuning decreased (-3 MHz) in order to provide a tighter confinement and more cooling to the trapped atom. In addition, the trapping laser and the probing laser beams were chopped alternately at 100 kHz such that, for each chopping period of $10\ \mu\text{s}$, only the probe laser beams were on for $2\ \mu\text{s}$, during which time the fluorescence signal was collected, and then only the trapping laser beams were on for $8\ \mu\text{s}$ to recapture and cool the atom. Meanwhile, the system scanned the frequency of the probing laser over a range of 18 MHz at a repetition rate of 85 kHz. This fast scanning and chopping was necessary to minimize systematic effects due to the heating/cooling of the atom by the probing light. Furthermore, in order to minimize the dependence of the spectrum on the magnetic field and on laser intensity, the probing laser beams consist of a pair of counter-propagating, linearly polarized beams with their intensities carefully matched.

All these controls and adjustments were tested extensively off-line on the stable ^4He and ^3He atoms. Figure 4(a) shows a typical spectrum of the $2\ ^3\text{S}_1-3\ ^3\text{P}_2$ transition accumulated over five minutes with a trap filled with a few ^4He atoms. Measurements on this transition, as well as on the fine structure partners $2\ ^3\text{S}_1-3\ ^3\text{P}_1$ and $2\ ^3\text{S}_1-3\ ^3\text{P}_0$ were performed while changing the intensity of the probing beams by as much as a factor of 60 and changing the magnetic field gradient of the MOT by a factor of 2. A group of 30 such

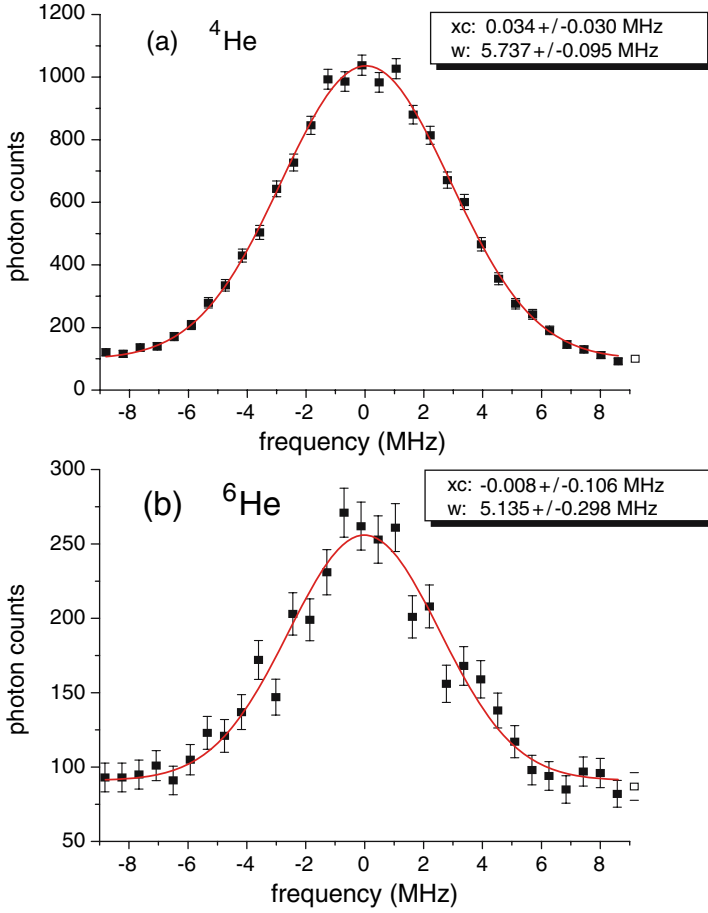


Fig. 4. Comparison of fluorescent spectra for ${}^4\text{He}$ and ${}^6\text{He}$

measurements had a standard deviation of 0.040 MHz, which represents the systematic error in the isotope shift measurement due to trap effects (Table 8), including any residual Zeeman shifts and the effects of heating/cooling of the atom.

Figure 4(b) presents a spectrum of the $2\ {}^3\text{S}_1\text{-}3\ {}^3\text{P}_2$ transition accumulated over 1 h with a total of 150 trapped ${}^6\text{He}$ atoms. The isotope shift between ${}^6\text{He}$ and ${}^4\text{He}$ was obtained by fitting a Gaussian function to the spectra and taking the difference of peak centers, with due allowance for the recoil effect shown in Table 8. A total of 18 such measurements was performed with comparable precision during two separate runs one month apart, yielding a statistical error of 0.033 MHz (reduced chi square = 0.85). The isotope shift on the $2\ {}^3\text{S}_1\text{-}3\ {}^3\text{P}_2$ transition between ${}^6\text{He}$ and ${}^4\text{He}$ was determined in this work to be $43\,194.772 \pm 0.056$ MHz.

Table 8. Errors and corrections in the isotope shift of the $2\ ^3S_1-3\ ^3P_2$ transition between ^6He and ^4He . The resulting corrected value for the measured isotope shift is $43\ 194.772 \pm 0.056$ MHz

Source	Correction (MHz)	Error (MHz)
Statistical		0.033
Trap effects		0.040
Uneven background		0.020
Frequency counter		0.009
Recoil effect	0.110	<0.001
Total	0.110	0.056

Based on the atomic theory illustrated in Sect. 2, the measured isotope shift translates into a difference between the mean-square charge radii $\langle r_c^2 \rangle_{\text{He6}} - \langle r_c^2 \rangle_{\text{He4}}$ of 1.418 ± 0.058 fm². Given the previously determined charge radius of ^4He of 1.676(8) fm [37], the charge radius of ^6He from this measurement is then 2.056 ± 0.015 fm. This value represents the first nuclear-model-independent determination. It has achieved a much improved accuracy and is in disagreement with that previously derived from the interaction cross-section, presumably reflecting the inadequacies of the model assumptions. The point-proton radius of ^6He has been calculated using a variety of nuclear structure models, including ab initio calculations based on either the no-core shell model [38] or the quantum Monte Carlo methods [39]. The experimental value was compared to the predictions and is used to check the validity of our understanding of the forces between nucleons.

As an interesting sidelight to this work and as a further check on the measurements, the fine structure splittings for the $1s3p\ ^3P_J$ states of ^4He with $J = 0, 1, 2$ were also measured. The results in fact disagree with older measurements by Yang, McNicholl, and Metcalf [40], but they agree with recent calculations of the fine structure splittings, including spin-dependent corrections up to order $\alpha^5 \ln \alpha$ Ryd. The results are presented in [41].

5 Experiments in Lithium

Since the halo nucleus ^{11}Li can be readily produced at ISOL facilities and due to the availability of spectral lines in the visible region for the neutral atom it was the first halo isotope that was studied with laser spectroscopy. However, this was always a challenge since the production rates for this isotope have never been exceeding 10,000 ions/s and its half-life is only 8.4 ms and therefore highly efficient and sensitive techniques are required. Already in the late 1980s the COLLAPS collaboration at ISOLDE determined the spin, the nuclear magnetic dipole, and the electric quadrupole moment of ^{11}Li in a combination of optical pumping in collinear laser spectroscopy and β -NMR

[42, 43, 44]. With respect to the halo structure of ^{11}Li , the most remarkable result is the small difference in the moments in ^9Li and ^{11}Li . The magnetic moments were found to be close to the Schmidt value and less than 10% different, while the quadrupole moments agreed within their uncertainties. This is a clear sign that a strong deformation cannot be the reason for the large matter radius. More recently, the collaboration could improve the accuracy of these measurements [45, 46] and a small difference in the ^9Li and ^{11}Li quadrupole moments was resolved. As mentioned above, the halo structure reveals itself most clearly as a difference between the nuclear matter and charge radius. Therefore, the question whether the nuclear charge radius of these exotic isotopes can be measured arose very early after their discovery. In principle, the collinear spectroscopy, as it has been applied for the optical pumping of ^{11}Li , is regularly used for isotope shift measurements and nuclear charge radii determination. However, for the light isotopes the uncertainties due to the insufficient knowledge of the acceleration voltage is too large to reach the required accuracy of a few 100 kHz for charge radius extraction of very light nuclei. Sophisticated techniques made it possible to measure charge radii of short-lived neon isotopes down to ^{17}Ne . Until 2003 this was the lightest radioactive isotope of which the nuclear charge radius has been determined [47].

5.1 Experimental Technique

The experimental setup used in the isotope shift measurements is shown in Fig. 5. Lithium isotopes $^{8,9}\text{Li}$ were produced at GSI with an 11.4 MeV/u ^{12}C beam impinging on a target made of carbon (for ^8Li) or tantalum and tungsten (for ^9Li). The halo nucleus ^{11}Li cannot be generated in this reaction, instead it was produced at TRIUMF (Vancouver) by bombarding a thick tantalum target with 40 μA of a 500 MeV proton beam. In both cases, the lithium atoms were ionized on hot surfaces, extracted with a 30–40 kV extraction voltage, mass separated, and transported to the setup for the isotope shift measurement. Here, the ion beam was focussed to a beam size of approximately 2 mm diameter with an electrostatic quadrupole triplet, stopped, and neutralized inside a thin graphite foil with a “layer thickness” of 80 $\mu\text{g}/\text{cm}^2$, corresponding to a real thickness of approximately 330 nm. Range straggling for 30 keV ions in graphite is on the order of 40 nm. Thus, the majority of ions were stopped and neutralized just before they could leave the foil. A quasi-continuous 4 W CO_2 laser beam was focussed with a similar spot size onto the foil and heated up to ≈ 2000 K. The neutralized lithium ions quickly diffused out of the foil. From a simple geometrical model it was estimated that about 70% of the atoms are released towards the side opposite to the incoming ion beam. A release time of less than 500 μs was measured, which is about 6% of the ^{11}Li half-life and clearly sufficient to have a good release efficiency for this isotope. Atoms released from the surface drifted through a hole of 3 mm diameter into the ionization region of a commercial quadrupole

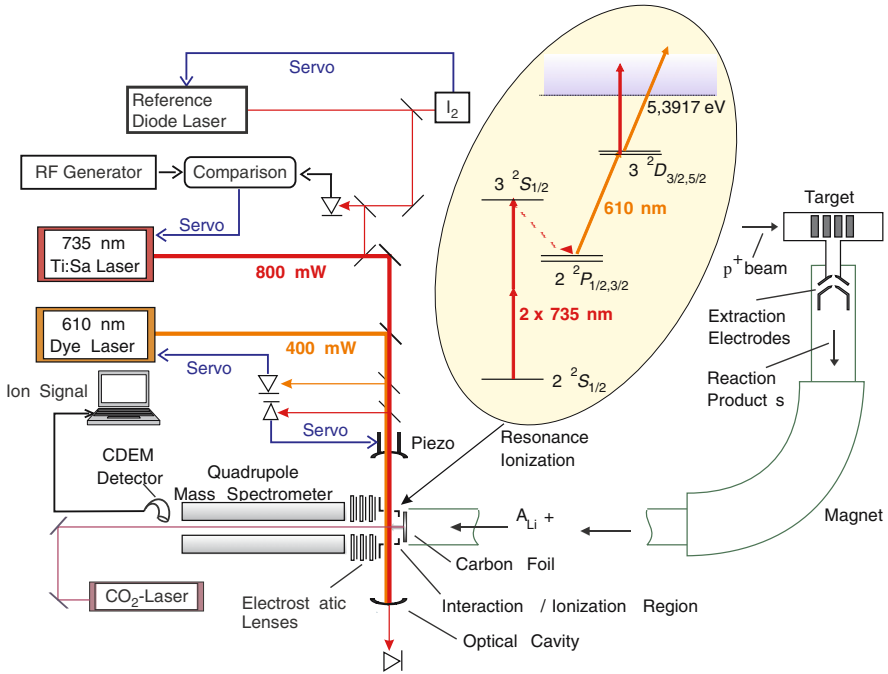


Fig. 5. Experimental setup of the lithium experiment including the production region for the radioactive isotopes, neutralization, resonance ionization scheme and laser system, the quadrupole mass spectrometer, and the continuous dynode electron multiplier (CDEM) detector

mass spectrometer. Surface ions produced on the hot graphite foil were repelled from the ionization region by a small positive offset voltage of +4 V relative to the graphite catcher.

The isotope shift between the different lithium isotopes was measured in the $2s\ ^2S_{1/2} \rightarrow 3s\ ^2S_{1/2}$ two-photon transition. Excitation of this transition with counter-propagating laser beams leads to first-order Doppler-free signals. The excitation and ionization scheme is shown in the inset of Fig. 5. Atoms excited into the $3s$ state relax to the $2p\ ^2P_{1/2,3/2}$ levels. Instead of resonance fluorescence detection, resonance ionization along the $2p\ ^2P_{1/2,3/2} \rightarrow 3d\ ^2D_{3/2,5/2} \rightarrow \text{Li}^+$ path was applied to observe the $2s \rightarrow 3s$ transition, which was found to be more efficient and gave a much better signal-to-noise ratio. This scheme was carefully chosen to obtain the required accuracy and to minimize systematic effects, like AC-Stark broadening and shifts. The spontaneous decay process into the $2p$ level separates the spectroscopy transition, where high accuracy was needed, from the resonance ionization step, which could then be independently optimized for high efficiency. High laser power could be applied for the $2p \rightarrow 3d$ transition in order to get as much ionization efficiency as possible. This would be prohibitive if the laser

would directly couple the $3s$ state with, e.g., the $5p$ state since the resonant AC-Stark shift and broadening of the $3s$ level would spoil the accuracy in the $2s \rightarrow 3s$ transition frequency.

The laser ionized particles could be easily extracted from the ionization region, mass analyzed in the quadrupole mass filter, and detected with a continuous secondary electron multiplier. The total efficiency for the detection of the laser-ionized particles is of the order of 80–90% as has been shown in extensive previous studies of this mass filter system [48].

The 735 nm light for the two-photon transition was produced by a titanium sapphire (Ti:Sa) laser pumped with 15 W of an argon-ion laser, while the 610 nm light was provided by a dye laser (Rhodamin 6G) pumped with 8 W of a VERDI V8 frequency-doubled Nd:YAG laser. A reference frequency for the isotope shift measurement was provided by an amplified diode laser system locked to the a_1 hyperfine component in the $X^1\Sigma_{0g}^+ \rightarrow B^1\Pi_{0u}^+$ R(114) 11-2 transition in molecular iodine by frequency modulation saturation spectroscopy [49]. The frequency of the Ti:Sa laser was measured and stabilized relative to the iodine-locked diode laser, by observation of the beat frequency between the two lasers.

The two-photon excitation as well as the nonresonant ionization requires high laser intensities to reach the efficiency that was needed in this experiment. This was realized by resonant enhancement of the two laser beams in an optical cavity that was formed by two mirrors in the vacuum chamber around the excitation region. A resonance enhancement of approximately 100 was obtained. The laser intensities inside the cavity were recorded during the experiment by measuring the light power leaking through the rear cavity mirror with two photodiodes.

5.2 Results

Resonance Profiles

Figure 6 shows a spectrum of the ${}^7\text{Li } 2s \rightarrow 3s$ transition on a logarithmic scale. Hyperfine selection rules restrict the possible excitations in an $s_{1/2} \rightarrow s_{1/2}$ transition to those with $\Delta F = 0$. Thus, all lithium isotopes exhibit two transitions connecting the respective $F = I \pm 1/2$ states. The spectrum of ${}^7\text{Li}$ shows two narrow peaks on a broad background. The narrow peaks are the Doppler-free components which arise from the absorption of two-photons, traveling in opposite directions. But the atoms can also absorb two photons from the same direction. In this case the resonance frequency depends on the velocity of the atom and this is the origin of the weak but very broad Doppler pedestal that is clearly visible with an intensity about three to four orders of magnitude smaller than the Doppler-free signal.

In on-line operation, spectra were taken only across the two resonances in a range of ± 15 MHz for the radioactive and ± 30 MHz for the stable isotopes while the intermediate region was skipped. For ${}^8,9\text{Li}$ the production rates were

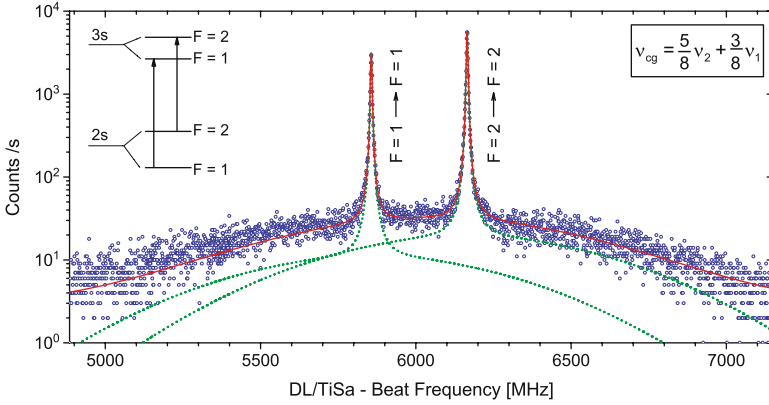


Fig. 6. Line profile of the ${}^7\text{Li } 2s \rightarrow 3s$ two-photon transition with narrow Doppler-free transitions and Doppler-broadened background

sufficient to fit each individual scan, as is demonstrated in Fig. 7 (a). For ${}^{11}\text{Li}$ about six consecutive scans were combined in order to improve fitting quality. A resulting resonance profile of ${}^{11}\text{Li}$ is shown in Fig. 7 (b). Overall 24 scans of comparable quality could be recorded during 4 days of ${}^{11}\text{Li}$ beamtime. The isotope shift is defined as the shift of the hyperfine center of gravity (cg) that can be calculated from the two transition frequencies ν_F and $\nu_{F'}$ according to

$$\nu_{\text{cg}} = \frac{C_F \nu_{F'} - C_{F'} \nu_F}{C_F - C_{F'}} \quad (16)$$

with C_F being the Casimir factor $C_F = F(F+1) - J(J+1) - I(I+1)$ of the respective F state.

AC-Stark Shift Correction

The strong laser fields inside the cavity, even though they are not resonant with any $s \rightarrow p$ transition, cause a weak nonresonant coupling of the p -states to the s -states. This leads to small energy shifts of the individual levels

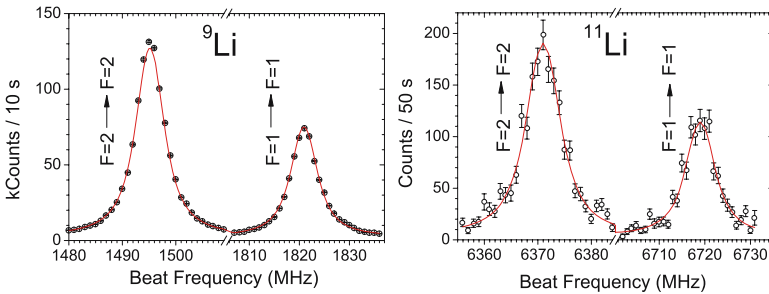


Fig. 7. Resonance spectra of ${}^9\text{Li}$ and ${}^{11}\text{Li}$ with skipped intermediate region

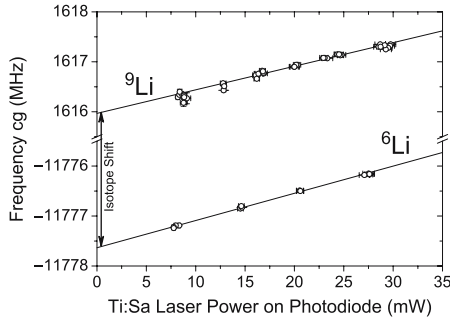


Fig. 8. Resonance frequency of the center of gravity (CG) of ${}^6,{}^9\text{Li}$ as a function of the Ti:Sa laser power on the photodiodes behind the enhancement cavity. The dye laser power was kept constant. AC-Stark shift is corrected by extrapolating the linear behavior back to zero laser powers

that have to be carefully considered when analyzing the isotope shift data. Therefore, the hyperfine cg frequencies of ${}^6,{}^7,{}^8,{}^9\text{Li}$ were measured as a function of the Ti:Sa laser power detected on the photodiodes behind the enhancement cavity. The dye laser power was kept constant during these measurements. Results for ${}^6,{}^9\text{Li}$ are shown in Fig. 8 and a clear linear behavior of the AC Stark shift is observed. For ${}^6\text{-}^9\text{Li}$, the isotope shifts were calculated determining the differences of the intersection points with the frequency axis. This method could not be used for ${}^{11}\text{Li}$ because of the small production rates and the limited statistics for measurements at lower laser power. However, it was found that the slope coefficients for all lithium isotopes agree within their uncertainties, showing no isotopic dependence of the AC-Stark shift. Hence, the isotope shift

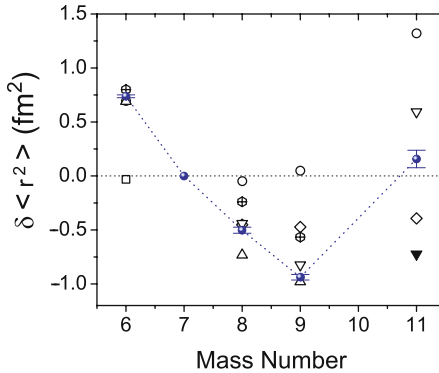


Fig. 9. Extracted $\delta \langle r^2 \rangle$ for all lithium isotopes (\bullet) and comparison with different nuclear model predictions: \triangle : Greens function Monte Carlo calculations [52, 53], ∇ : stochastic variational multi-cluster model [54, 55] (\blacktriangledown : assuming a frozen ${}^9\text{Li}$ core), \oplus : fermionic molecular dynamics [56], \circ : dynamic correlation model [57, 58], \square and \diamond : ab initio no-core shell model [59, 60]

can also be calculated as the difference between the ^{11}Li cg frequency and the reference isotope AC-Stark shift function at the corresponding laser intensity.

Isotope Shifts and Charge Radii

Isotope shift results for all lithium isotopes are summarized in Table 9. For ^{11}Li the standard error of the mean of the 24 measurements is 66 kHz. Including systematic uncertainties the total isotope shift amounts to $\delta\nu^{11,7} = 25\,101.226(125)$ MHz. Applying (15) from Sect. 3, the changes in the mean-square nuclear charge radii relative to ^7Li can be obtained. These values are also included in Table 9. In the original publications [6, 7] the absolute charge radii of all lithium isotopes were calculated according to $r_c(^A\text{Li}) = \sqrt{r_c(^7\text{Li}) + \delta\langle r^2 \rangle^{A,7}}$ based on a charge radius of $r_c = 2.39(3)$ fm for ^7Li . This reference radius has been obtained as a weighted average of ^7Li electron scattering measurements compiled in [50]. However, it was pointed out recently [51] that the uncertainty of the reference radius has probably been underestimated and that the charge radius of ^6Li has been determined more reliably. Charge radii uncertainties for the lithium isotopes are always dominated by the uncertainty of the reference radius.

To avoid this complication the mean-square charge radii differences rather than the charge radius itself is plotted in Fig. 9. For comparison, the $\delta\langle r^2 \rangle$ values predicted by a variety of theoretical models are included as well. In most theoretical papers the modeled charge radii are given as point-proton radii $\langle R_{\text{pp}}^2 \rangle$ [52, 53, 54, 55, 59, 60]. In the figure, the differences of these mean-square radii relative to ^7Li are plotted, taking into account also the contribution of the mean-square charge radius of the neutron $\langle R_{\text{n}}^2 \rangle = -0.117(4)$ fm² [61]. The neutron contribution was calculated according to

$$\delta\langle r_c^2 \rangle^{A,7} = \delta\langle R_{\text{pp}}^2 \rangle^{A,7} + \frac{\delta N}{Z} \cdot \langle R_{\text{n}}^2 \rangle = \delta\langle R_{\text{pp}}^2 \rangle^{A,7} + \frac{A-7}{3} \cdot \langle R_{\text{n}}^2 \rangle. \quad (17)$$

and is as large as -0.155 fm² for ^{11}Li .

Good agreement between predicted and measured mean-square radii of ^{6-9}Li is observed for the Greens function Monte Carlo (GFMC) [53, 52] and the stochastic variational multi-cluster (SVMC) model [54, 55]. From these

Table 9. Summary of the lithium isotope shift results. Measured isotope shifts $\delta\nu_{\text{exp}}^{A,7}$ relative to ^7Li , corresponding calculated mass shifts $\delta\nu_{\text{theo}}$, and changes in the mean-square charge radii $\delta\langle r^2 \rangle^{A,7}$ for all isotopes are given

Isotope	$\delta\nu_{\text{exp}}^{A,7}$ [MHz]	$\delta\nu_{\text{theo}}^{A,7}$ [MHz]	$\delta\langle r^2 \rangle^{A,7}$ [fm ²]
^6Li	-11 453.983 (20)	-11 452.822(2)(0)	0.738(13)
^8Li	8 635.782(44)	8 634.990(1)(1)	-0.503(28)
^9Li	15 333.272(39)	15 331.797(3)(13)	-0.938(26)
^{11}Li	25 101.226(125)	25 101.473(9)(21)	0.157(81)

descriptions, only the SVMC is able to model the ^{11}Li nucleus so far. However, its prediction does not agree with our measurement, either in the full calculation or in a frozen-core approximation where intrinsic excitation of the ^9Li core is not considered. The fermionic molecular dynamics (FMD) model [56] gives the correct trend from ^6Li to ^9Li but ^{11}Li has not been calculated yet. The agreement of other models with the experimental data is rather poor with exceptions for individual isotope pairs. It is striking that the difference between the stable isotopes $^6,7\text{Li}$, which has been known from electron scattering for decades [50], is particularly well described by almost all models with the exception of the no-core shell model [55].

6 Discussion and Future Work

It is clear from this work that the accuracy of both theory and experiment for isotope shifts has now reached the stage that the two can be combined to provide a powerful new tool for the measurement of nuclear radii in the low- Z region, and that the method can be applied even at the level of single-atom spectroscopy. The results for the radii of halo nuclei provide a significant new test of various models for nuclear structure and the effective low-energy nucleon–nucleon interaction potential. The principal limitation is that the measurements of nuclear radii are relative to a reference nucleus obtained by nuclear scattering. An important project for future work is to improve the accuracy of theory to the point that absolute measurements of nuclear radii can be extracted directly from atomic spectroscopy for a single isotope, rather than relative values from the shift between two isotopes. At present, theory is complete only up to QED terms of order α^3 Ryd. This is sufficient for isotope shift measurements because it is only the mass-dependent part of the QED shift that contributes, and so it is suppressed by a factor of $\mu/M \simeq 10^{-4}$. However, the suppression factor is no longer present for the absolute transition frequency of a single isotope, and so complete calculations of the relativistic and QED shifts must be extended to terms of order α^4 Ryd and α^5 Ryd. This has been done for the case of hydrogen (i.e., the one-electron Lamb shift), but only estimates and partial results are available for helium and lithium. However, there has been significant progress in recent years by Pachucki and co-workers [62, 63] and by Drake [64] especially for the spin-dependent parts of the operators. This gives hope that complete results may be within reach for these terms, using the methods of nonrelativistic QED [65].

On the experimental side, experiments with the even more exotic species ^8He have been performed recently at Argonne/GANIL, and are planned for $^{11}\text{Be}^+$ at GSI [66]. ^{11}Be is the archetype of a one-neutron halo structure, and the proposed measurement would be the first of its type to give a value for the charge radius in a way that does not depend on an assumed nuclear model. Calculations are currently in progress for the isotope shift of Be^+ similar to those already done for lithium.

Acknowledgements

This research was supported in Canada by the Canadian Natural Sciences and Engineering Research Council, by NRC through TRIUMF, and by SHARCnet. In the United States it was supported by the U.S. Department of Energy, Office of Nuclear Physics under contract No. DE-AC02-06CH11357, and by the U.S. DOE Office of Science (B.A.B.). In Germany it was supported by the European Community Programme IHP under contract No. HPMT-CT-2000-00197, and the German Ministry for Education and Research (BMBF) under contract $\phi 6\text{Tu}2\phi 3$.

References

1. I. Tanihata et al.: Phys. Rev. Lett. **55**, 2676 (1985). [131](#), [132](#)
2. I. Tanihata et al.: Phys. Lett. B **160**, 380 (1985). [131](#), [132](#)
3. P. G. Hansen, and B. Jonson: Europh. Lett. **4**, 409 (1987). [131](#)
4. I. Tanihata: J. Phys. G **22**, 157 (1996). [131](#)
5. I. Tanihata et al.: Phys. Lett. B **206**, 592 (1988). [132](#)
6. G. Ewald et al.: Phys. Rev. Lett. **93**, 113002 (2004): 94, 039901 (2005). [132](#), [150](#)
7. R. Sánchez et al.: Phys. Rev. Lett. **96**, 033002 (2006). [132](#), [150](#)
8. G.W.F. Drake, in *Long-range Casimir forces: Theory and recent experiments on atomic systems*, edited by F.S. Levin and D.A. Micha (Plenum, New York, 1993), pp. 107–217. [132](#), [134](#)
9. Z.-C. Yan, and G. W. F. Drake: Phys. Rev. A **61**, 022504 (2000). [132](#), [136](#)
10. G.W.F. Drake, W. Nörtershäuser, and Z.-C. Yan: Can. J. Phys. **83**, 311 (2005). [133](#)
11. D.C. Morton, Q.X. Wu, and G.W.F. Drake: Can. J. Phys. **84**, 83 (2006), and earlier references therein. [133](#)
12. G.W.F. Drake and W.C. Martin: Can. J. Phys. **76**, 679 (1998). [133](#)
13. G.W.F. Drake and Z.-C. Yan: Phys. Rev. A, **46**, 2378 (1992). [134](#), [135](#)
14. G.W.F. Drake: Adv. At. Mol. Opt. Phys. **31**, 1 (1993). [134](#), [135](#), [137](#)
15. G.W.F. Drake, M.M. Cassar, and R.A. Nistor: Phys. Rev. A **65**, 054501 (2002). [134](#), [135](#)
16. V.I. Korobov: Phys. Rev. A **66**, 024501 (2002). [135](#)
17. C. Schwartz: Int. J. Mod. Phys. E **15**, 877–888 (2006). [135](#)
18. S.P. Goldman: Phys. Rev. A **57**, R677 (1998). [135](#)
19. A. Bürgers, D. Wintgen, J.-M. Rost: J. Phys. B: At. Mol. Opt. Phys. **28**, 3163 (1995). [135](#)
20. J.D. Baker, D.E. Freund, R.N. Hill, J.D. Morgan III: Phys. Rev. A **41**, 1247 (1990). [135](#)
21. Z.-C. Yan and G.W.F. Drake: Phys. Rev. Lett. **81**, 774 (1998). [136](#), [139](#)
22. Z.-C. Yan and G.W.F. Drake: Phys. Rev. A, **66**, 042504 (2002). [136](#), [139](#)
23. Z.-C. Yan and G.W.F. Drake: Phys. Rev. Lett., **91**, 113004 (2003). [136](#), [139](#)
24. M. Puchalski, A.M. Moro, and K. Pachucki, Phys. Rev. Lett. **97**, 133001 (2006). [136](#), [139](#), [140](#), [141](#)
25. H.A. Bethe and E.E. Salpeter, *Quantum mechanics of one- and two-electron atoms*, (Springer-Verlag, New York, 1957). [136](#)

26. A.P. Stone: Proc. Phys. Soc. (London) **77**, 786 (1961); **81**, 868 (1963). [136](#)
27. P. K. Kabir and E. E. Salpeter: Phys. Rev. **108**, 1256 (1957). [137](#)
28. H. Araki: Prog. Theor. Phys. **17**, 619 (1957). [137](#)
29. J. Sucher: Phys. Rev. **109**, 1010 (1958). [137](#)
30. G.W.F. Drake and S.P. Goldman: Can. J. Phys. **77**, 835 (1999). [137](#), [138](#)
31. V.I. Korobov: Phys. Rev. A **69**, 054501 (2004). [138](#)
32. K. Pachucki and J. Sapirstein: J. Phys. B At. Mol. Opt. Phys. **36**, 803 (2003). [139](#)
33. M. Puchalski and K. Pachucki: Phys. Rev. A **73**, 022503 (2006). [139](#)
34. H.J. Metcalf and P. van der Straten, *Laser Cooling and Trapping*, (Springer, New York, 1999). [141](#)
35. L.-B. Wang, P. Mueller, K. Bailey, G.W.F. Drake, J.P. Greene, D. Henderson, R.J. Holt, R.V.F. Janssens, C.L. Jiang, Z.-T. Lu, T.P. O'Connor, R.C. Pardo, K.E. Rehm, J.P. Schiffer, and X.D. Tang: Phys. Rev. Lett. **93**, 142501 (2004). [141](#)
36. P. Mueller et al.: Nucl. Instrum. Methods Phys. Res. Sect. B **204**, 536 (2003). [142](#)
37. I. Sick: Phys. Lett. B **116**, 212 (1982). [144](#)
38. P. Navrátil et al.: Phys. Rev. Lett. **87**, 172502 (2001); E. Caurier and P. Navrátil: Phys. Rev. C **73**, 021302 (2006). [144](#)
39. S.C. Pieper et al.: Phys. Rev. C **64**, 014001 (2001). [144](#)
40. D.-H. Yang, P. McNicholls, and H. Metcalf: Phys. Rev. A **33**, 1725 (1986). [144](#)
41. P. Mueller, L.-B. Wang, G.W.F. Drake, et al.: Phys. Rev. Lett. **94**, 133001 (2005). [144](#)
42. E. Arnold et al.: Phys. Lett. B **197**, 311 (1987). [145](#)
43. E. Arnold et al.: Phys. Lett. B **281**, 16 (1992). [145](#)
44. E. Arnold et al.: Zeitschr. f. Phys. A **349**, 337 (1994). [145](#)
45. D. Borremans et al.: Phys. Rev. C **72**, 044309 (2005). [145](#)
46. R. Neugart et al: Phys. Rev. Lett., in preparation (2007). [145](#)
47. W. Geithner et al.: Phys. Rev. C **71**, 064319 (2005). [145](#)
48. K. Blaum *et al.*: Int. J. Mass Spectrom. **202**, 81 (2000). [147](#)
49. W. Nörtershäuser et al.: Nucl. Instr. Meth. Phys. Res. B **204**, 644 (2003). [147](#)
50. C. W. de Jager, H. deVries, and C. deVries: At. Data Nucl. Data Tables **14**, 479 (1974). [150](#), [151](#)
51. I. Sick: priv. comm. (2007). [150](#)
52. S.C. Pieper, K. Varga and R.B. Wiringa: Phys. Rev. C **66**, 044310 (2002). [149](#), [150](#)
53. S. C. Pieper and R. B. Wiringa: Annual Rev. Nucl. Part. Science **51**, 53 (2001). [149](#), [150](#)
54. K. Varga, Y. Suzuki, and I. Tanihata: Phys. Rev. C **52**, 3013 (1995). [149](#), [150](#)
55. K. Varga, Y. Suzuki, and R. G. Lovas: Phys. Rev. C **66**, 041302 (2002). [149](#), [150](#), [151](#)
56. T. Neff, H. Feldmeier, and R. Roth: in 21. Winter workshop on Nuclear Dynamics, Breckenridge, Colorado, USA, (2005). [149](#), [151](#)
57. M. Tomaselli et al.: Nucl. Phys. A **690**, 298 (2001). [149](#)
58. M. Tomaselli et al.: Hyperf. Int. **171**, 243 (2006) [149](#)
59. P. Navrátil and W. E. Ormand: Phys. Rev. C **68**, 034305 (2003). [149](#), [150](#)
60. P. Navrátil and B. R. Barrett: Phys. Rev. C **57**, 3119 (1998). [149](#), [150](#)
61. S. Kopecky et al.: Phys. Rev. C **56**, 2229 (1997). [150](#)
62. K. Pachucki: Phys. Rev. A **74**, 062510 (2006). [151](#)
63. K. Pachucki: Phys. Rev. A **74**, 022512 (2006). [151](#)
64. G.W.F. Drake: Can. J. Phys. **80**, 1195 (2002). [151](#)
65. U.D. Jentschur, A. Czarnecki, and K. Pachucki: Phys. Rev. A **72**, 062102 (2005). [151](#)
66. M. Žákova et al.: Hyperf. Int. **171**, 189 (2006) [151](#)

Exotic Atoms and Heavy Ions

Quantum Electrodynamics in Extreme Fields: Precision Spectroscopy of High- Z H-like Systems

Th. Stöhlker, A. Gumberidze, M. Trassinelli, V. Andrianov, H. F. Beyer,
S. Kraft-Bermuth, A. Bleile, P. Egelhof, and The FOCAL collaboration

Gesellschaft für Schwerionenforschung, Darmstadt, Germany
T.Stoehlker@gsi.de

Abstract. In this review we address the topic of X-ray spectroscopic investigations of the ground-state transitions in the heaviest one-electron systems by using the intense beams of cooled heavy ions provided by the Experimental Storage Ring (ESR) at GSI Darmstadt. Such experiments on high- Z ions open up unique possibilities for the investigation of the quantum electrodynamical (QED) effects in the nonperturbative domain of extremely strong electromagnetic fields. Particular emphasis is given to the developments as well as to the current progress for the future experiments aiming for the sensitive tests of the higher-order bound-state QED effects. These include novel high-resolution detection systems: crystal spectrometers in combination with position-sensitive solid-state detectors and bolometers.

1 The Current Status of the Experimental and Theoretical Investigations

Hydrogen-like ions traditionally serve as an important testing ground for fundamental atomic structure theories and for investigation of relativistic and QED effects. Atomic hydrogen has provided the unique venue for the development, testing and establishment of the quantum mechanical and relativistic theories. Furthermore, the discovery by Lamb and Rutherford [1] of a small difference between the binding energies of the $2s_{1/2}$ and $2p_{1/2}$ states, known as the Lamb shift, has triggered the decisive developments in the formulation of the QED theory. For the light one-electron systems such as atomic hydrogen, the QED predictions are now well confirmed with extraordinary precision [2, 3]. On the other hand, the developments in efficient production and storing of the heaviest one- and few-electron systems provide a complementary way for testing our understanding of relativistic and quantum electrodynamic effects in the formerly not accessible domain of extremely strong fields. Furthermore, during the last few years significant progress took place in the theoretical studies of these systems, resulting in nonperturbative (without expansion in αZ ,

in contrast to the methods applied for the low- Z ions) calculations for high- Z hydrogen-like systems which do now comprise all second-order (in α) corrections [4, 5]. For such ions, the most direct experimental approach for the investigation of the effects of quantum electrodynamics in strong Coulomb fields is a precise determination of X-ray energies for transitions into the ground state of the ion. In particular, the Lyman- α transitions are used as they appear most intense and well resolved in the X-ray spectra. In these experiments the Lamb shift value is deduced from the measured transition energy by comparison with the Dirac energy eigenvalue for the $1s$ ground state of a point-like nucleus and the additional assumption that the binding energies of the excited states involved are known to high accuracy.

The Experimental Storage Ring (ESR) at GSI with its brilliant beams of cooled heavy ions has proven to provide unique conditions for precision investigations of high- Z fundamental atomic systems. Experimental studies at the ESR devoted to precise spectroscopy of X-ray transitions from bound or continuum states into the ground state of the heavy ion-electron systems have provided substantial improvements in accuracy over the last decade. In Fig. 1 this is shown for the example of the $1s$ Lamb shift in H-like uranium (U^{91+}). Here, an increase of precision by more than an order of magnitude over the last decade has been achieved. The most recent value (from 2005) has been obtained at the electron cooler device of the ESR by utilizing the deceleration capability of the ring in combination with the 0° geometry [6].

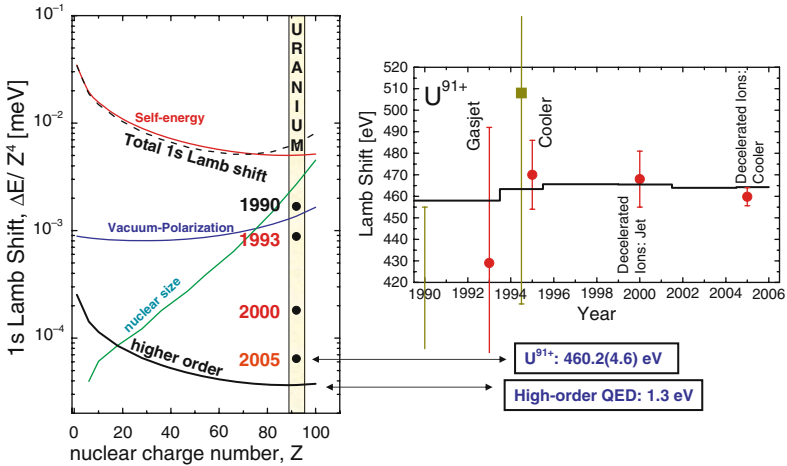


Fig. 1. Left side: Various individual contributions to the ground-state Lamb shift in H-like uranium together with the experimental accuracies achieved so far [6, 7, 8, 9]; **Right side:** Comparison between theoretical and experimental values for the $1s$ Lamb shift in H-like uranium. Squares show results obtained at the BEVALAC accelerator. Circles depict the values obtained at the ESR. The theory is represented by the line

Table 1. The ground-state Lamb shift for H-like uranium. All values are given in eV

Finite nuclear size	198.81
First order QED	266.45
Second order QED	-1.26(33)
Total theory [4, 5]	464.26±0.5
Experiment	460.2±4.6

The latest experimental result is presented in Table I in comparison with the most recent theoretical value. The latter includes all of the second-order (α^2) QED contributions whose evaluations have been completed very recently, following the work during the last decade (see [4, 5] and references therein). From the comparison, a good agreement between the theoretical prediction and the experimental value can be stated whereby the experimental result provides a test of the leading QED effects at the percent level.

2 Next Generation Spectroscopic Experiments on High- Z H-like Ions

The recent achievement of complete evaluation of all the second-order (α^2) QED effects opens up unique opportunities for probing higher-order QED effects in the most fundamental atomic system in the presence of strongest electromagnetic fields. Accordingly, the goal of the experiments is to achieve a precision which not only tests the higher-order contributions in αZ but also probes QED corrections which are beyond the one-photon exchange corrections, such as the two-photon exchange diagrams, i.e., α^2 contributions. These effects contribute on the level of about 1 eV (see Table I). Therefore, for the next generation experiments devoted to the ground-state Lamb shift in high- Z H-like systems, a dedicated high-resolution X-ray crystal spectrometer (FOCAL) has been developed at GSI [10, 11, 12]. This development is complemented by progress in production of semi-conductor position-sensitive (two-dimensional) detectors [13] which are indispensable for the crystal-spectrometer-based precision X-ray spectroscopy. In addition, a different kind of high-resolution X-ray detection system, a X-ray calorimeter, has been developed at GSI and will be exploited in the future Lamb shift studies [14].

Very recently, a first experiment utilizing these devices has been conducted at the gasjet target of the ESR devoted to a measurement of the ground-state Lamb shift in H-like Pb. The setup used in the experiment is shown in Fig. 2. The bare Pb ions injected from the SIS into the ESR were brought to interact with a supersonic jet of krypton atoms. Here, the ions may capture an electron thus populating bound states of a hydrogen-like lead ion (Pb^{81+}). The ground-state binding energy and thus the Lamb shift can be directly derived from the centroid energy of the Lyman α_1 X-rays which can be obtained with high

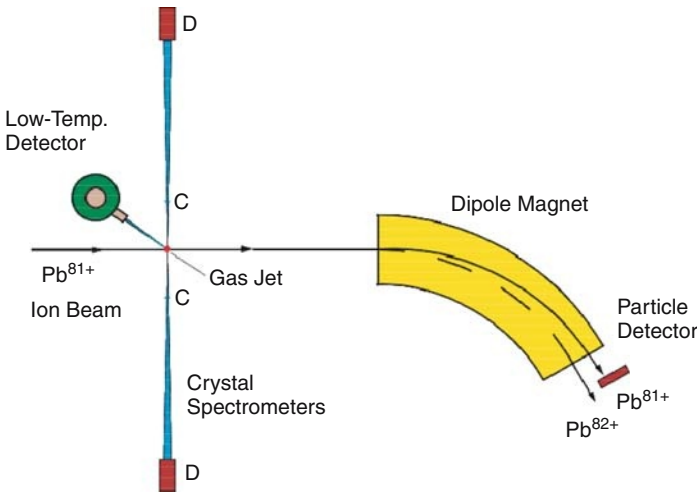


Fig. 2. The experimental arrangement used in the first beam-time dedicated to measure ground-state Lamb shift in H-like Pb exploiting high-resolution X-ray spectrometers in combination with position-sensitive Ge(i) detectors as well as the specially developed low-temperature microcalorimeter

accuracy from one hand by the spectrometer and the 2D-detector setup and from the other hand by the microcalorimeter. In the present experiment, two of the crystal spectrometers were aligned at 90° with respect to the beam direction in order to reduce uncertainties stemming from the relativistic Doppler transformation due to possible ion beam misalignment. Position-sensitive Germanium detectors were mounted behind both of the spectrometers for energy and time-resolved detection of Lyman X-rays deflected by the spectrometers.

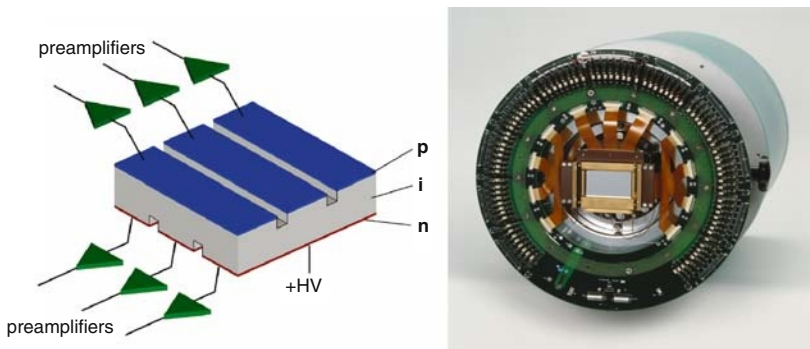


Fig. 3. Two-dimensional germanium X-ray detector developed at FZ Jülich [\[13\]](#). The front contact (128 strips and a pitch of 250 μm) and the rear contact (48 strips and a pitch of 1167 μm) are realized by means of plasma etching

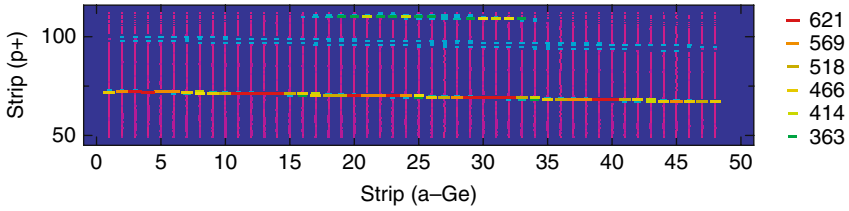


Fig. 4. Calibration line of the ^{169}Yb source projected on the position-sensitive detector mounted behind one of the spectrometers. For details see text

One of the detectors exploited in the experiment is shown in Fig. 3. The calorimeter was mounted at 145° with respect to the beam direction.

In Fig. 4 we show an X-ray image of the ^{169}Yb source as recorded by a 2D position-sensitive Germanium detector mounted behind one of the spectrometers. The intense line corresponds to the ^{169}Yb γ photons with an energy of 63.121 keV. This line is used for calibration purposes, and energies of the Lyman X-rays expected at about 60.98 and 63.13 keV in the laboratory frame will be determined relative to it. In addition, in Fig. 5 we present a preliminary X-ray spectrum recorded by the calorimeter for a run with H-like uranium. Here, the Lyman α_1 , Lyman α_2 as well as Lyman β lines are clearly identified along with 59.8 keV γ -line of the ^{241}Am source used for calibration. The data analysis is currently being conducted.

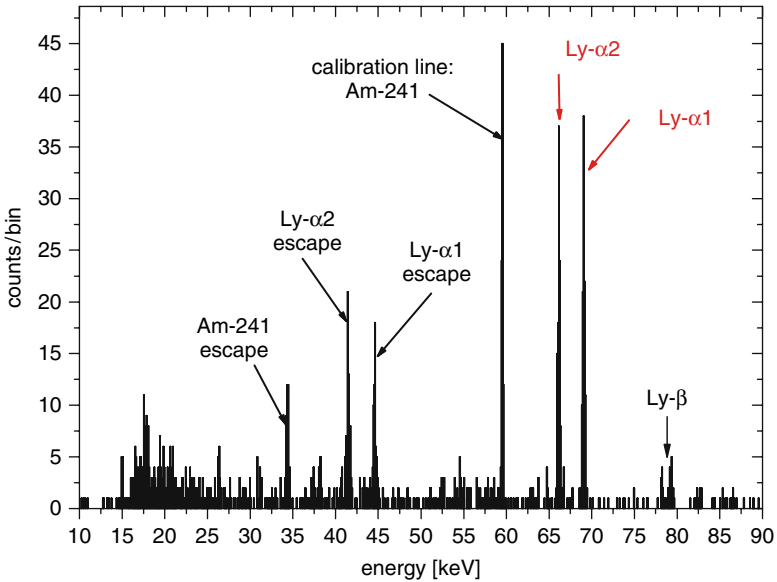


Fig. 5. The preliminary X-ray spectrum of the H-like uranium recorded by the calorimeter mounted at the 145° observation angle with respect to the beam axis

3 Conclusions

The current status and recent developments in experimental investigations of the strong field QED effects in heaviest hydrogen-like ions are reviewed. Comparison of the most recent experimental results with the state-of-the-art theoretical values shows a good agreement and provides test of the dominant QED contributions on a percent level. In order to reach the sensitivity needed for testing the higher-order QED contributions the next-generation spectroscopic experiments will exploit the high-resolution X-ray detection systems, the specially developed FOCAL crystal spectrometers in combination with the state-of-the-art position-sensitive germanium detectors and the low-temperature calorimeters. The beam-time utilizing both of these devices has already been conducted providing the first high-resolution spectra for ground-state transitions in hydrogen-like lead. From the current status of the data evaluation, we can conclude that the achievement of the envisioned accuracy will require improvements in the detection setup and thus reduction of various systematic uncertainties as well as developments for the digital signal processing which are currently being conducted [115](#).

Acknowledgment

The close collaboration and support by the members of the ESR team is gratefully acknowledged. One of the authors (M.T.) was sponsored by the Alexander von Humboldt Foundation. This work was supported by I3 EURONS under EC Contract No. 506065.

References

1. W. E. Lamb and R. C. Retherford: Phys. Rev. **72**, 241 (1947). [157](#)
2. M. Niering et al.: Phys. Rev. Lett. **84**, 5496 (2000). [157](#)
3. B. de Beauvoir et al.: European Physical Journal D**12**, 61 (2000). [157](#)
4. V. A. Yerokhin et al.: Phys. Rev. A**64**, 062507 (2001). [158](#) [159](#)
5. V. A. Yerokhin et al.: Phys. Rev. Lett. **91**, 073001, (2003). [158](#) [159](#)
6. A. Gumberidze, Th. Stöhlker, D. Banas, K. Beckert, P. Beller, et al.: Phys. Rev. Lett. **94**, 223001, (2005). [158](#)
7. Th. Stöhlker et al.: Phys. Rev. Lett. **71**, 2184 (1993). [158](#)
8. H. F. Beyer et al.: Z. Phys. D**35**, 169 (1995). [158](#)
9. Th. Stöhlker et al.: Phys. Rev. Lett. **85**, 3109 (2000). [158](#)
10. H. F. Beyer et al.: NIM A**400**, 137, (1997). [159](#)
11. H. F. Beyer, Th. Stöhlker, D. Banas, D. Liesen, D. Protic, K. Beckert, P. Beller, J. Bojowald, F. Bosch, E. Forster, B. Franzke, A. Gumberidze, S. Hagmann, J. Hoszowska, P. Indelicato, O. Klepper, H.-J. Kluge, S. König, C. Kozhuharov, X. Ma, B. Manil, I. Mohos, A. Orsic-Muthig, F. Nolden, U. Popp, A. Simionovici, D. Sierpowski, U. Spillmann, Z. Stachura, M. Steck, S. Tachenov, M. Trassinelli, A. Warczak, O. Wehrhan and E. Ziegler: Spectrochim. Acta, Part B **59**, 1535 (2004). [159](#)

12. S. Chatterjee et al.: NIM B**245**, 67 (2006). [159](#)
13. D. Protic et al.: IEEE Transactions on Nuclear Science **52**, 3194 (2005). [159](#), [160](#)
14. A. Bleile et al.: NIM B**444**, 488 (2000). [159](#)
15. M. Kajetanowicz, et al.: Radiation Physics and Chemistry **75**, 1972 (2006). [162](#)

Pionic Hydrogen

D. Gotta¹, F. Amaro², D. F. Anagnostopoulos³, S. Biri⁴, D. S. Covita²,
H. Gorke¹, A. Gruber⁵, M. Hennebach^{1,8}, A. Hirtl⁵, T. Ishiwatari⁵,
P. Indelicato⁶, Th. Jensen^{6,9}, E.-O. Le Bigot⁶, J. Marton⁵, M. Nekipelov¹,
J. M. F. dos Santos², S. Schlessler⁶, Ph. Schmid⁵, L. M. Simons⁷,
Th. Strauch¹, M. Trassinelli^{6,10}, J. F. C. A. Veloso², and J. Zmeskal⁵

¹ Institut für Kernphysik, Forschungszentrum Jülich, D-52425 Jülich, Germany
d.gotta@fz-juelich.de

² Department of Physics, Coimbra University, P-3000 Coimbra, Portugal

³ Department of Material Science and Engineering, University of Ioannina,
Ioannina, GR-45110, Greece

⁴ Institut of Nuclear Research, Hungarian Academy of Sciences, H-4001
Debrecen, Hungary

⁵ Stefan Meyer Institut, Austrian Academy of Sciences, A-1090 Vienna

⁶ Laboratoire Kastler Brossel, UPMC-Paris 6, ENS, CNRS; Case 74, 4 place
Jussieu, 75005 Paris, France

⁷ Paul Scherrer Institut, Villigen PSI, CH-5232 Villigen, Switzerland

⁸ WTI GmbH, D-52428 Jülich, Germany (present address)

⁹ Ringkjøbing Gymnasium, Vasevej 24, 6950 Ringkjøbing, Danmark (present
address)

¹⁰ Gesellschaft für Schwerionenforschung, Plankstr. 1, D-64291, Darmstadt,
Germany (present address)

Abstract. Strong-interaction shift ε_{1s} and broadening Γ_{1s} in the pionic hydrogen atom are determined from the energies and line widths of X-ray transitions to the $1s$ ground state. They are directly connected to the πN scattering lengths which are related to the πN coupling constant and the πN *sigma* term being a measure of chiral symmetry breaking. Therefore, the measurement of the pion–nucleon s -wave scattering lengths constitutes a high-precision test of the methods of chiral perturbation theory (χ PT), which is the low-energy approach of QCD. Additional constraints for the πN scattering lengths are obtained from the measurement of the ground-state shift in pionic deuterium. The hadronic width is linked to s -wave pion production in nucleon–nucleon collisions. A new experiment, set up at the Paul Scherrer Institut (PSI), has finished taking data recently and will allow the determination of the scattering lengths at the few per cent level.

1 Introduction

Quantum chromodynamics (QCD) is today’s microscopic theory of strong interaction based on colored fermions – the quarks – and colored massless spin

one-field quanta – the gluons. At highest energies, perturbative methods are applied with great success because of the decreasing strength of the interaction as described by a running strong coupling constant α_s (asymptotic freedom). At low energies, in the non-perturbative regime, a new framework – *chiral perturbation theory* (χ PT) – has been proposed [1], which exploits the left–right symmetry of the QCD Lagrangian in an *ideal world* of 2 (or 3) massless light quarks u , d (and s) (chiral limit). Here *chirality* is conserved forever and pions become stable and even massless. In the *real world* chiral symmetry of the strong force is explicitly broken because of finite masses of about 3, 5 and 95 MeV/ c^2 for the u , d and s quark [2]. Such small (current) quark masses are, however, unable to explain the masses of the hadron multiplets.

The weak decay of pseudoscalar (0^-) fields like pions corresponds to the non-conservation of the axial charge hiding the chiral symmetry. It results in a non-zero expectation value $B = |\langle 0 | \bar{q}q | 0 \rangle|$ (chiral condensate) of $q\bar{q}$ states between the QCD vacuum (spontaneous chiral symmetry breaking). This fact is known from current algebra as partially conserved axial current (PCAC) [3, 4]. Furthermore, neutron decay can be regarded as the strong decay $n \rightarrow p\pi^-$ and subsequent pion disintegration which connects the strong πN coupling constant $f_{\pi N}$, the weak pion decay constant F_π and the weak axial coupling g_A by $f_{\pi N} = m_{\pi^\pm} g_A / 2F_\pi$ (Goldberger–Treiman relation [5]). A comprehensive discussion is given, e. g., in [6].

Spontaneous symmetry breaking leads mandatorily to eight massless pseudoscalar particles (Goldstone bosons) which may be identified with the 0^- meson octet (π, K, η). Finite masses of these pseudoscalar mesons, though well below the usual hadronic scale of 1 GeV/ c^2 , especially in the case of pions, require both finite current quark mass values and a non-vanishing chiral condensate. In lowest order their masses are given by the Gell-Mann–Oakes–Renner relations [7]. For the case of pions, e. g., $m_\pi^2 = \frac{1}{2}(m_u + m_d)B/F_\pi^2 + \text{higher orders}$. The chiral condensate, equal for all pseudoscalar mesons, adjusts the physical masses of the pseudoscalar octet. The parameters B and F_π are principally calculable within lattice QCD, but precise values still must be determined from experiment. An introduction to the concepts describing the structure of hadrons and the methods of χ PT may be found elsewhere [8, 9, 10].

Approaching the chiral limit, degrees of freedom are field quanta like pions, to be described by the methods of field theory. Their interaction with (hadronic) matter can be regarded as a kind of residual interaction of QCD and is strongly influenced by the underlying chiral symmetry. On the strong-interaction scale corresponding to about the nucleon’s mass, the zero mass limit is closely approached considering light mesons like the pion because of $(m_\pi/M_p)^2 \approx 2\% \ll 1$. Therefore, a perturbative approach within an effective field theory (χ PT) becomes possible [1, 11, 12, 13] where symmetry properties of the QCD Lagrangian manifest in observables by means of low-energy theorems. A (chiral) expansion ordered by counting the powers of (small) momenta, the quark mass difference ($m_d - m_u$) and the fine structure constant

α allows to include on the same footing strong isospin breaking effects resulting from the mass difference ($m_d \neq m_u$) and those of electromagnetic origin. The unknown structure of QCD at short distances is parameterized by so-called low-energy constants (LECs) and, disregarding future lattice QCD calculations, must be taken from experiment.

According to its origin, χ PT works best for the lightest quarks u and d as combined in the lightest strongly interacting particle – the pion – and for the description of the pion–pion interaction [14, 15]. The experimental approach, however, is very demanding [16, 17]. On the other hand, it has been shown that such an approach can also be applied to the meson–nucleon case, then often denoted as *Heavy Baryon Chiral Perturbation Theory* (HB χ PT) [9, 10, 13, 18, 19].

So called *sigma terms* represent the contribution from the finite quark masses to a baryon’s mass. Applied, e.g., to the proton and u and d quarks the resulting πN σ term $\sigma_{\pi N} = \frac{1}{2}(m_u + m_d) | \langle p | \bar{q}q | p \rangle |$ measures that contribution from the quark–antiquark pairs $u\bar{u} + d\bar{d}$ at the (unphysical) Cheng–Dashen point $s - u = 0$, $t = 2m_\pi^2$ (s, t, u are the Mandelstam variables). Though located outside the physical region, *sigma terms* are related to observables by extrapolation of meson–baryon amplitudes into the unphysical region. Hence, scattering lengths are of great importance because they represent the closest approach in the real world. When comparing the result of the extrapolation to the HB χ PT result, $\sigma_{\pi N}$ is sensitive to the $\bar{s}s$ contents of the nucleon [20, 21].

Exotic atoms provide an ideal laboratory to study the low-energy strong meson–baryon interaction without the need of any extrapolation to threshold because relative energies are restricted to the keV range [22]. The experiment described here aims at a precise determination of the hadronic shift ε_{1s} and broadening Γ_{1s} by measuring the transition energies and line widths of the K X-radiation from pionic hydrogen (πH) [23] in order to extract the πN scattering lengths to an accuracy of a few per cent. Further constraints will be achieved by a similar measurement of pionic deuterium (πD) [24].

At first, relations between scattering lengths, pionic atom observables and mechanisms of formation and de-excitation of pionic-hydrogen atoms are outlined. The measurement strategy is introduced followed by a short description of the experimental approach. Results achieved in earlier measurements and preliminary ones of this experiment are briefly discussed.

2 Pion–Nucleon Interaction at Threshold

Pions and nucleons combine to isospin 1/2 or 3/2 systems. For the two parameters one may choose the isoscalar and isovector scattering lengths a^+ and a^- , which are given by the isospin combinations $a^+ = (a_{1/2} + 2a_{3/2})/3$ and $a^- = (a_{1/2} - a_{3/2})/3$ or in terms of the elastic reactions by $a^\pm = (a_{\pi^- p \rightarrow \pi^- p} \pm$

$a_{\pi^+p \rightarrow \pi^+p})/2$. In the limit of isospin conservation, the elastic channels are related to charge exchange by the isospin triangle, $a_{\pi^-p \rightarrow \pi^-p} - a_{\pi^+p \rightarrow \pi^+p} = -\sqrt{2} a_{\pi^-p \rightarrow \pi^0n}$. Obviously, then $a_{\pi^-p \rightarrow \pi^-p} = a^+ + a^-$ and $a_{\pi^-p \rightarrow \pi^0n} = -\sqrt{2} a^-$ holds. At threshold the πN interaction is completely described by two amplitudes reducing to two (real) numbers being identified with the s-wave scattering lengths.

Approaching threshold and considering negatively charged pions only two “nuclear” channels, $\pi^-p \rightarrow \pi^-p$ and $\pi^-p \rightarrow \pi^0n$, and the radiative capture reaction $\pi^-p \rightarrow \gamma n$ occur. The relative strength of charge exchange and radiative capture defines the Panofsky ratio determined to $P = 1.546 \pm 0.009$ [25].

The leading order result (LO) for a^+ and a^- derived from current algebra [26, 27] already revealed an important feature of the underlying chiral symmetry – the vanishing of the isoscalar combination a^+ in the chiral limit $a^+ = 0$ and $a^- = -0.079/m_\pi$. Deviations from these values are due to higher orders of the chiral expansion and should be small.

Within χ PT a^+ and a^- are pure QCD quantities and, therefore, substantial effort is undertaken to elaborate the corrections to relate the experimentally accessible quantities to a^+ and a^- [28, 29, 30, 31, 32, 33, 34]. The πN sigma term is determined by extrapolation of the amplitude a^+ to the Cheng–Dashen point. The πN coupling constant $f_{\pi N}^2/4\pi$ is related to a^- by dispersion relation methods (Goldberger–Miyazawa–Oehme sum rule [35]). The higher orders to be calculated by χ PT are obtained by comparison with the current algebra result $f_{\pi N, \text{LO}}^2/4\pi = 0.072$ (Goldberger–Treiman discrepancy Δ_{GT}) and are expected to be of the order of 2% [9, 10].

Access to the πN scattering lengths a^+ and a^- and $a_{\pi D}$ is given by

- Analysis of scattering data extrapolated to threshold
- Hadronic level shift $\varepsilon_{1s}^{\pi H}$ and broadening $\Gamma_{1s}^{\pi H}$ in pionic hydrogen as well as $\varepsilon_{1s}^{\pi D}$ in pionic deuterium.

In the limit of charge symmetry, $a_{\pi^-n \rightarrow \pi^-n} = a_{\pi^+p \rightarrow \pi^+p}$ holds. Then the isoscalar scattering length is also represented by $a^+ = (a_{\pi^-p \rightarrow \pi^-p} + a_{\pi^-n \rightarrow \pi^-n})/2$ which may be regarded as pion–deuteron scattering in the limit of a scattering on a free proton and neutron. To achieve the πD scattering length itself multiple scattering, nuclear structure and absorption must be taken into account. Significant corrections are expected, because the sum $a_{\pi^-p \rightarrow \pi^-p} + a_{\pi^-n \rightarrow \pi^-n}$ almost vanishes and, consequently, the hadronic shift in πD must be small compared to estimates using a simple geometrical scaling with respect to πH .

In πD scattering *true* inelastic channels are open and, hence, $a_{\pi D}$ becomes a complex number. The real part $\Re a_{\pi D}$, i. e., $a^+ + \text{corrections}$ accounts for single and multiple scattering and the imaginary part $\Im a_{\pi D}$ for true pion absorption ($\pi^-d \rightarrow nn$) and radiative capture ($\pi^-d \rightarrow nn\gamma$). The ratio of the dominant channels $(\pi^-d \rightarrow nn)/(\pi^-d \rightarrow nn\gamma)$ was found to be $P_{\pi^-d} = 2.83 \pm 0.04$ [36]. Other channels contribute only to 0.1%.

3 Scattering Lengths and Pionic Atoms

3.1 Pionic Hydrogen

The scattering lengths of the elastic channel $a_{\pi^-p \rightarrow \pi^-p}$ and the charge-exchange reaction $a_{\pi^-p \rightarrow \pi^0n}$ are related to the strong-interaction shift ε_{1s} and broadening Γ_{1s} by the Deser-type formulae [37, 38] with r_B being the exotic atom Bohr radius and B_{1s} the binding energy of the atomic ground state:

$$\frac{\varepsilon_{1s}}{B_{1s}} = -\frac{4}{r_B} a_{\pi^-p \rightarrow \pi^-p} (1 + \delta_\varepsilon), \quad (1)$$

$$\frac{\Gamma_{1s}}{B_{1s}} = 8 \frac{q_0}{r_B} \left(1 + \frac{1}{P}\right) [a_{\pi^-p \rightarrow \pi^0n} (1 + \delta_\Gamma)]^2. \quad (2)$$

In terms of the isospin odd and even amplitudes, $\varepsilon_{1s} \propto a^+ + a^-$ and $\Gamma_{1s} \propto (a^-)^2$ hold.

The quantities $\delta_{\varepsilon, \Gamma}$ represent the corrections to be applied to the experimentally determined scattering length in order to obtain pure strong-interaction quantities. Recent calculations for $\delta_{\varepsilon, \Gamma}$ performed within χ PT include the corrections for isospin breaking both from the electromagnetic interaction and the light quark mass difference on the same footing ($m_d - m_u$) [39, 40, 41, 42]. In the higher order terms of the chiral expansion further low-energy constants (LECs) appear. These constants have to be determined from experiment and not all of them are well known [39, 41]. Alternatively, a potential model [43] and phenomenological approaches [44] to $\delta_{\varepsilon, \Gamma}$ are presented, which differ substantially in the numerical values. Finally, the pionic-atom results must be consistent with the extrapolation of πN scattering data to threshold and πN phase-shift analyses [45, 46, 47].

3.2 Pionic Deuterium

In general, the complex pion-nucleus scattering length $a_{\pi A(Z, N)}$ is related to the measured shift ε_{1s} and width Γ_{1s} by the classical Deser formula [37]

$$\varepsilon_{1s} + i\Gamma_{1s}/2 = -(2\alpha^3 Z^3 m_{\text{red}}^2 c^4 / \hbar c) \cdot a_{\pi A}, \quad (3)$$

where m_{red} is the reduced mass of the pion-nucleus system. Because of the small ratio hadronic scattering length a to Bohr radius r_B of the exotic atom $|a|/r_B \ll 1$, second order corrections due to strong Coulomb interference as given by Trueman's expansion [48] have been neglected up to now in view of the experimental accuracy of several per cent. Then the relations $\varepsilon_{1s} \propto \Re a_{\pi D}$ and $\Gamma_{1s} \propto \Im a_{\pi D}$ are still sufficient.

Significant effort has been undertaken and is still going on to describe the πD interaction at threshold in the framework of chiral Lagrangians [49, 50, 51, 52, 53, 54], in particular, since the large contribution of the isospin breaking corrections has been realized [55]. The leading term is proportional to a^+ and,

hence, about one order of magnitude smaller than the corrections originating from multiple scattering.

$$\begin{aligned}
\Re a_{\pi d} &= S + D + \dots \\
&= \frac{1 + m_\pi/M}{1 + m_\pi/M_d} (a_{\pi^- p} + a_{\pi^- n}) \\
&\quad + 2 \frac{(1 + m_\pi/M)^2}{1 + m_\pi/M_d} \left[\left(\frac{a_{\pi^- p} + a_{\pi^- n}}{2} \right)^2 - 2 \left(\frac{a_{\pi^- p} - a_{\pi^- n}}{2} \right)^2 \right] \langle 1/r \rangle \\
&\quad + \dots \\
&= 2 \frac{1 + m_\pi/M}{1 + m_\pi/M_d} a^+ \\
&\quad + 2 \frac{(1 + m_\pi/M)^2}{1 + m_\pi/M_d} \left[\left(\frac{a^+}{2} \right)^2 - 2 \left(\frac{a^-}{2} \right)^2 \right] \langle 1/r \rangle \\
&\quad + \dots
\end{aligned} \tag{4}$$

Structure, multiple scattering and absorption effects are understood to be sufficiently under control [49, 50, 51, 56, 57, 58] and, consequently, $\Re a_{\pi d}$ *must* be expressible in terms of the elementary pion–nucleon amplitudes a^+ and a^- . Or vice versa, pionic deuterium yields a decisive constraint on the pionic hydrogen data.

In the limit of charge symmetry, pion absorption from the ground state in deuterium represents the inverse reaction of s-wave pion production $\pi^+ d \rightarrow pp$ at threshold. In both cases, the isospin $\Delta I = 1$ transition of the nucleon pair (${}^3S_1(I=0) \rightarrow {}^3P_1(I=1)$) is considered which has been found to dominate pion absorption at rest in the helium isotopes [59, 60]. The cross-section is parameterized by $\sigma(pp \rightarrow \pi^+ d) = \alpha C_0^2 \eta + \beta C_1^2 \eta^3$. The parameters α and β account for *s*- and *p*-wave production, respectively, $\eta = k_{\pi D}/M_\pi$ is the reduced momentum of the pion in the πD rest frame, and the factors C_i take into account the Coulomb interaction. Detailed balance relates α to the hadronic width in πD by $\Im a_{\pi D} = M_p \alpha / 6\pi$ [61].

Pion production in pp collisions is well studied at low energies. The average of the most recent data yield $\alpha \approx 215 \mu\text{b}$ [62, 63], which results in $\Im a_{\pi D} \approx (0.0037 \pm 0.0004) m_\pi^{-1}$. The result from the pionic deuterium width, corrected for $P_{\pi D}$, is $\Im a_{\pi D} = (0.0043 \pm 0.0005) m_\pi^{-1}$.

A first study in the approach of χ PT including the next-to-leading order (NLO) terms yields $\alpha^{\text{NLO}} \approx 220 \pm 70 \mu\text{b}$ [64]. The accuracy of the calculation is expected to improve by at least a factor of three within a few years [65]. Without the need of extrapolation to threshold the hadronic width of πD , to be significantly improved in the new πD experiment, provides the quantity α at the few per cent level.

4 Atomic Cascade in Pionic Hydrogen

Exotic atoms are formed when the kinetic energy of negatively charged particles like muons, pions or antiprotons are slowed down to a few eV. After capture by the Coulomb field of the nucleus into highly excited states a de-excitation cascade starts (Fig. 1). In atoms with $Z > 2$ the upper part of the cascade is dominated by Auger emission because the de-excitation rate depends on the energy difference $\Delta E_{nn'}$ between two levels n and n' by $\Gamma_{\text{Auger}} \propto (1/\sqrt{\Delta E_{nn'}})$. In the lower part X-ray emission becomes more and more important owing to $\Gamma_X \propto (\Delta E_{nn'})^3$. In the case of hadronic atoms the overlap of nuclear and atomic wave functions becomes significant and the occurrence of nuclear reactions from the low-lying states leads to level shifts and broadenings observable in X-ray transitions. A detailed discussion of the exotic-atom cascade may be found in [66].

In the case of a fully depleted electron shell already in the intermediate part X-ray emission dominates. Such a situation occurs for medium Z atoms when electron refilling is suppressed by using dilute targets [67, 68, 69]. This allows to use hydrogen-like exotic atoms as calibration standards in the few keV range because finite size effects are still negligibly small [70].

In $Z = 1$ exotic atoms, i. e., hydrogen, additional de-excitation processes play a decisive role. Because internal cascade processes proceed like $\Gamma_X \propto Z^4$,

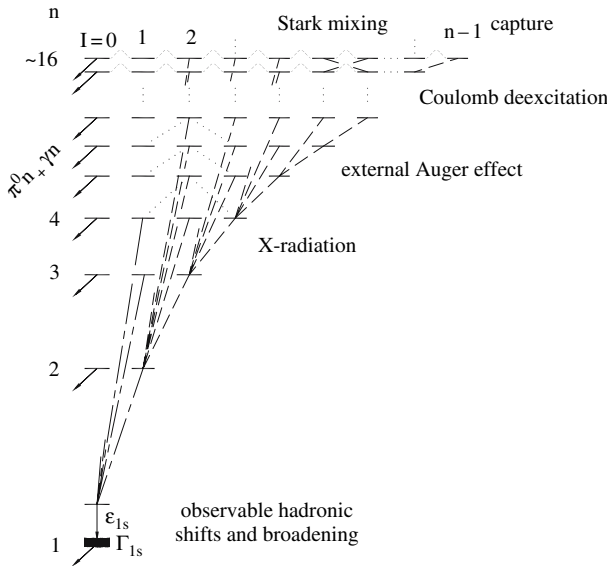


Fig. 1. Atomic cascade in pionic hydrogen. The transition energies of the $2p - 1s$, $3p - 1s$ and $4p - 1s$ X-rays are 2.4, 2.9 and 3.0 keV. The hadronic parameters ε_{ns} and Γ_{ns} scale with $1/n^3$. In case of pionic hydrogen, the s-wave interaction is attractive resulting in an increase of the binding energy ($\varepsilon_{1s} > 0$)

there is a frequent chance for collisions during the life time of the exotic system. In addition, exotic hydrogen is electrically neutral and, therefore, penetrates easily into other molecules of the target and experiences a strong Coulomb field there. Several processes competing during the cascade are briefly discussed below.

- *Stark mixing:* Within an electric field, to the pure parity states $|n\ell m\rangle$ admixtures are induced from states of the same principal quantum number n but different angular momentum according to the selection rules $\Delta\ell = \pm 1$ and $\Delta m = 0$ [71]. In the case of pions the induced low angular momentum leads to nuclear reactions already in high n states, which in turn depletes the cascade and reduces significantly the X-ray yields (Day–Snow–Sucher effect [72]). In the case of pionic hydrogen, only s-wave components experience the strong interaction.
- *Coulomb de-excitation:* The energy release for the de-excitation step $(\pi p)_{nl} \rightarrow (\pi p)_{n'l'}$ may be converted to a kinetic energy increase between the collision partners π^-p and H (bound in an H_2 molecule). Coulomb de-excitation has been observed directly first by a Doppler broadening of time-of-flight distributions of neutrons from the two-body reaction $\pi^-p \rightarrow \pi^0n$ [73]. Doppler contributions from several radiationless transitions $n \rightarrow n'$ were identified and kinetic energies up to 209 eV corresponding to 3–2 transitions have been seen both in liquid hydrogen and at a pressure of 40 bar. The acceleration increases (i) the collision probability and (ii) in the case of subsequent photon emission leads also to Doppler broadening of X-ray lines. As observed in the time-of-flight experiment, Coulomb transitions occur at any stage of the cascade, hence, a superposition of the various components is measured. Coulomb de-excitation even at lowest densities has been observed in muonic hydrogen μH [74]. There, however, no depletion of the cascade occurs by hadronic effects.
- *Inelastic and elastic scattering:* Between two radiationless transitions the velocity of the πH system is moderated by elastic and inelastic collisions, e. g., external Auger effect. For a precise determination of the hadronic width, the knowledge of the correction owing to the Doppler broadenings is indispensable. Important to mention, the Doppler broadening as measured by the neutrons may be composed very differently. The reaction $\pi^-p \rightarrow \pi^0n$ takes place from ns states with mainly $n = 2-5$, whereas initial states $\pi H(np - 1s)$ X-ray transitions can be populated only by transitions from the outer part of the cascade.
- *Molecular formation:* As well established in muon-catalyzed fusion the collision of a μH atom with H_2 leads to resonant formation of complex molecules like $(\pi H)_{nl} + H_2 \rightarrow [(pp\pi)_{nvj} p]2e^-$ [75]. The quantum numbers v and j denote vibrational and total angular momentum of the 3-body molecular state. Similarly the 3-body system $(pp\pi)_{nvj}$ should be formed which is assumed to de-excite mainly by Auger emission [76, 77, 78]. But beforehand it cannot be excluded that a small fraction of a few per cent

of πH atoms bound into such molecules decays radiatively to the ground state. Decaying from molecular states small X-ray line shifts occur – always to lower energies – which cannot be resolved and, hence, could falsify the extracted hadronic shift. In the case of πD , it is predicted that the fraction of X-ray emission increases significantly [78]. However, it must be mentioned that metastable $2s$ states cannot occur for pions because of the nuclear reactions.

Besides small shifts due to the existence of molecular levels, Auger stabilization of $[(pp\pi)_{nvj} p]$ molecules is discussed. Again Auger transitions with lowest energy difference are preferred and satellites may occur a few eV below the line energy of the isolated system.

5 Experimental Approach

Both Coulomb de-excitation and molecule formation are scattering processes and, hence, depend on the collision rate, i. e., on density. Consequently, the strategy of the experiment was to study X-ray transitions at different densities. To be in addition sensitive to the initial state dependence of the maximal Doppler broadening, all πH transitions of sufficient line yield were also measured.

- The $\pi H(3p - 1s)$ line (only in this case a suitable calibration line is available) was studied in the density range equivalent to 3.5 bar to liquid hydrogen, which corresponds to about 700 bar pressure.
- Information on Coulomb de-excitation is obtained by measuring besides the $\pi H(3p - 1s)$ also the $\pi H(4p - 1s)$ and the $\pi H(2p - 1s)$ transitions. An increasing total line width with decreasing initial state must be expected because of the larger energy gain possible for the feeding transition, whereas the hadronic broadening is due to the $1s$ level only and therefore the same for all three lines.
- The measurement of the line width in muonic hydrogen allows the determination of the Doppler broadening without the necessity to subtract the hadronic line width. In this way a detailed comparison with predictions from cascade calculations on effects caused by Coulomb de-excitation becomes possible.

5.1 Set-Up at PSI

The new pionic hydrogen experiment is performed at the Paul Scherrer Institut (PSI, Switzerland). The experiment is set up at the high-intensity low-energy pion beam $\pi E5$ and consists of the cyclotron trap II, a cryogenic target, a reflection-type crystal spectrometer equipped with spherically bent crystals and a large-area CCD array for position-sensitive X-ray detection (Fig. 2). It is based on techniques developed and applied to the precision spectroscopy

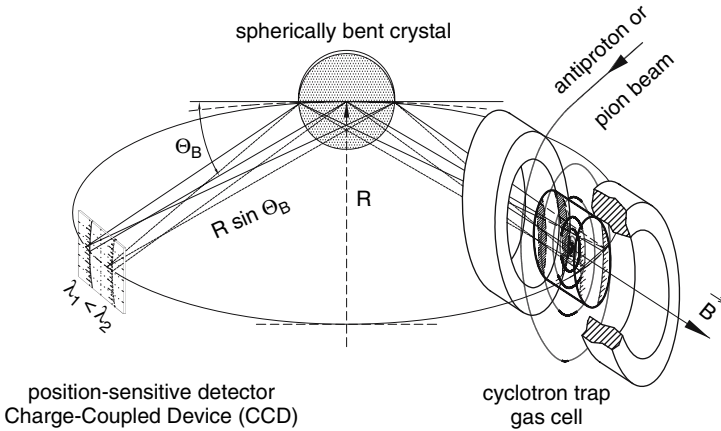


Fig. 2. Johann-type set-up of the Bragg spectrometer using the cyclotron trap to produce a high stop density for pions and a two-dimensional X-ray detector allowing the simultaneous measurement of an energy interval of several eV

of X-rays with the cyclotron trap I from antiprotonic and pionic atoms [22] together with substantial improvements in background suppression compared to the earlier πH experiments [79, 80].

The cyclotron trap, basically consisting of a superconducting split coil magnet, provides a concentrated X-ray source of suitable extension for a focusing low-energy Bragg spectrometer. Such a device is superior in stop density to a linear stop arrangement by two orders of magnitude [81] and is indispensable because Stark mixing and hadronic reactions reduce the πH K X-ray line to a few per cent only [82].

After injection into the trap the beam is degraded by moderators in order to spiral into a gas cell positioned in the axis of the trap with a few revolutions only because of short pion life time. The wall of the gas cell is made of $50\ \mu\text{m}$ thick kapton stabilized by a metallic frame and with a thin window of typically $7.5\ \mu\text{m}$ mylar towards the crystal spectrometer. Higher densities than 1 bar of the target gases hydrogen and deuterium are established by cooling. At a pressure of 1 bar, about 0.5% of the incoming pions are stopped in the gas increasing linearly with density. In this experiment, cyclotron trap II has been used. Having a larger gap between the coils, one order of magnitude higher stop rates for muons could be achieved than for trap I. The muons are produced inside the trap from slow pions decaying close to the center of the magnet. Muon stop rates are typically 10% of the ones for pions.

X-rays emitted from the target gas are reflected by spherically bent silicon or quartz Bragg crystals of 10 cm diameter having a radius of curvature of about 3 m. To keep aberrations (mainly from Johann broadening) small, the reflecting area is restricted to 60 mm horizontally. The spherical bending leads

to a partial vertical focusing, which increases the count rate. Typical Bragg angles are between 40° and 54° .

The X-rays are detected by a large-area two-dimensional position-sensitive detector built up from an array of six charge-coupled devices (CCDs) of type CCD22 with frame storage option [83]. Each CCD provides 600×600 pixels of $40 \mu\text{m} \times 40 \mu\text{m}$ size yielding a total sensitive area of $48 \text{ mm} \times 72 \text{ mm}$ for the full array. With a depletion depth of about $30 \mu\text{m}$ the efficiency is maximal around 3.5 keV, ideally suited for the pionic and muonic X-rays having energies between 1.9 and 3.1 keV. The devices are cooled to -100°C and located inside a cryostat, which is separated from the spectrometer vacuum by an $5 \mu\text{m}$ thick aluminized mylar window.

An important feature when using CCDs as X-ray detectors is due to their two-dimensional sensitivity, the capability to analyze the hit pattern *and* having an energy resolution as good as high-performance Si(Li) detectors of typically 140 eV at 6 keV. At hadron machines, a high beam-induced background level is present from nuclear reactions. Such events, typically originating from Compton-induced processes, produce large structures. In comparison, the charge produced by few keV X-rays is collected in one or two pixels only. Together with massive concrete shielding (Fig. 3), a background reduction of more than two orders of magnitude is achieved, which is an decisive progress in view of exotic-atom X-ray rates of 20–100 per hour.

5.2 Energy Calibration

Johann-type spectrometers do not provide measurements of the absolute Bragg angle and, therefore, need a calibration line as close in energy as possible. The best choice is a narrow and intense transition in a hydrogen-like pionic atom not affected by strong interaction. In the case of pionic hydrogen the pair $\pi H(3p - 1s)$ and $\pi O(6h - 5g)$ fulfills these conditions. The large sensitive area of the X-ray detector allows the measurement of the $\pi H(3p - 1s)$ transition and a calibration line without any change in the spectrometer set-up (Fig. 4 – left). This calibration method is basically free of systematic errors due to long-term instability. At higher densities hydrogen and oxygen have to be measured alternately to prevent the oxygen gas from freezing (Fig. 4 – right).

Fluorescence X-rays are much broader due to the large Auger width and may show satellite structures depending even on the excitation mechanism. Unfortunately, for the other πH lines considered as well as for πD no pionic lines are available. For pionic deuterium the fluorescence X-rays from gallium (measured in third order) and chlorine had to be used to determine the energy of the $\pi D(3p - 1s)$ and $\pi D(2p - 1s)$ transition, respectively. The accuracy is about a factor of 2 less compared to the exotic-atom case.



Fig. 3. Set-up for the pionic hydrogen experiment in the $\pi E5$ area at PSI. The concrete shielding of about 1 m thickness is essential to reduce the pion-induced background

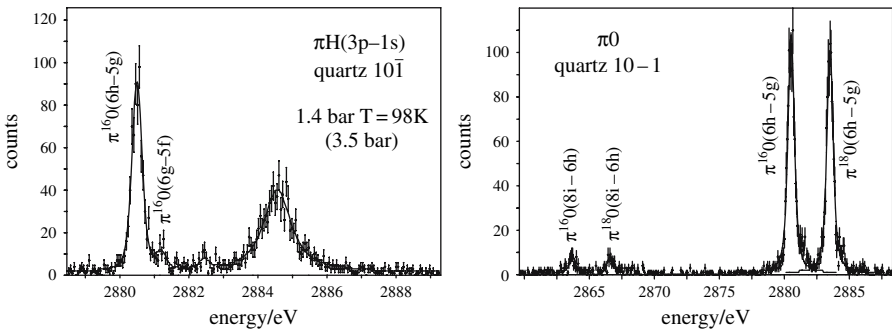


Fig. 4. Left: $\pi H(3p-1s)$ transition measured simultaneously with the $\pi O(6h-5g)$ transition by using an H_2/O_2 (90%/10%) gas mixture at an equivalent density of 3.5 bar. **Right:** $\pi O(6h-5g)$ transitions from the isotopes ^{16}O and ^{18}O . The energy splitting is used to verify the angular dispersion of the crystal spectrometer

5.3 Response Function

For the precise determination of the Lorentz contribution to the πH X-ray line shapes the knowledge of the crystal spectrometer response is required in detail. Because narrow fluorescence X-rays or few keV Γ lines for testing Bragg crystals are not available in practical cases, as a first approach narrow pionic-atom transitions were used [22, 80, 84]. Such lines have a natural width of a few tens of meV being negligible compared to the rocking curve width of silicon or quartz crystals of about 500 meV around 3 keV. Using CH_4 gas as target the experimental line shape was determined from the $\pi C(5g-4f)$ line, the energy of which is between the $\pi H(3p-1s)$ and $\pi H(4p-1s)$ transitions (Fig. 5 – left). In CH_4 a measurable Doppler broadening from Coulomb explosion is not expected, but cannot be completely excluded. The πC measurements reveal interesting cascade features by comparing the circular transition $\pi C(5g-4f)$ to the parallel transitions $\pi C(5f-4d)$ and $\pi C(5d-4p)$ and the $\pi C(5d-4p)$ line gives in addition access to the strong-interaction effects in the $4p$ states.

For a detailed measurement of the tails of the rocking curve the limited count rate, even at the high-flux pion channels, leads to unacceptable long measuring periods. Furthermore, a calibration line close to the $\pi H(2p-1s)$ transition at 2.4 keV is also desirable. Therefore, to allow an ultimate determination of the crystal properties, the technique of an Electron-Cyclotron-Resonance source has been used. In such a device few electron atoms are produced at high rates, in particular hydrogen- and helium-like systems which emit narrow X-ray lines because of the absence of Auger transitions.

The Electron-Cyclotron-Resonance Ion Trap (ECRIT), set up at PSI, uses the split coil magnet of the cyclotron trap to produce a bottle field with a high mirror ratio of about 4 [85]. A hexapole magnet is inserted in between the coils and the plasma is created by means of a 6.4 GHz high-frequency

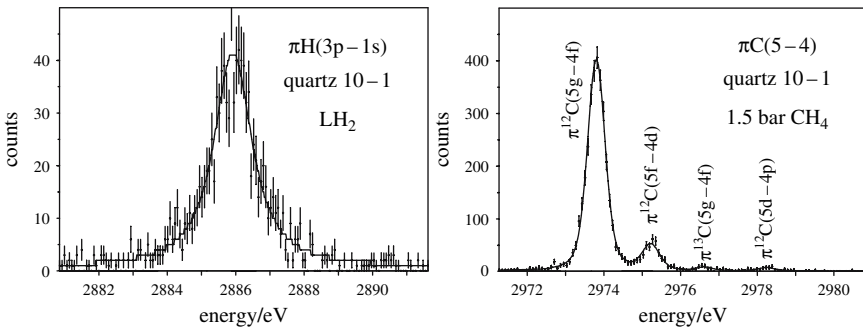


Fig. 5. Left: Preliminary determination of the crystal spectrometer response with the $\pi C(5g-4f)$ transition. The displayed spectra represent about 15% of the total width of the CCD array. **Right:** $\pi H(3p-1s)$ transitions as measured from liquid hydrogen

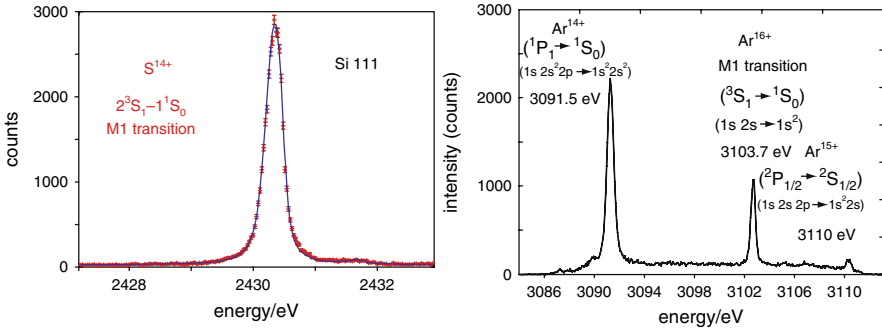


Fig. 6. Electronic X-rays from highly ionized sulfur and argon measured with a Si 111 crystal. The spectrometer response is determined from the M1 transition in He-like atoms

emitter. The crystal spectrometer was attached to one of the bore holes of the magnet. A cleaning magnet between ECRIT and Bragg crystal deflects the numerous electrons emitted on the magnet's axis in order to avoid a large background due to the scattered particles.

The plasmas were produced from sulfur, chlorine and argon, because for these elements the energies of the $2^3S_1 \rightarrow 1^1S_0$ M1 transitions coincide with the ones of the $\pi H(2p-1s)$, $\pi H(3p-1s)$ and $\pi H(4p-1s)$ lines. Count rates of up to 30000 per hour could be achieved allowing for a comprehensive diagnosis of the crystals (Fig. 6). In this way, focal lengths, the dependence of the resolution on apertures as well as the (asymmetric cut) angle between reflecting planes and surface could be determined precisely from the diffracted X-rays themselves [86]. A detailed study of X-ray emission from multiple charge states is in progress.

5.4 Muonic Hydrogen

The experimental response given, any additional broadening in muonic hydrogen transitions owes to Coulomb de-excitation. In Fig. 7 – left, the line shape of the $\mu H(3p-1s)$ line is compared to the resolution function as derived from the sulfur M1 transition.

Three components of the Doppler broadening are easily identified numerically by fitting the line shape. The kinetic energy distribution is modeled by four boxes adapted to cascade calculation (Fig. 7 – right) result with the relative weight being a free parameter in the fit. The two high energetic ones originating from Coulomb de-excitation between the states 5–4 and 4–3 are visible in the tails and as a kink at about 20% of the peak intensity, respectively. A low-energy component collects the transitions between higher states.

The spectrometer was set up in a way that an energy range of 10 eV to lower energies was accessible to allow the search for such satellite transitions stemming from Auger stabilization of molecule levels with subsequent X-ray

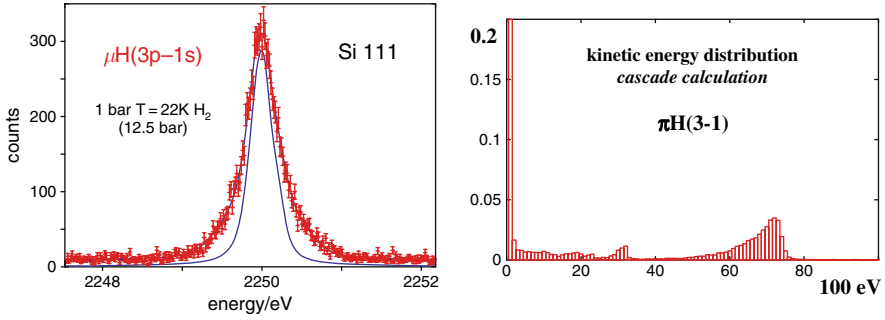


Fig. 7. **Left:** $\mu H(3p-1s)$ transition measured at an equivalent density of 10 bar. **Right:** Kinetic energy distribution as adapted from the cascade code of [88]. For fitting the measured $\pi H(3p-1s)$ spectrum the distribution was approximated by four Doppler boxes (0–2, 2–20, 29–33, 65–75) eV according to a low-energy component, (6–5), (5–4), (4–3) Coulomb transitions

de-excitation. No evidence was found for such nearby X-ray transitions from molecular states at the 1% level. This corroborates the findings from pionic hydrogen measurements where no pressure dependence of the $K\beta$ transition energy could be identified.

As an additional result the fit to the line shape gives a triplet to singlet ratio of 2.96 ± 0.63 as expected from a statistical population of 3:1 for the $3p$ hyperfine levels. Leaving even the energy splitting as a free parameter the result is consistent with the calculated ground-state splitting of 183 meV [87].

6 Results

6.1 Transition Energy and Hadronic Shift

In pionic hydrogen, no density dependence was observed for the energy of the $\pi H(3p-1s)$ transition within the full density range of 3.5 bar to liquid [84] (Fig. 5 – right). It is concluded that the radiative decay of molecules is suppressed in hydrogen. The energy values obtained at all densities are consistent within the errors. A weighted average was calculated and compared to the pure electromagnetic $\pi H(3p-1s)$ transition energy calculated to $E_{3p-1s}^{\text{QED}} = 2878.809 \pm 0.001$ eV [89]. The preliminary result for the shift in hydrogen of the new experiment ($R-98.01$) is

$$\epsilon_{1s}^{\pi H} = 7120 \pm 11 \text{ meV}. \quad (5)$$

The error represents the quadratic sum of the statistical accuracy and all systematic effects, which originate from spectrometer set-up, imaging properties of extended Bragg crystals, analysis and instabilities. The contribution

from the uncertainty of the pion mass is negligible because the energy calibration was performed with the pionic-atom transition $\pi^{16}O(6h - 5g)$. The new value for ε_{1s} is in good agreement with the result of the previous experiment (7.108 ± 0.036 eV), which used the cyclotron trap I and an energy calibration with argon $K\alpha$ fluorescence X-rays [80].

For pionic deuterium, two earlier measurements of the transitions $\pi D(3p - 1s)$ at 15 bar and $\pi D(2p - 1s)$ at 2.5 bar pressure found $\varepsilon_{1s}^{\pi D} = -2.43 \pm 0.10$ eV [79] (energy calibration with Ar $K\alpha$) and $\varepsilon_{1s}^{\pi D} = -2.469 \pm 0.055$ eV [90] (Cl $K\alpha$). Both experiments are of limited statistics and small contributions from satellites due to molecular formation cannot be excluded. The $\pi D(3p - 1s)$ experiment suffers in addition from a significant background level. The uncertainty of the $\pi D(2p - 1s)$ line energy is dominated by the accuracy of the Cl $K\alpha$ energy [91]. Therefore, a new high statistics measurement was performed recently, studying also the density dependence [24]. The analysis is in progress.

6.2 Line Width and Hadronic Broadening

For the $\pi H(2p - 1s)$ line, a significant increase of the total width was found compared to the $\pi H(3p - 1s)$ transition, which is explained by the higher energy release available from preceding transitions. Correspondingly, the $\pi H(4p - 1s)$ line was found to be narrower [84] (Fig. 8 – left).

Already from the $\pi H(4p - 1s)$ transition and using the $\pi C(5g - 4f)$ line for the spectrometer response, an upper limit for $\Gamma_{1s} < 0.850$ eV can be determined. A more refined analysis using the ECRIT measurements corroborates this finding. To extract the hadronic width, the Doppler broadening was modeled by 2, 3 and 4 components for the $\pi H(4p - 1s)$, $\pi H(3p - 1s)$ and $\pi H(2p - 1s)$ transitions. Very important is, due to the size of the detector, the possibility to cover fully the tails of the πH transitions. As important is a large enough region of background to the left and right.

The analyses of the three transitions $\pi H(2p - 1s)$, $\pi H(3p - 1s)$ and $\pi H(4p - 1s)$ lines, treating the relative intensities of the Doppler broadening as free parameters, yield consistent values for the hadronic broadening

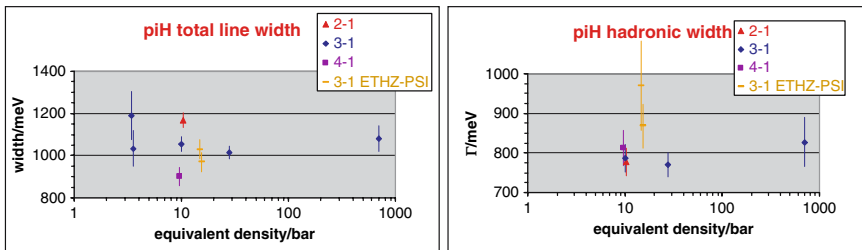


Fig. 8. Left: Total line width after subtraction of the spectrometer response only. **Right:** Hadronic width after subtraction of response and Doppler contributions

both for the various transitions and different densities (Fig. 8 – right). The averaged *preliminary* result of experiment R-98.01 is

$$\Gamma_{1s}^{\pi H} = 823 \pm 19 \text{ meV} \quad (6)$$

consistent with the result of the previous experiment ($\Gamma_{1s} = 865 \pm 69 \text{ meV}$ [80]).

The hadronic width in pionic deuterium extracted first from the $\pi D(3p - 1s)$ transition, $\Gamma_{1s}^{\pi D} = 1020 \pm 210 \text{ meV}$ [79], is in good agreement with the $\pi D(2p - 1s)$ measurement yielding $\Gamma_{1s}^{\pi D} = 1093 \pm 129 \text{ meV}$ [90]. Due to limited statistics the fit is not sensitive to any Doppler contribution to the line width. The value given for $\pi D(2p - 1s)$ line contains an estimate for the correction of $5 \pm 5\%$. The resolution function was obtained here from a measurement of the $\pi^{20}\text{Ne}(7i - 6h)$ line. In the new πD experiment a 20-fold higher statistics was collected and the ECRIT results are available for an ultimate description of the experimental response.

6.3 Scattering Length and Pion–Nucleon Coupling Constant

The shift ε_{1s} in πH yields the sum $a^+ + a^-$ of the isoscalar and isovector scattering lengths. In view of the precise experimental values, the accuracy is determined by the knowledge of the correction δ_ε (see Sect. 3). Within χ PT $\delta_\varepsilon = (-7.2 \pm 2.9)\%$ [41] has been obtained. The uncertainty originates mainly from one particular LEC (f_1), which is practically unknown and dominates the uncertainty of a^+ (see Fig. 9). The result also obtained within χ PT for the correction of the level broadening is reported to be $\delta_\Gamma = (0.6 \pm 0.2)\%$, [42]. Here, the LEC f_1 does not contribute and no significant uncertainty for the isovector scattering length a^- emerges from δ_Γ . An earlier approach for δ_ε and δ_Γ within a potential model ansatz led to $\delta_\varepsilon = (-2.1 \pm 0.5)\%$ and $\delta_\Gamma = (-1.3 \pm 0.5)\%$ [43] which, however, has been criticized to be incomplete.

As discussed earlier, any determination of a^+ from the hadronic shift in πD must be consistent with the values extracted from the πH results. Discrepancies have been reduced substantially by a recent calculation taking into account so-far neglected isospin breaking correction [55] (Fig. 9). Due to the smallness of a^+ these corrections amount to 42% in second order. The new and more precise measurement of $\varepsilon_{1s}^{\pi D}$ [24] will improve the constraints on a^+ and, in addition, for the electromagnetic LEC f_1 , which appears in χ PT calculations of charged pion scattering [39, 41, 55, 92].

Using the corrections calculated within χ PT [41, 42], we obtain

$$a^+ = 0.0069 \pm 0.0031 m_\pi^{-1}, \quad (7)$$

$$a^- = 0.0864 \pm 0.0012 m_\pi^{-1}. \quad (8)$$

With the GMO sum rule analysis according to Ericson et al. [57], but inserting directly our value for a^- the πN coupling constant reads $f_{\pi NN}^2/4\pi = 0.076 \pm 0.001$ which yields $\Delta_{GT} = (1.98 \pm 0.02)\%$.

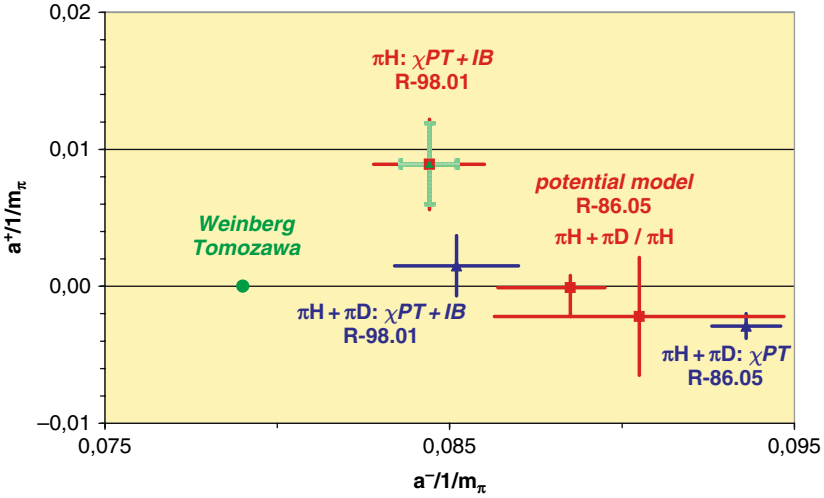


Fig. 9. Isoscalar and isovector πN scattering lengths a^+ and a^- . The results from this experiment ($R-98.1$) are obtained using δ_ε and δ_Γ as calculated within χ PT [41, 42], whereas the previous experiment ($R-86.05$) applied the corrections determined in a potential approach [43]. Also given are the values from two analyses of the πH data together with $\varepsilon_{1s}^{\pi D}$ without ($\pi H + \pi D : \chi$ PT) and with ($\pi H + \pi D : \chi$ PT + IB) inclusion of isospin breaking corrections [54, 55]

An independent source for a^- is the photoproduction reaction $\gamma n \rightarrow \pi^- p$. The electric dipole amplitude is related to the isovector scattering length by $(a^-)^2 = (q/k_0) \cdot |E_{0+}^{\text{thres}}(\pi^- p)|^2$, where q and k_0 are c.m.s. momenta of the photon and the pion [8]. With the result of Kovash et al., $E_{0+}^{\text{thres}}(\pi^- p) = (-31.5 \pm 0.8) \cdot 10^{-3} m_\pi^{-1}$ [93], one obtains $a^- = 0.0842 \pm 0.022 m_\pi^{-1}$. In turn a^- from πH yields a precise value $|E_{0+}^{\text{thres}}(\pi^- p)| = (-32.5 \pm 0.4) \cdot 10^{-3} m_\pi^{-1}$ in good agreement with the prediction of χ PT [94].

The hadronic width in pionic deuterium yields an imaginary part of the πd scattering length of $\Im a_{\pi D} = (0.0063 \pm 0.0007) m_\pi^{-1}$ [90]. Corrected for radiative capture the threshold parameter for pion production reads $\alpha = 250 \pm 30 \mu\text{b}$. An improvement by a factor of about 4 is expected from the new πD experiment to be compared with the continuously improving χ PT calculations.

7 Summary and Outlook

A second series of high-precision experiments has been performed to determine strong interaction effects in pionic hydrogen and deuterium. A thorough study of the density dependence of X-ray energies and line widths together with a new method for an ultimate precision measurement of the crystal spectrometer response allows to a large extent the separation of atomic cascade and hadronic

effects resulting in an accuracy of about 1.5% for the πN scattering lengths. An extension to $A = 3$ systems may give additional clarification on how to build up light nuclei within the approach of χ PT [95].

The accuracy in the determination of the πN scattering length concerning the presently available techniques have almost exploited their potentialities. Limitations now are mainly due to the understanding of the atomic cascade. First steps have been undertaken by including the development of the kinetic energies in order to develop a dynamical picture which is able to provide boundary conditions for the intensity of the components of the Doppler broadening [96, 97]. But up to now, the cross-sections used as input to such calculations do not allow a satisfactory description of the line shape measured in the $\mu H(3p - 1s)$ experiment or the K-line intensities from high-lying states in πH . More detailed cross-section calculations are planned [98], and in particular the inclusion of molecular effects during the collisions seems to be needed.

References

1. S. Weinberg: *Physica A* **96**, 327 (1979). [166]
2. W.-M. Yao et al. (PDG): *J. Phys. G* **33**, 1 (2006). [166]
3. M. Gell-Mann, M. Lévy: *Nuovo Cim.* **16**, 705 (1960). [166]
4. Y. Nambu: *Phys. Rev. Lett.* **4**, 380 (1960). [166]
5. M. L. Goldberger, S. B. Treiman: *Phys. Rev.* **110**, 1478 (1958). [166]
6. E. D. Commins, P. H. Bucksbaum: *Weak interaction of leptons and quarks* (Cambridge University Press 1983). [166]
7. M. Gell-Mann, R. Oakes, and B. Renner: *Phys. Rev.* **122**, 2195 (1968). [166]
8. T. E. O. Ericson and W. Weise: *Pions and Nuclei* (Clarendon, Oxford 1988). [166, 182]
9. A. W. Thomas, W. Weise: *The Structure of the Nucleon* (WILEY-VCH, Berlin 2001). [166, 167, 168]
10. S. Scherer: 'Introduction to Chiral Perturbation Theory'. In: *Advances in Nuclear Physics* **27**, ed. by J. W. Negele, E. W. Vogt (Springer, 2003). [166, 167, 168]
11. J. Gasser and H. Leutwyler: *Ann. Phys.* **158**, 142 (1984). [166]
12. J. Gasser and H. Leutwyler: *Nucl. Phys. B* **250**, 465 (1985). [166]
13. G. Ecker: *Prog. Part. Nucl. Phys.* **35**, 1 (1995), and references therein. [166, 167]
14. J. Gasser et al.: *Phys. Rev. D* **64**, 016008 (2001). [167]
15. G. Colangelo, J. Gasser, and H. Leutwyler: *Nucl. Phys. B* **603**, 125 (2001). [167]
16. B. Adeva et al.: *Phys. Lett B* **619**, 50 (2005). [167]
17. CERN experiment PS212: <http://dirac.web.cern.ch/DIRAC> [167]
18. E. Jenkins, A. V. Manohar: *Phys. Lett. B* **255**, 558 (1991). [167]
19. V. Bernard, N. Kaiser, U.-G. Meissner: *Int. J. Mod. Phys. E* **4**, 193 (1995). [167]
20. J. Gasser, H. Leutwyler, M. P. Locher, M. E. Sainio: *Phys. Lett. B* **213**, 85 (1988). [167]
21. M. E. Sainio: 'Pion-nucleon σ -term – a review'. In: *Proc. of the 9th Symp. on Meson-Nucleon Physics and the Structure of the Nucleon (MENU'01)*, πN newsletter **16**, 138 (2002), and references therein. [167]
22. D. Gotta: *Prog. Part. Nucl. Phys.* **52**, 133 (2004). [167, 174, 177]

23. PSI experiment R-98.01, <http://pihydrogen.web.psi.ch>. [167](#)
24. PSI experiment R-06.03. [167](#), [180](#), [181](#)
25. J. Spuller et al.: Phys. Lett. B **67**, 479 (1977). [168](#)
26. S. Weinberg: Phys. Rev. Lett. **17**, 616 (1966). [168](#)
27. Y. Tomozawa: Nuovo Cim. A, 707 (1966). [168](#)
28. V. Bernard, N. Kaiser, U.-G. Meißner: Phys. Lett. B **309**, 421 (1993). [168](#)
29. V. Bernard, N. Kaiser, U.-G. Meißner: Phys. Rev. C **52**, 2185 (1995). [168](#)
30. V. Bernard, N. Kaiser, U.-G. Meißner: Nucl. Phys. A **615**, 483 (1997). [168](#)
31. N. Fettes, U.-G. Meißner, S. Steininger: Nucl. Phys. A **640**, 199 (1998). [168](#)
32. M. Mojžiš: Eur. Phys. J. C **2**, 181 (1998). [168](#)
33. N. Fettes, U.-G. Meißner: Nucl. Phys. A **676**, 311 (2000). [168](#)
34. N. Fettes, U.-G. Meißner: Nucl. Phys. A **693**, 693 (2001). [168](#)
35. M. L. Goldberger, H. Miyazawa, and R. Oehme: Phys. Rev. **99**, 986 (1955). [168](#)
36. V. L. Highland et al.: Nucl. Phys. A **365**, 333 (1981). [168](#)
37. S. Deser, L. Goldberger, K. Kaufmann, and W. Thirring: Phys. Rev. **96**, 774 (1954). [169](#)
38. G. Rasche and W. S. Woolcock: Nucl. Phys. A **381**, 405 (1982). [169](#)
39. V. E. Lyubovitskij, A. Rusetsky: Phys. Lett. B **494**, 9 (2000). [169](#), [181](#)
40. V. E. Lyubovitskij, Th. Gutsche, A. Faessler, R. Vinh Mau: Phys. Lett. B **520**, 204 (2001). [169](#)
41. J. Gasser et al.: Eur. Phys. J. C **26**, 13 (2002). [169](#), [181](#), [182](#)
42. P. Zemp: In *Proc. of Chiral Dynamics 2003*, p. 128, Bonn, Germany, September 8–13 (2003), arXiv: hep-ph/0311212v1 and ‘Pionic Hydrogen in QCD + QED: Decay Width at NNLO’, Thesis univ. of Bern (2004). [169](#), [181](#), [182](#)
43. D. Sigg et al.: Nucl. Phys. A **609**, 310 (1996). [169](#), [181](#), [182](#)
44. T. E. O. Ericson, B. Loiseau, A. W. Thomas: Phys. Lett. B **595**, 76 (2004). [169](#)
45. R. Koch: Nucl. Phys. A **448**, 1986 (1986). [169](#)
46. *Proc. of MENU’01*, Washington, USA, π N newsletter **16**, (2002). [169](#)
47. R. A. Arndt et al.: ‘SAID phase shift analysis’, <http://gwdac.phys.gwu.edu>. [169](#)
48. T. L. Trueman: Nucl. Phys. **26**, 57 (1961). [169](#)
49. S. R. Beane, V. Bernard, T.-S. Lee, U.-G. Meißner: Phys. Rev. C **57**, 424 (1998). [169](#), [170](#)
50. A. Deloff: Phys. Rev. C **64**, 065205 (2001). [169](#), [170](#)
51. S. R. Beane, V. Bernard, E. Epelbaum, U.-G. Meißner, D. R. Phillips: Nucl. Phys. A **720**, 399 (2003). [169](#), [170](#)
52. B. Burasoy, H. W. Griebhammer: Int. J. Mod. Phys. E **12**, 65 (2002). [169](#)
53. M. Döring, E. Oset, M. J. Vicente Vacas: Phys. Rev. C **70**, 045203 (2004). [169](#)
54. U. G. Meißner, U. Raha, A. Rusetski: Eur. Phys. J. C **41**, 213 (2005). [169](#), [182](#)
55. U.-G. Meißner, U. Raha, and A. Rusetski, Phys. Lett. B **639**, 478 (2006). [169](#), [181](#), [182](#)
56. V. V. Baru, A. E. Kudryavtsev: Phys. of At. Nucl. **60**, 1475 (1997). [170](#)
57. T. E. O. Ericson, B. Loiseau, A. W. Thomas: Phys. Rev. C **66**, 014005 (2002). [170](#), [181](#)
58. V. Lensky et al.: FZJ-IKP(TH)-2006-20, HISKP-TH-06-02, arXiv: nucl-th/0608042v1 (2006). [170](#)
59. D. Gotta et al.: Phys. Rev. C **51**, 469 (1995). [170](#)
60. E. Daum et al.: Nucl. Phys. A **589**, 553 (1995). [170](#)
61. J. Hüfner: *Pions interact with Nuclei*, Phys. Rep. **21**, 1 (1975), formula (4.6). [170](#)
62. P. Heimberg et al.: Phys. Rev. Lett. **78**, 1012 (1996). [170](#)
63. M. Drochner et al.: Nucl. Phys. A **643**, 55 (1998). [170](#)

64. V. Lensky et al.: Eur. Phys. J. A **27**, 37 (2006). [170](#)
65. C. Hanhart: priv. comm. [170](#)
66. In: *Proc. of the Fifth Course of the International School of Physics of Exotic Atoms*, ed. L. M. Simons, D. Horváth, G. Torelli, Erice, Italy, May 14–20, 1989, (Plenum Press, New York 1990), and references therein. [171](#)
67. R. Bacher et al.: Phys. Rev. Lett. **54**, 2087 (1985). [171](#)
68. R. Bacher et al.: Phys. Rev. A **38**, 4395 (1988). [171](#)
69. K. Kirch et al.: Phys. Rev. A **59**, 3375 (1999). [171](#)
70. D. F. Anagnostopoulos, D. Gotta, P. Indelicato, L. M. Simons: Phys. Rev. Lett. **91**, 240801 (2003). [171](#)
71. H. A. Bethe, E. E. Salpeter: *Handbuch der Physik*, Band XXXV, (Springer-Verlag, Berlin 1957). [172](#)
72. T. B. Day, G. A. Snow, J. Sucher: Phys. Rev. Lett. **3**, 61 (1959); Phys. Rev. **118**, 864 (1960). [172](#)
73. A. Badertscher et al.: Europhys. Lett. **54**, 313 (2001). [172](#)
74. R. Pohl et al.: Phys. Rev. Lett. **97**, 193402 (2006). [172](#)
75. D. Taqqu: In *Muon Catalyzed Fusion*, AIP Conference Proceedings**181**, 217 (1989). [172](#)
76. S. Jonsell, J. Wallenius, P. Froelich: Phys. Rev. A **59**, 3440 (1999). [172](#)
77. E. Lindroth, J. Wallenius, S. Jonsell: Phys. Rev. A **68**, 032502 (2003). [172](#)
78. S. Kilic, J.-P. Karr, L. Hilico: Phys. Rev. A **70**, 042506 (2004). [172](#), [173](#)
79. D. Chatellard et al.: Nucl. Phys. A **625**, 855 (1997). [174](#), [180](#), [181](#)
80. H.-Ch. Schröder et al.: Eur. Phys. J. C **21**, 433 (2001). [174](#), [177](#), [180](#), [181](#)
81. L. M. Simons: Physica Scripta **T22**, 90 (1988); Hyperfine Int. **81**, 253 (1993). [174](#)
82. A. J. Rusi El Hassani et al.: Z. Phys. A **351**, 113 (1995). [174](#)
83. N. Nelms et al.: Nucl. Instr. Meth. A **484**, 419 (2002). [175](#)
84. M. Hennebach: Precision Measurement of Ground State Transitions in Pionic Hydrogen. PhD Thesis, Universität zu Köln (2003). [177](#), [179](#), [180](#)
85. S. Biri, L. M. Simons, D. Hitz: Rev. Sci. Instrum. **71**, 1116 (2000). [177](#)
86. D. F. Anagnostopoulos et al.: Nucl. Instr. Meth. A **545**, 217 (2005). [178](#)
87. R. N. Faustov, A. P. Martynenko: J. Exp. Theor. Phys. **98**, 39 (2004). [179](#)
88. Th. Jensen: priv. comm. [179](#)
89. P. Indelicato: priv. comm. [179](#)
90. P. Hauser et al.: Phys. Rev. C **58**, R1869 (1998). [180](#), [181](#), [182](#)
91. R. Deslattes et al.: Rev. Mod. Phys., **75**, 35 (2003). [180](#)
92. U.-G. Meißner, S. Steininger: Phys. Lett. B **419**, 403 (1998). [181](#)
93. M. A. Kovash et al.: π N Newsletter **12**, 51 (1997). [182](#)
94. V. Bernard, N. Kaiser, U.-G. Meißner: Phys. Lett. B **383**, 116 (1996). [182](#)
95. V. Baru, J. Haidenbauer, C. Hanhart, and J. A. Niskanen: Eur. Phys. J. A **16**, 437 (2003). [183](#)
96. T. S. Jensen and V. E. Markushin: Eur. Phys. J. D **19**, 165 (2002); Eur. Phys. J. D **21**, 261 (2002); Eur. Phys. J. D **21**, 271 (2002). [183](#)
97. T. S. Jensen: Eur. Phys. J. D **31**, 11 (2004). [183](#)
98. T. S. Jensen, V. Popov, V. Pomerantsev: priv. comm. [183](#)

Precision Spectroscopy of Antiprotonic Helium Atoms and Ions – Weighing the Antiproton

R. S. Hayano

The University of Tokyo, Bunkyo-ku, Tokyo 113-0033, Japan
ryugo.hayano@cern.ch

Abstract. A radiofrequency quadrupole antiproton decelerator, a femtosecond optical frequency comb and continuous-wave pulse-amplified laser were used to measure 12 transition frequencies of antiprotonic helium (metastable three-body neutral atom consisting of an electron, an antiproton and a helium nucleus) to fractional precisions of $(9-16) \times 10^{-9}$. Comparisons with three-body QED calculations yielded an antiproton-to-electron mass ratio of $m_{\bar{p}}/m_e = 1836.152674(5)$. The physics of antiprotonic helium atom spectroscopy and the method of $m_{\bar{p}}/m_e$ determination are presented, and future prospects are discussed.

1 Introduction

Spectroscopy of exotic atoms, the atoms which comprise an ordinary nucleus and a negatively charged particle such as μ^- , π^- , K^- , \bar{p} , Σ^- , offers a powerful tool to study fundamental interactions as well as particle properties. For example, the μ^- mass [1] as listed in the review of particle physics [2] was determined by the exotic-atom X-ray spectroscopy, and the ‘CPT theorem’ was used to assign the same value to the mass of its antiparticle, μ^+ . Here, the CPT theorem states that physical laws remain invariant under the simultaneous reflections of charge, parity and time, and if the CPT symmetry holds, the masses of a particle and its antiparticle must be identical. The masses of π^\pm [3] and K^\pm [4] were similarly determined.

The situation is different for the proton, since the proton mass rather than the antiproton mass can be more precisely determined using Penning traps. The 1998 CODATA (Committee on Data for Science and Technology) recommended value [1] for m_p/m_e of 1836.152 6675(39) (relative standard uncertainty of 2.1×10^{-9} , see Fig. 1) was based on the measurement conducted by the University of Washington group [6], who compared the cyclotron frequencies $\omega_c = qB/m$ of a single C^{6+} ion and a single electron trapped in a Penning trap (i.e., the determination of the electron mass in units of the

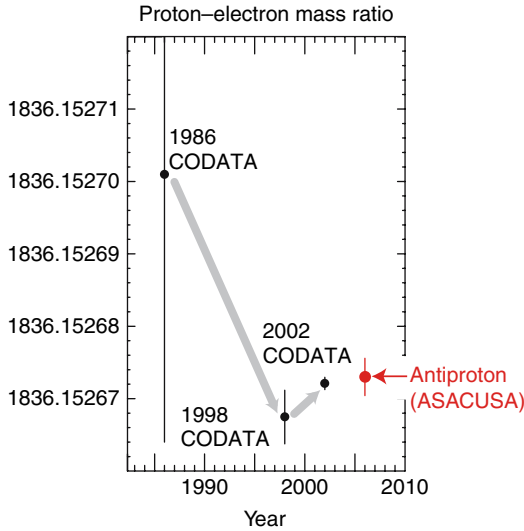


Fig. 1. Proton-to-electron [5] and antiproton-to-electron [10] mass ratios

atomic mass unit). This was then combined with their comparison of the cyclotron frequencies of a single proton and a single C^{4+} ion [7], yielding the m_p/m_e value.

The 2002 CODATA recommended value [1] for m_p/m_e of 1836.152 672 61(85) (relative standard uncertainty of 4.6×10^{-10}) is based on a new measurement carried out by the GSI-Mainz collaboration [8], who compared the $^{12}C^{5+}$ cyclotron frequency and its spin precession frequency $\omega_L = geB/(2m_e)$. From the measured ratio ω_c/ω_L and the quantum electrodynamical (QED) prediction for the bound-electron g factor, the electron's mass in units of the atomic mass unit was obtained. The proton mass values thus obtained are so much more precise than the antiproton mass value obtained by the antiprotonic-atom X-ray measurements (having relative uncertainties of $\sim 4 \times 10^{-5}$) [9].

Recently, the ASACUSA (*atomic spectroscopy and collisions using slow antiprotons*) collaboration at CERN's antiproton decelerator facility (AD) measured the transition frequencies of antiprotonic helium atoms ($\bar{p}He^+$, a neutral three-body system made of an electron, an antiproton and a helium nucleus) using the laser-spectroscopic method to some 10 ppb [10]. By comparing the experimental results with the results of high-precision three-body QED calculations, the antiproton-to-electron mass ratio $m_{\bar{p}}/m_e$ was determined to be 1836.152 674(5) (relative standard uncertainty of 2.7×10^{-9}). Using the CPT theorem, this result can be directly compared with the m_p/m_e , as in Fig. 1, which shows that the precision of $m_{\bar{p}}/m_e$ has come close to that of m_p/m_e .

In the following, the physics of antiprotonic helium atom spectroscopy and the method of $m_{\bar{p}}/m_e$ determination are presented, and future prospects are discussed.

2 Antiprotonic Helium Atoms

Normally, when an antiproton is stopped in matter, the antiproton annihilates on a nucleus within picoseconds, leaving no time for high-precision spectroscopy. The only exception is known to occur in helium, due to the formation of the antiprotonic helium atom (hereafter denoted $\bar{p}\text{He}^+$), a naturally-occurring antiproton trap in which an antiproton can be “stored” for several microseconds. This was serendipitously discovered at the 12 GeV proton synchrotron of KEK, Japan, and has subsequently been studied in detail at CERN [11].

The $\bar{p}\text{He}^+$ atoms have the following remarkable features:

1. The atom has a metastable lifetime in excess of a microsecond. This longevity occurs when the antiproton occupies a near-circular orbit having a large n (~ 38) and also large ℓ ($\gtrsim 35$).
2. The $\bar{p}\text{He}^+$ atoms can be abundantly produced just by stopping antiprotons in a helium target. Then, about 3% of the stopped antiprotons automatically become trapped in the metastable states.
3. We usually use low-temperature ($T \sim 10$ K) helium gas as the target. The $\bar{p}\text{He}^+$ atoms that are produced collide with the surrounding helium atoms and are thermalized. Therefore, the antiprotonic helium atoms are already cold and are well suited for high-precision spectroscopy (i.e., small Doppler width).
4. We have demonstrated already that we can perform laser spectroscopy of $\bar{p}\text{He}^+$. Note that we are not changing the electronic state as in ordinary laser spectroscopy, but are inducing transitions between different antiproton orbits.

Figure 2 shows an energy level diagram of $\bar{p}^4\text{He}^+$. The levels indicated by the continuous lines have metastable ($\gtrsim 1\mu\text{s}$) lifetimes and de-excite radiatively, while the levels shown by wavy lines are short lived ($\lesssim 10$ ns) and de-excite by Auger transitions to antiprotonic helium ion states (shown by dotted lines). Since the ionic states are hydrogenic, Stark collisions quickly induce antiproton annihilation on the helium nucleus, as indicated in Fig. 2.

3 Principle of the $\bar{p}\text{He}^+$ Laser Spectroscopy

Laser spectroscopy of $\bar{p}\text{He}^+$ works as follows: As shown in Fig. 2, there is a boundary between metastable states and short-lived states. For example, $(n, \ell) = (35, 33)$ is metastable, while $(n, \ell) = (34, 32)$, which can be reached from $(35, 33)$ by an $E1$ transition, is short lived. Thus, if we use a laser ($\lambda = 372.6$ nm in this particular case) to induce a transition from $(35, 33)$ to $(34, 32)$, (and of course if an antiproton happens to be occupying the $(35, 33)$ level at the time of laser ignition), the antiproton is de-excited to the short-lived state, which then Auger decays to an ionic $(n_i, \ell_i) = (30, 29)$ state within $\lesssim 10$ ns. The ionic state is then quickly (usually within \sim ps) destroyed by Stark collisions, leading to the nuclear absorption or annihilation of the antiproton. Adding all these together, we expect to see a sharp increase in the \bar{p} annihilation rate in coincidence with the laser pulse, as shown in Fig. 3. We measure the intensity of the laser-induced annihilation spike as a function of laser detuning to obtain the transition frequency ν_{exp} .

The transition frequency from the state (n, ℓ) to (n', ℓ') can be (approximately) written similarly to the well-known hydrogen formula,

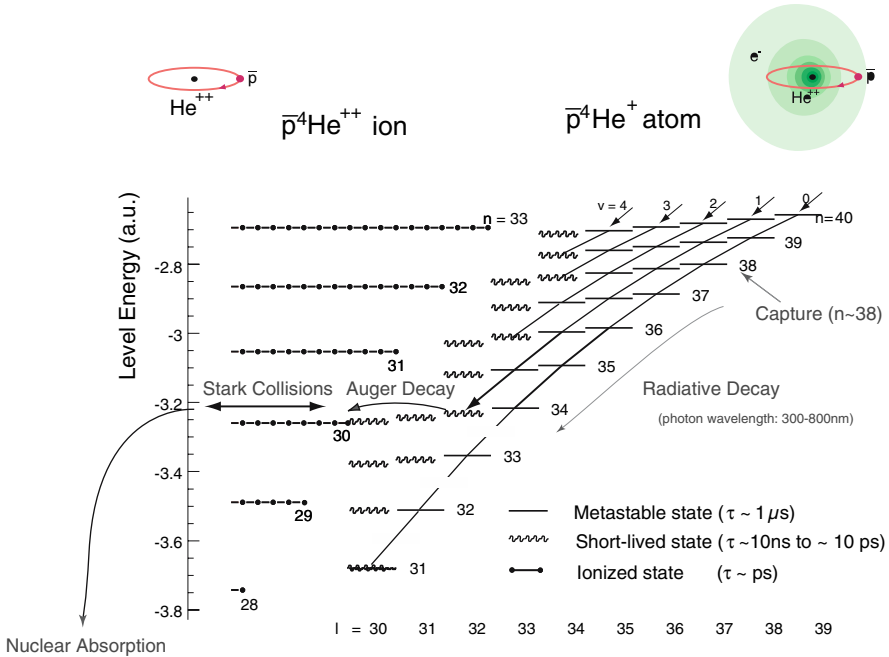


Fig. 2. Level diagram of $\bar{p}^4\text{He}^+$ in relation to that of $\bar{p}^4\text{He}^{2+}$. The continuous and wavy bars stand for metastable and short-lived states, respectively, and the dotted lines are for l -degenerate ionized states

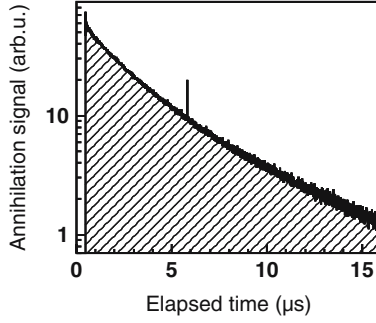


Fig. 3. Delayed-annihilation time spectrum of $\bar{p}^4\text{He}^+$, with laser-induced annihilation spike of the transition $(35, 33) \rightarrow (34, 32)$ [20]

$$\nu_{n,\ell \rightarrow n',\ell'} = Rc \frac{m_{\bar{p}}^*}{m_e} Z_{\text{eff}}^2(n, \ell, n', \ell') \left(\frac{1}{n^2} - \frac{1}{n'^2} \right), \quad (1)$$

where R is the Rydberg constant, c is the speed of light, $m_{\bar{p}}^*/m_e$ is the reduced antiproton-to-electron mass ratio and Z_{eff} is the effective nuclear charge. Here, $Z_{\text{eff}} = 2$ for the antiprotonic helium ion ($\bar{p}\text{He}^{2+}$), but is < 2 in the case of $\bar{p}\text{He}^+$ due to the nuclear-charge shielding by the remaining electron, and it must be calculated by three-body QED theories. This formula shows how $m_{\bar{p}}/m_e$ can be deduced from the precision measurement of ν_{exp} with the help of three-body calculations.

4 Why Further \bar{p} Deceleration Using an “Inverse Linac” Is Needed?

Our first series of measurements, conducted at CERN’s low-energy antiproton ring (LEAR, closed down at the end of 1996), were of exploratory nature, in which we established the formation and structure of the antiprotonic helium atoms [11]. Our first successful observation of the $(n, \ell) = (39, 35) \rightarrow (38, 34)$ laser resonance of $\bar{p}^4\text{He}^+$ at $\lambda = 597.3$ nm [12] triggered theoretical efforts to perform high-precision three-body QED calculations [13, 14, 15], which in turn helped us guide the search for new transitions. The most important outcome of the LEAR era was the study of the density-dependent shifts and widths of the transition frequencies as shown in Fig. 4(a) [16]. Since the $\bar{p}\text{He}^+$ atoms were produced by stopping antiprotons in a helium gas target of temperature $T \sim 5$ K and pressure $P \sim 0.5$ bars, or atomic density of $\rho \sim 10^{21}$ atoms-cm $^{-3}$, the atoms undergo many collisions against ordinary helium atoms, producing density-linear (as well as state-dependent) shift of the transition frequencies of ~ 500 MHz. By taking data at several different target densities in the range $0.1 - 3 \times 10^{21}$ cm $^{-3}$ and determining the zero-density-extrapolated value, we were able to determine two transition frequencies of

$\bar{p}^4\text{He}^+$ ($(n, \ell) = (39, 35) \rightarrow (38, 34)$ and $(37, 34) \rightarrow (36, 33)$) with precisions $\delta\nu/\nu$ of $0.5 - 1 \times 10^{-6}$ [16].

In the first experiment of ASACUSA collaboration at CERN's antiproton decelerator (AD), we measured six transition frequencies of $\bar{p}^4\text{He}^+$ to $\delta\nu/\nu = 1 - 10 \times 10^{-7}$ [17]. The essential difference between the LEAR and the AD experiments was the time structure of the antiproton beam. At LEAR, antiprotons were slowly extracted from the LEAR ring, so that an excimer-pumped dye laser was fired for each $\bar{p}\text{He}^+$ -candidate event which occurred randomly with a mean rate of about 300 Hz. In contrast, the AD provides a short pulse of ~ 100 ns wide containing some 3×10^7 \bar{p} s, repeated every 100 s. A single laser pulse in this case irradiates some 10^6 metastable atoms. The conventional event-by-event collection of antiproton-annihilation events used at LEAR is impossible with the pulsed beam at AD. We thus developed an entirely new detection scheme based on analog-waveform-recording of Čerenkov detectors viewed by gateable photomultipliers [18]. Good control of systematic errors by stabilizing the laser frequency, intensity, the antiproton-beam position, etc., over a long measuring time of ~ 8 hours was essential to achieve high precision. As was in the case of the LEAR experiments, the zero-density extrapolation procedure was inevitable in the first AD experiment (see Fig. 4(b)), but this was largely eliminated as follows by using an ultra-low-energy \bar{p} beam generated by a radiofrequency quadrupole decelerator (RFQD) [19], the first successful “inverse linac” constructed by ASACUSA in collaboration with CERN.

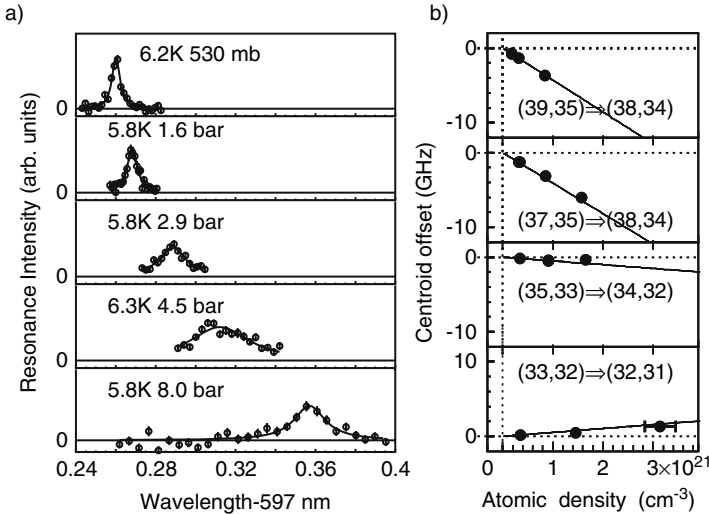


Fig. 4. (a) The density-dependent shift and broadening of the 597 nm transition of $\bar{p}^4\text{He}^+$ ($(n, \ell) = (39, 35) \rightarrow (38, 34)$) observed at LEAR [16]. (b) The density dependence of the $\bar{p}^4\text{He}^+$ transition frequencies measured in the first AD experiment [17]. Linear extrapolations to zero density were used to deduce the “in vacuo” values

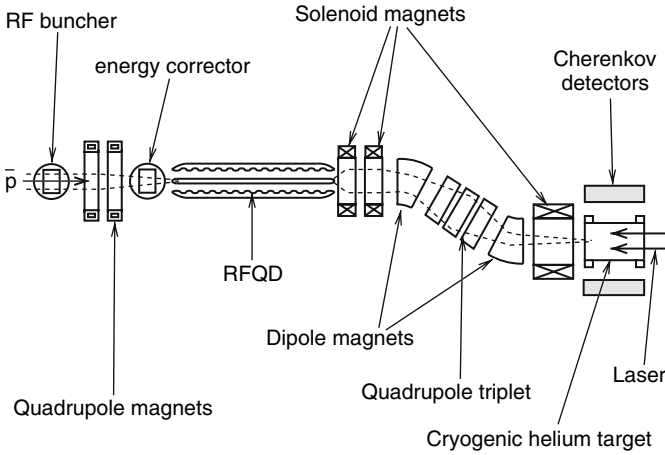


Fig. 5. Experimental layout using the RFQD. Dashed lines indicate trajectories of the antiproton beam. Drawing not to scale [20]

The experimental arrangement using the RFQD is schematically shown in Fig. 5. The 5.3 MeV antiprotons from the AD were first time-wise compressed by the RF buncher so as to be in phase with the decelerating rf field in the RFQD, entered the 3.5-m-long quadrupole electrode structure, operated at 202.5 MHz, and were decelerated to 65 ± 20 keV with an efficiency of 20–25%. In order to separate the decelerated \bar{p} s from the undecelerated component which nevertheless reach the end of the RFQD, a magnetic spectrometer was installed between the RFQD and the low-density helium target (150 mm in diameter, 300 mm in length). A thin ($0.8 \mu\text{m}$) polyethylene window was used to contain the 10 K helium gas of $10^{16} - 10^{18}$ atoms/cm³. In 2003, we used this setup to measure seven transition frequencies of $\bar{p}^4\text{He}^+$ and six of $\bar{p}^3\text{He}^+$, with errors of $\delta\nu/\nu \sim 0.5 - 2 \times 10^{-7}$ [20], about a factor 6 better than the pre-RFQD measurement.

5 Further Improvement Using an Optical Frequency Comb

Having eliminated the collisional shift, the line width of the laser and its frequency calibration were the large source of errors, as shown in Table 1. Only pulsed lasers can provide the megawatt-scale intensities needed here to induce the $\bar{p}\text{He}^+$ transitions. However, fluctuations in their frequency and linewidth and the difficulty of calibrating the wide range of $\bar{p}\text{He}^+$ wavelengths indicated in Fig. 6 have limited our experimental precision. We circumvented these problems by basing our experiments on a continuous-wave (CW) laser whose frequency ν_{cw} could be stabilized with a precision $< 4 \times 10^{-10}$ against an optical comb. Its intensity was then amplified by a factor 10^6 to produce

a pulsed laser beam of frequency $\nu_{pl} \sim \nu_{cw}$ with an accuracy and resolution 1–2 orders of magnitude higher than before.

A schematic diagram of the laser system which enabled this improvement is shown in Fig. 7. A Nd:YVO₄ laser (in block (C) of Fig. 7) pumped either a ring Ti:sapphire or dye laser (Coherent MBR-110 or 899-21), thus producing CW laser beams covering the required wavelengths $\lambda = 574.8 - 941.4$ nm with linewidth $\Gamma = 1$ or 4 MHz and power $P \sim 1$ W. This seed beam was amplified in three dye cells pumped by a pulsed Nd:YAG laser. This is shown in Fig. 7 block (E), where we also show a pulse stretcher, which stretched the laser pulse length to 20 ns to decrease the Fourier-limited linewidth. The cells emitted laser pulses with $\Gamma \sim 60$ MHz and $E = 5 - 20$ mJ. The shorter wavelengths $\lambda = 264.7 - 470.7$ nm were obtained by frequency doubling beta-barium borate (BBO) or lithium triborate (LBO) crystals as shown in Fig. 7 block (E) or by frequency tripling using both crystals.

The optical frequency comb (Menlo Systems FC-8004, shown in block (D)) [21, 22] constituted a mode-locked Ti:sapphire laser pumped by a CW Nd:YVO₄ laser, which produced 15-fs-long laser pulses of repetition rate $f_{rep} = 200$ MHz. The spectral width $\lambda = 750 - 850$ nm of this pulsed beam was first broadened to $\lambda = 500 - 1100$ nm by propagating it through a microstructure fiber. This beam was then used to stabilize (i) the frequency offset $f_{off} = 20$ MHz common to all the modes of the comb and (ii) the CW seed laser to frequency $\nu_{cw} = n_c f_{rep} + f_{off} + f_{dif}$ which was $f_{dif} = 20$ MHz above the n_c th mode of the comb. The value n_c was measured using a Fizeau wavelength meter. All frequencies f_{rep} , f_{off} , and f_{dif} were synchronized to a quartz oscillator, which was stabilized to a timing signal provided by global positioning satellites. The seed (and consequently the pulsed dye) laser was scanned over a region 4 GHz around the $\bar{p}\text{He}^+$ lines by changing the above repetition rate from $f_{rep} = 200.000$ to 200.004 MHz. Doppler-free spectroscopy of Rb and I₂ in the seed beam (blocks (A) and (B)) indicated that its frequency precision was $< 4 \times 10^{-10}$.

Table 1. Various factors contributing to the precision of $\bar{p}\text{He}^+$ laser spectroscopy

	ASACUSA2001 [17] (MHz)	ASACUSA 2003 [20] (MHz) RFQD	ASACUSA2006 [10] CW laser + Comb
Natural width	20–100	←	← ¹
Collisional shift	~ 500	< 10	0.1 – 2 MHz
Collisional width	~ 500	< 10	< 10 MHz
Doppler width	~ 500	←	←
Laser line width	800 – 2000	←	< 60 MHz
Calibration	10 – 60	←	~ 2 – 4 ²

¹ In [10], we also measured for the first time a metastable–metastable transition $(n, \ell) = (36, 34) \rightarrow (35, 33)$, having a narrow natural width of 100 kHz.

² The uncertainty of 2 – 4 MHz is due to frequency chirp correction.

The frequency ν_{pl} of the dye laser pulse can deviate from the seed value ν_{cw} due to sudden changes in the refractive index of the dye during the amplification. This so-called chirp effect of magnitude $\Delta\nu_c(t) = \nu_{\text{pl}}(t) - \nu_{\text{cw}}$ can shift the measured $\bar{p}\text{He}^+$ frequencies ν_{exp} from their true values, so it had to be corrected. The time evolution of $\Delta\nu_c(t)$ was measured by the setup shown in blocks (F) and (G) of Fig. 7. We also minimized $\Delta\nu_c(t)$ using an electro-optic modulator (EOM, shown in block (E)) to apply a frequency shift of opposite sign to the seed laser, which canceled the chirp induced in the dye cells.

The profile of the $(n, \ell) = (36, 34) \rightarrow (37, 33)$ resonance in $\bar{p}^3\text{He}^+$ is shown in Fig. 8(a). It contains (i) eight intense lines (indicated by four arrowed pairs) corresponding to E1 transitions involving no spin-flip between the eight hyperfine substates [23] of states $(36, 34)$ and $(37, 33)$ and (ii) 12 weak lines wherein one of the constituent particles flips its spin. Only the two peaks separated by 1.8 GHz that arise from the interaction between the orbital angular momentum of the antiproton and electron spin could be resolved, however, due to the 400 MHz Doppler broadening caused by the motion of the $\bar{p}^3\text{He}^+$ thermalized to $T = 10$ K. The spin-averaged transition frequency ν_{exp} was determined by fitting this profile with the theoretical line shape (solid line) obtained from the optical Bloch equations which describe the evolution of the $\bar{p}\text{He}^+$ state

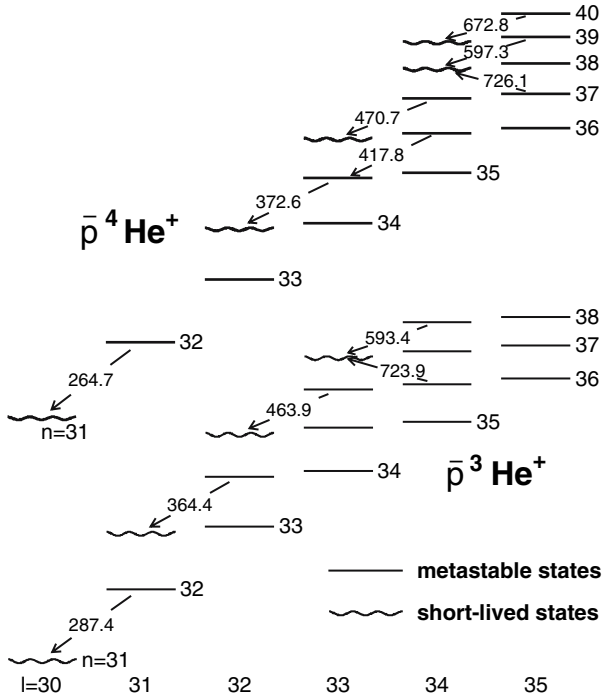


Fig. 6. Partial level diagrams of $\bar{p}^4\text{He}^+$ and $\bar{p}^3\text{He}^+$. Wavelengths of transitions studied in [10] are indicated in nanometers

populations during laser irradiation. The small remaining chirp introduced a time dependence to $\nu_{pl}(t)$ when performing the Bloch equation integration. In this we took transitions between all hyperfine and magnetic substates into account, using the theoretical values for their splittings (precision < 1 MHz) and dipole moments [23]. Doppler broadening, laser power broadening, and

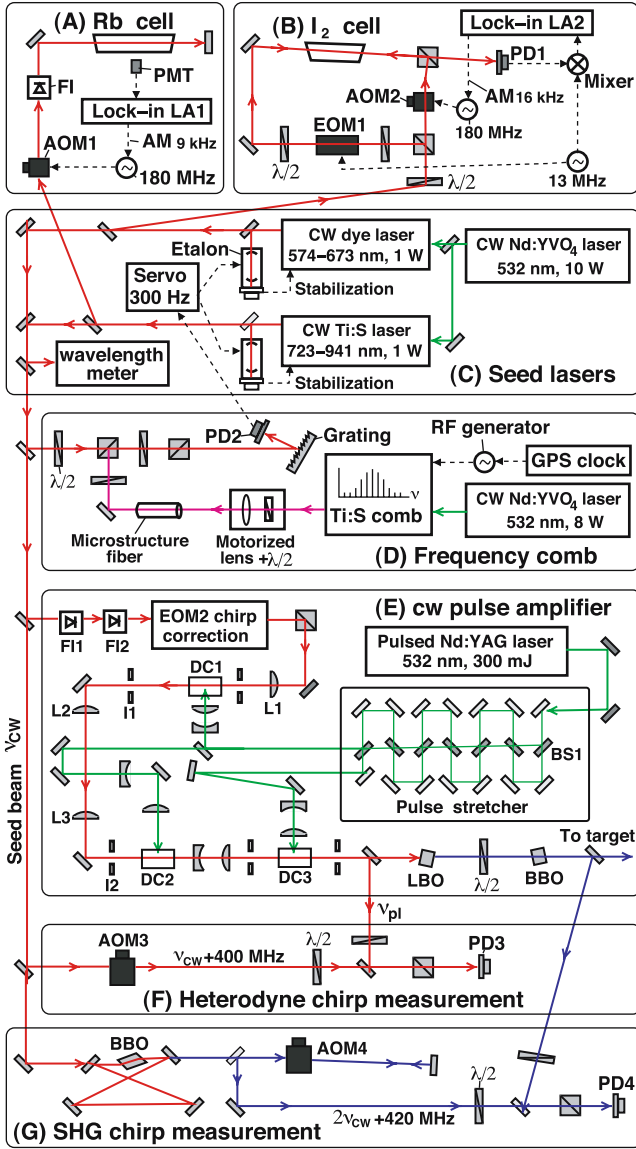


Fig. 7. Stabilization of CW pulse-amplified laser to femtosecond frequency comb

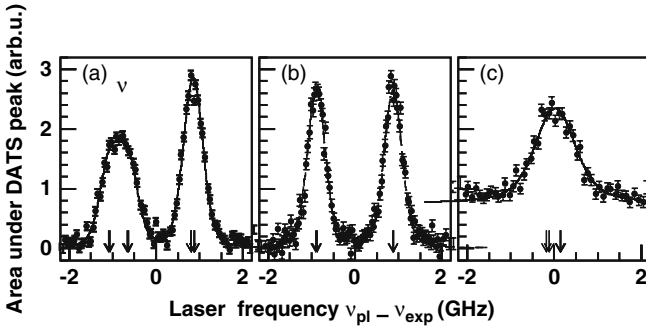


Fig. 8. Frequency profiles (laser detuning plotted against the laser-induced annihilation spike in the delayed-annihilation time spectrum (DATS)) of the transition (a) $(36, 34) \rightarrow (37, 33)$ in $\bar{p}^3\text{He}^+$ and (b) $(37, 35) \rightarrow (38, 34)$ and (c) $(36, 34) \rightarrow (35, 33)$ in $\bar{p}^4\text{He}^+$

collisional dephasing effects were also included. The ν_{exp} values of $\bar{p}^4\text{He}^+$ resonances (Fig. 8(b)), which contain four intense, non-spin-flip lines and four weak, spin-flip ones, were similarly obtained. The ac Stark shifts caused by the laser interacting with $\bar{p}\text{He}^+$ are estimated to be \lesssim MHz, due to the small scalar (-3 to 2 a.u.) and tensor ($(0.1 - 2) \times 10^{-3}$ a.u.) terms of the dynamic polarizability for these transitions [24].

6 The First Measurement of a Metastable-to-Metastable Transition Frequency

All transitions heretofore accessible to our precision laser spectroscopy involved a daughter state with a short Auger lifetime, the natural width $\Gamma_n \gtrsim 20$ MHz of which would ultimately limit the achievable precision on ν_{exp} to around $\sim 10^{-9}$. We have now extended our studies to include one $\bar{p}^4\text{He}^+$ transition $(36, 34) \rightarrow (35, 33)$ between two metastable states (see Fig. 6) with $\Gamma_n \sim 100$ kHz. This implies an ultimate precision of $\sim 10^{-12}$, although our present experiments are Doppler rather than natural width limited. To measure this transition we developed the following three-laser method (see Fig. 9), which also utilizes the above CW pulse-amplified laser: (i) An additional dye laser pumped by a 355 nm Nd:YAG laser (not shown in Fig. 7) first irradiated the $\bar{p}\text{He}^+$ with a 3-ns-long pulse at $\lambda = 372.6$ nm. This depleted the population in state $(35, 33)$ at $t = t_1$ by inducing the transition $(35, 33) \rightarrow (34, 32)$ to a short-lived state. (ii) At $t = t_2 \sim t_1 + 50$ ns, the CW pulse-amplified laser tuned to $(36, 34) \rightarrow (35, 33)$ at $\lambda = 417.8$ nm equalized the population in the parent and daughter states. (iii) Another 372.6 nm dye laser probed the increased population of $(35, 33)$ at $t = t_3 \sim t_1 + 100$ ns resulting from the transitions stimulated by the 417.8 nm laser pulse and produced an annihilation peak at $t = t_3$. The profile of the

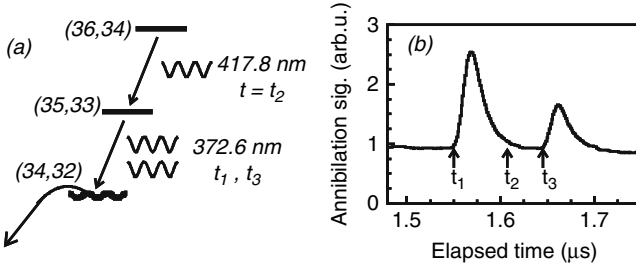


Fig. 9. (a) A part of the $\bar{p}^4\text{He}^+$ energy diagram. (b) Delayed-annihilation time spectrum with three lasers fired at $t = t_1, t_2, t_3$ to measure the 417.8 nm transition

$(36, 34) \rightarrow (35, 33)$ resonance obtained by plotting the intensity of this peak against the frequency of the 417.8 nm laser is shown in Fig. 8(c).

7 Experimental Results

The ν_{exp} values thus obtained are compared with two sets of theoretical values ν_{th} [25, 26] in Fig. 10, both of which include QED and nuclear-size ($\Delta\nu_{\text{nuc}} = 2 - 4$ MHz) effects. Values from [25] scatter within $7 - 8\sigma$ of ν_{exp} . Those of [26], the only calculation claiming precision $\sigma_{\text{th}} = 1 - 2$ MHz commensurate with ν_{exp} , agree within $< 1 \times 10^{-8}$ with the four highest-precision measurements in $\bar{p}^4\text{He}^+$ and $(36, 34) \rightarrow (37, 33)$ in $\bar{p}^3\text{He}^+$. Four of its $\bar{p}^3\text{He}^+$ frequencies were $\sim 2\sigma$ below our ν_{exp} values. Concerning [25], unpublished results from the authors have recently moved by $3 - 100$ MHz from those in Fig. 10. We therefore use only the values from [26] in the following.

The theoretical calculations for ν_{th} were performed using the 2002 CODATA recommended values for fundamental constants, including $m_{\bar{p}}/m_e = m_p/m_e = 1836.15267261$, $m_{^4\text{He}}/m_e = 7294.2995363(32)$ and $m_{^3\text{He}}/m_e = 5495.885269(11)$. Theory [26] also provided coefficients for $d\nu_{\text{th}}/d(m_p/m_e)$. These we used to determine the antiproton-to-electron mass ratio as the value

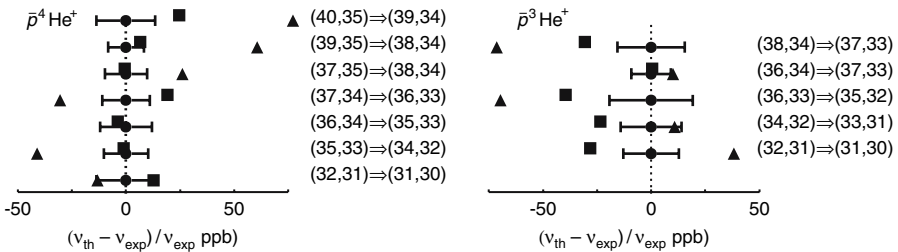


Fig. 10. Experimental ν_{exp} (circles with 1σ errors) vs theoretical ν_{th} (triangles [25] and squares [26]) transition frequencies

$m_{\bar{p}}/m_e = 1836.152674(5)$ by minimizing the sum $\Sigma[\nu_{\text{th}}(m_{\bar{p}}/m_e) - \nu_{\text{exp}}]^2/\sigma_{\text{exp}}^2$ over the 12 transitions. Here ν_{exp} , the experimental 1 standard deviation (1σ) error $\sigma_{\text{exp}} = 4 - 15$ MHz (Fig. [10](#)) was the quadratic sum of the statistical ($3 - 13$ MHz) and systematic ones σ_{syst} arising from the chirp ($2 - 4$ MHz), collisional shifts ($0.1 - 2$ MHz) and the harmonic generation ($1 - 2$ MHz). The error 5 on the last digit of $m_{\bar{p}}/m_e$ is the quadratic sum of 4 (the minimization error) and the systematic ones 3 (arising from σ_{syst}) and 2 (from σ_{th}).

8 Summary and Outlook

A radiofrequency quadrupole antiproton decelerator, a femtosecond optical frequency comb and continuous-wave pulse-amplified laser were used to measure 12 transition frequencies of antiprotonic helium to fractional precisions of $(9 - 16) \times 10^{-9}$. Comparisons with three-body QED calculations yielded an antiproton-to-electron mass ratio of $m_{\bar{p}}/m_e = 1836.152674(5)$. Since our first observation of the $\bar{p}^4\text{He}^+$ laser resonance in 1993 [\[12\]](#), with precision $\delta\nu/\nu$ of $\sim 5 \times 10^{-4}$, the experimental precision has improved by 6 orders of magnitude. Meanwhile, theoretical precision has also improved by using more elaborate schemes to solve the three-body problem and by adding higher-order QED corrections. As shown in Fig. [10](#), precisions of experiment and theory have reached similar order, and in order to further improve the precision of $m_{\bar{p}}/m_e$ determination, both experiment and theory must improve. On the theory side, we need at least two theoretical predictions which agree with each other within quoted numerical errors.

Experimentally, it is possible to achieve higher frequency precision by performing a metastable-to-metastable spectroscopy using the two-photon $(36, 34) \rightarrow (34, 32)$ transition (by using two counter-propagating beams of $\lambda_1 \sim 372$ nm and $\lambda_2 \sim 417$ nm, we can approximately cancel the Doppler width).

Another possibility is to try laser spectroscopy of antiprotonic helium ions, recently discovered by stopping antiprotons in a very low density helium target of 10^{16} atoms/cm³ [\[27\]](#), since the transition frequencies of the two-body $\bar{p}\text{He}^{2+}$ can be calculated without theoretical ambiguities. Let us go back again to Fig. [2](#) and consider the fate of $\bar{p}\text{He}^{2+}$ ions at very low target densities. The destruction of the $\bar{p}\text{He}^{2+}$ states usually takes place in a matter of pico seconds due to the Stark collisions. If the $\bar{p}\text{He}^{2+}$ ion is isolated in a vacuum, there are no collisions, and hence the $\bar{p}\text{He}^{2+}$ states should become metastable (the radiative lifetimes of the circular states around $n_i \sim 30$ is several hundred ns). We, therefore, expect the prolongation of [\[27\]](#) lifetimes at very low target densities.

This is exactly what we recently observed. In the left panel of Fig. [11](#), we show the annihilation spike produced by inducing the $\bar{p}^4\text{He}^+$ transition $(n, \ell) = (39, 35) \rightarrow (38, 34)$ measured by using the RFQD-decelerated beam at a low target density of 2×10^{18} atom/cm³. At this density, the decay time

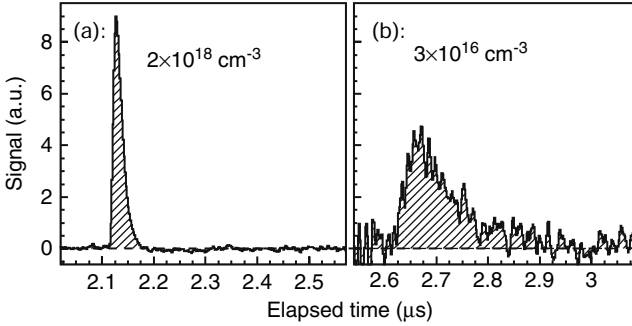


Fig. 11. Annihilation spike produced by inducing the $\bar{p}\text{He}^+$ transition $(n, \ell) = (39, 35) \rightarrow (38, 34)$, measured at a high target density (a). A prolongation of the tail is observed at ultra-low densities (b), indicating the formation of long-lived $\bar{p}\text{He}^{2+}$ ions.

constant of the laser spike is still consistent with the Auger lifetime of the $(38, 34)$ level. However, as shown in the right panel, the shape of the laser-induced spike changes drastically in an ultra-low target density of 3×10^{16} atoms/cm³. Lifetime prolongation was also observed in the case of antiprotonic helium 3 ions. Systematic measurements of the ion lifetimes at various target densities have been done, which showed that the ionic-level lifetimes get shorter for larger principle quantum numbers [27]. Experiments to observe laser-resonant transitions of $\bar{p}^4\text{He}^{2+}$ and $\bar{p}^3\text{He}^{2+}$ are being carried out by the ASACUSA collaboration.

If both experiment and theory are improved, it appears possible to determine $m_{\bar{p}}/m_e$ as good as or even better than m_p/m_e within a few years. Assuming that the CPT symmetry is valid at this level of precision, these efforts will then contribute to the better determination of a fundamental constant.

Acknowledgements

I would like to thank my ASACUSA collaborators, Drs M. Hori, A. Dax, J. Eades, W. Pirkel, E. Widmann, H.A. Torii, B. Juhász, D. Barna and D. Horváth. This work was supported by Monbukagakusho (Grant No. 15002005) and the Hungarian Scientific Research Fund (OTKA T046095).

References

1. F.G. Mariam et al.: Phys. Rev. Lett. **49**, 993 (1982). ($m_{\mu}/m_e = 206.768259(62)$). [187](#), [188](#)
2. W.-M. Yao et al.: Journal of Physics G **33**, 1 (2006). [187](#)

3. S. Lenz et al.: Phys. Lett. B **416**, 50 (1998). [187](#)
4. K.P. Gall: Phys. Rev. Lett. **60**, 186 (1988); A.S. Denisov et al.: ZETF Lett. **54**, 557 (1991). [187](#)
5. P.J. Mohr and B.N. Taylor: Rev. Mod. Phys. **72**, 351 (2000); **77**, 1 (2005). [188](#)
6. D. L. Farnham, R. S. Van Dyck, Jr., and P. B. Schwinberg: Phys. Rev. Lett. **75**, 3598 (1995). [187](#)
7. R. S. Van Dyck, Jr., D. L. Farnham, and P. B. Schwinberg: Phys. Scr. **T59**, 134 (1995). [188](#)
8. T. Beier et al.: Phys. Rev. Lett. **88**, 011603 (2002). [188](#)
9. J. Eades and F.J. Hartmann: Reviews of Mod. Phys. **71**, 373 (1999) and references therein. [188](#)
10. M. Hori et al.: Phys. Rev. Lett. **96**, 243401 (2006). [188](#), [194](#), [195](#)
11. T. Yamazaki, N. Morita, R. Hayano, E. Widmann, and J. Eades: Phys. Rep. **366** (2002) 183. [189](#), [191](#)
12. N. Morita et al.: Phys. Rev. Lett. **72**, 1180 (1994). [191](#), [199](#)
13. V.I. Korobov: Phys. Rev. **A54**, R1749 (1996); V.I. Korobov: Hyperfine Interact. **119**, 185(1999). [191](#)
14. V.I. Korobov and D.Bakalov: Phys. Rev. Lett. **79**,3379 (1997). [191](#)
15. Y. Kino et al.: Hyperfine Interact. **119**, 201(1999); [191](#)
16. H.A. Torii et al.: Phys. Rev. A **59**, 223 (1999). [191](#), [192](#)
17. M. Hori et al.: Phys. Rev. Lett. **87**, 093401 (2001). [192](#), [194](#)
18. M. Hori et al.: Nucl. Instr. Meth. A **496**, 102 (2003). [192](#)
19. A.M. Lombardi et al.: in Proceedings of the 2001 Particle Accelerator Conference, Chicago, 2001 (IEEE, Piscataway, NJ, 2001), pp. 585–587. [192](#)
20. M. Hori et al.: Phys. Rev. Lett. **91**, 123401 (2003). [191](#), [193](#), [194](#)
21. Th. Udem, R. Holzwarth, and T.W. Hänsch: Nature (London) **416**, 233 (2002). [194](#)
22. D. J. Jones et al.: Science **288**, 635 (2000). [194](#)
23. V. I. Korobov: Phys. Rev. A **73**, 022509 (2006). [195](#), [196](#)
24. V. I. Korobov: private communication (2007). [197](#)
25. Y. Kino, H. Kudo, and M. Kamimura: Mod. Phys. Lett. A **18**, 388 (2003); (private communication). [198](#)
26. V. I. Korobov: in Proceedings of the EXA05 International Conference on Exotic Atoms and Related Topics, edited by A. Hirtl, J. Marton, E.Widmann, and J. Zmeskal (Austrian Academy of Sciences Press, Vienna, 2005). [198](#)
27. M. Hori et al.: Phys. Rev. Lett. **94**, 063401 (2005). [199](#), [200](#)

Simple Molecules

Precision Spectroscopy of Molecular Hydrogen Ions: Towards Frequency Metrology of Particle Masses

B. Roth¹, J. Koelemeij¹, S. Schiller¹, L. Hilico^{2,3}, J.-P. Karr^{2,3},
V. Korobov⁴, and D. Bakalov⁵

¹ Institut für Experimentalphysik, Heinrich-Heine-Universität Düsseldorf
40225 Düsseldorf, Germany

² Département de Physique et Modélisation, Université d'Evry Val d'Essonne
Boulevard F. Mitterrand, 91025 Evry cedex

³ Laboratoire Kastler Brossel, Université Pierre et Marie Curie
T12, Case 74, 4 place Jussieu, 75252 Paris, France
jean-philippe.karr@univ-eury.fr

⁴ Joint Institute for Nuclear Research, 141980 Dubna, Russia

⁵ Institute for Nuclear Research and Nuclear Energy, Bulgarian Academy of
Sciences, Sofia 1784, Bulgaria

Abstract. We describe the current status of high-precision ab initio calculations of the spectra of molecular hydrogen ions (H_2^+ and HD^+) and of two experiments for vibrational spectroscopy. The perspectives for a comparison between theory and experiment at a level of 1 part in 10^9 are considered.

1 Introduction

The molecular hydrogen ion (MHI) is the simplest stable molecule, containing just two nuclei and a single electron. Since the birth of the field of molecular physics it has played an important role: it is on the one hand an important benchmark system for detailed studies of energy levels [1], for collisions and chemical reactions between charged molecules and neutral atoms/molecules, of interactions with laser radiation and energetic charged particles and for testing the respective theoretical descriptions. On the other hand, the MHI is also an astrophysically important molecule, involved in reaction chains leading to the production of polyatomic molecules. Over 800 publications have been written on this molecule in the last 35 years [2]. The large majority are theoretical studies.

Concerning high-resolution spectroscopy of MHIs, only a limited number of investigations have been carried out, most of which a long time ago. Radiofrequency spectroscopy of the hyperfine structure in several vibrational

levels has been performed on H_2^+ trapped in a Paul trap [3]; several low-lying fundamental ro-vibrational transitions of HD^+ have been measured using laser spectroscopy on an ion beam [4], while rotational and ro-vibrational transitions of H_2^+ , D_2^+ and HD^+ close to the dissociation limit were investigated using microwave and laser spectroscopy, also on an ion beam [5, 6]. The highest spectroscopic accuracies reported so far were achieved in the experiments of Jefferts and of Wing et al. [4, 7], $\simeq 3.8 \cdot 10^{-7}$ in relative units. Recently, the dissociation energies have also been obtained with accuracies $\simeq [0.6 - 1.2] \cdot 10^{-6}$ [8]. Thus, the experimental accuracies have been far less than those achieved in hydrogen or helium spectroscopy.

In the late 1990s, it was recognized that there are attractive reasons and many opportunities to study MHIs in novel ways and to achieve a much higher precision than previously possible [9]. Several techniques, not used before on MHIs, appeared to be applicable, including translational cooling, internal cooling, spectroscopy with reduced Doppler broadening, Doppler-free spectroscopy, high-sensitivity ion detection. Novel laser systems not available at the time of the earlier precision spectroscopic studies can be used advantageously, among them diode lasers, quantum cascade lasers and the femtosecond frequency comb. The prospect of significantly improved experimental precision has also motivated us to develop more extended theoretical treatments of the MHI; in the course of these efforts, the accuracy of the energy levels has been increased by approximately two orders of magnitude compared to previous work.

Some of the above techniques have by now been implemented and are reported here; the remaining appear to be feasible in the near future. These recent developments open up a number of novel applications of MHIs:

- (i) Test advanced ab initio molecular calculations (in particular, QED contributions);
- (ii) Measure fundamental constants;
- (iii) Test concepts for the manipulation of molecules (state preparation, alignment);
- (iv) Sense fields (blackbody radiation [10]);
- (v) Probe fundamental physics laws (e.g. Lorentz Invariance [11], time invariance of fundamental constants [12, 13]);
- (vi) Study electric dipole interactions between molecules [14];
- (vii) Explore elastic, reactive and charge exchange collisions with neutral atoms and molecules at ultra-low collision energies.

The successful demonstration of manipulation of MHIs at the quantum-state level could also open up the possibility to study collisions with quantum-state resolution, i.e. where all parent particles are in specific quantum states.

An attractive perspective of our work pursued under (i) is to eventually determine the ratios of electron-to-proton mass (m_e/m_p), proton-to-deuteron mass (m_p/m_d) and proton-to-triton mass (m_p/m_t) from a comparison between accurate experimental and theoretical energy level data. The basis for

this possibility is the dependence of the vibrational and rotational transition frequencies on the fundamental constants. For fundamental vibrational and rotational transitions, the frequencies scale approximately as

$$\nu_{\text{vib}} \sim \sqrt{m_e/\mu} R_\infty c, \quad \nu_{\text{rot}} \sim (m_e/\mu) R_\infty c, \quad (1)$$

where $\mu = M_1 M_2 / (M_1 + M_2)$ is the reduced mass of the two nuclei and R_∞ is the Rydberg energy. The precise dependencies have been computed in [12, 15, 16]. The mass ratios m_p/m_d , m_p/m_t and m_e/m_p are conventionally determined by Penning ion trap mass spectrometry on single particles or by electron spin resonance of single hydrogen-like ions in a Penning ion trap. Relative accuracies are currently $2.0 \cdot 10^{-10}$ [17], $2 \cdot 10^{-9}$ and $4.6 \cdot 10^{-10}$ [17, 18], respectively. Note that in the case of m_e/m_p , the determination involves the use of QED [19]. Clearly, the corresponding accuracies of ν_{vib} , ν_{rot} represent the goal levels for our ongoing experimental and theoretical efforts on H_2^+ and HD^+ .

Several aspects support the expectation that such accuracies can be reached in the near future. First, the lifetimes of vibrational levels are long, the shortest ones occurring for low-lying levels in HD^+ are $\simeq 10$ ms. The relative linewidth due to spontaneous decay is thus of the order or smaller than 10^{-13} . Second, Doppler broadening can be strongly reduced or eliminated by either cooling the molecular ions or by performing two-photon Doppler-free spectroscopy. Finally, collision broadening and time-of-flight broadening can also be minimized by both cooling and providing a good ultra-high vacuum environment. Systematic shifts due to light fields, trap electric fields and trap and environmental magnetic fields will need to be considered; hereby it will be helpful that these influences be calculated accurately, using the relative simplicity of the MHI. The theoretical determination of the energy levels at the goal accuracy level will need as input nuclear properties such as the proton and deuteron nuclear radii, which may be obtained, e.g. from hydrogen spectroscopy or nuclear scattering experiments.

In this contribution we present an overview of our theoretical and experimental results achieved recently on MHIs. Section 2 describes the theoretical approaches for a precise computation of energy levels, including hyperfine and QED effects and the computation of one- and two-photon spectra. Section 3 presents the development and results from an experiment for trapping and spectroscopy of H_2^+ performed at the Université d'Evry Val d'Essonne. Section 4 summarizes an experiment on HD^+ at the Universität Düsseldorf.

2 Ab Initio Theory of H_2^+ and HD^+

The dissociation energies of 462 states in H_2^+ and 619 in HD^+ in a wide range of v and L , vibrational and rotational quantum numbers, have been calculated some time ago by R.E. Moss [20, 21] with a relative accuracy of $\sim 5 \cdot 10^{-9}$

(including the leading-order relativistic and radiative corrections). Later the numerical precision of the nonrelativistic energies have been improved up to 10^{-15} – 10^{-24} a.u. [12, 15, 22, 23, 24, 25, 26] by using variational methods. The ultimate accuracy of $\sim 10^{-24}$ a.u. has been obtained for the H_2^+ ground state [26]. These calculations demonstrate that at least the nonrelativistic ro-vibrational transition frequencies can be determined with an uncertainty well below the 1 kHz level. In this section we describe the calculation of QED corrections as an expansion in terms of α , the fine structure constant. The numerical method exploits a variational approach based on the Slater-type exponentials as basis functions. We demonstrate that the frequencies of ro-vibrational transitions can be obtained in this way with a precision better than 1 part in 10^9 (1 ppb).

2.1 Variational Expansion

The variational bound state wave functions are calculated by solving the three-body Schrödinger equation with Coulomb interaction using the variational approach based on the exponential expansion with randomly chosen exponents. Details and the particular strategy of choice of the variational nonlinear parameters and basis structure that have been adopted in the present work can be found in [23].

Briefly, the wave function for a state with a total orbital angular momentum L and a total spatial parity $\pi = (-1)^L$ is expanded as follows:

$$\begin{aligned} \Psi_{LM}^\pi(\mathbf{R}, \mathbf{r}_1) &= \sum_{l_1+l_2=L} \mathcal{Y}_{LM}^{l_1 l_2}(\hat{\mathbf{R}}, \hat{\mathbf{r}}_1) G_{l_1 l_2}^{L\pi}(R, r_1, r_2), \\ G_{l_1 l_2}^{L\pi}(R, r_1, r_2) &= \sum_{n=1}^N \left\{ C_n \operatorname{Re} [e^{-\alpha_n R - \beta_n r_1 - \gamma_n r_2}] \right. \\ &\quad \left. + D_n \operatorname{Im} [e^{-\alpha_n R - \beta_n r_1 - \gamma_n r_2}] \right\}. \end{aligned} \quad (2)$$

Here $\mathcal{Y}_{LM}^{l_1 l_2}(\hat{\mathbf{R}}, \hat{\mathbf{r}}_1) = R^{l_1} r_1^{l_2} \{Y_{l_1} \otimes Y_{l_2}\}_{LM}$ are the solid bipolar harmonics, \mathbf{R} is the position vector of nucleus 2 relative to nucleus 1 and $\mathbf{r}_1, \mathbf{r}_2$ are positions of an electron relative to nuclei 1 and 2, respectively. The complex exponents, α, β, γ , are generated in a pseudorandom way.

When the exponents α_n, β_n and γ_n are real, the method reveals slow convergence for molecular-type Coulomb systems. The use of complex exponents allows to reproduce the oscillatory behaviour of the vibrational part of the wave function and to improve convergence [23, 27].

The advantage of choice (2) is the simplicity of the basis functions. It allows evaluating analytically matrix elements of the Breit–Pauli Hamiltonian and the leading-order radiative corrections and, more importantly, to treat in a systematic way the singular integrations encountered in higher-order contributions [28].

2.2 Leading-Order Relativistic and Radiative Corrections

Relativistic corrections of the leading $R_\infty\alpha^2$ order, the Breit–Pauli Hamiltonian, are well known and can be found in many textbooks [29, 30]. The nuclear finite size effects are considered as contributions to this order. Details, relevant particularly to the case of the MHIs, can be found in [31]. In what follows we assume that the nuclear charges are $Z_1 = Z_2 = Z = 1$ and nuclear masses are denoted by capital M_i . The units adopted are ($\hbar = e = m_e = 1$).

The radiative corrections of an order $R_\infty\alpha^3$ for a one-electron molecular system can be expressed by the following set of equations (see [32, 33, 34]).

The one-loop self-energy correction (orders $R_\infty\alpha^3$ and $R_\infty\alpha^3(m/M)$) is

$$E_{\text{se}}^{(3)} = \frac{4\alpha^3 Z}{3} \left(\ln \frac{1}{\alpha^2} - \beta(L, v) + \frac{5}{6} - \frac{3}{8} \right) \langle \delta(\mathbf{r}_1) + \delta(\mathbf{r}_2) \rangle + \alpha^3 Z^2 \sum_{i=1,2} \left[\frac{2}{3M_i} \left(-\ln \alpha - 4\beta(L, v) + \frac{31}{3} \right) \langle \delta(\mathbf{r}_i) \rangle - \frac{14}{3M_i} Q(r_i) \right], \quad (3)$$

where

$$\beta(L, v) = \frac{\langle \mathbf{J}(H_0 - E_0) \ln((H_0 - E_0)/R_\infty) \mathbf{J} \rangle}{\langle [\mathbf{J}, [H_0, \mathbf{J}]]/2 \rangle} \quad (4)$$

is the Bethe logarithm. The latter quantity presents the most difficult numerical problem in computation of QED corrections for the three-body bound states. In [34, 35] the calculations for a wide range of ro-vibrational states in H_2^+ and HD^+ have been performed to an accuracy of about seven significant digits. The operator \mathbf{J} in (4) is the electric current density operator of the system.¹ The last term, $Q(r)$, in (3) is the mean value of a regularized operator introduced by Araki and Sucher [36] for the $1/(4\pi r^3)$ potential:

$$Q(r) = \lim_{\rho \rightarrow 0} \left\langle \frac{\Theta(r - \rho)}{4\pi r^3} + (\ln \rho + \gamma_E) \delta(\mathbf{r}) \right\rangle. \quad (5)$$

The values of this matrix element for ro-vibrational states are calculated in [31].

The remaining contributions in this order can be obtained from the Pauli form factor of an electron (anomalous magnetic moment),

$$E_{\text{anom}}^{(3)} = \pi\alpha^2 Z \left[\frac{1}{2} \left(\frac{\alpha}{\pi} \right) \right] \langle \delta(\mathbf{r}_1) + \delta(\mathbf{r}_2) \rangle, \quad (6)$$

and from the one-loop vacuum polarization,

$$E_{\text{vp}}^{(3)} = \frac{4\alpha^3 Z}{3} \left[-\frac{1}{5} \right] \langle \delta(\mathbf{r}_1) + \delta(\mathbf{r}_2) \rangle. \quad (7)$$

¹ $\mathbf{J} = \sum_a z_a \mathbf{p}_a / m_a$, where z_a , \mathbf{p}_a , m_a are the charge, momentum and mass of particle a . The sum is performed over all particles of the system.

2.3 $R_\infty\alpha^4$ Order Corrections in the Nonrecoil Limit

The contribution of recoil corrections, proportional to (m/M) , in the $R_\infty\alpha^4$ order are too small for our present consideration and may be neglected. Radiative corrections for a bound electron in an external field are known analytically [38, 39]:

$$\begin{aligned}
 E_{\text{se}}^{(4)} &= \alpha^4 Z^2 \left[4\pi \left(\frac{139}{128} - \frac{1}{2} \ln 2 \right) \right] \langle \delta(\mathbf{r}_1) + \delta(\mathbf{r}_2) \rangle, \\
 E_{\text{vp}}^{(4)} &= \alpha^4 Z^2 \left[\frac{5\pi}{48} \right] \langle \delta(\mathbf{r}_1) + \delta(\mathbf{r}_2) \rangle, \\
 E_{\text{anom}}^{(4)} &= \alpha^2 Z\pi \left[\left(\frac{\alpha}{\pi} \right)^2 \left(\frac{197}{144} + \frac{\pi^2}{12} - \frac{\pi^2}{2} \ln 2 + \frac{3}{4} \zeta(3) \right) \right] \langle \delta(\mathbf{r}_1) + \delta(\mathbf{r}_2) \rangle, \\
 E_{\text{2loop}}^{(4)} &= \alpha^2 Z\pi \left[\left(\frac{\alpha}{\pi} \right)^2 \left(-\frac{6131}{1296} - \frac{49\pi^2}{108} + 2\pi^2 \ln 2 - 3\zeta(3) \right) \right] \langle \delta(\mathbf{r}_1) + \delta(\mathbf{r}_2) \rangle.
 \end{aligned} \tag{8}$$

The last equation includes both the Dirac form factor and polarization operator contributions.

The $R_\infty\alpha^4$ relativistic correction is obtained using the adiabatic “effective” potential for an $m\alpha^6$ term in the α expansion of the two-center Dirac energy (see Fig. 1). Averaging over the squared wave function density of a state, one gets $E_{\text{rc}}^{(4)}$. The adiabatic potentials have been obtained recently with about five

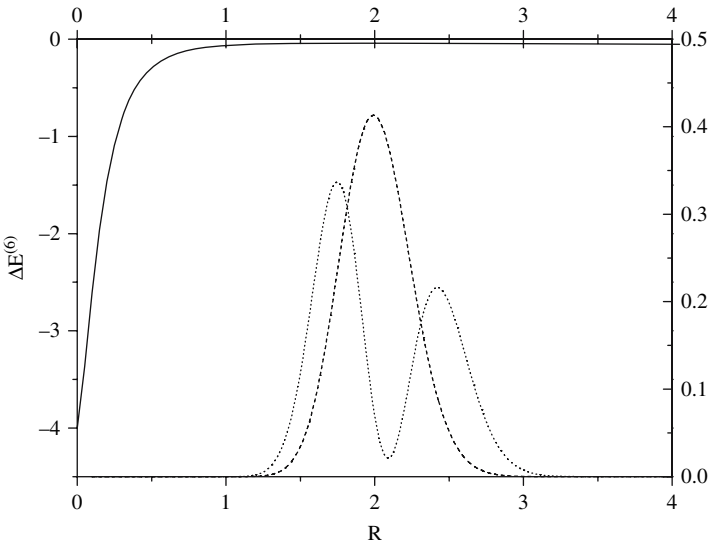


Fig. 1. Adiabatic potential of the $m\alpha^6$ order contribution (in atomic units) to the Dirac energy of the two-center problem ($Z_1 = Z_2 = 1$). Dashed curves are the squared densities of the ground and first vibrational state wave functions of the H_2^+ ion

significant digits [37], and the Born–Oppenheimer solution yields approximate wave functions at the $(m/M) \approx 10^{-4}$ level, which allows to claim that $E_{\text{rc}}^{(4)}$ is now known to four digits.

Some higher-order radiative corrections for a bound electron in an external field are also known in an analytic form [38, 39] and can be included:

$$E_{\text{se}}^{(5)} = \alpha^5 Z^3 \ln^2(Z\alpha)^{-2} [-1] \langle \delta(\mathbf{r}_1) + \delta(\mathbf{r}_2) \rangle. \quad (9)$$

The electron ground state wave function may be approximated by $\psi_e(\mathbf{r}_e) = C[\psi_{1s}(\mathbf{r}_1) + \psi_{1s}(\mathbf{r}_2)]$, where ψ_{1s} is the hydrogen ground state wave function and C is a normalization coefficient. Thus, one may use this approximation to evaluate other contributions in the $R_\infty \alpha^5$ order:

$$\begin{aligned} E_{\text{se}}^{(5')} &= \alpha^5 Z^3 [A_{61} \ln(Z\alpha)^{-2} + A_{60}] \langle \delta(\mathbf{r}_1) + \delta(\mathbf{r}_2) \rangle, \\ E_{2\text{loop}}^{(5)} &= \frac{\alpha^5}{\pi} Z^2 [B_{50}] \langle \delta(\mathbf{r}_1) + \delta(\mathbf{r}_2) \rangle, \end{aligned} \quad (10)$$

where the constants A_{61} , A_{60} and B_{50} are taken equal to the constants of the $1s$ state of the hydrogen atom $A_{61} = 5.419\dots$ [40], $A_{60} = -30.924\dots$ [41] and $B_{50} = -21.556\dots$ [42] (see also [39] and references therein). The final theoretical uncertainty in the transition frequency (see Table I) is determined by the total contribution of the last two equations.

2.4 Hyperfine Structure of States

The leading-order contribution to the hyperfine splitting of the ro-vibrational states is calculated using the spin-dependent part of the Breit–Pauli interaction Hamiltonian, with phenomenological values for the nuclear magnetic moments and the electron anomalous magnetic moment. The hyperfine levels of HD^+ , E_{vLFSJ} , are labelled with the quantum numbers F , S and J of the intermediate angular momenta $\mathbf{F} = \mathbf{I}_p + \mathbf{s}_e$, $\mathbf{S} = \mathbf{F} + \mathbf{I}_d$ and of the total angular momentum $\mathbf{J} = \mathbf{L} + \mathbf{S}$ [43]. In case of H_2^+ due to the Pauli exclusion principle the total nuclear spin I is uniquely defined by L and the parity of

Table 1. Summary of contributions to the $(v=0, L=0) \rightarrow (v'=1, L'=0)$ transition frequency (in MHz). $\Delta E - \text{nr}$ is the nonrelativistic energy

	H_2^+	HD^+
ΔE_{nr}	65 687 511.0686	57 349 439.9717
ΔE_{α^2}	1091.041(03)	958.152(03)
ΔE_{α^3}	-276.544(02)	-242.118(02)
ΔE_{α^4}	-1.997	-1.748
ΔE_{α^5}	0.120(23)	0.106(19)
ΔE_{tot}	65 688 323.688(25)	57 350 154.368(21)

the electronic state. The following coupling scheme is adopted: $\mathbf{F} = \mathbf{I} + \mathbf{s}_e$ and $\mathbf{J} = \mathbf{L} + \mathbf{F}$ [44]. The hyperfine structure (HFS) of the ro-vibrational states of HD^+ consists of 4, 10 or 12 hyperfine sub-levels for $L=0$, $L=1$ and $L \geq 2$, respectively (see Fig. 2). The multiplicity of the HFS of H_2^+ is reduced to 1 for $L=0$, 5 for $L=1$, 2 for even and 6 for odd $L > 1$ states. Typically, the hyperfine splitting of the lower ro-vibrational states of HD^+ and H_2^+ is about 1 GHz. The uncertainty in the hyperfine spectrum is related to the unknown contribution of the spin interaction terms of orders $O(R_\infty \alpha^4 (m/M))$ and higher, which have not yet been taken into consideration, and is estimated not to exceed 100 kHz.

Each transition line between ro-vibrational states is split into a multiplet of hyperfine components, corresponding to the allowed transitions $i \rightarrow f$ between the states of the hyperfine structure of the initial and final states. Whether these hyperfine components will be resolved or not depends on the initial and final state lifetime and on the experimental conditions (effective transition linewidth Γ_f , laser intensity I , temperature, interaction time, etc.) Examples of spectral data are presented in experimental sections of our review (see Fig. 13). The shape of the profile also depends on the population of the initial hyperfine states. The general expressions for the probability per unit time for one- and two-photon transitions between ro-vibrational states of the MHIs with account of the hyperfine structure are given in [45].

The probability per unit time for the hyperfine transition $i \rightarrow f$ at resonance (averaged over the magnetic numbers of initial and final states), $\Gamma_{f,i}$, may be represented in the form:

$$\Gamma_{f,i} = T_{f,i}^2 \Gamma_{v'L',vL} \quad , \quad \Gamma_{v'L',vL} = \frac{2\pi\alpha}{3\hbar} \frac{I}{\Gamma_f} \frac{\langle v'L' || \mathbf{d} || vL \rangle^2}{2L+1}. \quad (11)$$

Here $\Gamma_{v'L',vL}$ is the probability per unit time of laser-stimulated dipole transitions between ro-vibrational states, $\langle v'L' || \mathbf{d} || vL \rangle$ is the reduced matrix

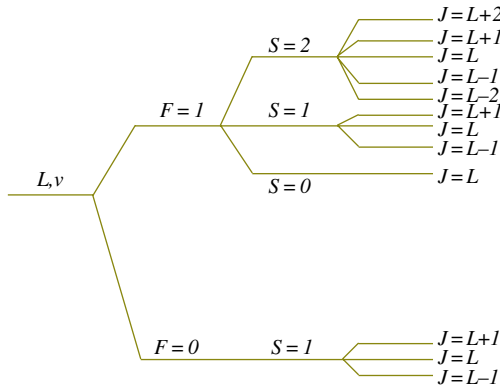


Fig. 2. Hyperfine structure of a ro-vibrational state of HD^+ with $L \geq 2$

element of the electric dipole moment of the HD^+ ion $\mathbf{d} = \sum_a z_a \mathbf{r}_a$ and

$$T_{f,i} = \sqrt{(2J'+1)(2L+1)} \sum_{F''S''} (-1)^{S''+J+L'} \begin{Bmatrix} L & 1 & L' \\ J' & S'' & J \end{Bmatrix} \beta_{F''S''}^f \beta_{F''S''}^i, \quad (12)$$

where $\beta_{F''S''}^{vLFSJ}$ are constant amplitudes of the state vectors of the hyperfine states,

$$|vLFSJ, J_z\rangle = \sum_{F''S''} \beta_{F''S''}^{vLFSJ} \sum_{M\zeta} C_{LM,S''\zeta}^{JJ_z} \Psi_{vLM}(\mathbf{R}, \mathbf{r}_1) \chi(F''S'', \zeta), \quad (13)$$

determined from the effective Hamiltonian of spin interaction. Here $\chi(FS, \zeta)$ are basis spinors of definite values of F , S and S_z in the space of the spin variables. The relative intensity of the hyperfine components of a transition line between ro-vibrational states is thus determined by the amplitudes $T_{f,i}$. In case the individual hyperfine components cannot be resolved, the observable intensity is reduced to the intensity of the dipole ro-vibrational transition $\Gamma_{v'L',vL}$, in agreement with the identity $\sum_f T_{f,i}^2 = 1$.

The hyperfine structure of the one- and two-photon transition lines includes a large number of components, most of which, however, are suppressed. There are as well dominant (or “*favoured*”) transitions between states with similar spin structure, such as $(vL F J) \rightarrow (v' L' F' J')$ with $\Delta J = \Delta L$ (for H_2^+). In such pairs of homologous hyperfine states the spin-dependent corrections to the ro-vibrational energies $E_{v'L'F'J'}$ and $E_{vL F J}$ have close values, which partially cancel each other when evaluating the spin correction to the resonance transition frequency $(E_{v'L'F'J'} - E_{vL F J})/h$. Indeed, the *favoured* hyperfine transitions span over a frequency interval less than 25 MHz (see Fig. 3). It is natural to expect that the unknown contributions to the frequency of the favoured transitions from the spin interactions of order $R_\infty \alpha^4 (m/M)$ and higher also tend to cancel each other; therefore, the theoretical uncertainty of the resonance frequency of the *favoured* hyperfine sublines will be less than ~ 5 kHz.

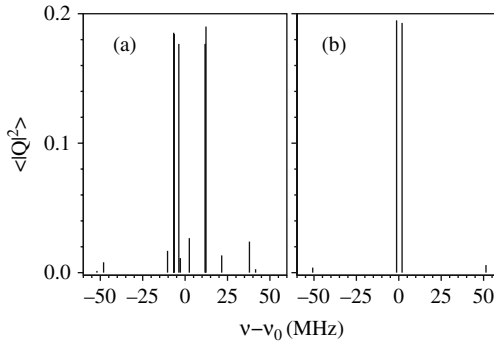


Fig. 3. Hyperfine splitting and intensities of the two-photon ro-vibrational transitions of the H_2^+ ion: (a) $(v=0, L=1) \rightarrow (v'=1, L'=1)$, (b) $(v=0, L=2) \rightarrow (v'=1, L'=2)$

2.5 Two-Photon Transition Probabilities

In order to assess the feasibility of Doppler-free two-photon spectroscopy in H_2^+ or HD^+ , it is essential to evaluate transition probabilities between ro-vibrational states. This can be done using the formula from second-order perturbation theory [46] and the accurate wavefunctions provided by variational calculations. Assuming that magnetic sublevels are equally populated, the two-photon transition probability at resonance between states v, L and v', L' is

$$\Gamma_{v,L,v',L'} = \left(\frac{4\pi a_0^3}{\hbar c} \right)^2 \frac{4I^2}{\Gamma_f} \overline{Q}_{v,L,v',L'} \quad (14)$$

where I is the excitation intensity, Γ_f the transition linewidth and

$$\overline{Q}_{v,L,v',L'} = \frac{1}{2L+1} \sum_{k=0,2} \frac{|\langle vL \| Q^{(k)} \| v'L' \rangle|^2}{2k+1}. \quad (15)$$

$Q^{(0)}$, $Q^{(2)}$ are, respectively, the scalar and tensor parts of the two-photon transition operator

$$Q = \frac{1}{4\pi\epsilon_0 a_0^3} \mathbf{d} \cdot \boldsymbol{\epsilon} \frac{1}{E-H} \mathbf{d} \cdot \boldsymbol{\epsilon}. \quad (16)$$

Here, $E = [E(v, L) + E(v', L')]/2$ is the one-photon resonance energy and $\boldsymbol{\epsilon}$ the exciting field polarization. The two-photon transition probabilities were calculated in [22, 47].

For the H_2^+ case [47] there exists a quasi-selection rule $\Delta v = \pm 1$, and the dimensionless transition probabilities $\overline{Q}_{v,L,v',L'}$ are rather small, of the order of 1, which is due to the level structure of H_2^+ . If we consider the example of transitions between $L = 0$ states, these states are of $^1S^e$ symmetry, and there is no resonant intermediate level of $^1P^o$ symmetry that could enhance the transition probability.

The situation is different in the HD^+ case [22], since there is no splitting between singlet and triplet states due to the loss of exchange symmetry between the nuclei. As a result, for a transition between $L = 0$ (S^e) states, there exist intermediate bound P^o levels which can be very close in energy and efficiently enhance the transition probability. This is most likely to happen if the difference between v and v' (the initial and final vibrational quantum numbers) is an even number. In this case, the state $(v'' = (v+v')/2, L'' = L \pm 1)$ is often close to the middle energy $E = [E(v, L) + E(v', L')]/2$, because of the quasi-harmonic structure of vibrational levels. As a result, some of the most intense two-photon lines are $\Delta v = 2$ transitions in the 5–6 μm range or $\Delta v = 4$ transitions in the 2.5–3 μm range, accessible, e.g., with continuous-wave optical parametric oscillator or quantum cascade lasers. The dimensionless transition probabilities $\overline{Q}_{v,L,v',L'}$ can reach values as high as 300 for the $(v=0, L=1) \rightarrow (v=2, L=1)$ transition at 5.366 μm . Thus, the HD^+ molecular ion is a promising candidate for precise two-photon spectroscopy.

The next step is to consider the hyperfine structure of two-photon transition lines. The representation of the hyperfine state vectors in the H_2^+ case is

$$|vL F J J_z\rangle = \sum_{F'} \beta_{F'}^{vL F J} \sum_{M\zeta} C_{LM, F'\zeta}^{JJ_z} \psi_{vLM}(\mathbf{R}, \mathbf{r}_1) \chi(F', \zeta). \quad (17)$$

The definitions for $\chi(F', \zeta)$ and $\beta_{F'}^{vL F J}$ are similar to those in (13). Assuming equal populations for hyperfine magnetic sublevels, the dimensionless transition probability between levels $|i\rangle = |vL F J\rangle$ and $|f\rangle = |v' L' F' J'\rangle$ is

$$\bar{Q}_{i,f} = (2J' + 1) \sum_{k=0,2} \frac{\left| \langle vL \| Q^{(k)} \| v' L' \rangle \sum_{F''} (-1)^{J'+L+F''} \begin{Bmatrix} L & k & L' \\ J' & F'' & J \end{Bmatrix} \beta_{F''}^f \beta_{F''}^i \right|^2}{2k + 1}. \quad (18)$$

The hyperfine structure of two different transitions for linear polarization is shown in Fig. 3. Transitions between odd L states (Fig. 3(a)) comprise between 25 and 34 components, 5 or 6 of which are favoured. Transitions between even L states (Fig. 3(b)) have a much simpler structure, the total nuclear spin being zero. The nonzero even L spectrum comprises only two main components (verifying $\Delta J = 0$) together with two weak satellites. Transitions between $L=0$ states are structureless, which makes them especially attractive from a metrological point of view.

3 Two-Photon Spectroscopy of H_2^+

A two-photon vibrational spectroscopy experiment aimed at the determination of the electron-to-proton mass ratio is being set up at the Kastler Brossel Laboratory. We begin by recalling the basic spectral features of the MHI and discuss the planned experimental sequence. In the second part, we report on the present status of the experimental setup. It is composed of a hyperbolic Paul trap in which a few thousand H_2^+ ions can be confined, a UV laser for ion preparation and detection by state-selective photodissociation and a narrow-line, tunable laser system that will excite the two-photon transition.

3.1 H_2^+ Level Structure

Although the Born–Oppenheimer (BO) approximation is not relevant for highly accurate calculations, it remains a very convenient tool to get useful insight into the H_2^+ level structure. In order to understand the processes discussed here, it is enough to consider the first two BO electronic curves: the ground state $1s\sigma_g$ and first excited state $2p\sigma_u$, which are depicted in Fig. 4.

The exact symmetries of the system are the total spatial parity π and the exchange of nuclei P_{12} ; the g/u electronic parity π_e used in the BO approach is related to them by $\pi_e = \pi P_{12}$. The bound levels of H_2^+ can be labelled $v, (2I+1)L^{e,o}$ where v and L are the vibrational and orbital quantum numbers,

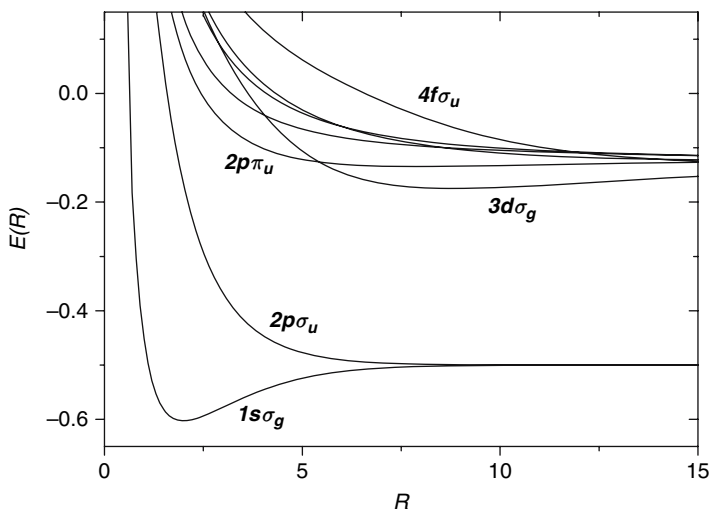


Fig. 4. Born–Oppenheimer electronic energies (in a.u.) of the adiabatic potential terms

I is the total nuclear spin quantum number and (e, o) stands for the total parity. Since the total spatial parity is $\pi = (-1)^L$, the $1s\sigma_g$ curve only supports $^1S^e, ^3P^o, ^1D^e \dots$ levels.

The $2p\sigma_u$ electronic curve presents at large internuclear distances a weak attractive potential that supports two bound $L = 0$ energy levels [20, 48]. Some of those states have been observed by microwave or laser spectroscopy experiments [49]. At higher L the $2p\sigma_u$ potential supports bound or dissociative $^1P^o, ^3D^e, ^1F^o \dots$ states that can be calculated numerically using either the variational or the complex coordinate rotation method.

3.2 One-Photon Transitions: Photodissociation

The selection rules for one-photon dipole transitions are $\Delta L = \pm 1$ and $\Delta I = 0$. As a consequence, transitions between $1s\sigma_g$ bound ro-vibrational states of H_2^+ are forbidden (in contrast with the HD^+ case), resulting in very long-lived states. On the other hand, one-photon photodissociation transitions from $1s\sigma_g$ to $2p\sigma_u$ electronic states are allowed. The photodissociation cross-sections σ_v of the $(^1S^e, v)$ states have been first computed by Dunn [50] in the Born–Oppenheimer approximation and then using the perimetric coordinate variational method in [51]. The results are given in Fig. 5. They show that a laser source in the 250 nm range can be used to selectively photodissociate the $v = 1, 2, 3, \dots$ vibrational states while keeping the ions in the $v = 0$ level since the successive cross-section ratios σ_{v+1}/σ_v are 214, 40, 10, for $v = 0, 1, 2$, respectively.

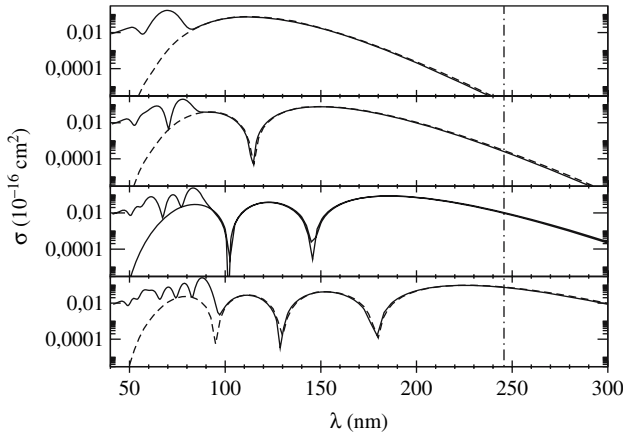


Fig. 5. Photodissociation cross-sections of the $L = 0$, v levels of H_2^+ . The dashed lines are the result of a Born–Oppenheimer calculation [50], which takes the $1s\sigma_g$ and $2p\sigma_u$ electronic curves into account. The nodal structure of the cross-section reflects that of the vibrational wavefunction. The solid lines are obtained from an exact variational method which fully takes into account the three-body dynamics [51]. The additional nodal structure appearing in the short wavelength domain can be interpreted as the photodissociation to higher excited electronic states ($3d\sigma_g$, $2p\pi_u$, $4f\sigma_u$, ...). The dot-dashed vertical line corresponds to the KrF laser wavelength of 248 nm

3.3 Two-Photon Transitions: Choice of the Transition

One-photon transitions between bound states being forbidden, a high-resolution study of the vibrational structure of H_2^+ is only possible using Doppler-free two-photon spectroscopy. Two-photon transitions obey the selection rule $\Delta L = 0, \pm 2$ as well as the quasi-selection rule $\Delta v = \pm 1$, as discussed in Sect. 2.5. The corresponding $(v, L) \rightarrow (v' = v + 1, L')$ transition frequencies lie in the 8–12 μm range. Among them, we have chosen to probe the $v = 0 \rightarrow v = 1$ transitions, for L and L' equal to 0 or 2 and eventually 1 or 3. We now give the arguments that explain this choice.

The first condition to fulfil is that it should be possible to prepare a large enough number of H_2^+ in the initial state of the transition. The ro-vibrational populations of H_2^+ ions, after creation by electron impact ionization of a low-pressure H_2 gas, have been studied both theoretically and experimentally [52]. The vibrational populations are linked to the overlap of the H_2 and H_2^+ vibrational wave functions (Franck–Condon principle); they are found to be of the order of 12, 19, 19, 15, 12, 8, 5, 4% for the first few levels. The rotational populations of the H_2^+ ions are those of the H_2 mother molecules, i.e. 13, 66, 12, 8% at 300 K. Moreover, we have shown in the previous paragraph that UV photodissociation provides a convenient way to prepare ions in the ground vibrational state; it is then desirable to choose a $v = 0$ state as initial state

of the transition, with L between 0 and 3, $L=1$ being the best choices with respect to the number of ions. The same photodissociation process can be used to detect the ions in the excited $v=1$ state.

The hyperfine structure of two-photon lines should also be considered; it is apparent from Fig. 3 that it is simpler for transitions between even L states. This makes such transitions much more attractive, since the ion fraction in a given hyperfine substate of the initial state will be larger, as will be the intensities of the various hyperfine components of the transition line.

The intensities of the various $(v=0, L) \rightarrow (v'=1, L')$ (with low L) two-photon lines are of the same magnitude; the choice of a particular transition depends mostly on the availability and characteristics of laser sources at the required wavelength. The whole mid-infrared range is accessible by the recently developed quantum cascade lasers (QCL); $L'=L$ transitions are especially attractive, because they lie within the spectrum of CO₂ lasers ($\lambda \simeq 9\text{--}10\ \mu\text{m}$). Also, a number of frequency reference molecular absorption lines are known in this range [53]. The first transition that is going to be probed in our experiment is the $(v=0, L=2) \rightarrow (v'=1, L'=2)$ line at 9.166 nm. The details of coincidences with CO₂ lines and molecular reference lines, which make this transition favourable, are explained below.

3.4 Experimental Sequence

The two-photon transition matrix elements $|Q_{v,L,v',L'}|^2$ of the “favoured” hyperfine components of two-photon transitions are of the order of 0.2 (see Fig. 3). A typical QCL can deliver about 50 mW of single-mode optical power. Assuming a perfect coupling to a build-up cavity of finesse 1000 with a waist of 1 mm, one obtains a laser flux of 15 W/mm². Assuming an instrumental width $\Gamma_f \approx 10$ kHz (see below) yields transition rates of about 70 per second. This order of magnitude shows that long interaction times are needed and that one has to work with a cloud of trapped ions, having a radius of the order of the beam waist.

The considerations of the previous paragraph show that vibrational two-photon spectroscopy of H₂⁺ can be performed by $(2+1')$ resonance-enhanced multiphoton dissociation (REMPD). This process is very similar to that implemented for HD⁺ vibrational spectroscopy and described in more detail in Sect. 4.

The experiment will be conducted in the following stages:

- Simultaneous creation, trapping and selection of $(L, v=0)$ H₂⁺ ions;
- Excitation of the $(L, v=0) \rightarrow (L', v'=1)$ two-photon transition;
- Photodissociation of the $(L, v=1)$ H₂⁺ ions;
- Time-of-flight detection of H⁺ and H₂⁺ ions.

3.5 Experimental Setup

The ion trap is depicted in Fig. 6(a). It is a hyperbolic Paul trap with a ring of inner radius $r_0 = 4.2$ mm and two end caps separated by $2z_0 = 6$ mm. Two pairs of holes (5 mm in diameter) are drilled in the ring along two orthogonal axes to shine the ion cloud with the UV and IR light. Both end cap electrodes are AC grounded. A RF voltage (about 200 V peak-to-peak amplitude at 10.3 MHz) and a continuous voltage of a few volts are applied to the ring electrode, resulting in trapping well depths of a few eV.

The H_2^+ ions are produced by electron impact ionization from the residual H_2 gas. The electron gun is made of a tungsten wire and a Wehnelt cylinder; it is typically turned on for 100–200 ms. A 1 mm hole in one of the end cap electrodes allows access to the trap.

The contents of the trap are analysed by applying a short negative high-voltage pulse to the second end cap, thus extracting the ions from the trap through a 2 mm hole. The extracted ions are accelerated and focused onto a multichannel plate (MCP) detector located 7 cm away, a long enough distance to separate by time of flight the H^+ , H_2^+ and H_3^+ ions that are simultaneously produced and trapped. A typical time-of-flight spectrum is shown in Fig. 6(b). Up to a few thousand H_2^+ ions can be stored in the trap. The ion lifetime is of a few seconds and is limited by the residual pressure in the vacuum chamber.

The undesirable H^+ and H_3^+ ions are eliminated using the parametric excitation of their secular motion, by applying RF voltage in the MHz range on one of the end cap electrodes during the ionization process. A KrF excimer laser at 248 nm is used to photodissociate the $v \geq 1$ states in order to produce a ($L, v=0$) ions cloud. The ions are shined by 20 mJ pulses during the filling of the trap. The characterization of ro-vibrational populations of the resulting ion cloud is now in progress.

Since all the bound states of H_2^+ are metastable, the natural widths of the two-photon transitions are extremely small. In Paul traps, the ion cloud

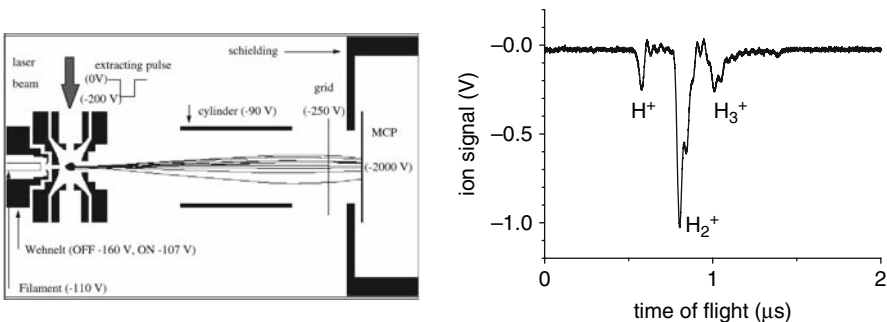


Fig. 6. (a) Simulation of the experimental setup for ion creation, trapping and detection using the SIMION7 software. MCP is a multichannel plate detector. (b) Time-of-flight spectrum showing the H^+ , H_2^+ and H_3^+ species confined in the Paul trap

temperature is of the order of magnitude of the potential depth expressed in K, i.e. $\approx 10^4$ K in our trap. Under those conditions, the two-photon linewidth expected to be limited by the second-order Doppler effect, i.e. of the order 10 kHz. It will limit the ultimate frequency resolution of the experiment at the $3 \cdot 10^{-10}$ level and the mass ratio resolution at the $6 \cdot 10^{-10}$ level.

Ion cooling will thus be necessary in order to reach the metrological objective of the experiment at the 10^{-10} level. Nevertheless, the first step of the experiment is the observation of a two-photon transition, which is feasible with hot ions using a kHz linewidth laser source.

3.6 Two-Photon Excitation Laser Source

The laser system we have built is aimed at exciting the $(L=2, v=0) \rightarrow (L'=2, v'=1)$ two-photon transition at $9.166 \mu\text{m}$. In this range, two kinds of laser sources are available. Single-mode CO_2 lasers have high output power and sub-kHz linewidths, but are hardly tunable on ranges exceeding 100 MHz, i.e. much smaller than the 1.65 GHz gap between the closest CO_2 emission line (9R(42)) and the H_2^+ line (see Fig. 7(b)). Recently, single-mode quantum cascade laser (QCL) became commercially available. They can be tuned over about 10 cm^{-1} (300 GHz) through their temperature and injection current, but have large linewidths of the order of a few MHz. Several experiments have shown that the linewidth can be reduced well below the kHz level by injection-current locking the QCL to a molecular line [54] or to a high-finesse Fabry–Perot cavity resonance [55]. We have developed a laser source that takes

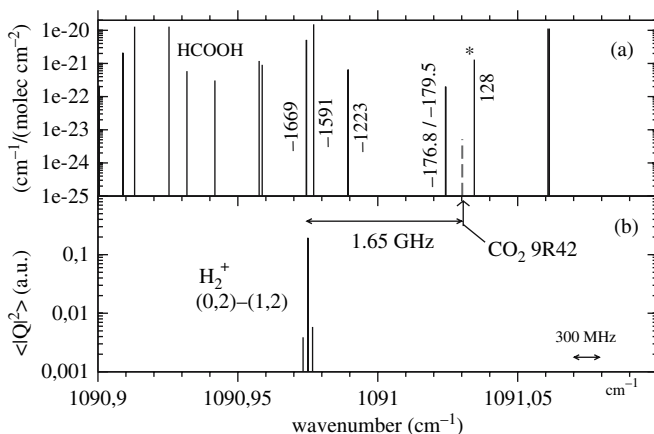


Fig. 7. (a) Absorption spectrum of formic acid (HCOOH) [53]. The line intensities are given in $\text{cm}^{-1}/(\text{molecule cm}^{-2})$. (b) Two-photon transition probabilities in atomic units. The central peak is made of two close-photon components (see Fig. 3). The dashed line is the 9R(42) CO_2 emission line. The detunings between the 9R(42) CO_2 line and the HCOOH lines are indicated in MHz. The CO_2 laser is locked to the HCOOH line indicated by the star

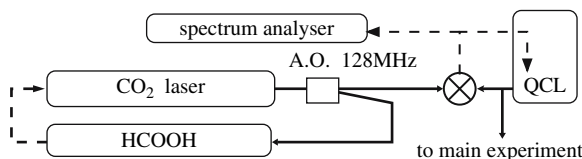


Fig. 8. Simplified setup of the CO₂/HCOOH phase-locked quantum cascade laser source. The QCL is mounted in a liquid nitrogen optical cryostat. The mixer is a room temperature HgCdZnTe detector. Solid lines are optical paths. Dashed lines are electrical paths and servo loops. A.O. is an acousto-optic modulator

advantage of both the narrow linewidth of the CO₂ laser and the tunability of the QCL [56].

The setup is shown in Fig. 8. A CO₂ laser oscillating on the 9R(42) line is frequency shifted by 128 MHz and stabilized on the intracavity saturated absorption signal of the (21, 3, 19) → (21, 2, 20) line of the ν_6 band of formic acid (HCOOH) (see Fig. 7(a)). The absolute frequency of that transition (32 708 263 980.5 kHz) has recently been determined with an uncertainty of 1 kHz [57] by sum frequency mixing with a 30 THz wide visible femtosecond frequency comb [58]. The QCL is operated in a liquid nitrogen optical cryostat. The output power is 50 mW with a 700 mA injection current and a temperature of 80 K. The QCL is phase-locked to the CO₂ laser with a tunable frequency offset in the 500–2000 MHz range [56]. The analysis of the beat note spectrum under locked conditions (see Fig. 9) shows that we have realized a narrow-line

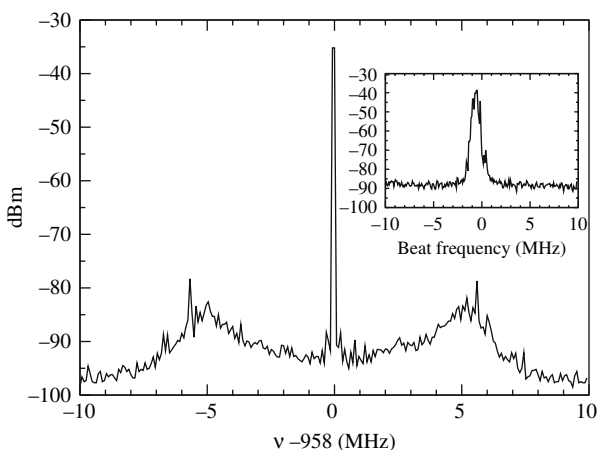


Fig. 9. Phase-locked beat note between the QCL and the CO₂/HCOOH frequency reference. RBW 10 kHz, VBW 1 kHz. The spectrum shows a loop bandwidth of the order of 6 MHz. The central peak is extremely narrow, with a -3 dB width smaller than the 200 Hz resolution of the spectrum analyser. The inset shows the free running beat note with the same scale and a 500 kHz RBW

tunable laser source well suited to probe the H_2^+ two-photon lines and also the ro-vibrational spectrum of HCOOH [58] or other molecules (NH_3, \dots) of atmospheric or astrophysical interest.

4 Cooling and Spectroscopy of HD^+

In experiments performed at the Universität of Düsseldorf, the MHIs H_2^+ , D_2^+ and HD^+ were cooled to temperatures of $\simeq 10$ mK in a radiofrequency trap, by sympathetic cooling with laser-cooled beryllium ions. High-resolution spectroscopic studies of several ro-vibrational infrared transitions in HD^+ were performed. Hyperfine splitting of the lines was observed and is in good agreement with theoretical predictions. The transitions were detected by monitoring the decrease in ion number after selective photodissociation of HD^+ ions in the upper vibrational state.

4.1 Preparation and Characterization of Cold MHI Ensembles

MHIs are just a few of a multitude of ion species that can be cooled to mK temperatures, by sympathetic cooling [59, 60] where the molecular species and a laser-coolable atomic species, with the same sign of charge, are simultaneously stored in a radiofrequency trap. Laser cooling the atoms then also efficiently cools the molecular ions via the long-range Coulomb interaction. Temperatures below 20 mK can be reliably reached. We have shown that using Be^+ ions as coolant permits to cool sympathetically ions from mass 1 to 200 amu [61, 62, 63]. A heavier atomic coolant species can be used to extend the mass range. For example, using $^{138}\text{Ba}^+$ as coolant molecular ions up to mass 410 amu have recently been cooled [64].

We use a linear quadrupole trap to simultaneously store both Be^+ and MHIs. The radiofrequency trap is driven at 14 MHz, with a peak-to-peak amplitude of 380 V. This results in a radial Mathieu stability parameter $q_r \simeq 0.13$ for HD^+ . The trap is enclosed in a UHV chamber kept below 10^{-10} mbar. The chamber is equipped with a leak valve for the controlled introduction of gases. An all-solid-state 313 nm laser system is used for cooling Be^+ [65].

To load Be^+ ions into the trap, atoms are thermally evaporated from a beryllium wire and ionized by an electron beam. The molecular loading is achieved by leaking in neutral gas at a pressure of $\sim (1-3) \cdot 10^{-10}$ mbar, ionized by an electron beam with an energy of 200 eV and a current of $\sim 30 \mu\text{A}$, for a loading time of 2 s. This produces mixed-species crystals like those shown in Fig. 10(a,b). The ions with a higher charge-to-mass ratio (in this case the molecular ions) experience a stronger trap pseudopotential, and thus form a dark (nonfluorescing) core in the crystal. The asymmetric distribution of species along the z -axis observed in Fig. 10(b) is caused by the light pressure of the cooling laser on the beryllium ions.

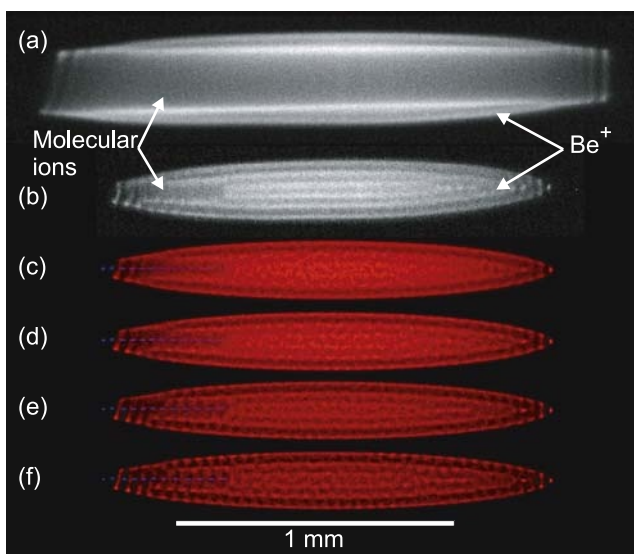


Fig. 10. Fluorescence images of (a) a large ion crystal with a high fraction of sympathetically cooled ions (approximately 1200 light ions and 800 Be^+ ions), (b) a smaller crystal containing approx. 690 Be^+ ions and 12 (exactly) HD^+ ions, and simulated images of this crystal at (c) 20 mK, (d) 12 mK, (e) 8 mK and (f) 6 mK. Laser cooling beam propagation is to the right, along the z -axis [61]

The observed crystals are well reproduced by molecular dynamics (MD) simulations [61, 66]. Visual matching of overall structure, structural details and blurrings of CCD and simulated images allows fitting the ion numbers and temperatures of the different species. The number of ions of different species given in Fig. 10(b) are found in this way. In the simulations we assume an ideal linear trap, use the quasi-potential approximation and model heating effects by stochastic forces on the ions. The obtained temperatures are thus secular temperatures. Figure 10 shows a determination of the temperature; agreement between observed and simulated images is found for a Be^+ temperature of approx. 10 mK. This sets an upper limit, as our experimental images are also limited in sharpness by our detection optics, CCD resolution and sensor noise, which are not considered. The temperature varies depending on crystal size and cooling parameters and is typically in the range 5 to 15 mK, with smaller crystals generally colder. These temperatures are consistent with measurements of the fluorescence lineshape of the Be^+ ions.

For the MHI species discussed here, our MD simulations show that the sympathetically cooled molecular ion ensemble is also crystalline, i.e. its time-averaged ion distribution is strongly inhomogeneous, and that it is strongly thermally coupled to the Be^+ ions. Assuming similar heating effects for the molecular ions and the Be^+ ions, the simulations show that the molecular

ions have a temperature similar to that of Be^+ , due to the strong Coulomb coupling.

The trapped species are identified and the time evolution of their numbers is monitored by excitation of their mass-dependent radial (secular) modes, using a spatially homogenous and temporally oscillating electric field. For HD^+ ions the measured secular frequency was ≈ 770 kHz, significantly shifted from the calculated single-particle frequency, due to Coulomb coupling between different species in the trap [67]. Excitation amplitude, sweep rate and covered frequency range were chosen so that the ion crystal had sufficient time to cool back to its initial temperature between individual excitation cycles. The excitation heats both the molecular ions and the atomic coolants, which changes the scattering rate of 313 nm cooling light by the Be^+ ions. The HD^+ secular resonance becomes visible in the Be^+ fluorescence, and its strength is proportional to the amount of HD^+ ions in the ion crystal.

4.2 Spectroscopy of HD^+

The choice of HD^+ for spectroscopic studies was made because of the availability of dipole-allowed ro-vibrational transitions which simplify the spectroscopic techniques. Nevertheless, vibrational spectroscopy in the electronic ground state in near-absence of collisions, as is the case for the present molecular ions ensembles, is faced with the difficulty that molecules excited to a vibrational level decay only slowly, implying very low fluorescence rates. As the fluorescence wavelengths are in the mid to far infrared, photon counting would require a sophisticated detection system. We circumvent this difficulty by applying the technique of $(1+1')$ resonance-enhanced multiphoton dissociation (REMPD): the molecules are excited by an infrared (IR) laser and then selectively photodissociated from the upper vibrational state by a second, fixed-wavelength ultraviolet (UV) laser (Fig. 11). The remaining number of molecular ions is the quantity measured as a function of the frequency of the IR laser. As the molecular sample is small (typically 40–100 ions) the spectroscopy requires the spectra to be obtained by repeated molecular ion production and interrogation cycles. The lasers employed are a single-frequency, widely tunable diode laser at 1.4 μm (Agilent 81480A) and a resonantly frequency-doubled Yb:YAG laser at 266 nm. The IR laser linewidth was ~ 5 MHz, and its frequency was calibrated with an accuracy of 40 MHz by absorption spectroscopy in a water vapour cell.

Due to the weak coupling between external and internal (rotational) degrees of freedom, the internal temperature of the HD^+ ions is close to room temperature, in thermal equilibrium with the vacuum chamber [70, 10]. There is significant ($> 5\%$) population for rotational levels up to $L=6$. Indeed, we have observed 12 transitions between 1391 and 1471 nm, from lower rotational levels $L=0$ to $L=6$.

The loss of HD^+ ions depends not only on the REMPD process, but also on transitions induced by blackbody radiation (BBR). We modelled the loss

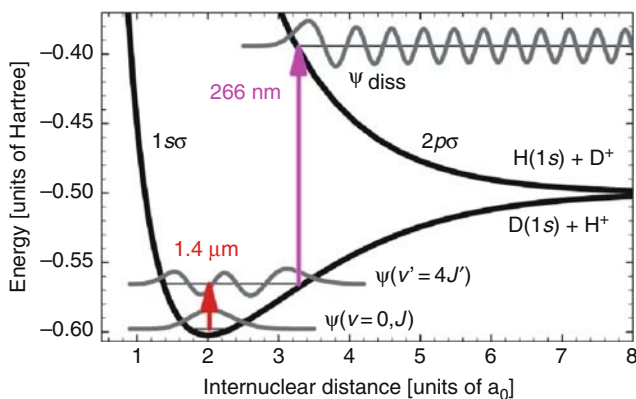


Fig. 11. Principle of $(1+1')$ REMPD spectroscopy of HD^+ ions. A tunable IR diode laser excites a ro-vibrational overtone transition $(v=0, L) \rightarrow (v'=4, L')$. The HD^+ ions excited to the $v'=4$ vibrational level are dissociated using cw 266 nm laser radiation: $\text{HD}^+(v'=4) + h\nu \rightarrow \text{H} + \text{D}^+$, or $\text{H}^+ + \text{D}$. Due to different Franck–Condon wavefunction overlap, the calculated UV absorption cross-section from the $v'=4$ level ($\sim 2.4 \times 10^{-17} \text{ cm}^2$) is about 7 orders of magnitude larger than from $v=0$ [68]. Energy values represent total binding energies of the molecule [69].

of HD^+ by solving the rate equations for the populations of all (v, L) levels interacting with the IR and UV lasers, as well as with the BBR radiation at 300 K. The theoretically obtained excitation spectrum (see Fig. 113 and text below) of the levels probed by the IR laser is included, but for the remainder of the analysis hyperfine structure is ignored. The ro-vibrational transition moments involved are taken from [71]. The rate of dissociation by UV light is obtained using cross sections from [68]. For typical UV intensities, dissociation rates of 10^2 – 10^3 s^{-1} are found. The rate equation model reveals two different timescales at which the HD^+ number declines during a typical experiment. A first, fast ($< 1 \text{ s}$) decay occurs when the IR laser selectively promotes HD^+ ions from a specific $(v=0, L)$ level to a rotational level in $v'=4$, from which they are efficiently photodissociated. This process rapidly dissociates those $(v=0, L)$ HD^+ ions which are in the hyperfine states probed by the IR laser. The remaining molecular ions (a significant fraction of the total initial number) are dissociated significantly slower, essentially at the rate at which the hyperfine levels of $(v=0, L)$ are repopulated by BBR and spontaneous emission. For example, for the $(v=0, L=2) \rightarrow (v'=4, L'=1)$ transition and for typical intensities of 6 W/cm^2 for the IR and 10 W/cm^2 for the UV laser, the fast HD^+ decay takes place at a rate $\sim 10 \text{ s}^{-1}$ (which is not resolved experimentally), whereas the decay due to BBR-induced repopulation occurs at a rate of $\sim 0.04 \text{ s}^{-1}$. The latter rate is fairly consistent with the measured decay depicted in Fig. 112(b), but observed decay rates depend strongly on which part of the hyperfine spectrum is interrogated. This points at a shortcoming of the simple rate equation model used here, and our observations can probably

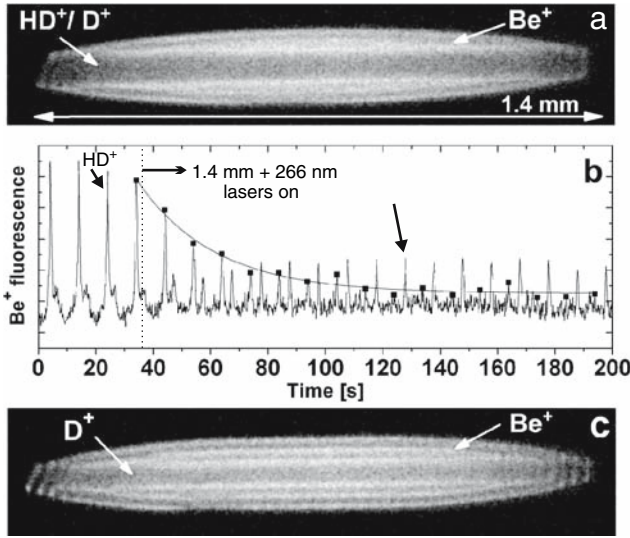


Fig. 12. (a) Initial ion crystal: ≈ 1100 Be⁺, ≈ 100 HD⁺ and ≈ 20 D⁺ ions at ≈ 20 mK (the presence of cold HD⁺ ions is obvious from the dark crystal core). (b) Repeated secular excitation of the crystal in (a) at 3 V amplitude. The excitation frequency was swept between 500 and 1500 kHz. The IR laser is tuned to the maximum of the $(v=0, L=2) \rightarrow (v'=4, L'=1)$ line. The curve is an exponential fit with a decay constant of 0.04 s^{-1} . (c) Ion crystal after dissociation of all HD⁺ ions: ≈ 1100 Be⁺ and ≈ 50 D⁺ ions at ≈ 20 mK. (d) Measurement cycle consisting of repeated probing of the number of HD⁺ ions before and after exposure to the spectroscopy lasers [69]

be explained precisely only by a rate equation model which takes the full hyperfine structure of all involved (v, L) levels into account.

As an example, Fig. 12(b) shows the time evolution of the HD⁺ secular excitation resonance while the HD⁺ ions are excited on the maximum of the ro-vibrational line $(v=0, L=2) \rightarrow (v'=4, L'=1)$ at 1430.3883 nm. The decrease of the HD⁺ resonance in the secular excitation spectrum, induced by the REMPD process, is accompanied by a decrease of the dark crystal core containing the MHIs. The secular excitation spectrum also shows an increase of the number of D⁺ ions, which result from the dissociation of excited HD⁺ ions. These ions are sympathetically cooled and remain in the crystal core. Fig. 12(c) shows the mixed-species ion crystal after all HD⁺ was dissociated. The dark crystal core has shrunk significantly, and the crystal now contains ≈ 1100 Be⁺ and ≈ 50 D⁺ ions. Assuming equal probability for photodissociation to D⁺ and H⁺, this number indicates that most generated D⁺ ions are sympathetically cooled and trapped. Loss rates are obtained by exponential fitting to the maxima of the HD⁺ resonances in the secular excitation spectrum (solid line in Fig. 12(b)). In this way, a 0.01 s^{-1} background loss rate of HD⁺ ions from the trap is obtained when both the IR and UV lasers

are turned off. This loss is due to chemical reactions between HD^+ ions and background gases. The observed background loss rate is fitted well by a single exponential decay, which rules out strong nonlinear dependence of the Be^+ fluorescence during secular excitation on the number of HD^+ ions.

The spectroscopic signal used to produce the spectra in Fig. 13 is the molecular ion dissociation probability, obtained as the relative change of the heights of the HD^+ secular resonances in the Be^+ fluorescence before and after the REMPd excitation (Fig. 12(d)). For each transition, the HD^+ dissociation probability was measured as a function of the frequency of the IR laser, in steps of 15 MHz. Each data point was obtained by averaging over several individual measurements of the HD^+ dissociation probability occurring over ~ 5 s. Each data point requires a new loading of HD^+ ions in the Be^+ crystal. For all measurements, comparable HD^+ ion numbers were used, as deduced from the size of the crystal core after loading. However, during each HD^+ loading cycle a small fraction of the Be^+ is lost from the trap, due to chemical reactions with neutral HD gas [63]. The same Be^+ ion crystal can be used for up to 40 HD^+ loadings, sufficient for obtaining the spectra in Fig. 13. A typical spectrum is taken within 1–2 hours.

Detailed measurements for two transitions $(v=0, L=2) \rightarrow (v'=4, L'=1, 3)$ are shown in Fig. 13(a,b). Both spectra reveal a partly resolved hyperfine structure, which can be compared with the prediction from an effective spin Hamiltonian, written as [72, 73]:

$$H_{\text{eff}} = b_1 \mathbf{I}_p \cdot \mathbf{S} + c_1 I_{pz} S_z + b_2 \mathbf{I}_d \cdot \mathbf{S} + c_2 I_{dz} S_z + \gamma \mathbf{S} \cdot \mathbf{J}.$$

Here, \mathbf{I}_p , \mathbf{I}_d and \mathbf{S} denote the spin of the proton, deuteron and electron, respectively; the subscript z indicates the projection on the internuclear axis.

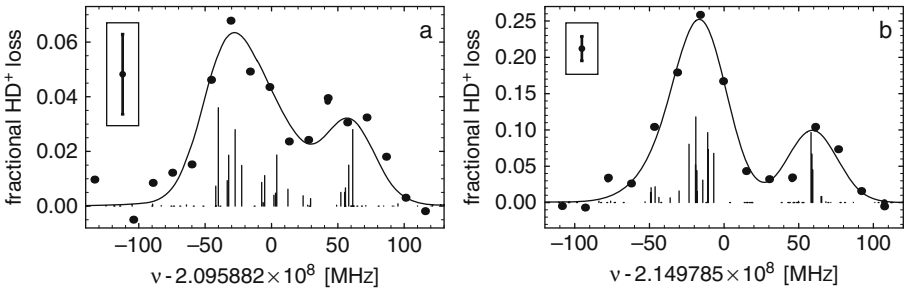


Fig. 13. Ro-vibrational transition spectra with partially resolved hyperfine splitting: (a) $(v=0, L=2) \rightarrow (v'=4, L'=1)$ at 1430 nm, (b) $(v=0, L=2) \rightarrow (v'=4, L'=3)$ at 1394 nm. The curves are fits to the data (\bullet), where the theoretical stick spectra were broadened by ≈ 40 MHz. The theoretical spectrum exhibits a large number of very weak transitions, due to weak mixing of pure coupled angular momentum states. The ordinate values are the molecular ion dissociation probability for a 5 s irradiation of 0.65 W/cm^2 IR and 10 W/cm^2 UV light. The insets show typical error bars [69]

The hyperfine coefficients b_1 , b_2 , c_1 , c_2 and γ have been recently calculated to high accuracy [43], see Sect. 2.4. The hyperfine level energies and eigenfunctions are found by diagonalization of the matrix representation of H_{eff} in a suitable angular momentum coupling scheme. Terms arising from the nuclear spin-rotation and deuteron quadrupole interactions are neglected as they contribute $\ll 1$ MHz to the hyperfine level energies [43]. The results of the diagonalization were subsequently used to calculate line strengths (11) of the individual hyperfine components within a given ro-vibrational transition, leading to “stick spectra”, as shown in Fig. 13. Inhomogeneous broadening of the spectra may be accounted for by convolving each line with a Gaussian lineshape of a given width.

The broadened stick spectra are fitted to the experimental spectra using the linewidth, the vertical scale and the frequency offset as fit parameters (Fig. 13). The frequency offset corresponds to the deperturbed ro-vibrational transition frequency, which is thus determined to within the accuracy of the wavelength calibration of the IR laser (40 MHz) and the fit uncertainty (3 MHz). The measured deperturbed ro-vibrational transition frequency is in good agreement with the ab initio results from [21], see Fig. 13. The partly resolved hyperfine structure in the measured spectra agrees well with the theoretical results obtained from [72, 43]. We find both theoretically and experimentally that the hyperfine structure for other transitions in the P and R branches is similar to that in Fig. 13(a,b).

We observe a typical line broadening of 40 MHz, which corresponds to $k_B(0.2\text{ K})$ of energy in the axial motion. The kinetic energy in the secular motion (as inferred from molecular dynamics simulations) of the HD^+ ions can give rise to broadening of about 10 MHz only [61]. Saturation broadening also does not play a significant role, as confirmed by comparing spectra taken at different IR and UV intensities. Using the polarization-dependent 313 nm fluorescence of the Be^+ ions as a magnetic field probe, the magnetic field (which is along the direction of propagation of the 313 nm laser beam) has been adjusted and verified to be 50 mT and to vary by no more than 40 mT over the extent of the crystal, which implies Zeeman broadening of less than 1 MHz. This leaves Doppler broadening due to micromotion as the most probable cause for the observed line broadening. This micromotion could arise from phase shifts in the rf potentials applied to the various electrodes and from coupling between axial (IR laser beam direction) and radial ion motion. For our trap, in which the HD^+ ions are located at least 10 μm away from the trap axis, the (radial) micromotion energy exceeds $k_B(0.5\text{ K})$.

The results described are of significance in several respects. They demonstrate, for the first time, the possibility of high-resolution spectroscopy of small, trapped molecular ion samples, sympathetically cooled well into the millikelvin range. We have achieved a spectral resolution 10 times higher than with any previous cold molecular ion method, and the same enhancement was obtained for the excitation rate. The observed population dynamics demonstrated the weakness of collisions. The methods used for trapping, cooling and

detection are quite general and are applicable to a host of other molecular ion species. This includes other ions of astrophysical and cosmological interest such as H_3^+ and its isotopomers, which have been trapped in our setup [61, 62]. Also, the spectral resolution achieved here may be further improved: for instance, first-order Doppler broadening may be circumvented by use of a tightly confining trap which holds the ions in the Lamb–Dicke regime, or by two-photon spectroscopy. Furthermore, the presence of the atomic coolant ions offers an in situ tool to detect possible perturbing fields.

5 Conclusion and Outlook

In summary, the development of high-accuracy laser spectroscopy of trapped MHIs has made significant progress. On the theory side, the energies have been calculated with a relative accuracy of the order of 1 ppb. Detailed predictions of the line strengths of one- and two-photon transitions have been given, which are important guides for the experiments. Certain systematic shifts (dc and ac Stark shifts [15, 22]) have also been calculated, but are not described here. On the experimental side, several important techniques have been demonstrated: cooling of MHIs to tens of mK, vibrational-state selective photodissociation, one-photon vibrational spectroscopy with spectral resolution at the level of $2 \cdot 10^{-7}$, rotational population measurement, in situ ion detection, tunable, high-power, continuous-wave narrow-linewidth laser for two-photon spectroscopy. Based on the present results, it is expected that the two-photon H_2^+ spectroscopy experiment will ultimately allow a spectral resolution at the level of $3 \cdot 10^{-10}$, while the one-photon $1.4 \mu\text{m}$ HD^+ spectroscopy in the current apparatus will be limited by Doppler broadening to several parts in 10^8 . One-photon spectroscopy of HD^+ vibrational transitions having longer wavelength or the use of a trap with stronger confinement should allow reaching the Lamb–Dicke regime, with a strong increase in spectral resolution. As described above, two-photon spectroscopy is another alternative.

For both ion species, the investigation of systematic shifts will become an important task. It is expected that Zeeman shifts and Stark shifts can be reduced or measured to a level below one part in 10^{10} in a cold ion ensemble. This should enable comparisons of experimental and theoretical transition frequencies at levels below 1 ppb and, in the longer term, the development of a novel approach to the measurement of mass ratios of electron and hydrogen isotopes.

In the future, it may become attractive to use the method of quantum-logic-enabled spectroscopy [74, 75]. Some of the experimental limitations (broad state population distribution, need for destructive detection of molecular excitation, systematic effects) encountered with the approaches described here could be substantially alleviated.

The transition frequency ($v = 4, L' = 3$) \leftarrow ($v = 0, L = 2$) of cold HD⁺ molecules has been measured with a relative accuracy of $2.3 \cdot 10^{-9}$ and agrees within the experimental error with the theoretical value [76].

Acknowledgements

We thank P. Blythe and H. Daerr for their contributions and M. Okhupkin, A. Nevsky, I. Ernsting and A. Wicht for discussions and assistance. This work was supported by the German Science Foundation and the EC Network HPRN-CT-2002-00290 ‘‘Cold Molecules’’. We also thank S. Kilic, F. Bielsa, A. Douillet, T. Valenzuela and O. Acef for their contributions, as well as the LNE-SYRTE (Paris Observatory) and LPL (Université Paris 13) laboratories for lending IR optical components and their absolute frequency measurement setup. V.K. acknowledges support of RFBR, grant No. 05-02-16618.

References

1. C.A. Leach and R.E. Moss: *Annu. Rev. Phys. Chem.* **46**, 55 (1995). [205]
2. see e.g. the DIREF database, <http://deref.uwaterloo.ca>; P.F. Bernath and S. McLeod: *J. Mol. Spectrosc.* **207**, 287 (2001). [205]
3. K.B. Jefferts: *Phys. Rev. Lett.* **23**, 1476 (1969). [206]
4. W.H. Wing, G.A. Ruff, W.E. Lamb, J.J. Spezeski: *Phys. Rev. Lett.* **36**, 1488 (1976). [206]
5. A. Carrington: *Science* **274**, 1327 (1996), and references therein. [206]
6. A.D.J. Critchley, A.N. Hughes, I.R. McNab: *Phys. Rev. Lett.* **86**, 1725 (2001). [206]
7. J.J. Spezeski: Ph.D. thesis, Yale University (1977). [206]
8. Y.P. Zhang, C.H. Cheng, J.T. Kim, J. Stanojevic, and E.E. Eyler: *Phys. Rev. Lett.* **92**, 203003 (2004), and references therein. [206]
9. H. Schnitzler: Ph.D. dissertation, Univ. Konstanz (2001). [206]
10. J.C.J. Koelemeij, B. Roth, and S. Schiller: *Phys. Rev. A* **76**, 023413 (2007). [206, 224]
11. H. Müller, S. Herrmann, A. Saenz, A. Peters, C. Lämmerzahl: *Phys. Rev. D* **70**, 076004 (2004). [206]
12. S. Schiller and V. Korobov: *Phys. Rev. A* **71**, 032505 (2005). [206, 207, 208]
13. J.P. Uzan: *Rev. Mod. Phys.* **75**, 403 (2003). [206]
14. D. DeMille: *Phys. Rev. Lett.* **88**, 067901 (2002). [206]
15. L. Hilico, N. Billy, B. Grémaud, and D. Delande: *Eur. Phys. J. D* **12**, 449 (2000). [207, 208, 229]
16. J.-Ph. Karr and L. Hilico: *J. Phys. B* **39**, 2095 (2006). [207]
17. P.J. Mohr and B.N. Taylor: *Rev. Mod. Phys.* **77**, 1 (2005). [207]
18. J. Verdu, S. Djekic, S. Stahl, T. Valenzuela, M. Vogel, G. Werth, T. Beier, H.J. Kluge, W. Quint: *Phys. Rev. Lett.* **92**, 093002 (2004). [207]
19. S.G. Karshenboim: *Phys. Reports* **422**, 1 (2005). [207]
20. R.E. Moss: *Molecular Physics* **80**, 1541 (1993). [207, 216]

21. R.E. Moss: *Molecular Physics* **78**, 371 (1993). [207](#) [228](#)
22. J.-Ph. Karr, S. Kilic, and L. Hilico: *J. Phys. B* **38**, 853 (2005). [208](#) [214](#) [229](#)
23. V.I. Korobov: *Phys. Rev. A* **61**, 064503 (2000). [208](#)
24. D.H. Bailey and A.M. Frolov: *J. Phys. B* **35**, 4287 (2002). [208](#)
25. Zong-Chao Yan, Jun-Yi Zhang, and Yue Li: *Phys. Rev. A* **67**, 062504 (2003). [208](#)
26. M.M. Cassar and G.W.F. Drake: *J. Phys. B* **37**, 2485 (2004). [208](#)
27. A.M. Frolov and V.H. Smith: Jr. *J. Phys. B* **28**, L449 (1995). [208](#)
28. V.I. Korobov: *J. Phys. B* **35**, 1959 (2002); F.E. Harris A.M. Frolov, and V.H. Smith: Jr., *J. Chem. Phys.* **121**, 6323 (2004). [208](#)
29. H.A. Bethe and E.E. Salpeter: *Quantum mechanics of one- and two-electron atoms*, Plenum Publishing Co., New York, 1977. [209](#)
30. V.B. Berestetsky, E.M. Lifshitz and L.P. Pitaevsky: *Relativistic Quantum Theory*, Pergamon, Oxford, 1982. [209](#)
31. V.I. Korobov: *Phys. Rev. A* **74**, 052506 (2006). [209](#)
32. K. Pachucki: *J. Phys. B* **31**, 3547 (1998). [209](#)
33. A. Yelkhovsky: *Phys. Rev. A* **64**, 062104 (2001). [209](#)
34. V.I. Korobov: *Phys. Rev. A* **70**, 012505 (2004). [209](#)
35. V.I. Korobov: *Phys. Rev. A* **73**, 024502 (2006). [209](#)
36. H. Araki: *Prog. Theor. Phys.* **17**, 619 (1957); J. Sucher: *Phys.Rev.* **109**, 1010 (1958). [209](#)
37. V.I. Korobov and Ts. Tsogbayar: *J. Phys. B* **80**, 2661, (2007) [211](#)
38. J.R. Sapirstein, D.R. Yennie: in T. Kinoshita (Ed.), *Quantum Electrodynamics*, World Scientific, Singapore, 1990, p. 560. [210](#) [211](#)
39. M.I. Eides, H. Grotch, and V.A.Shelyuto: *Phys. Reports* **342**, 63 (2001). [210](#) [211](#)
40. A.J. Layzer: *Phys. Rev. Lett.* **4**, 580 (1960). [211](#)
41. K. Pachucki: *Ann. Phys. (N.Y.)* **226**, 1 (1993). [211](#)
42. K. Pachucki: *Phys. Rev. Lett.* **72**, 3154 (1994); M.I. Eides and V.A. Shelyuto: *Phys. Rev. A* **52**, 954 (1995). [211](#)
43. D. Bakalov, V.I. Korobov, and S. Schiller: *Phys. Rev. Lett.* **97**, 243001 (2006) [211](#) [228](#)
44. V.I. Korobov, L. Hilico, and J.-Ph. Karr: *Phys. Rev. A* **74**, 040502(R) (2006). [212](#)
45. D. Bakalov, V.I. Korobov, S. Schiller: In *Proceedings of the International Conference on exotic atoms "EXA 2005"*, February 21-25, 2005, Vienna, Austria. [212](#)
46. B. Cagnac, G. Grynberg and F. Biraben: *J. Physique* **34**, 845 (1973); J.C. Garreau, M. Allegrini, L. Julien and F. Biraben: *J. Physique* **51**, 2275 (1990). [214](#)
47. L. Hilico, N. Billy, B. Grémaud and D. Delande: *J. Phys. B* **34**, 491 (2001). [214](#)
48. A.V. Matvienko and L.I. Ponomarev: *J. Phys. B* **5**, 27 (1972); J. Carbonel, R. Lazauskas, D. Delande, L. Hilico, S. Kilic: *Europhysics Letter* **64**, 316 (2003). [216](#)
49. A. Carrington et al.: *J. Chem. Soc. Faraday Trans.* **89**, 603 (1993); A. Carrington, C.A. Leach, and M.R. Viant: *Chem. Phys. Lett.* **206**, 77 (1993). [216](#)
50. G.H. Dunn: *Phys. Rev.* **172**, 1 (1968). JILA report **92** (1968). [216](#) [217](#)
51. Senem Kilic: Thèse de l'université Pierre et Marie Curie (Paris 6), 2005. [216](#) [217](#)
52. Y. Weijun, R. Alheit, G. Werth: *Z Physik D* **28**, 87 (1993). [217](#)
53. L.S. Rothman et al.: *J. Quant. Spec. Rad. Tr.* **96**, 139 (2005). [218](#) [220](#)
54. R.M. Williams et al.: *Optics Letters* **24**, 1844 (1999). [220](#)
55. M.S. Taubman et al.: *Optics Letters* **27**, 2164 (2002). [220](#)

56. F. Bielsa, A. Douillet, T. Valenzuela, J.-Ph. Karr, and L. Hilico, *Optics Letters* **32**, 1641 (2007). [221](#)
57. F. Bielsa, K. Djerroud, A. Goncharov, T. Valenzuela, A. Douillet, C. Daussy, A. Amy-Klein, and L. Hilico, *J. Mol. Spec.* (to be published). [221](#)
58. A. Amy-Klein et al.: *Optics Letters* **30**, 3320 (2005). [221](#), [222](#)
59. D.J. Larson et al.: *Phys. Rev. Lett.* **57**, 70 (1986). [222](#)
60. K. Molhave and M. Drewsen: *Phys. Rev. A* **62**, 0011401(R) (2000). [222](#)
61. P. Blythe et al.: *Phys. Rev. Lett.* **95**, 183002 (2005). [222](#), [223](#), [228](#), [229](#)
62. B. Roth et al.: *J. Phys. B* **39**, S1241 (2006). [222](#), [229](#)
63. B. Roth et al.: *Phys. Rev. A* **73**, 042712 (2006). [222](#), [227](#)
64. A. Ostendorf et al.: *Phys. Rev. Lett.* **97**, 243005 (2006). [222](#)
65. H. Schnitzler et al.: *Applied Optics* **41**, 7000 (2002). [222](#)
66. B. Roth, A. Ostendorf, H. Wenz, and S. Schiller: *J. Phys. B* **38**, 3673 (2005). [223](#)
67. B. Roth, P. Blythe, and S. Schiller, *Phys. Rev. A* **75**, 023402 (2007). [224](#)
68. M. Tadjeddine and G. Parlant: *Mol. Phys.* **33**, 1797 (1977); A. Kondorskiy, private communications (2006). [225](#)
69. B. Roth, J.C.J. Koelemeij, H. Daerr, and S. Schiller: *Phys. Rev. A* **74**, 040501(R) (2006). [225](#), [226](#), [227](#)
70. A. Bertelsen, S. Jorgensen, and M. Drewsen: *J. Phys. B* **39**, 83 (2006). [224](#)
71. E.A. Colbourn and P.R. Bunker: *J. Mol. Spect.* **63**, 155 (1976). [225](#)
72. R.D. Ray and P.R. Certain: *Phys. Rev. Lett.* **38**, 824 (1977). [227](#), [228](#)
73. A. Carrington, I. McNab, and C. Montgomerie: *J. Phys. B* **22**, 3551 (1989). [227](#)
74. D.J. Wineland et al.: in *Proceedings of the 6th Symposium on Frequency Standards and Metrology*, edited by P. Gill, World Scientific, Singapore, p. 361 (2002). [229](#)
75. P.O. Schmidt et al.: *Science* **309**, 749 (2005). [229](#)
76. Koelemeij et al., *Phys. Rev. Lett.* **98**, 173002 (2007). [230](#)

Nuclear Magnetic Dipole Moments from NMR Spectra – Quantum Chemistry and Experiment

M. Jaszuński¹ and K. Jackowski²

¹ Institute of Organic Chemistry, Polish Academy of Sciences, Kasprzaka 44, 01-224 Warsaw, Poland
michaljz@icho.edu.pl

² Laboratory of NMR Spectroscopy, Department of Chemistry, University of Warsaw, Pasteura 1, 02-093 Warsaw, Poland
kjack@chem.uw.edu.pl

Abstract. We discuss new values of nuclear magnetic dipole moments, obtained from accurate absolute shielding constants and gas-phase NMR data, for a series of nuclei. The generally accepted previous values of magnetic moments were for many isotopes derived from NMR spectra. However, in the procedure applied to determine the moments of bare nuclei the effects of the molecular electronic structure have been often described in a very approximate manner. Accurate absolute shielding scales can be presently established analysing gas-phase NMR spectra and shielding constants determined by ab initio methods of quantum chemistry.

We present a systematic analysis of the nuclear magnetic moments, based on the relation between these moments, the resonance frequencies and the shielding constants. With the new values of nuclear magnetic dipole moments the relations between the NMR parameters of different nuclei are fulfilled in a consistent manner, whereas using the literature values leads to significant errors.

1 Introduction

The magnetic dipole moment is an important physical constant, related to the spin of a particle and determining its electromagnetic interaction. There is no satisfying theory predicting the nuclear magnetic moments, their accurate values in practice are obtained from experiment. Several experimental techniques, such as optical spectroscopy (hyperfine structure of spectra) and measurements in molecular beams, have been used; the most accurate results for many stable nuclei were obtained from nuclear magnetic resonance (NMR) spectra. A standard reference for nuclear magnetic dipole moments is the review by Raghavan [1]; for many isotopes this is the source of the data quoted in more recent literature [2, 3, 4]. Although these commonly used values of nuclear magnetic moments were tabulated and published in 1989, they are often based on NMR experiments done in 1950s–1960s (see for instance [5, 6, 7, 8]).

It appears that very approximate treatment of the magnetic shielding was the main origin of inaccuracies in these predictions of magnetic moments.

The existence of NMR spectra is due to the interaction of external magnetic fields with nuclei with nonzero spin. The values of spin-related nuclear magnetic dipole moments, which determine the spectrum, are usually treated as physical constants, defined for bare nuclei. The essential role of NMR in many applications – for instance in chemistry – is related to the shielding of the external field by electrons, specific for each nucleus in a molecule and strongly dependent on the molecular structure. The same effect had to be considered when NMR was used for determining the nuclear magnetic dipole moments – the experiments were not performed for bare nuclei; the nuclear moments were obtained analysing molecular spectra. However, in many cases when the nuclear moments were determined the NMR shielding constants needed to derive the bare nucleus moment from the molecular spectrum were not properly taken into account. For many isotopic species the relevant experiments were performed 50 years ago, when the absolute shielding scales were not known and inaccurate treatment of magnetic shielding led to systematic errors in the derived nuclear moments. A satisfactory solution of this problem requires simultaneous accurate *ab initio* calculations of the nuclear magnetic shielding constant and precise gas-phase NMR measurements.

The recent advances in the *ab initio* methods in quantum chemistry have enabled practical calculations leading to reliable and accurate results. Within the modern *ab initio* methods [9] one can define a hierarchy of approximations converging to the exact solution of the Schrödinger equation. The corresponding perturbation theory methods can be applied to study molecular properties, such as the NMR shielding constants [10, 11, 12]. Moreover, the implementation and development of the computer codes have made the calculations applying these advanced methods feasible, at least for small molecules.

The precision of NMR experiments 50 years ago was rather poor and the studies were limited to nuclei with large natural abundance, like ^1H , ^{19}F or ^{31}P . During the last decades more advanced spectrometers became available and the sensitivity of new instruments was greatly improved due to the progress in electronics and to the development of stable cryomagnets. As a result NMR studies in gases became available also for nuclei with low natural abundance. For instance, the first density-dependent spectra of ^{13}C were observed in 1977 [13, 14], ^{17}O in 2001 [15] and ^{33}S in 2002 [16, 17].

We shall begin with an interpretation of the NMR parameters, based on the NMR effective spin Hamiltonian. Next, we discuss *ab initio* studies of NMR shielding constants, with very brief comments on the relevant quantum chemistry methods and approximations. We describe the differences between the calculated and measured NMR parameters and present the most important aspects of the analysis of gas-phase NMR results. We discuss next the determination of nuclear magnetic moments from NMR spectra, and inverting the relevant equations we obtain a very useful formula to examine the obtained nuclear magnetic dipole moments. This relation between the

resonance frequencies, shielding constants and nuclear moments of two different nuclei provides an excellent test of the consistency of all these NMR parameters. In the discussion of the results we concentrate on selected examples. We consider a sequence of approximations, analyse the convergence of the computed shielding constants with the improvement of the ab initio method and estimate the error bars for the absolute shielding constants and nuclear magnetic moments.

Before we proceed, let us note that a similar approach is successfully used to determine the nuclear electric quadrupole moments. The property needed is the electric field gradient, and – as in our case – ab initio methods of quantum chemistry are used to describe all the effects due to molecular electronic structure (see [18] and references therein). Let us finally add that the need for remeasurement of nuclear magnetic dipole moments has been recognised, the issue was discussed mainly for heavy nuclei [19, 20].

2 NMR Shielding Constants

2.1 NMR Effective Spin Hamiltonian

In the analysis of NMR spectra only the nuclear spins, proportional to the magnetic moments, are considered. The observed resonance frequencies are determined by the energy levels in the space spanned by the available nuclear spin states. They can be calculated using the NMR spin Hamiltonian \mathcal{H}^{NMR} , an effective Hamiltonian designed to interpret the spectrum:

$$\mathcal{H}^{\text{NMR}} = - \sum_X \mathbf{B}^T (1 - \sigma_X) \boldsymbol{\mu}_X + \dots \quad (1)$$

where \mathbf{B} and $\boldsymbol{\mu}_X$ denote the external magnetic field induction and the nuclear magnetic moment. We neglect here and in the following discussion all the effects not related to the shielding, such as the spin–spin coupling, since in the applications we discuss they can be eliminated in the analysis of the results. The first term in the parentheses represents the direct Zeeman interaction between the nucleus and the field, the second term involving σ_X – the shielding tensor – describes the role of the chemical environment of the nucleus. All the electronic structure effects are incorporated in the effective Hamiltonian in this manner.

For a rotating molecule in an isotropic medium, assuming the external magnetic field along the z axis, (1) is reduced to

$$\mathcal{H}_{\text{iso}}^{\text{NMR}} = - \sum_X B_z (1 - \sigma_X) \mu_X^z + \dots, \quad (2)$$

where $\sigma_X = \text{Tr } \sigma_X / 3$, and Tr is the trace of the tensor. The shielding constant σ_X is dimensionless, and in chemical applications usually given in ppm (parts

per million) because of the range of chemical effects – for instance, for $^1\text{H} \approx 10$ ppm, $^{13}\text{C} \approx 200$ ppm, $^{31}\text{P} \approx 1000$ ppm. For our purposes it is essential to keep in mind that σ_X is the absolute shielding constant [21], that is the shielding relative to bare nucleus. The resonance frequency ν_X observed in NMR spectroscopy is determined by the splitting of the energy levels in the magnetic field.

The nuclear magnetic moment is a property related to nuclear spin:

$$\boldsymbol{\mu}_X = \hbar\gamma_X\mathbf{I}_X = \mu_N g_X\mathbf{I}_X, \quad (3)$$

where μ_N is the nuclear magneton and γ_X and g_X denote the magnetogyric ratio and the g factor for the bare nucleus, respectively. From the NMR experiment one determines the nuclear magnetic dipole moment μ_X as the maximum projection of the vector on the axis of the external field (related to the maximum projection of the nuclear spin). The NMR resonance frequency ν_X for nucleus X in an isotropic sample is

$$h\nu_X = \Delta\mu_X^z(1 - \sigma_X)B_z, \quad (4)$$

where $\Delta\mu_X^z$ is the transition-related change of the projection of the magnetic moment on the field axis. In the standard NMR spectra, transitions between spin states which differ in spin projections by one are observed, ($\Delta I_X^z = 1$), and the frequency is proportional to $\Delta\mu_X^z = \mu_X\Delta I_X^z/I_X$. We note that various definitions of nuclear dipole moment are used, for comparison with [4] one needs $\mu_X^{\text{length}} = (\sqrt{I_X(I_X + 1)}/I_X)\mu_X$ instead of μ_X . We assume in what follows that the nuclear spin and the sign of the magnetic moment are known, the quantity to be accurately determined which we discuss is the proportionality coefficient – the gyromagnetic (magnetogyric) ratio γ_X or the nuclear factor g_X . With this assumption, NMR data are sufficient to determine the magnetic moment; we shall consequently often use a simplified notation and replace the symbol $\Delta\mu_X^z$ by μ_X in the text.

2.2 Ab Initio Studies of NMR Shielding Constants

Recalling that the shielding tensor describes the bilinear interaction in the effective NMR spin Hamiltonian (1), we consider in the molecular Hamiltonian the terms linear and bilinear in the external magnetic field induction and the nuclear magnetic moments. We obtain then each component of the nuclear magnetic shielding tensor as the (bilinear) second-order perturbation correction to the electronic energy E^{el} , with the Cartesian $\alpha\beta$ component of σ_X determined as

$$\sigma_{X,\alpha\beta} = \left. \frac{\partial^2 E^{\text{el}}(\mathbf{B}, \boldsymbol{\mu}_X)}{\partial B_\alpha \partial \mu_{X,\beta}} \right|_{\mathbf{B}=0, \boldsymbol{\mu}_X=0}. \quad (5)$$

The shielding can thus be evaluated as the mixed second-order derivative of the energy using linear response methods [22] of the time-independent perturbation theory. We need to consider here only perturbation theory equations for closed-shell molecules in their ground electronic states.

Numerous advanced methods of quantum chemistry suitable for the calculation of linear response properties have been developed in the last decade. In practice, we now have at our disposal a hierarchy of methods of increasing reliability [23]. Using these methods in a series of calculations we can often reach the convergence region, with the consecutive changes in the results predictable and diminishing. This applies also to the NMR shielding constants in small molecules and allows for an extrapolation of the results and for an estimate of the remaining errors within a given model.

In the commonly used approach based on the nonrelativistic Schrödinger equation the Born–Oppenheimer approximation is applied. We start with the calculations for the clamped nuclei and next add to the shielding constant at the equilibrium molecular geometry the corrections for zero-point vibrations (larger) and temperature (smaller). We shall discuss repeatedly the shielding constants computed in the hierarchy including the SCF (self-consistent field), MP2 (Møller–Plesset second-order perturbation theory), CCSD (coupled cluster singles and doubles) and CCSD(T) (CCSD with noniterative account of triple excitations) approximations. In the discussion of the results, we shall also consider the relativistic effects. The NMR shielding is a property strongly dependent on the electronic structure close to the nucleus, therefore these effects are often more important for the shielding than for other properties.

Vibrational and Temperature Corrections

To obtain accurate shielding constants it is not sufficient to perform calculations at the molecular equilibrium geometry. The strong dependence of NMR shielding on molecular geometry leads to significant vibrational effects and observable temperature dependence of the shielding. The dominant effect may usually be obtained considering the zero-point vibrational (ZPV) contribution, the temperature effects can be determined via Boltzmann averaging over rovibrational states. For small polyatomic molecules these effects can be described using the expansion [24]

$$\sigma = \sigma_e + \sum_i \frac{\partial \sigma}{\partial Q_i} \langle Q_i \rangle + \frac{1}{2} \sum_i \frac{\partial^2 \sigma}{\partial Q_i^2} \langle Q_i^2 \rangle, \quad (6)$$

where σ_e is the shielding at the equilibrium, Q_i represents a normal coordinate and $\langle Q_i \rangle$ is its average in a given rovibrational state (a similar expression can be used for temperature averages). The harmonic frequencies needed in the approximate formulae for $\langle Q_i \rangle$ and $\langle Q_i^2 \rangle$ can be obtained as second analytical derivatives of the energy; however, finite field methods are generally used for cubic force constants and first and second derivatives of properties.

In addition to a calculation at the very accurately optimised equilibrium geometry one thus needs several (≈ 10 for a small molecule) shielding constant calculations at additional geometries, thus the analysis of ZPV corrections is more time demanding and often restricted by the computational possibilities. It is advantageous to apply different approximations or basis sets to describe the energy surface (equilibrium geometries and force constants) and the property surface (for instance, to describe the core correlation effects needed for shielding constants).

3 Comparison of the Gas-Phase NMR Spectra with Ab Initio Results

In a standard ab initio calculation the NMR shielding constant is determined considering as the unperturbed reference state the wavefunction of an isolated molecule. The result is in agreement with the concept of the shielding constant as a property characterising the nucleus in a specific molecule, but does not correspond to the easily available experimental data. The difficulties in the comparison of ab initio result with experiment are illustrated in Fig. 1.

The state-of-the-art ab initio calculations are usually done for the absolute shielding constant at a single molecular geometry, whereas the experimental results are usually obtained in the condensed phase. Moreover, the quantities available from experiment are the chemical shifts, that is the shielding constants on a relative scale, defined with respect to a chosen reference molecule 4:

$$\delta_X = \frac{\nu_X - \nu_{X,\text{ref}}}{\nu_{X,\text{ref}}} = \frac{\sigma_{X,\text{ref}} - \sigma_X}{1 - \sigma_{X,\text{ref}}} \cong \sigma_{X,\text{ref}} - \sigma_X . \quad (7)$$

However, when NMR is used to determine magnetic dipole moments of nuclei, absolute shielding constants are required in 4.

To fix the scale for the absolute shielding, one should take into account all the effects shown in Fig. 1. It appears that presently the best way to do it is to include within the theory the zero-point vibrational and temperature contributions. Unfortunately, the intermolecular forces in the liquid, which are not easily described by theory, change significantly the shielding constants. We shall therefore discuss primarily the results of systematic NMR gas-phase experiments, in which the pressure dependence is analysed and extrapolation to zero density enables the elimination of the effects due to intermolecular forces.

To construct an absolute shielding scale for nucleus X , enabling a direct comparison of theoretical and experimental results, it is sufficient to determine the absolute shielding constant for this nucleus in a single molecule. This can be achieved within ab initio methods of quantum chemistry. Moreover, as discussed in Sect. 2.2, for an isolated small molecule the accuracy of the

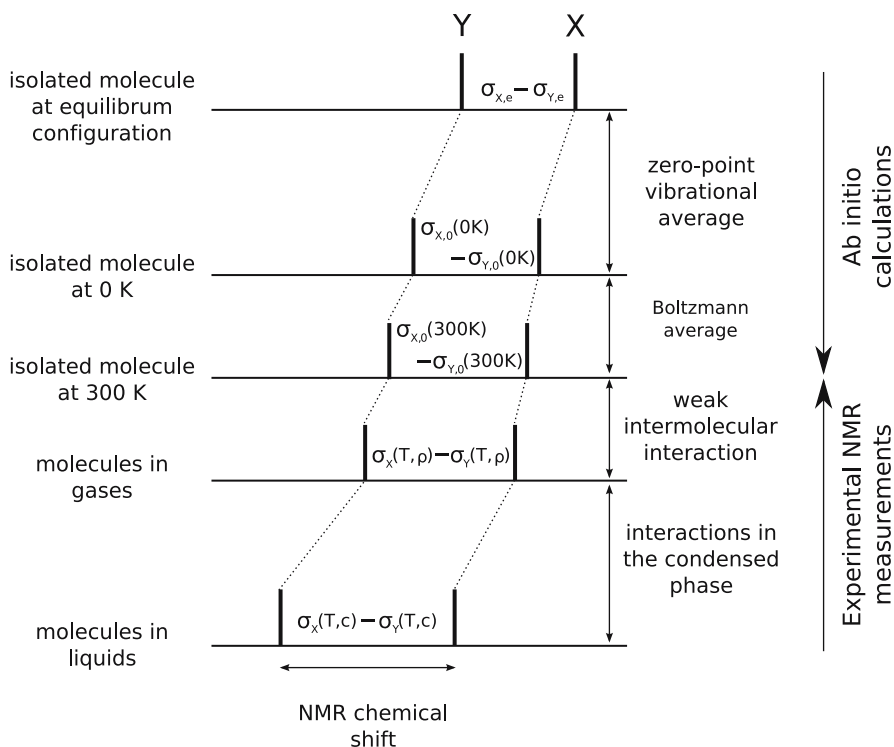


Fig. 1. Comparison of the theoretical shielding constants and the experimental chemical shifts

calculated shielding constant can be estimated. One can next proceed using the measured chemical shifts and determine the absolute shielding in other molecules. Another option to fix the absolute shielding scale is to use the measured spin-rotation constant (see Sect. 3.1) and compute ab initio the diamagnetic part of shielding. Unfortunately, there are not too many accurate spin-rotation constants available.

3.1 Spin-Rotation Constants

The spin-rotation constant \mathcal{M}_K is defined within perturbation theory as the parameter describing the coupling of the rotational angular momentum of the molecule and the magnetic dipole moment of nucleus. In the discussed nonrelativistic approximation the spin-rotation constant is proportional to the paramagnetic shielding, defined with the gauge origin at \mathbf{R}_K , the nucleus of interest. It is best evaluated as the total shielding minus the diamagnetic part, that is

$$\mathcal{M}_K^{\text{el}} = \mathcal{M}_K - \mathcal{M}_K^{\text{nucl}} = \frac{\hbar\mu_{\text{NGK}}}{2\pi\mu_{\text{B}}} \sigma_K^{\text{para}}(\mathbf{R}_K) \mathbf{I}^{-1} = \frac{\hbar\mu_{\text{NGK}}}{2\pi\mu_{\text{B}}} \left[\sigma_K^{\text{GIAO}} - \sigma_K^{\text{dia}}(\mathbf{R}_K) \right] \mathbf{I}^{-1}, \quad (8)$$

where the superscripts denote the electronic and nuclear parts of \mathcal{M}_K , \mathbf{I} is the moment of inertia tensor and μ_{B} the Bohr magneton.

Therefore, we can compare a fully ab initio value of the absolute shielding constant with another one derived using the experimental spin-rotation constant and ab initio diamagnetic shielding contribution (this contribution is very simply calculated). However, (8) does not have a relativistic equivalent and the discrepancy due to relativistic effects appears to be nonnegligible already for the third-row atoms.

4 NMR Experiment in the Gas Phase

NMR spectroscopy is widely used for routine analyses of molecular structure. However, in NMR the spectral parameters are not usually measured for isolated molecules and consequently almost all the conclusions drawn from experiment are based on approximate data. Let us consider the chemical shift, that is the difference of the shielding measured for the magnetic nuclei present in reference and sample molecules, see (7), as an example. As shown in Fig. 1 the magnetic shielding of each nucleus is modified by intramolecular dynamics and intermolecular interactions. Both these effects, although similar, are never perfectly equal for two different molecules. Therefore, the NMR chemical shift observed for any macroscopic sample only represents, in a better or worse approximation, the real difference of the shielding constants in isolated molecules. The above difficulties can partly be overcome if the magnetic shielding is studied as a function of density in the gas phase. This approach allows for the elimination of all the intermolecular effects in NMR shielding and therefore gives the shielding constants for isolated molecules, suitable for comparison with the results of a corresponding standard ab initio calculation.

In the gas phase, the effects related to intermolecular interactions and intramolecular motion are observed as a dependence of the shielding $\sigma(T, \rho)$ on density and temperature [25]:

$$\sigma(T, \rho) = \sigma_0(T) + \sigma_1(T) \rho + \sigma_2(T) \rho^2 + \dots, \quad (9)$$

where $\sigma_0(T)$ is the shielding for an isolated molecule and the next terms depend on the density ρ and describe the intermolecular interactions in gases. The observed frequency $\nu(T, \rho)$ may also be defined in terms of a virial expansion, with $\nu_0(T)$ representing the resonance frequency at the zero density limit (the resonance frequency, the chemical shift and the shielding constant are linearly dependent when the properties of the reference molecule are constant, see (7)). For most gaseous compounds at constant temperature the shielding $\sigma(T)$ varies linearly with density if the pressure of gas does not exceed 40 atm [26]. In such a case the $\sigma_2(T)$ and higher-order coefficients in (9) can be

safely neglected and the remaining parameters, that is $\sigma_0(T)$ and $\sigma_1(T)$, can be precisely determined from the linear equation

$$\sigma(T, \rho) = \sigma_0(T) + \sigma_1(T) \rho, \quad (10)$$

in which $\sigma_1(T)$ is solely responsible for all the intermolecular effects and includes the bulk susceptibility correction, dependent on the magnetic susceptibility of sample medium (χ_v), the shape of the sample and the direction of external magnetic field [27].

Similar measurements of the shielding can also be carried out for chemical compounds which exhibit stronger intermolecular interactions and remain liquid at standard ambient temperature and pressure, that is at 298.15 K and 1 bar. It is convenient to use as a solvent (B, matrix) a chemically inert gas and a small amount of the investigated compound (A, solute), then the solvent molecules will hold the solute molecules apart. For a binary gaseous mixture of compound A and gas B as the solvent (10) can be rewritten for molecule A as follows:

$$\sigma^A = \sigma_0^A + \sigma_1^{AA} \rho_A + \sigma_1^{AB} \rho_B, \quad (11)$$

where ρ_A and ρ_B are the densities of A and B, respectively, and σ_0^A is the shielding at the zero density limit, that is the value for an isolated A molecule. The coefficients σ_1^{AA} and σ_1^{AB} (we use here the superscripts to denote the molecules, identical equation applies to each nucleus within the molecule) contain the bulk susceptibility corrections and the terms taking account of intermolecular interactions during the binary collisions of A–A and A–B molecules. At the very low density of solute (ρ_A) the second term in (11) is negligibly small and this simplifies the description of the experiment to linear dependence of σ^A on the density of the solvent gas (B):

$$\sigma^A = \sigma_0^A + \sigma_1^{AB} \rho_B. \quad (12)$$

The shielding parameters in (11) and (12) are obviously temperature dependent and the measurements for various densities must be performed at constant temperature.

We have used (12) to determine the $\sigma_{H,0}$ and $\sigma_{O,0}$ shielding constants of water observed in xenon gaseous matrix [28], while (10) was applied for the measurements of all the other shielding constants cited in this work [16, 29, 30, 31, 32].

Gas samples were prepared condensing pure gases or their mixtures from the calibrated part of vacuum line as described earlier [31, 32]. NMR chemical shifts were measured relative to the external reference standards. For this purpose the absolute frequency of the reference standard was determined in the conditions of lock system tuned to the CD_3 signal of external toluene- d_8 . The constant frequency of the lock system at our Varian UNITYplus-500 multinuclear spectrometer allows us to preserve the same magnetic field for all measurements and to compare resonance frequencies for different samples.

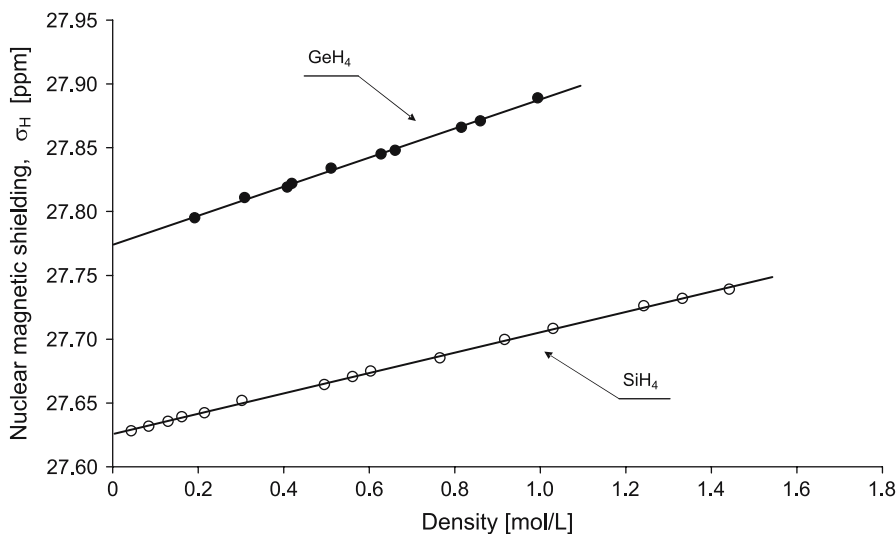


Fig. 2. Extrapolation of the proton shielding observed in SiH₄ and GeH₄ to the zero density limit. For the exact values of the σ_0^A and σ_1^{AB} parameters, see [32]

Figure 2 shows an example of the results – the shielding of ¹H in silane and germane as a function of the density. The dependence on density is linear for both these compounds, which confirms that $\sigma_2(T)$ and higher-order coefficients in (9) can be neglected. The isolated molecule values clearly cannot be extracted from the results of a single measurement; however, with linear dependence of $\sigma(T, \rho)$ on the density both parameters $\sigma_0(T)$ and $\sigma_1(T)$ can be easily determined (see [32, 33] for examples). For our purposes, the extrapolation to zero density permits precise determination of the shielding constants for isolated molecules, σ_0 , while all intermolecular effects from gas medium described by σ_1 are removed. The precision of extrapolation of experimental points to the zero density limit varied for different nuclei, but it was always better than ± 0.01 ppm.

5 Nuclear Magnetic Moments – A General Scheme for Different Nuclei

Let us consider how the unknown nuclear magnetic dipole moment can be obtained using (4). The resonance frequency can be very accurately measured; the absolute shielding constant is not known from experiment, but it can be obtained from theoretical results and measured chemical shifts. Nevertheless, (4) cannot be used to determine directly the magnetic moment because the strength of the external magnetic field within the NMR sample cannot be measured with sufficient accuracy. To bypass this problem one can compare

experimental frequencies for two different nuclei, possibly even in different molecules:

$$h\nu_X = \Delta\mu_X^z(1 - \sigma_X)B_z, \quad (13)$$

$$h\nu_Y = \Delta\mu_Y^z(1 - \sigma_Y)B_z, \quad (14)$$

and next eliminate B_z :

$$\Delta\mu_Y^z = \frac{\nu_Y(1 - \sigma_X)}{\nu_X(1 - \sigma_Y)}\Delta\mu_X^z. \quad (15)$$

One can thus determine the magnetic moment μ_Y using the measured frequency ratios and the shielding constants for appropriate source compounds (X and Y indices now specify both the nucleus and the molecule) assuming that μ_X is known. This is the standard procedure used to establish the nuclear magnetic dipole moment from an NMR spectrum. In practice, this approach was applied for nuclei Y and X in the same molecule, to avoid experimental errors. The most suitable nucleus X to be used as the reference is ^1H , because the magnetic moment $\mu(^1\text{H}) = 2.792847337(29)\mu_N$ [34] is known with high accuracy.

When the magnetic moments of two nuclei are known, we can verify their accuracy by rewriting (15) in a generalised scheme as

$$\sigma_X = 1 - \frac{\nu_X}{\nu_Y} \frac{\Delta\mu_Y^z}{\Delta\mu_X^z} (1 - \sigma_Y) \quad (16)$$

or equivalently

$$\sigma_X = 1 - \frac{\nu_X}{\nu_Y} \frac{\gamma_Y}{\gamma_X} (1 - \sigma_Y). \quad (17)$$

We stress that these equations should be fulfilled for any pair of nuclei in any molecules. In this scheme, we shall use repeatedly (16) to test the consistency of the ab initio and experimental data, with the old and new values of magnetic moments of nuclei. In summary, to determine μ_Y and/or to verify its accuracy we need to know ν_X, ν_Y, σ_X and σ_Y ; we use experimental frequencies and the shielding constants from theory, if needed with the experimental chemical shifts.

For light nuclei, the accuracy of known σ_X values is often $\approx 1\text{--}3$ ppm. Obviously, to reproduce so well a known shielding constant we need accurate input data, in particular μ_Y and μ_X , and thus (16) provides a very strict test of the consistency of their values. Simple checks indicate that with the literature values of nuclear magnetic moments we obtain often completely wrong results. For example, let us use $\sigma(^1\text{H in TMS, liquid})$ as input (TMS, tetramethylsilane, $\text{Si}(\text{CH}_3)_4$ is the reference standard for the chemical shifts of ^1H , ^{13}C and ^{29}Si nuclei). We find for the derived shielding $\sigma(^{15}\text{N in CH}_3\text{NO}_2, \text{liquid}) = 330$ ppm, whereas it is known to be approximately -135.8 ppm; so the error, almost 500 ppm, is two orders of magnitude too large.

To find the origin of these errors, we should consider various experimental problems – such as sample preparation, bulk susceptibility (in the liquids), influence of intermolecular forces or insufficiently accurate measurement of the frequency ratio. For instance, in the performed in 1951 studies of ^{33}S magnetic moment the ratio $\nu(^{33}\text{S})/\nu(^{14}\text{N}) = 1.06174(13)$ [8] was used. However, simple numerical tests based on (16) indicate that the most obvious and most important problem is the error in the nuclear magnetic moments.

6 Results and Discussion

In the studies of NMR properties discussed below practically only the standard Dunning’s basis sets [35, 36] of Gaussian-type orbitals have been used. They are built in a systematic manner and they are suitable to describe electron correlation effects. The NMR properties depend on the description of the region close to the nucleus, thus primarily the sequence of core-valence (cc-pCVXZ) basis sets has been used. An important problem arising whenever one of the perturbing operators represents the external magnetic field is to ensure gauge invariance of the results, which may otherwise strongly depend in approximate calculations on the choice of the vector potential. This problem is bypassed in the methods we discuss by the application of gauge-including atomic orbitals (GIAOs) [37, 38] in the calculation of the shielding constants.

The most reliable presently available methods to obtain NMR shielding constants in polyatomic molecules are based on the application of perturbation theory for coupled cluster reference wavefunctions. These methods, developed by Gauss and Stanton [39, 40], have been implemented with the use of GIAOs, for a variety of coupled cluster levels. The CCSD and CCSD(T) approximations can be applied successfully with large basis set. Kállay and Gauss [41] considered higher level approaches (CCSDT, CCSDTQ, ... up to full CI), but these benchmark studies are so far limited to small molecules and basis sets.

Most of the discussed ab initio results, taken from [31, 32, 42, 43], were obtained using the program packages ACES II [44], DALTON [45] and DIRAC 04 [46].

6.1 NMR Shielding Constants for the First- and Second-Row Atoms

Two-Electron Systems

The most accurate results can be obtained for two-electron systems. For these, CCSD is equivalent to full configuration interaction (FCI), so the description of electron correlation is determined in the standard CCSD approach by the basis set size. For He, wavefunctions explicitly dependent on the interelectronic distance have also been successfully used. For a closed-shell atom the shielding

constant is proportional to the expectation value $\langle 1/r \rangle$ (r is the electron–nucleus distance) and for ^3He it is 1.688316800717 a.u. [47], corresponding to ≈ 59.93677 ppm.

A study of H_2 [48] and its isotopomers provided benchmark results, which are used to set the scale for ^1H shielding. The results of [48] have been confirmed recently in a new calculation with significantly larger [15s7p6d5f4g3h2i] CGTO basis set [49]. The total shielding constant was 26.2983 ppm [48], the new result is 26.2980 ppm, with the basis set error now estimated to be < 0.001 ppm. Unfortunately, there is no simple way to include in such calculations the nonadiabatic effects, so for instance in the HD isotopomer we have $\sigma(\text{H}) = \sigma(\text{D})$.

For both systems, the relativistic effects have been analysed; the corrections are ≈ 0.04 ppm for He [50] and ≈ 0.0005 ppm for $\sigma(\text{H})$ in H_2 [49].

Methane

To illustrate the accuracy of the ab initio methods we present in some detail the results for CH_4 and, in the next section, for SiH_4 . The convergence in a series of CCSD(T) calculations for methane is shown in Table 1. We have chosen a sequence of correlation-consistent basis sets (the cc-PCV5Z basis was truncated for computational reasons) and a special smaller basis set.

The quality of the ab initio absolute shielding constants in methane can be, in contrast to most other systems, analysed considering experimental data. Namely, there are gas-phase NMR results, spin-rotation constants and accurate ab initio values for other molecules available for comparison: CO for ^{13}C and H_2 for ^1H . For ^{13}C , the best result in Table 1 is 198.9 ppm; the ZPV correction is -3.2 ppm [52] and the temperature correction is negligible [53], so the total shielding is 195.7 ppm. The measured ^{13}C chemical shift between CH_4 and CO is 194.27 ppm [28], which leads to $\sigma(^{13}\text{C} \text{ in CO}) = 1.43$ ppm. The computed ab initio value is 2.9(20) ppm, and the value derived using the spin-rotation constant is 0.9(9) ppm [51]. The measured chemical shift and the

Table 1. Basis set convergence of the CCSD(T) shielding constants in CH_4

Basis set	C	H	Basis set	$\sigma(\text{C})$	$\sigma(\text{H})$
	CGTO	CGTO	size	(ppm)	(ppm)
cc-PCVTZ	6s5p3d1f	3s2p1d	99	200.321	31.446
cc-PCVQZ	8s7p5d3f1g	4s3p2d1f	204	199.223	31.359
cc-PCV5Z(-1g1h)	10s9p7d5f2g	5s4p3d1f	281	198.870	31.320
pz3d2p/pz3p2d ^a	8s5p3d2f	5s3p2d	148	199.029	31.391

^aFor a description of this basis set, suitable for NMR calculations, see [51].

calculated difference in the shielding are therefore in very good agreement, and this indicates that the absolute shielding constants are also reliable. Similarly, for ^1H in CH_4 the ZPV correction is -0.6 ppm [52] and the chemical shift between CH_4 and H_2 is 4.403 ppm [28], leading to $\sigma(^1\text{H in H}_2) = 26.317$ ppm. The fully ab initio result is $26.298(20)$ ppm, using the spin-rotation constant leads to $26.288(2)$ ppm [51]. The results for the carbon shielding constant are practically converged to ± 1 ppm, for the hydrogen constant to ± 0.1 ppm. It does not appear worthwhile (even if it were possible) to increase the basis set further, because the errors due to other approximations are of the same order of magnitude or larger.

6.2 NMR Shielding Constants for the Third-Row and Heavier Atoms

We present the problems arising in the studies of absolute shielding scales for third-row and heavier atoms beginning with the calculations of NMR shielding for hydrides of third-row atoms – SiH_4 , PH_3 and H_2S [42].

The new results, recommended as reference for absolute shielding scales [42], were combined from CCSD(T)/cc-pCVQZ shielding constants at the equilibrium geometry (optimised at the CCSD(T)/cc-pVTZ level), 300 K rovibrational contribution computed at the CCSD/cc-pCVTZ level and an estimate of the relativistic effects determined using Dirac–Hartree–Fock (DHF) four-component approximation and cc-pwCV5Z basis set (at the equilibrium geometry).

The convergence within the hierarchy of approximations was studied to estimate additional corrections and error bars of the results. To analyse the convergence of the basis set, correlation treatment and relativistic contribution the following differences were considered:

- Basis set: cc-pwCV5Z – cc-pCVQZ ; at the MP2 level;
- Correlation method: CCSD(T) – CCSD ; with the cc-pCVQZ basis;
- Relativistic contribution: DHF/cc-pwCV5Z – DHF/cc-pCVQZ.

In the analysis of the computed values, as well as in the analysis of convergence, additivity of different contributions is assumed.

The results for the equilibrium geometry, shown in Table 2, indicate convergence with respect to both main parameters of the calculation: the basis set size and the electron correlation model (the results for $\sigma(^1\text{H})$ in PH_3 and H_2S are similar to the SiH_4 values).

In principle, convergence can be investigated also for the zero-point vibrational and temperature corrections. However, since these corrections are much smaller than the total shielding constant and the calculations are (see Sect. 2.2) much more expensive, usually the ZPV and temperature effects are treated in a more approximate manner than the equilibrium geometry calculation. The results shown in Table 3 confirm that the rovibrational contributions are significant and cannot be totally neglected; in many cases they

Table 2. SiH₄, PH₃ and H₂S equilibrium geometry NMR shielding constants (ppm)^a

	Basis set	SCF	MP2	CCSD	CCSD(T)
²⁹ Si in SiH ₄	cc-pCVTZ	477.214	474.986	475.575	476.067
	cc-pCVQZ	474.331	469.246	470.146	470.640
	cc-pwCV5Z	473.953	467.104		
¹ H in SiH ₄	cc-pCVTZ	28.345	28.127	28.148	28.099
	cc-pCVQZ	28.344	28.057	28.081	28.023
	cc-pwCV5Z	28.331	28.020		
³¹ P in PH ₃	cc-pCVTZ	587.240	614.376	606.126	608.965
	cc-pCVQZ	584.052	610.508	602.378	605.831
	cc-pwCV5Z	584.025	609.464		
³³ S in H ₂ S	cc-pCVTZ	713.602	755.587	736.083	738.990
	cc-pCVQZ	710.510	753.827	734.256	737.923
	cc-pwCV5Z	710.902	754.024		

^aFor details, see [\[42\]](#).

are larger than the estimated error of the equilibrium value of the shielding constant. It should also be recalled that within the clamped nuclei model the shielding of a nucleus in the molecule does not depend on the isotopic species, the differences in the shielding leading to the isotope shift arise only when the nuclear motion is considered.

We have also computed the spin-rotation constants for these three hydrides. The results for the heavy atoms are: $\mathcal{M}(^{29}\text{Si}) = 41.387$, $\mathcal{M}(^{31}\text{P}) = -113.593$ and $\mathcal{M}(^{33}\text{S}) = -35.104$ kHz [\[42\]](#). Unfortunately, the experimental data are not very helpful when one wants to analyse the computed paramagnetic shielding contributions. The experimental results for ²⁹Si and ³³S are

Table 3. ZPV corrections to the heavy atom NMR shielding constants (in ppm)

Molecule	ZPV	Method ^a	Molecule	ZPV	Method
CH ₄	-3.3	MCSCF [52]	SiH ₄	-1.4	CCSD [42]
	-2.909	CCSD(T) [42]			
NH ₃	-7.0	MBPT [54]	PH ₃	-9.2	CCSD [42]
H ₂ O	-12.04	MCSCF [55]	H ₂ S	-20.9	CCSD(T) [42]

^aMCSCF = Multiconfiguration SCF; MBPT = many body perturbation theory.

not sufficiently accurate (in fact, the ^{33}S value should apparently be revised). On the other hand, for ^{31}P the experiment is very accurate, the tensor average is -115.39 ± 0.21 kHz [56]. However, it is difficult to say how large the relativistic contribution is – for the ^{31}P shielding in PH_3 the relativistic correction is $\approx 2.5\%$ of the total value. The difference between the computed and experimental spin-rotation constant is similar, so we cannot estimate the quality of the nonrelativistic calculation using the experimental result.

Relativistic Effects

A reliable ab initio relativistic calculation of shielding constants would require simultaneous and accurate treatment of relativistic effects, electron correlation and gauge invariance. In practice the available options are restricted; we shall discuss mainly the results obtained using the DHF linear response [57] or perturbational treatment [58].

Table 4 shows the differences between the nonrelativistic SCF and relativistic DHF values for three hydrides. In these calculations the unrestricted kinetic balance approach was used to generate the small component basis set, and the gauge origin was placed on the heavy atom. For comparison, in another approach the relativistic corrections are 13.61 ppm for $\sigma(^{29}\text{Si}$ in SiH_4) (at the MCSCF level [43]) and 23 ppm for $\sigma(^{33}\text{S}$ in H_2S) [59].

Clearly, the relativistic effects are not negligible, they are far larger than the errors in the nonrelativistic results. Unfortunately, as shown in Table 4 the relativistic contribution is not easy to determine, because large basis sets are needed to reach convergence. The remaining basis set error in the relativistic correction may be as important as the error in the much larger nonrelativistic

Table 4. Relativistic corrections to NMR shielding at DHF level (in ppm)^a

	Basis set	SCF	DHF	DHF – SCF
^{29}Si in SiH_4	cc-pCVTZ	478.02	484.18	6.16
	cc-pCVQZ	474.08	484.25	10.18
	cc-pwCV5Z	473.80	486.92	13.11
^{31}P in PH_3	cc-pCVTZ	577.95	587.13	9.19
	cc-pCVQZ	581.74	595.21	13.47
	cc-pwCV5Z	582.73	598.09	15.36
^{33}S in H_2S	cc-pCVTZ	695.30	704.68	9.38
	cc-pCVQZ	703.75	721.20	17.45
	cc-pwCV5Z	707.38	726.92	19.55

^aThe large component basis set is specified. For details, see [42].

part (we note here that in a recent version of the DIRAC 04 programme [46] GIAOs may be used in the DHF calculations).

For heavier atoms the treatment of the relativistic effects may become the dominant issue. This is demonstrated when the total shielding constant is computed as the sum of the nonrelativistic part and a perturbation correction, which accounts for the relativistic effects [58]. For instance, for $\sigma(^{73}\text{Ge})$ in GeH_4 the nonrelativistic value is 1809 ppm and the correction is 179 ppm; the corresponding values for ^{119}Sn in SnH_4 are 3324 and 694 ppm [43]. To obtain reliable absolute shielding constants it is therefore essential to describe properly the relativistic contribution. We recall that when the relativistic effects become large, one cannot apply the nonrelativistic relationship between the spin-rotation constant and the paramagnetic term to determine the total shielding. Therefore, even though the computed shielding constants are often not as accurate as for the molecules containing only light atoms, the only way to fix the shielding scale and derive the nuclear magnetic moment for a heavy nucleus may be to use an ab initio result.

7 Consistency of the New Values of Nuclear Magnetic Moments

Let us consider as the first example the magnetic dipole moment of ^{13}C . The generally accepted, literature value of ^{13}C magnetic moment tabulated by Raghavan [1] is $0.7024118(14)\mu_N$. It is based on the measured [5] frequency ratio $\nu(^{13}\text{C})/\nu(^1\text{H})$ in CH_3I molecule. However, to extract the ^{13}C bare nucleus magnetic moment the so-called “diamagnetic correction”, corresponding to the shielding in the ground state C atom (267 ppm), was used. The corresponding ab initio result [60] for the isolated molecule is $\sigma(^{13}\text{C} \text{ in } \text{CH}_3\text{I}) = 227$ ppm, a recent experimental gas-phase value is 220.59 ppm [61], and it is very unlikely that they differ by 40 ppm from the required experimental value in the liquid. The inaccurate treatment of NMR shielding led to systematic errors; it appears that when the “diamagnetic correction” was used the shielding was generally overestimated, and thus the magnetic moments of bare nuclei were also overestimated.

7.1 New Values of the Nuclear Magnetic Dipole Moments

To illustrate the dependence of the nuclear magnetic dipole moments on the source data and the effect of the corrections to the moments we discuss in general four approaches:

- (a) We use the literature magnetic moments from Raghavan [1].
- (b) We consider the old literature NMR data, that is the same source molecules and frequency ratios ν_X/ν_Y as in (a); but we use modified, more recent literature data for the shielding constants of X and Y nuclei in these molecules (see [31, 32] for details and references). In this approach, improved values of

magnetic moments may be derived extracting the required information from previously available literature data.

(c) In this approximation, accurate frequency ratios and chemical shifts determined from new gas-phase spectra (see Table 5) are used. Thus, the experimental results are not contaminated by intermolecular interactions and describe well the relevant parameters for the isolated molecules.

(d) The same experimental data as in (c) are used, but the absolute shielding constants are determined from new ab initio calculations [31, 32, 42, 43].

We note in Table 6 that the differences between (b), (c) and (d) nuclear magnetic moments are much smaller than the differences between the new values and the old literature data. Further improvement of the input data would not change significantly the magnetic moments. We have checked that for instance using for $\sigma(^1\text{H}$ in CH_4) an ab initio value instead of the experimental one (taken from H_2 and chemical shift), $\mu(^{13}\text{C}) = 0.7023706 \mu_{\text{N}}$. Similarly, including the relativistic correction to the ^{13}C shielding in methane, 1.07 ppm [43], leads to a very small change, $\mu(^{13}\text{C}) = 0.7023707 \mu_{\text{N}}$.

7.2 Derived Shielding Constants

To our knowledge (16),

$$\sigma_X = 1 - \frac{\nu_X}{\nu_Y} \frac{\Delta\mu_Y^z}{\Delta\mu_X^z} (1 - \sigma_Y)$$

has not previously been applied to examine the derived shielding constants, most likely because using literature values of magnetic moments one obtains meaningless results. The nuclear magnetic moments are in this approach

Table 5. Source data from gas-phase NMR and ab initio calculations^a

Molecule	Frequency ^b		Shielding ^b		Frequency ^b		Shielding ^b	
	Y	ν_Y (Hz)	σ_Y (ppm)	X	ν_X (Hz)	σ_X (ppm)		
CH_4	^{13}C	125.87667513(20)	195.02	^1H	500.60854854(13)	30.61		
H_2O	^{17}O	67.862408(4)	322.81	^1H	500.608828(5)	30.05		
CH_3F	^{19}F	470.9104056(50)	470.85	^1H	500.6105529(25)	26.60		
SiH_4	^{29}Si	99.4462169(1)	482.85	^1H	500.610044(2)	27.625		
SF_6	^{33}S	38.4198861(6)	379.89	^{19}F	471.0665830(5)	139.31		
GeH_4	^{73}Ge	17.4570625(2)	1988.71	^1H	500.609969(4)	27.774		

^aData for isolated molecules.

^bFrequencies from experiment; absolute shielding constants from ab initio calculations combined, when needed, with measured chemical shifts. For estimates of the error bars and other details, see [31, 32].

Table 6. Nuclear magnetic dipole moments^a (in μ_N)

Nucleus	Gas sample molecule ^b	Magnetic moment, μ_X			
		11		31 , 32 ^c	
¹³ C	(a)	0.7024118(14)	(b)	0.7023715	
	CH ₄		(c)	0.7023694(35)	
	CH ₄		(d)	0.7023698	
¹⁴ N	(a)	0.40376100(6)	(b)	0.4035729(20)	
¹⁵ N	(a)	-0.283188842(45)	(b)	-0.2830569(14)	
¹⁷ O	(a)	-1.89379(9)	(b)	-1.8935693	
	H ₂ O		(c)	-1.8935428(95)	
	H ₂ O		(d)	-1.8935493	
¹⁹ F	(a)	2.628868(8)	(b)	2.6284316	
	CH ₃ F		(c)	2.628321(13)	
²⁹ Si	(a)	-0.55529(3)	(d)	-0.5550520(31)	
	SiH ₄				
³¹ P	(a)	1.13160(3)	(b)	1.130903(17)	
³³ S	(a)	0.6438212(14)	(b)	0.6431603	
	SF ₆		(c)	0.643247(11)	
⁷³ Ge	(a)	-0.8794677(2)	(d)	-0.878241(44)	
	GeH ₄				
¹¹⁹ Sn	(a)	-1.04728(7)	(b)	-1.04506(11)	

^aThe approximations (a–d) are described in the text.

^bGas samples were used in [31](#), [32](#); (a) and (b) values are derived from other (condensed phase) data, see the references for more details.

^cFor the recommended values we have given estimated error bars, see [31](#), [32](#).

treated as fixed input data and we check the consistency of the NMR frequencies and shielding constants. Thus, we compute σ_X assuming that the frequency ratios ν_X/ν_Y are known, and using a known value of σ_Y (a single index X or Y denotes here both the nucleus and the molecule). The main idea is that we check the consistency of all the NMR parameters in a series of different tests; obviously when the same data that served to determine the magnetic moment from [\(15\)](#) are used in [\(16\)](#) it is fulfilled by default. The test provided by [\(16\)](#) is most demanding when all the data are taken from different sources, for instance we consider the same pair of nuclei but in two different molecules (thus with different resonance frequencies and shielding constants).

In the tests discussed below we use either

- A fixed X and a loop over Y , that is we derive a chosen σ_X from various input data, or
- A fixed Y and a loop over X , that is we derive the shielding constants of various other nuclei using a chosen reference.

Most importantly, in each sequence the results obtained using old and new values of the magnetic moments in (16) will be compared.

Experimental frequency ratios for ≈ 100 nuclei (in molecules which constitute recommended chemical standards for NMR) with respect to ^1H frequency in TMS are tabulated [4]. We have confirmed in our own studies that the inaccuracies of the measured frequencies are negligible in comparison with the other sources of error; we shall similarly assume that these tabulated values of frequency ratios ν_X/ν_Y are exact for our analysis. In the discussed examples, when we derive the shielding constants applying old and new magnetic moments, in addition to our own results we use these tabulated frequency ratios.

As the first example illustrating in detail the consistency of the new NMR data we present the derived shielding constant in atomic helium. The correct value of $\sigma(^3\text{He})$ is known with high accuracy from ab initio calculations (see Sect. 6.1). The values of $\sigma(^3\text{He})$ derived using as input σ_Y the best estimated shielding constants for a series of nuclei are shown in Table 7. With the old values of nuclear magnetic moments most of the results are completely wrong. In analogous calculations, but with the new values of the magnetic moments we obtain very reasonable results; the errors with respect to the correct value, 59.93677 ppm, are reduced by an order of magnitude or more. The shielding of ^3He derived from ^1H data is 56.02 ppm, therefore to obtain higher consistency one has to analyse the accuracy of the ^3He experiment.

The results of another test are shown in Table 8. We have cross-examined the new nuclear moments; we can take the shielding of any nucleus as input in

Table 7. Derived NMR shielding constant for ^3He atom (in ppm)^a

Nucleus Y	Input		Input					
	old	μ_Y	new	μ_Y				
^{13}C	(a)	-3.61	(b)	53.85	(c)	56.76	(d)	56.28
^{17}O	(a)	-80.33	(b)	39.55	(c)	53.53	(d)	50.11
^{19}F	(a)	-151.55	(b)	14.48	(c)	56.42		
^{33}S	(a)	-836.55	(b)	190.89	(c)	55.52		
^{29}Si	(a)	-373.94					(d)	54.35
^{73}Ge	(a)	-1340.67					(d)	55.64

^a For the description of (a–d) approximations, see the text.

(16). We observe similar systematic improvements, the errors in the derived shielding constants decrease from a few hundred to a few ppm – on the average by more than an order of magnitude. The improvement obtained using the new values of the magnetic moments is proven by the overall consistency of the set of the derived shielding constants.

7.3 Accuracy of the Results

The accuracy of ab initio results is in practice determined by the computational limits of the applied programs. In the discussed nonrelativistic calculations of the shielding constants these limits usually depend on the basis set size and on the approximation describing the electron correlation effects, not on the size or structure of the studied molecule. Not surprisingly, within such predefined limits we can reach most accurate results for the smallest atoms and molecules, like He and H₂; the accuracy is lower for molecules like CH₄ (5 nuclei, 10 electrons), lower again for molecules containing third-row atoms with more electrons, etc.

Table 8. Derived shieldings constants for NMR standards (in ppm)

Nucleus	Reference	$\sigma(X)$	$\sigma(X)$	$\sigma(X)$
X	standard ^a	μ_X old ^b	μ_X new ^b	best estimate
		input: $\sigma(^1\text{H in TMS}) = 33.440 \text{ ppm}^c$		
¹³ C	TMS	246.73	186.38	186.37 [33]
¹⁹ F	CFCl ₃	400.87	192.97	192.7 [29]
³³ S	(NH ₄) ₂ SO ₄	1096.31	205.17	204.0 [17]
		input: $\sigma(^{13}\text{C in TMS}) = 186.44 \text{ ppm}^a$		
¹ H	TMS	-26.86	33.03	33.440 ^c
¹⁷ O	D ₂ O	364.19	290.25	287.5 [62]
¹⁹ F	CFCl ₃	340.59	192.56	192.7 [29]
²⁹ Si	TMS	746.65	378.53	378.51 ^d
³³ S	(NH ₄) ₂ SO ₄	1036.07	204.77	204.0 [17]

^a For a detailed description of the compounds considered as NMR standards, see [4].

^b μ_X old: (a) values; μ_X new: (c) values from Table 6 when available, (d) for ²⁹Si; (b) values otherwise.

^c Obtained using 32.775 ppm [33] and a shift of 0.665 ppm between pure liquid TMS and TMS, 1% solution in deuterated chloroform.

^d See Sect. 7.3

Basis Set and Correlation Errors

The practical limit for coupled cluster calculations of shielding constants (on a standard workstation) is presently ≈ 300 CGTO basis set functions. This means that relatively accurate results may be obtained for instance at the CCSD(T)/cc-pCVQZ level for SiH₄, but it is not possible to achieve similar accuracy for SF₆ molecule.

For the second-row hydrides, methane (see Table 1) and water the shielding constants at the equilibrium geometries were obtained applying large basis sets (cc-pCVQZ, cc-pCV5Z and intermediate). The basis set errors were estimated as ≈ 0.2 ppm for the H atom and ≈ 0.5 ppm for C and O atoms [31]. In analogous CCSD(T) calculations for the third-row hydrides [42], cc-pCVQZ basis becomes the limit and the basis set incompleteness error is more significant. It has to be examined at a correlated level, and larger bases could be used in MP2 calculations. The error varied from -2.1 to 0.2 ppm in the MP2 results, and we have estimated it should not exceed ≈ 3 ppm for the CCSD(T) approximation.

The highest approximation suitable for practical applications is CCSD(T); a comparison with the CCSD results indicated that it is sufficiently accurate for the studied molecules. In the analysis of the contributions of higher clusters to NMR shielding, Kállay and Gauss [41] observed that $\sigma(\text{full CI}) - \sigma(\text{CCSD(T)}) \ll \sigma(\text{CCSD(T)}) - \sigma(\text{CCSD})$. Although for computational reasons the analysis was restricted to small molecules including only first- and second-row atoms, and small basis sets, it appears that one can use $(1/2)[\sigma(\text{CCSD(T)}) - \sigma(\text{CCSD})]$ as an estimated correction for the incomplete treatment of electron correlation effects. For the shielding of heavy atoms in the third-row hydrides this error due to the truncated cluster expansion has been estimated in this way as ≈ 3 ppm [42].

Accuracy of the Absolute Shielding Scales

As an example illustrating the accuracy of the computed shielding constants we consider various contributions to the absolute shielding of ²⁹Si and ¹H in SiH₄.

The literature absolute shielding scale for ²⁹Si was based on the experimental spin-rotation constants and chemical shifts of SiF₄ and SiH₄ [63]. The spin-rotation constant of ²⁹Si in SiH₄ was estimated to be 41.3 ± 1.0 kHz, the calculated value was 41.387 kHz [42]; the agreement with experiment is partly fortuitous. The value of $\sigma(^{29}\text{Si in SiH}_4)$ derived from experiment is 475.3 ± 10 ppm, the ab initio results [42] are shown in Table 9. The error of the basis set has been estimated as ≈ -2.1 ppm, the correlation error as ≈ 0.2 ppm and the error of the relativistic contribution as ≈ 2.9 ppm, with the cumulative correction estimated to be ≈ 1.0 ppm. The total $\sigma(^{29}\text{Si in SiH}_4, 300\text{ K})$ including an estimate of all the corrections was 483.4 ppm, the differences between our various results are much smaller than the assumed (see below) error bar of 5.0 ppm.

Table 9. Absolute shielding constants in SiH₄ (in ppm)

²⁹ Si in SiH ₄	σ_e [CCSD(T)/cc-pCVQZ]	470.640
	vibrational contribution [CCSD/cc-pCVTZ, 300 K]	-1.404
	relativistic correction [DHF] ^a	13.11
	σ ab initio	482.35
¹ H in SiH ₄	σ_e [CCSD(T)/cc-pCVQZ]	28.023
	vibrational contribution [CCSD/cc-pCVTZ, 300 K]	-0.379
	σ ab initio	27.644
	σ , experiment (ab initio H ₂ + chemical shifts ^b)	27.625

^aA perturbation theory result [43], 13.61 ppm, was used as a better estimate in Table 5 and to obtain $\mu(^{29}\text{Si})$ in Table 6

^b Gas-phase NMR experiment [32]; chemical shift, SiH₄ vs liquid TMS: ¹H: -5.150 ppm.

The NMR reference standard for ²⁹Si is liquid TMS. Combining the SiH₄ ab initio shielding constant and the experimental chemical shift of ²⁹Si between isolated SiH₄ molecule and TMS, 104.34 ppm [32], leads to 378.51 ppm for the shielding of ²⁹Si in liquid TMS at 300 K. This value is in our opinion more reliable than the earlier reference result, 368.50±10 ppm [63]. Consequently, the absolute shielding $\sigma(^{29}\text{Si in SiH}_4, 300 \text{ K})$ is taken from the described ab initio calculations.

The results for the proton shielding in SiH₄ are shown in Table 9, and in this case the experimental value is preferred. The absolute shielding scale for ¹H was derived using very accurate calculations for H₂, the measured chemical shifts are also accurate and it would be very difficult to obtain a more reliable value of $\sigma(^1\text{H in SiH}_4, 300 \text{ K})$ from a direct calculation. The values of $\sigma(^{29}\text{Si})$ and $\sigma(^1\text{H})$, together with $\mu(^1\text{H})$ and the measured ²⁹Si/¹H frequency ratio in SiH₄, were used to obtain the nuclear magnetic moment of ²⁹Si [32].

In general, for the NMR shielding at the equilibrium geometry accuracy of a few ppm can be reached, at least for the third-row hydrides. The basis set and correlation errors can be estimated. The vibrational and temperature corrections can be computed accurately to ≈1 ppm. The relativistic effects on NMR shieldings become important already for the third-row atoms, up to 25 ppm for H₂S (≈3% of nonrelativistic value). They require large or specially designed basis sets to reach accuracy of a few ppm. In fact, the largest uncertainty comes from the relativistic correction; the basis set convergence and the role of electron correlation in relativistic calculations have to be examined in more detail.

The inaccuracy of the absolute shielding scale varies with the nucleus, similar to the magnitude and the span of the shielding constants in different molecules. It is a fraction of a ppm for ¹H, several ppm for third-row nuclei

like ^{33}S and larger and more difficult to estimate for heavier nuclei. For heavy nuclei the relativistic effects become large and that puts in doubt the assumed additivity of various corrections to the shielding.

Accuracy of the Magnetic Dipole Moments

The accuracy of the studied magnetic dipole moment depends on the errors in the frequency ratio and in the shielding constants of X and Y nuclei as well as on the error in the reference dipole moment μ_X . We have observed that the frequency ratios measured in the gas phase and extrapolated to the zero density limit can be treated as exact. Also, the error in the reference dipole moment μ_X is negligible when the reference nucleus is ^1H . Otherwise, the analysis of the error bars unfortunately requires an arbitrary decision: what is the known input and what is to be determined. For example, the magnetic moment of ^{33}S in the discussed approximation (c) was determined using as input the previously determined moment of ^{19}F ; that sequence could be reversed.

Practically, the error of the computed magnetic moment is proportional to the error in the shielding constants. This inaccuracy of the shielding constants depends on the error in the absolute shielding scale and, possibly, the error in the measured chemical shift. However, the latter is in the discussed experiments 0.1 ppm or smaller, as confirmed for instance by our own measurement of the chemical shift between gaseous $o\text{-H}_2$ and liquid TMS [28]. It is therefore negligible in comparison with the error in the absolute scale; that is why we examined in detail the accuracy of all the contributions to the ab initio shielding constants.

The following estimates of the errors in the absolute shieldings: 0.5 ppm for ^1H , 5 ppm for second-row atoms (^{13}C , ^{14}N , ^{15}N , ^{17}O , ^{19}F) and 15 ppm for third-row atoms (^{31}P , ^{33}S) have been used [31] to derive the magnetic moments shown in Table 6. In [32], these values were estimated to be ^1H : 0.5 ppm (in all the studied molecules), ^{13}C : 3.0, ^{29}Si : 5.0, ^{73}Ge : 50, and ^{119}Sn : 100 ppm, respectively. Hopefully, the uncertainties in the absolute shielding constants are in fact smaller than these assumed values; only estimates can be given. Let us return to the magnetic moment of ^{29}Si . The discussed dominant basis set errors in the nonrelativistic and relativistic part of the shielding constant largely cancelled out; we have nevertheless assumed a maximum error of 5.0 ppm in $\sigma(^{29}\text{Si}$ in SiH_4). With this estimate and the data of Table 9 we have $\mu(^{29}\text{Si}) = -0.5550520(31)\mu_{\text{N}}$, to be compared with $-0.55529(3)\mu_{\text{N}}$ [1], thus the predicted improvement is an order of magnitude larger than our error estimate.

The accuracy of all the data decreases for the heavier nuclei – for instance, in the ab initio studies [43] of GeH_4 and SnH_4 rovibrational corrections were not taken into account, the experimental values for SnH_4 [20] have not been extrapolated to zero density, etc. However, for these nuclei the accuracy of the magnetic moments depends primarily on the proper description of the large

relativistic effects. Regrettably, there are at the moment no ab initio methods that would enable a reliable and highly accurate description of these effects in heavier nuclei, such as for example ^{207}Pb .

8 Conclusions

In the simplest approach, the values of nuclear magnetic dipole moments can be significantly improved using literature NMR resonance frequencies if more accurate absolute shielding constants are presently available. Further improvement is obtained for many nuclei using absolute shielding constants derived from new and more accurate ab initio calculations, combined with new gas-phase NMR frequencies and chemical shifts. In the gas-phase NMR experiments extrapolation to the zero density point eliminates the effects due to intermolecular forces, providing isolated molecule values for comparison with ab initio results. The absolute shielding scale is defined applying state-of-the-art ab initio methods to obtain the shielding constant in the same molecule. The electron correlation effects are well described using coupled cluster perturbation approaches, the basis set convergence can be examined and the final results for the equilibrium geometries obtained with high accuracy. In addition, the zero-point vibrational and temperature contributions are included and the relativistic effects can be estimated. It appears that for light atoms the accuracy of the Schrödinger equation is exhausted and a careful analysis of the relativistic corrections is essential to reach higher accuracy of the total shielding constants.

The final values of the constants are used to fix reliable shielding scales, and consequently to derive new, more accurate values of the nuclear magnetic dipole moments. The changes of the nuclear moments with respect to the previous values are $\approx 10^{-4} \mu_{\text{N}}$ for many nuclei. Thus, although the literature values of the moments are given with more digits, we observe a change on the fourth decimal when we describe systematically the role of the shielding. In the discussion of the results we have concentrated primarily on the nuclei of interest for standard chemical applications, a similar analysis can be performed for any other isotope with nonzero magnetic moment.

We have shown that the corrected values of nuclear magnetic moments give much better consistency of NMR parameters. The absolute shielding constants derived with the new values of the magnetic moments are much closer to the best available experimental data. With the old values of the magnetic moments we find large errors in the derived shielding constants; in analogous calculations, but with the new values of nuclear magnetic moments, the errors are reduced by an order of magnitude or more. The differences between the old and new values are small, $\approx 10^{-4}$ of the total moment, but their importance for the consistency of all the NMR spectroscopic parameters becomes clear when we attempt to reproduce a shielding constant known accurately to a few parts per million.

Acknowledgements

We appreciate the help of A. Antušek, W. Makulski and M. Wilczek at the early stages of this work.

References

1. P. Raghavan: *Atomic Data and Nuclear Data Tables*, **42**, 189 (1989). [233](#), [249](#), [251](#), [256](#)
2. I. Mills, T. Cvitaš, K. Homann, N. Kallay, and K. Kuchitsu: *IUPAC, Physical Chemistry Division: Quantities, Units and Symbols in Physical Chemistry*. Blackwell Science, Oxford, (1993). [233](#)
3. R. B. Firestone, V. S. Shirley, C. M. Baglin, S. Y. F. Chu, and J. Zipkin: *Table of Isotopes, 8th edition*. John Wiley & Sons, Inc., New York, (1996). [233](#)
4. R. K. Harris, E. D. Becker, S. M. C. de Menezes, R. Goodfellow, and P. Granger: *Pure Appl. Chem*, **73**, 1795 (2001). reprinted in *Magn. Reson. in Chem.* **40**, 489 (2002). [233](#), [236](#), [238](#), [252](#), [253](#)
5. V. Royden: *Phys. Rev.*, **96**, 543 (1954). [233](#), [249](#)
6. F. Alder and F. C. Yu: *Phys. Rev.*, **81**, 1067 (1951). [233](#)
7. M. R. Baker, C. H. Anderson, and N. F. Ramsey: *Phys. Rev.*, **133A**, 1533 (1964). [233](#)
8. S. S. Dharmatti and H. E. Weaver, Jr.: *Phys. Rev.*, **83**, 845 (1951). [233](#), [244](#)
9. T. Helgaker, P. Jørgensen, and J. Olsen: *Molecular Electronic-Structure Theory*; J. Wiley, Chichester, (2000). [234](#)
10. J. Gauss: *Ber. Bunsenges. Phys. Chem*, **99**, 1001 (1995). [234](#)
11. T. Helgaker, M. Jaszúński, and K. Ruud: *Chem. Rev.*, **99**, 293 (1999). [234](#)
12. J. Gauss and J. F. Stanton: *Adv. Chem. Phys.*, **123**, 355 (2002). [234](#)
13. K. Jackowski and W. T. Raynes: *Mol. Phys.*, **34**, 465 (1977). [234](#)
14. K. Jackowski, E. Dayan, and W. T. Raynes: *Mol. Phys.*, **34**, 1189 (1977). [234](#)
15. W. Makulski and K. Jackowski: *Chem. Phys. Lett.*, **341**, 369 (2001). [234](#)
16. K. Jackowski, M. Wilczek, W. Makulski, and W. Kozminski: *J. Phys. Chem. A*, **106**, 2829 (2002). [234](#), [241](#)
17. K. Jackowski, W. Makulski, and W. Koźmiński: *Magn. Reson. Chem.*, **40**, 563 (2002). [234](#), [253](#)
18. V. Kellö and A. J. Sadlej: *J. Chem. Phys.*, **120**, 9424 (2004). [235](#)
19. M. G. H. Gustavsson and A.-M. Mårtensson-Pendrill: *Phys. Rev. A*, **58**, 3611 (1998). [235](#)
20. A. Laaksonen and R. E. Wasylishen: *J. Am. Chem. Soc.*, **117**, 392 (1995). [235](#), [256](#)
21. C. J. Jameson: In D. M. Grant and R. K. Harris, editors, *Encyclopedia of NMR*, page 1273. J. Wiley & Sons Ltd., New York, 1996. [236](#)
22. J. Olsen and P. Jørgensen: *J. Chem. Phys.*, **82**, 3235 (1985). [237](#)
23. T. Helgaker, T. A. Ruden, P. Jørgensen, J. Olsen, and W. Klopper: *J. Phys. Org. Chem.*, **17**, 913 (2004). [237](#)
24. T. A. Ruden and K. Ruud: Ro-Vibrational Corrections to NMR Parameters. In M. Kaupp, M. Bühl, and V. G. Malkin, editors, *Calculation of NMR and EPR parameters. Theory and applications*, page 153, Weinheim, 2004. Wiley-VCH. [237](#)
25. W. T. Raynes, A. D. Buckingham, and H. J. Bernstein: *J. Chem. Phys.*, **36**, 3481 (1962). [240](#)

26. C. J. Jameson: *Bull. Magn. Reson.*, **3**, 3 (1980). [240](#)
27. J. A. Pople, W. G. Schneider, and H. J. Bernstein: In *High-resolution Nuclear Magnetic Resonance*, pages 80–82. McGraw-Hill Book Company, London, 1959. [241](#)
28. W. Makulski, M. Wilczek, and K. Jackowski: to be published. [241](#), [245](#), [246](#), [256](#)
29. K. Jackowski, M. Kubiszewski, and W. Makulski: *J. Mol. Struct.*, **614**, 267 (2002). [241](#), [253](#)
30. K. Jackowski, M. Jaszúński, W. Makulski, and J. Vaara: *J. Magn. Reson.*, **135**, 444 (1998). [241](#)
31. A. Antušek, K. Jackowski, M. Jaszúński, W. Makulski, and M. Wilczek: *Chem. Phys. Lett.*, **411**, 111 (2005). [241](#), [244](#), [249](#), [250](#), [251](#), [254](#), [256](#)
32. W. Makulski, K. Jackowski, A. Antušek, and M. Jaszúński: *J. Phys. Chem. A*, **110**, 11462 (2006). [241](#), [242](#), [244](#), [249](#), [250](#), [251](#), [255](#), [256](#)
33. K. Jackowski, M. Wilczek, M. Pecul, and J. Sadlej: *J. Phys. Chem. A*, **104**, 5955 (2000); (erratum) **104**, 9806 (2000). [242](#), [253](#)
34. P. J. Mohr and B. N. Taylor: *Rev. Mod. Phys.*, **77**, 1 (2005). [243](#)
35. D. E. Woon and T. H. Dunning Jr.: *J. Chem. Phys.*, **98**, 1358 (1993). [244](#)
36. K. A. Peterson and T. H. Dunning Jr.: *J. Chem. Phys.*, **117**, 10548 (2002). [244](#)
37. F. London: *J. Phys. Radium*, **8**, 397 (1937). [244](#)
38. K. Wolinski, J. F. Hinton, and P. Pulay: *J. Am. Chem. Soc.*, **112**, 8251 (1990). [244](#)
39. J. Gauss and J. F. Stanton: *J. Chem. Phys.*, **102**, 251 (1995). [244](#)
40. J. Gauss and J. F. Stanton: *J. Chem. Phys.*, **104**, 2574 (1996). [244](#)
41. M. Kállay and J. Gauss: *J. Chem. Phys.*, **120**, 6841 (2004). [244](#), [254](#)
42. A. Antušek and M. Jaszúński: *Mol. Phys.*, **104**, 1463 (2006). [244](#), [246](#), [247](#), [248](#), [250](#), [254](#)
43. M. Jaszúński and K. Ruud: *Mol. Phys.*, **104**, 2139 (2006). [244](#), [248](#), [249](#), [250](#), [255](#), [256](#)
44. *Aces II Mainz-Austin-Budapest-Version 2005, a quantum chemical program package*. written by J. F. Stanton, J. Gauss, J. D. Watts, P. G. Szalay, R. J. Bartlett with contribution from A. A. Auer, D. B. Bernholdt, O. Christiansen, M. E. Harding, M. Heckert, O. Heun, C. Huber, D. Jonsson, J. Juselius, W. J. Lauderdale, T. Metzroth, K. Ruud and the integral packages MOLECULE (J. Almlöf and P. R. Taylor), Props (P. R. Taylor), and ABACUS (T. Helgaker, H. J. Aa. Jensen, P. Jørgensen, and J. Olsen). See also J. F. Stanton, J. Gauss, J. D. Watts, W. J. Lauderdale, R. J. Bartlett, *Int. J. Quantum Chem. Symp.* **26**, 879 (1992) as well as: <http://www.aces2.de> for the current version. [244](#)
45. *DALTON, a molecular electronic structure program, Release 2.0 (2005)*, see <http://www.kjemi.uio.no/software/dalton/dalton.html>. [244](#)
46. *DIRAC 04, a relativistic ab initio electronic structure program, Release DIRAC04.0 (2004)*. written by H. J. Aa. Jensen, T. Saue, and L. Visscher with contributions from V. Bakken, E. Eliav, T. Enevoldsen, T. Fleig, O. Fossgaard, T. Helgaker, J. Laerdahl, C. V. Larsen, P. Norman, J. Olsen, M. Pernpointner, J. K. Pedersen, K. Ruud, P. Salek, J. N. P. van Stralen, J. Thyssen, O. Visser, and T. Winther. [244](#), [249](#)
47. G. W. F. Drake. High Precision Calculations for Helium. In G. W. F. Drake, editor, *Springer Handbook of Atomic, Molecular and Optical Physics*, page 199. Springer, 2006. [245](#)
48. D. Sundholm and J. Gauss: *Mol. Phys.*, **92**, 1007 (1997). [245](#)
49. M. Jaszúński and G. Lach: unpublished results. [245](#)

50. J. Vaara and P. Pyykkö: *J. Chem. Phys.*, **118**, 2973 (2003). [245](#)
51. D. Sundholm, J. Gauss, and A. Schäfer: *J. Chem. Phys.*, **105**, 11051 (1996). [245](#), [246](#)
52. K. Ruud, P.-O. Åstrand, and P. R. Taylor: *J. Chem. Phys.*, **112**, 2668 (2000). [245](#), [246](#), [247](#)
53. W. T. Raynes, P. W. Fowler, P. Lazzeretti, R. Zanasi, and M. Grayson: *Mol. Phys.*, **64**, 143 (1988). [245](#)
54. H. Fukui, T. Baba, J. Narumi, H. Inomata, K. Miura, and H. Matsuda: *J. Chem. Phys.*, **105**, 4692 (1996). [247](#)
55. J. Vaara, J. Lounila, K. Ruud, and T. Helgaker: *J. Chem. Phys.*, **109**, 8388 (1998). [247](#)
56. P. B. Davies, R. M. Neumann, S. C. Wofsy, and W. Klemperer: *J. Chem. Phys.*, **35**, 3564 (1971). [248](#)
57. L. Visscher, T. Enevoldsen, T. Saue, H. J. Aa. Jensen, and J. Oddershede: *J. Comput. Chem.*, **20**, 1262 (1999). [248](#)
58. J. Vaara, P. Manninen, and P. Lantto: Perturbational and ECP Calculation of Relativistic Effects in NMR Shielding and Spin–Spin Coupling. In M. Kaupp, M. Bühl, and V. G. Malkin, editors, *Calculation of NMR and EPR parameters. Theory and applications*, page 209, Weinheim, 2004. Wiley–VCH. [248](#), [249](#)
59. P. Manninen, K. Ruud, P. Lantto, and J. Vaara: *J. Chem. Phys.*, **122**, 114107 (2005). erratum, *J. Chem. Phys.*, **124**, 149901 (2006). [248](#)
60. J. Vaara, K. Ruud, and O. Vahtras: *J. Chem. Phys.*, **111**, 2900 (1999). [249](#)
61. M. Wilczek, M. Kubiszewski, and K. Jackowski: *J. Mol. Struct.*, **704**, 311 (2004). [249](#)
62. R. E. Wasylishen and D. L. Bryce: *J. Chem. Phys.*, **117**, 10061 (2002). [253](#)
63. C. J. Jameson and A. K. Jameson: *Chem. Phys. Lett.*, **149**, 300 (1988). [254](#), [255](#)

The Negative Ion of Positronium: Decay Rate Measurements and Prospects for Future Experiments

F. Fleischer

Max-Planck-Institut für Kernphysik, Heidelberg, Germany
f.fleischer@mpi-hd.mpg.de

Abstract. Consisting of two electrons and a positron ($e^+e^-e^-$), the negative ion of positronium (Ps^-) represents the simplest three-body system with a bound state. Its constituents are stable, point-like particles, and it is essentially free from perturbations by strong interaction effects. Together with the rather unique mass ratio, these properties make the positronium ion an interesting object for studying the quantum-mechanical three-body problem. Accordingly, there is a considerable number of theoretical publications on this exotic ion, but experimental data are very scarce. In this article, after giving a short overview of the theoretical results on Ps^- , we review the measurements of its decay rate, and we discuss the prospects for further experiments now becoming possible at the new high-intensity positron source NEPOMUC at the FRM-II research reactor in Garching (Germany).

1 Introduction

For several decades it has been known that there is a particle-stable bound state consisting of a positron and two electrons. The first one to discover this was J.A. Wheeler, who calculated a lower limit for its binding energy in 1946 [1], using the variational principle with a 3-parameter Hylleraas-type wavefunction. Obtaining an expectation value of -6.96 eV, he concluded that the second electron is bound by at least 0.19 eV with respect to the ground state of positronium – calculated to have an energy of -6.77 eV in the same paper. For such systems made of electrons and positrons he proposed the name “polyelectrons”. He could not establish the stability of species consisting of more than three particles; nevertheless, he suggested that larger clusters of electrons and positrons might explain the nature of the mesons, which had been discovered in the cosmic radiation not long before.

While Wheeler’s two-body polyelectron – today known as positronium – has been the object of intense studies both on the theoretical and experimental side, the three-body polyelectron or positronium ion (Ps^-) almost exclusively found the interest of theoreticians. Up to now, a considerable

number of articles covering theoretical calculations of different parameters of the positronium ion have been published. In 1981 A.P. Mills succeeded in producing Ps^- using a beam-foil method [2], identifying the ions by the Doppler-shifted annihilation radiation of Ps^- decaying in flight. Following the same approach he made a first decay rate measurement of Ps^- [3] in 1983 (see Sect. 3.2).

Both the neutral positronium atom and the Ps^- ion exhibit a number of attractive features, which also explains the theoretical interest in these systems. According to our present knowledge, their constituents, electrons and positrons, are stable, point-like particles without any structure. To a very good approximation Ps and Ps^- are purely quantum-electrodynamical systems. Other simple atomic systems like hydrogen have to deal with nuclear size effects; in fact the theoretical prediction of the atomic properties of hydrogen is limited by the poor knowledge of the proton charge radius. By turning the problem around and assuming the validity of bound-state QED, a comparison of higher-order calculations and precision measurements of simple atomic systems can be used to determine such nuclear parameters. Obviously, this approach excludes a use of the experimental data as a test of QED. As pointed out in [4], positronium (being free from the effects mentioned above) is ideally suited for high-precision bound-state QED tests. The positronium ion in principle has the same advantages, but due to the complication introduced by the third particle, it is less interesting as a high-precision QED test. On the other hand, it is just the three-body nature of Ps^- which makes this an attractive system to study: with all three constituents having the same mass, the positronium ion has a rather unique mass ratio between H_2^+ and H^- . It is intrinsically a three-body problem, and simplifications like the Born–Oppenheimer approximation or the assumption of an infinitely heavy nucleus are not applicable. Lying in the middle between the two extremes of H_2^+ and H^- , Ps^- also allows for a study of the transition from the atomic to the molecular set of quantum numbers. Altogether, it is ideally suited to test the different approaches which have been applied to the solution of the quantum-mechanical three-body problem.

2 A Brief Survey of the Properties of Ps^-

This section gives a short overview of the theoretically calculated properties of Ps^- . After starting with the ground-state properties of the positronium ion, the results on the different decay branches are discussed, and finally excitations and resonances are considered.

2.1 Ground-State Binding Energy

The positronium ion represents a genuine three-body problem, where the molecular Born–Oppenheimer approximation as well as the assumption of

an infinitely heavy nucleus must necessarily fail. With practically useful analytical solutions of the three-body problem being unavailable, a theoretical treatment is possible only on the basis of numerical approximations.

As a sufficiently precise wavefunction is the necessary prerequisite for all further theoretical considerations, quite a few attempts have been made to calculate this fundamental quantity. Mainly, these are variational calculations [1, 5, 6, 7, 8, 9, 10, 11, 12, 13], but there has also been a non-variational approach [14, 15]. It turns out that, as in the case of H^- , the ground state is the only state which is stable against dissociation. In this state the two electrons are in a singlet S-state, the parity is even (${}^S L^\pi = 1\text{S}^e$).

The large number of significant figures (up to 20) in the more precise of the above-mentioned ground-state energy results is somewhat misleading. As a physical quantity (as opposed to a mathematical measure of the properties of the variational trial function), it is certainly not meaningful without consideration of relativistic effects or QED contributions. A partial evaluation can be found in [16], where Bhatia and Drachman considered the relativistic corrections to the energy and started to compute the relevant expectation values. Also Frolov [5] discussed the relativistic corrections, but an evaluation of the necessary expectation values was still missing. A complete calculation of the lowest-order relativistic and QED corrections has only recently been published by Drake, giving a ground-state energy of $E = -0.261\,998\,108\,122(1)$ a.u. [17].

Given the wavefunction, also the expectation values of the interparticle distances can be calculated. Looking at the values $\langle r_{1p} \rangle$ and $\langle r_{12} \rangle$ shown in Fig. 1, the rather large size of the positronium negative ion is remarkable: the two electrons are separated by a distance of several Ångström. It is important to note, however, that the basic structure of the positronium negative ion is not that of an equilateral triangle. In fact, the two electron–positron distances are rather different and the system can be crudely described as a positronium atom plus a second, loosely bound electron [7].

2.2 Annihilation and Decay Rates

Due to the possibility of electron–positron annihilation, the positronium ion has a finite lifetime. Many aspects of the Ps^- decays can be understood in terms of the corresponding decay channels of neutral positronium. Given the

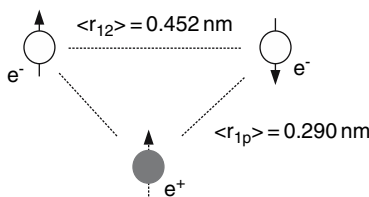


Fig. 1. Average interparticle distances (see, for example, [5]) and spin orientations in the positronium negative ion

above-mentioned geometrical structure, this is not too surprising: in a first approximation, the decay of the positronium ion can be considered as a positronium decay plus a spectator electron. For this reason, it is worth recalling the decays of the ground state of neutral Ps atoms, which form two distinct spin states, depending on the relative spin orientation of the electron and the positron: a singlet state 1S_0 (para-Ps) and a triplet state 3S_1 (ortho-Ps). Both decay by electron–positron annihilation, but due to their different behaviour under charge conjugation, they differ in the possible numbers of final-state photons. While the singlet state can decay only into an even number of photons ($\Gamma(\text{Ps}, ^1S_0) = 7990.9(17)\mu\text{s}^{-1}$ [18]), for the triplet state only odd numbers are possible ($\Gamma(\text{Ps}, ^3S_1) = 7.0404(10)(8)\mu\text{s}^{-1}$ [19]). In the Ps^- ion, the two electrons are in a relative singlet spin state, a spherically symmetric configuration without a preferred axis of orientation of the positron spin. Therefore, either combination of electron and positron spins is available, and a positronium ion may decay into any number of photons. With the presence of a third particle to help ensure the energy–momentum conservation, even one-photon decays are possible.

Nevertheless, as one might expect, the 2γ decay channel is clearly dominating. The 3γ decay and all channels involving more photons are higher-order effects in the QED perturbation expansion, and the 1γ decay requires a three-body interaction, which is extremely unlikely. Also the $3\gamma/2\gamma$ branching ratio in the decays of Ps^- can be understood from the simple picture of a Ps atom plus a spectator electron, as it reflects the ratio of the triplet and singlet positronium decay rates, weighted by their respective multiplicity: $\Gamma_{3\gamma}/\Gamma_{2\gamma} \approx 3\Gamma(\text{Ps}, ^3S_1)/\Gamma(\text{Ps}, ^1S_0)$.

The first theoretical calculation of the 2γ and 3γ decay rates has been made by Ferrante [20], analogous to the corresponding computation for positronium [21]. The 2γ result – apart from the wavefunction-dependent expectation value $\langle\delta(\mathbf{r}_{1p})\rangle$ to find the electron and the positron at the same place – only differs by a factor of 1/2 from the one for the decay of 1S_0 positronium. This simply reflects the availability of a second electron and the different probabilities to find the electron–positron pair in a singlet state. In other words, there is no qualitative difference between the Ps and Ps^- decays in our approximation.

Experimentally it is much easier to measure the total decay rate $\Gamma = \Gamma_{1\gamma} + \Gamma_{2\gamma} + \Gamma_{3\gamma} + \dots$, summing up the contributions from all possible branches, than the decay rate for a single branch. Approximately, this quantity is given by the expression

$$\Gamma = 2\pi\alpha^4 \frac{c}{a_0} \left[1 - \alpha \left(\frac{17}{\pi} - \frac{19\pi}{12} \right) \right] \langle\delta(\mathbf{r}_{1p})\rangle, \quad (1)$$

where $\alpha = e^2/(\hbar c)$ is the fine-structure constant, c the speed of light and $a_0 = \hbar^2/(m_e e^2)$ the Bohr radius [7]. Equation (1) gives Γ as the dominating 2γ decay rate [20], multiplied by a factor $(1 + \eta_1 + \eta_2)$ to account for the 3γ decays ($\eta_1 = \Gamma_{3\gamma}/\Gamma_{2\gamma} = \alpha/\pi(4\pi^2/3 - 12)$) and to correct for the leading radiative corrections to the 2γ decay rate ($\eta_2 = \alpha/\pi(5 - \pi^2/4)$).

The 3γ correction η_1 was taken from the work of Ore and Powell [22], who calculated the probability of 3γ decays (in lowest order) for the case of neutral positronium. Likewise, Harris and Brown originally investigated the radiative correction η_2 to the annihilation amplitudes for free particles and positronium atoms [23]. According to [7], there are still contributions of order α missing, but unfortunately no estimates of the size of these contributions – which define the theoretical uncertainty of (1) – can be found in the literature. As a conservative estimate, we may assume that they are at most of a magnitude comparable to the corrections η_1 and η_2 . Consequently, the uncertainty could still be of the order of 3×10^{-3} .

As the numerical calculation of the decay rate from (1) requires the knowledge of the wavefunction, more precisely of the expectation value $\langle \delta(\mathbf{r}_{1p}) \rangle$, virtually all authors who have published a numerical result for the wavefunction also have given a value for Γ . Combining their results with our guess for the theoretical uncertainty, the calculated total decay rate is given by

$$\Gamma = 2.086(6) \text{ ns}^{-1} . \quad (2)$$

Another decay parameter of Ps^- which stimulated theoretical interest is the one-photon decay rate $\Gamma_{1\gamma}$. As already discussed above, this is a genuine three-body effect. It has been investigated by Kryuchkov [24], for the first time including all lowest-order Feynman diagrams contributing to the process. He arrived at the expression

$$\Gamma_{1\gamma}^{(0)} = \frac{64\pi^2}{27} \alpha^3 m_e^{-5} |\Psi(0, 0, 0)|^2 , \quad (3)$$

with m_e being the electron mass. In this equation, $|\Psi(0, 0, 0)|^2$ is the probability density to find all three particles at the same point. There is an earlier calculation [25], giving a result which is larger by a factor $9/4$; the difference is attributed to the fact that only four of eight diagrams have been considered in this calculation [24]. Numerical results can be found in a few papers [5, 12, 24], the most recent one resulting in a partial decay rate of $\Gamma_{1\gamma} = 3.823 \times 10^{-2} \text{ s}^{-1}$ [5].

In connection with the γ -decays, not only the decay rates, but also the photon energies and the angular correlations are of interest. Considering a positronium ion at rest – or equivalently, viewing it in its centre-of-mass system – the sum of all final-state momenta has to be zero. As one would expect from the $\text{Ps} + e^-$ picture, a large momentum transfer to the second electron is quite unlikely. Therefore, the two gamma rays from a two-photon decay have an energy of about $m_e c^2 = 511 \text{ keV}$ each, and their momenta are approximately equal and opposite. Reference [26] calculated the corresponding angular correlation function, which turns out to be narrower than its equivalent for neutral positronium. This is in accordance with what one would expect in a loosely bound system: as the particles are less strongly confined in position, their momentum distribution becomes narrower.

In the case of the 3γ decay, the situation is slightly more complex; while it is still true that the second electron to a good approximation remains unaffected, there are now three photons to share the energy and the momentum. For this reason, the gamma energies are not fixed but continuously varying. But except for the small momentum transfer to the remaining electron, they have to sum up to a total energy of $2m_e c^2 = 1022$ keV and to zero total momentum.

Finally, the 1γ decay gives rise to a free electron and a photon, both of them having fixed energies. As a simple relativistic kinematics calculation shows, the electron gains a kinetic energy of $2/3 \times m_e c^2 = 341$ keV, and a 681 keV photon is emitted. In the initial Ps^- rest frame, these two are sent out in exactly opposite directions.

Annihilation into four or more gamma rays is suppressed by additional factors of the fine-structure constant α . Because of the very small contribution of these decays, none of them seems to have been investigated in more detail.

2.3 Excitation and Resonances

As already mentioned, the ground state of the positronium ion is the only state which is stable against dissociation. Nevertheless, Ps^- features a number of doubly excited states in the continuum, which show up as resonances in electron–Ps scattering or in the Ps^- photodetachment cross-section. Experimentally, measurements of the photodetachment process



are the most promising means of accessing the predicted resonances, but they give access only to the $^1\text{P}^o$ resonances. Regarding the spin state of the so-produced neutral positronium atom, one expects to find *ortho*- ($^3\text{S}_1$) and *para*-Ps ($^1\text{S}_0$) with a probability given by the respective multiplicity of these spin states: this means that 1/4 of the positronium should be in the singlet state and 3/4 in the triplet state.

For an experimental observation of the doubly excited states of Ps^- , it is important to consider the possible decay channels of the doubly excited states, namely annihilation, autodetachment and de-excitation in a radiative cascade to the ground state. An investigation by Ho [27] has shown that the autodetachment rates are several orders of magnitude larger than those for direct annihilation. Accordingly, the doubly excited states should be observable in the photodetachment cross-section. Ho also concluded that the de-excitation by photon emission should be far less probable than the autodetachment process. This has important consequences for the decay rate measurements to be discussed later (see Sect. 3.2) because it means that feeding effects are negligible as a source of systematic errors: even if a significant fraction of the positronium ions was formed in one of the excited states, they would decay by autodetachment rather than by radiative transitions to the ground state.

A number of publications can be found on the subject of Ps^- resonances, including, for example, calculations of resonance positions and widths for a

large number of resonances up to the Ps ($n = 6$) threshold [28, 29, 30, 31, 32, 33, 34, 35, 36, 37, 38].

In [39], the photodetachment cross-section has been calculated. Part of the results is shown in Fig. 2, which additionally displays the off-resonant cross-section below the Ps($n = 2$) threshold as computed by other authors [40, 41, 42] for comparison. The obvious deviations between the different results are discussed in [39]. For every Ps(n) threshold in the energy range considered in the photodetachment cross-section calculations (in [39], up to $n = 6$), there is a series of Feshbach resonances just below threshold. These resonances can be interpreted as a consequence of the attractive dipole potential which results from the degeneracy of the excited states in positronium. Further, there is a shape resonance above the $n = 2$ threshold. As already discussed at the beginning of this section, only resonances of $^1P^0$ symmetry contribute to the photodetachment cross-section in the dipole approximation. For this reason, these are the only resonances showing up in this calculation.

From an experimental point of view, the doubly excited resonances below the Ps($n = 2$) threshold can provide a way of measuring the ground-state binding energy of Ps $^-$ in a photodetachment experiment: the photon energies

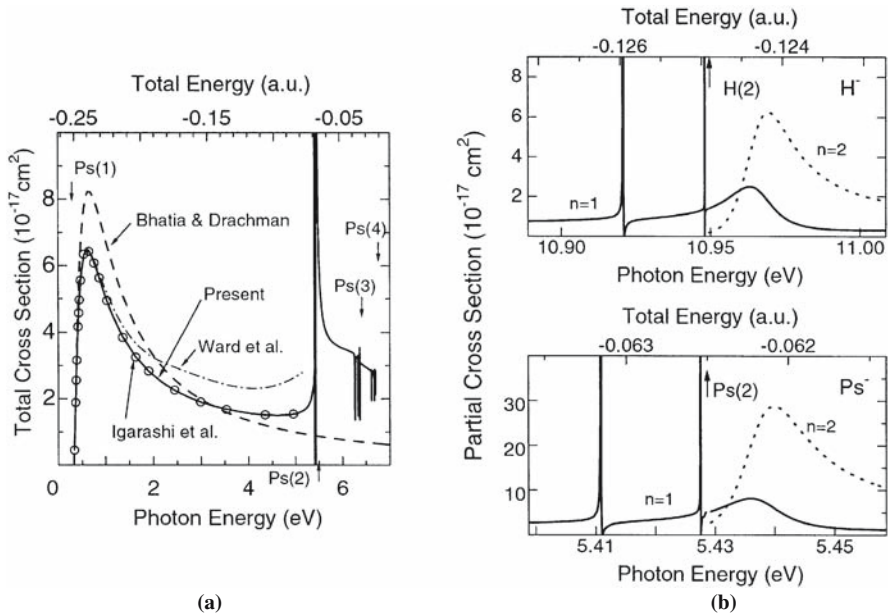


Fig. 2. The photodetachment cross-section of the positronium negative ion. (a) Results of a calculation by Igarashi et al. for the total cross-section. (b) Partial cross-sections for the production of Ps($n = 1$) (solid line) and Ps($n = 2$) (dotted line) and the corresponding graph for H $^-$ for comparison. Only the first two resonances of the series below the $n = 2$ threshold of the neutral atom are shown. For further resonances, the distance to the threshold decreases exponentially (from [39].)

at the Feshbach resonances correspond to the energy differences between the ground state and the respective resonances, and these in turn rapidly converge to the known $n = 2$ threshold of neutral positronium.

In the context of the doubly excited states, the possibility for a metastable ${}^3\text{P}^e$ state should also be mentioned. Such a state, which is predicted to exist in H^- [43], would be experimentally interesting because of its comparably long lifetime: if energetically lower than the Ps ($n = 2$) threshold, it could not decay by autodissociation, there were no dipole-allowed transitions to the ground state, and direct annihilation was strongly suppressed by the form of the wavefunction. The first one to point out this possibility and its consequences was Mills [43]. He tried to establish its stability against dissociation, but he could not obtain a binding energy below the $n = 2$ threshold of neutral positronium. Later, it has been shown that the ${}^3\text{P}^e$ metastable state, in contrast to H^- , lies above the $\text{Ps}(n = 2)$ threshold [44] and is therefore rapidly decaying by autodetachment.

3 Experiments with the Negative Positronium Ion

Despite the wealth of theoretical results, experimental data on Ps^- is extremely scarce: to our knowledge only three experiments on the positronium ion have been performed and published so far. The first two established the existence of this exotic ion [2] and determined its lifetime [3]. This year, we have presented an improved decay rate measurement [45], and we are planning further experiments which are becoming possible now at the high-intensity positron source NEPOMUC at the FRM-II research reactor in Garching.

3.1 Production of Ps^-

Until a recent observation of positronium ion emission from a polycrystalline tungsten surface [46], the only known Ps^- production method was the one used in the first experiments by Mills [2, 3], which is based on sending a beam of low-energy positrons through an extremely thin carbon foil of only a few nanometres thickness. When a suitable positron energy is chosen, a fraction of roughly 10^{-4} of the positrons picks up two electron and leaves the foil as Ps^- . Already these first experiments indicated that the optimum yield is reached for kinetic energies of a few hundred eV, rather precisely the energy, where about half of the positrons are transmitted. Our systematic studies using a number of diamondlike carbon (DLC, see [47]) and standard carbon foils of different thicknesses confirmed this observation and showed that the maximum formation efficiency does not seem to vary by more than a factor of 2–3 for foils between 4 and 13 nm thickness [48].

Once formed, the low mass of Ps^- and its opposite charge as compared to a positron allows for a separation of the ions from the transmitted positrons and for an easy acceleration to velocities of a few percent the speed of light.

The first observation in [2] took advantage of this fact and detected the blue-shifted annihilation radiation of in-flight decaying positronium ions with a germanium detector placed in forward direction. With such a setup, already moderate acceleration voltages lead to Doppler shifts large enough to distinguish the decays of Ps^- from the large background of other electron-positron annihilations. A voltage of 3900 V, for example, gives rise to a shift of 37.8 keV, much more than the energy resolution of a germanium detector of typically a few keV. As the measurement of the Doppler shift allowed to determine the charge-to-mass ratio of the decaying ions from the known acceleration voltage, it was used to prove the existence of the positronium ion.

3.2 Measurements of the Decay Rate

The decay rate of Ps^- is not only a genuinely quantum-electrodynamical effect, it is also the property of this elusive ion which is most straightforward to measure. Therefore, it is not surprising that this is the only quantity known from experiment so far. In the following, the two published decay rate experiments are discussed.

The First Decay Rate Measurement

In 1983, a first decay rate measurement was published by Mills [3]. The positronium ions were produced in the way described above from a beam of low-energy positrons transmitted through a thin carbon foil, using a positron source consisting of a 150 mCi ^{58}Co β^+ source and a single crystal tungsten moderator. The decay of Ps^- was observed by accelerating it in a homogeneous electric field and monitoring the survival rate when crossing the precisely variable acceleration gap d to the detection section.

In order to extract the decay rate from such a measurement, the relativistic relation between the distance d and the time of flight t' in the rest frame of the ion is needed. Correct up to terms of order $\Lambda^{3/2}$ and Λ_0/Λ , one obtains

$$t' = \frac{d}{\Lambda c} \ln \left[1 + \Lambda + \sqrt{\Lambda^2 + 2\Lambda} \right] \left(1 - \sqrt{\Lambda_0/\Lambda} \right), \quad (5)$$

where $\Lambda = eU/3m_e c^2$ and $\Lambda_0 = T_0/3m_e c^2$. U denotes the acceleration voltage, m_e the electron mass and T_0 the initial longitudinal kinetic energy of the positronium ions on leaving the production foil. Thus, the rate of surviving Ps^- exponentially decreases with the distance as $R(d) \propto \exp(-\mu d)$, where μ is defined by

$$\Gamma \left(1 - \sqrt{\Lambda_0/\Lambda} \right) = \mu \left[\Lambda c / \ln \left(1 + \Lambda + \sqrt{\Lambda^2 + 2\Lambda} \right) \right], \quad (6)$$

with Γ being the decay rate of the positronium ion. Equation (6) allows to calculate the decay constant Γ from the experimentally measurable quantity

μ . The conversion factor depends not only on the acceleration voltage U but also on T_0 , the average longitudinal kinetic energy of the Ps^- when leaving the production foil. Repeating the experiment with different acceleration voltages U and plotting the quantity $\Gamma^* = \Gamma(1 - \sqrt{\Lambda_0/\Lambda})$ (i.e. the left-hand side of (6)) as a function of $\Lambda^{-1/2}$, both Γ and T_0 can be obtained by extrapolating to $\Lambda \rightarrow \infty$. In such a plot, a significant $T_0 > 0$ shows up as a negative slope — for smaller values of U the contribution of the initial energy T_0 becomes more important, and correspondingly a smaller uncorrected decay rate Γ^* is measured.

A principle sketch of the setup used in the original decay rate experiment of Mills is shown in Fig. 3. For the production of Ps^- , the already mentioned beam-foil technique was employed, and as a means of detection, a Ge(Li) gamma detector placed in forward direction was used as explained above. Following the variable acceleration gap d , the positronium ions entered the field-free region inside a Faraday cage, where they were allowed to decay in flight. Only those ions which survived the acceleration across the gap reached the full velocity and contributed to the fully Doppler-shifted photo peak, while the ions which decayed before reaching the acceleration grid only contribute to the continuous background between the unshifted 511 keV positron annihilation line and the fully shifted peak. The gap width d could be changed by moving the production foil, which was mounted on a long manipulator with a micrometer. For calibration of the manipulator, a travelling microscope was used. Figure 4(a) shows a few examples of such gamma spectra for different values of d and different acceleration voltages.

The area of the fully Doppler-shifted photo peak, normalized to the solid-angle corrected 511 keV peak area, was plot as a function of the distance. After fitting the results by an exponential $R_0 \exp(-\mu d)$ with μ and R_0 as fit parameters, (6) was used to determine the uncorrected decay rate Γ^* . Such a measurement was performed for two different acceleration voltages, $U = 1000$ V and $U = 3936$ V, and the decay rate Γ was calculated using the procedure

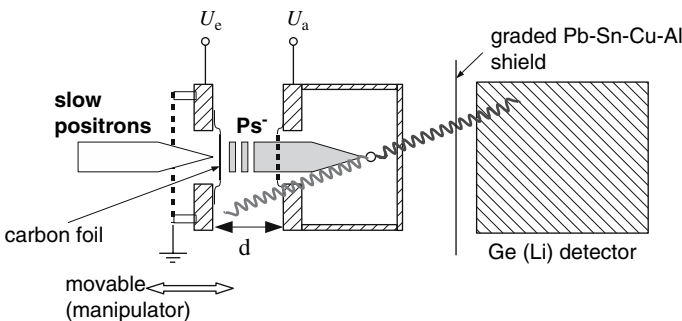


Fig. 3. A schematic view of the experimental setup used for the first Ps^- decay rate measurement in [3]. The positronium ions are detected by observing their Doppler-shifted annihilation photons when decaying in flight

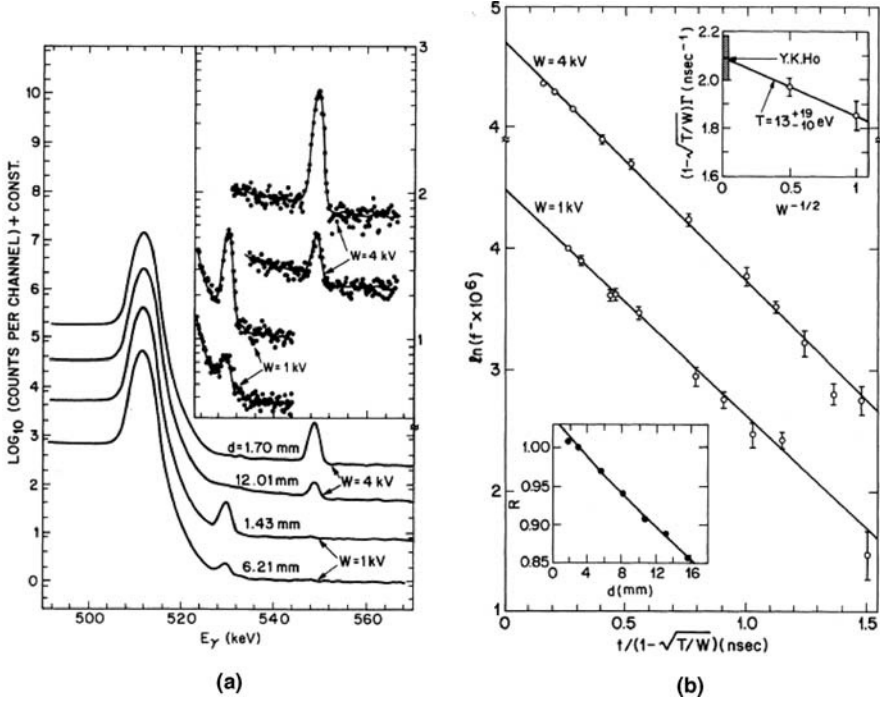


Fig. 4. Results of the first decay rate measurement of the positronium ion. **(a)** Gamma spectra for different acceleration gap widths d and different acceleration voltages W (in the text, this voltage is named U). The prominent peak on the left is the unshifted 511 keV annihilation line, the smaller peak on the right (larger view in the inset) is the fully Doppler-shifted signal from Ps^- decaying in flight. **(b)** Decay curves for acceleration voltages of 1000 V and 3936 V, respectively. The upper inset shows the extrapolation explained in the text, the lower inset shows the count rate in the 511 keV peak as a function of d . Reprinted figure with permission from *A.P. Mills, Jr.*, *Phys. Rev. Lett.* **50**, 671 (1983). Copyright 1983 by the American Physical Society

discussed above. Figure 4(b) displays the measured decay curves and the extrapolation (upper inset). As a final result, this extrapolation yielded a decay rate of

$$\Gamma = 2.09(9) \text{ ns}^{-1}. \quad (7)$$

For the initial kinetic energy of the ions, a value of $T_0 = 13_{-10}^{+19} \text{ eV}$ was obtained from the extrapolation. The errors were completely dominated by statistics.

Improved Measurement Based on a Stripping Method

Recently, we have performed an improved decay rate measurement at the Max-Planck-Institut für Kernphysik. Although this is the only property of Ps^- where there already was experimental data available and the previous result is in perfect agreement with the calculated value, a serious challenge of the theoretical predictions required a substantial increase in precision.

Concerning the Ps^- production by a beam-foil method and the variable acceleration gap for adjusting the time of flight, the experiment followed the same basic approach already used in the earlier measurement by Mills (see above). But instead of detecting the annihilation photons from positronium ions decaying in flight, our experiment relied on a stripping method and a particle detector for counting the ions surviving the acceleration.

In order to provide the experiment with the necessary beam of low-energy positrons, a laboratory positron source with a 40 mCi ^{22}Na source and a 4 μm thick polycrystalline tungsten moderator foil was used. The moderated positrons were extracted by a 30 V bias voltage and the resulting beam of 7 mm diameter and $1.5 \times 10^5 \text{ e}^+/\text{s}$ was filtered and guided to the experiment chamber by a longitudinal magnetic field of about 60 G. The details of the positron source design have been described elsewhere [48, 49].

A schematic sketch of the setup used in our decay rate measurement is shown in Fig. 5. The positrons were accelerated towards a diamondlike carbon foil of roughly 5 nm thickness supported by a 12 mm diameter copper grid of 86% transmission. The bias voltage U_e of the foil could be varied in order to maximize the yield of Ps^- ions, resulting in a rate of about 15 s^{-1} . Following the foil, a grid of the same type as used for the foil support was mounted, biased to a positive voltage U_a . While the positronium ions were accelerated by the resulting field, transmitted positrons were stopped and repelled.

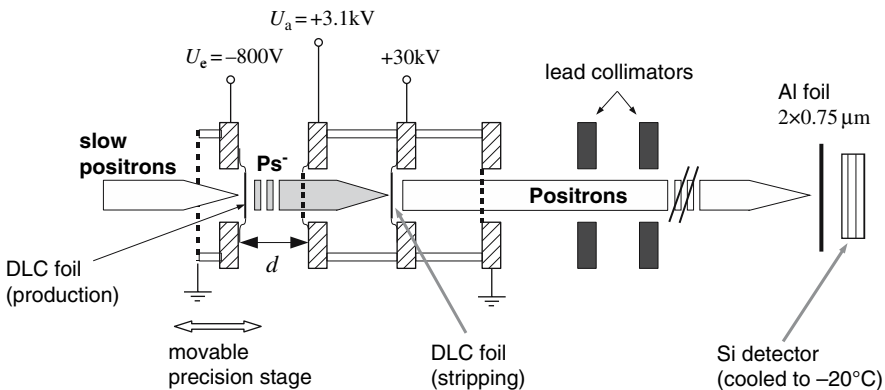


Fig. 5. Schematic view of the experimental arrangement used at the Max-Planck-Institut für Kernphysik to measure the decay rate of Ps^- with a stripping technique. The setup is surrounded by a solenoidal magnetic field of 100–130G

Mounting the Ps^- production foil on top of a motorized precision linear translation stage with a position reproducibility better than $1\ \mu\text{m}$ allowed for a precise variation of the gap d between the foil and the grid in the range of 2.7–28 mm. Additionally, the translation stage carried a grounded entrance grid on the upstream side of the foil to ensure a homogeneous electric field for the energy adjustment of the incoming positrons. Up to this point, the setup differed from the one used by Mills only by a few minor improvements, among these especially the use of a motorized linear translation stage with an optical position encoder in closed-loop operation for setting the foil-grid separation d .

As in the earlier experiment, the positronium ions entered the detection setup after passing the variable acceleration gap. But this time, instead of letting them decay in flight, the Ps^- ions were further accelerated over a distance of 16.8 mm towards a second DLC foil mounted on a grid biased at +30 kV. When traversing this foil, the electrons were stripped off, and the remaining positrons experienced another accelerating field between the stripper foil and a grounded grid. The electrons, having the opposite charge, were decelerated and returned to the stripper foil. In this way, only those positrons which had been part of a positronium ion when reaching the stripper foil could make it through the setup. These positrons could then be easily transported out of the region of high gamma background to a silicon particle detector. All other particles (positive or negative) with an energy in the relevant range were stopped or turned back at some point. As the positron and each of the two electrons had a kinetic energy of about 10 keV after the stripping process, the positron acquired a final energy of ~ 40 keV. In order to be able to detect these particles without being disturbed by electronic noise, we employed an ion-implanted silicon detector of $300\ \text{mm}^2$ active surface area and $100\ \mu\text{m}$ depletion depth cooled down to -20°C and a low-noise preamplifier. In the detection section, all spacings and all voltages were kept fixed to ensure a constant, d -independent detection probability.

In principle, this method should be largely background-free, but as it turned out, there is a significant contribution of ions and electrons to the spectrum. The ions could be easily stopped by two $0.75\ \mu\text{m}$ Al foils¹ which were mounted close to the front face of the detector. While this effectively removed the ionic background, the positrons we are interested in lost only about 800 eV. For the electrons, which originate from Compton scattering events of the high intensity 511 keV gamma radiation in the experiment chamber, there is no such simple solution. However, at least the number of electrons hitting the detector could be reduced considerably by inserting two lead collimators of 20 mm inner diameter. They absorbed electrons with large transversal energies because of their greater cyclotron radii, and they prevented the annihilation γ -rays from hitting the inner wall of the tube leading to the Si detector,

¹ Due to the fact that no pin-hole free aluminum foils of less than a few microns are available, a sandwich of two foils was used.

thus avoiding the production of further Compton electrons. As an additional means of background suppression, the detector section was covered by a lead housing of 5 cm lead bricks with an inner lining of 5 mm of copper to shield the detector from room background. The overall efficiency for detecting Ps^- with this setup was of the order of 1%. The main loss in efficiency has to be attributed to the angular scatter introduced by the stripper foil, which could be compensated only partly by the guiding magnetic field.

As already explained above, the exponential decay needs to be measured for a number of different acceleration voltages. Over the duration of the experiment of roughly 8 months, ten runs at six different voltages $U = U_a - U_e$ (985 V, 1285 V, 1882 V, 3875 V, 3973 V and 4766 V) have been performed. In all cases, the voltage varied was the acceleration voltage U_a . The foil bias U_e , which defines the positron energy when hitting the production foil, influences the primary Ps^- yield and was therefore kept constant. To be sure of the reproducibility of the results, a separately analysed control run at the first voltage (3875 V) has been made near the end of the data-taking period. For each voltage, the set of d values was chosen in such a way that the count rate drops by roughly a factor of ten from the shortest to the longest distance. Additionally, the largest possible gap width of 28 mm has been included in all the runs to obtain an approximation of the background. More data-taking time per cycle has been assigned to the larger values of d in order to compensate for the lower count rate, thus the total number of counts is more or less the same for all data points of a given run except for the background measurements.

The option to set the acceleration gap d automatically using the motorized linear translation stage allowed us to switch frequently between the different d values. A measurement at a given voltage consisted of a loop, where for each cycle data were taken at the previously defined gap widths d in random order. This not only averages out possible long-term fluctuations of the primary positron flux, but also avoids the need for an explicit correction for the slowly decaying ^{22}Na positron source when normalizing the number of Ps^- counts to the respective measuring time instead of the number of counts, e.g. in the 511 keV peak. After checking that there are no short-term fluctuations in the positron beam, we decided to use this approach.

The left panel of Fig. 6 shows a typical sample spectrum, taken at $U = 3875$ V and $d = 2.7$ mm. In order to extract the Ps^- count rate from the spectrum, an approximation to the background was obtained from the spectrum taken at the largest distance, $d = 28.0$ mm. An iterative procedure was employed to correct the background measurement for the residual contribution due to positronium ions surviving the acceleration across the 28.0 mm gap. After fitting the spectra with a linear combination of the corrected background and an empirical line shape, the background was subtracted and the number of Ps^- counts was determined by integrating the counts in the interval from channel 90 to 135.

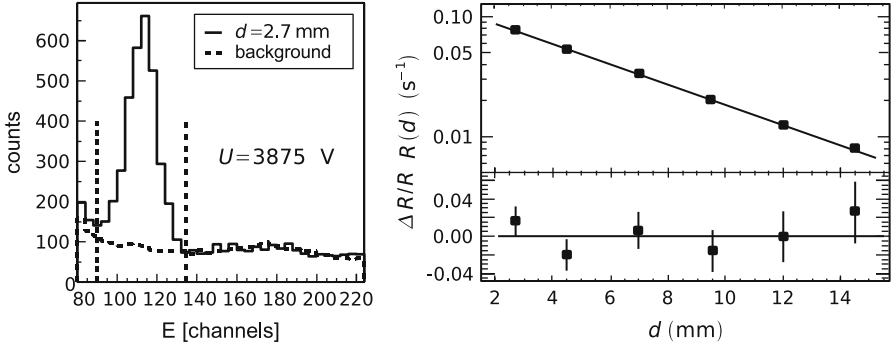


Fig. 6. **Left panel:** energy spectrum recorded with the silicon detector for an acceleration voltage of $U = 3875$ V and a gap width $d = 2.7$ mm. The prominent peak around channel no. 115 is due to the positrons resulting from the stripping of the positronium ions. Additionally, an appropriately scaled approximation to the background is drawn (*dotted line*), produced from a measurement at $d = 28.0$ mm by applying an iterative correction for the residual Ps^- contribution. The vertical lines mark the integration interval which has been used to evaluate the number of positronium ions. **Right panel:** decay curve for $U = 3875$ V. In the upper part, the count rate of surviving positronium ions is plotted as a function of the gap width d . The best fit by an exponential $R_0 \exp(-\mu d)$ is shown (*solid line*). Below, the residuals after subtracting the fit values from the data are displayed

In the right panel of Fig. 6, the resulting rates for the $U = 3875$ V run, calculated from the number of positron events in the spectrum and the respective dead-time corrected measuring time, are plotted as a function of the distance d . The errors have been determined by error propagation from the counting errors for the signal and the corrected background. The uncertainties of the measuring times make a negligible contribution. Beside the data points, the figure also shows the best fit by an $R_0 \exp(-\mu d)$ function (solid line), from which the decay constant μ was obtained. R_0 and μ were used as fit parameters, the error was determined from the $\Delta\chi^2 = +1$ contour line in a plot of χ^2 over the R_0 vs μ parameter plane. After careful checking for the consistency of the results [45], the uncorrected decay constants $\Gamma^* = \Gamma(1 - \sqrt{\Lambda_0/\Lambda})$ have been calculated from (6). Figure 7 displays Γ^* plotted as a function of $1/\sqrt{eU}$. Accounting for the constraint $m = \sqrt{T_0} \geq 0$, the best fit using $\Gamma(1 - m/\sqrt{eU})$ as a fitting function is obtained for $\Gamma = 2.089 \text{ ns}^{-1}$ and $m = 0$. Again using the $\Delta\chi^2 = +1$ contour of a χ^2 plot over the parameter plane, the 1σ uncertainty of Γ was determined to be $\pm 0.013 \text{ ns}^{-1}$. For T_0 , a 90% confidence level upper limit of $T_0 < 0.12 \text{ eV}$ has been calculated following the suggestions of the particle data group [50]. While details of the Ps^- formation process are not known and a substantial influence of the foil's surface conditions could be possible, this value meets the expectation that the energy of a positronium ion leaving the foil be in the range between thermal energies and the binding energy of the system, i.e. $0.025 \text{ eV} < T_0 < 0.3 \text{ eV}$. The value of $T_0 = 13_{-10}^{+19} \text{ eV}$

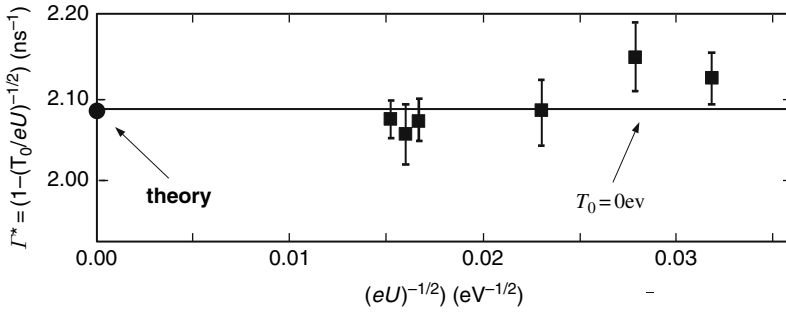


Fig. 7. Results of the Heidelberg decay rate measurement runs: the uncorrected decay rate $\Gamma^* = \Gamma(1 - \sqrt{\Lambda_0/\Lambda})$ is plotted as a function of $1/\sqrt{eU}$. In order to show the results more clearly, the data points for $U = 3875$ V and 3973 V are drawn at slightly shifted positions along the horizontal axis. A finite value of the average initial (longitudinal) kinetic energy T_0 would show up as a negative slope. The best fit (*solid line*) corresponds to $T_0 = 0$ eV, leading to a fit result of $\Gamma = 2.089(13)$ ns $^{-1}$. For comparison, the theoretical value from (2) is also shown

obtained by Mills (see Sect. 3.2) is considerably higher but – given the large uncertainty – statistically still compatible with our result.

A thorough investigation of the possible sources of systematic errors has been done, taking into account fluctuations of the primary positron beam flux, errors in the beam alignment, the positioning precision of the linear translation stage, the stability of the acceleration voltage and the geometrical imperfections of the production foil and acceleration grid arrangement. For a discussion of the individual contributions and an estimate of their sizes, please refer to [45]. As a result, including the systematic error estimates, we obtained a Ps $^-$ decay rate of

$$\Gamma = 2.089(15) \text{ ns}^{-1} . \quad (8)$$

This value is in perfect agreement both with the theoretical value of $\Gamma = 2.086(6)$ ns $^{-1}$ [5] and with the previous experimental value of $\Gamma = 2.09(9)$ ns $^{-1}$ measured by Mills (see above), and it is a factor of six more precise than the latter.

3.3 Outlook: Current Status of the Decay Rate Measurements and Prospects for Further Experiments

As the study of systematic errors [45] has shown, our present decay rate result is still limited by statistics, and a further improvement in precision by a factor of 4–5 seems feasible with minor modifications to the present setup. Prerequisite for such a measurement is a sufficiently high intensity of the positron beam. With the new NEPOMUC positron source at the FRM-II research reactor in Munich, which is now operational and delivers a flux of $\geq 5 \times 10^8$ moderated positrons per second, such a facility has become available. In

preparation for an improved decay rate measurement, we are currently working on adapting our setup to the characteristics of the NEPOMUC positron beam. Two parameters, its significantly larger diameter of roughly 20 mm as compared to our 7 mm diameter laboratory beam and its much greater transverse energy, prevent us from using it directly and require some extra effort in order to shape it for the Ps^- decay rate measurement. In the course of these modifications, we are also implementing a few improvements to further minimize the systematic errors.

The high intensity of the NEPOMUC positron facility not only allows for an improved decay rate measurement, it also opens up new experimental possibilities, which are not accessible with standard laboratory positron beams based on β^+ emitters. Properties of the positronium ion, which so far have never been investigated experimentally, are coming within reach now.

The next step in studying the positronium ion will be a photodetachment experiment. Several properties of Ps^- can be addressed by this technique: while resonant photodetachment allows for a study of the predicted doubly excited resonances of Ps^- and offers the chance to gain information on the Ps^- binding energy; the non-resonant process is of interest mainly because of its prospect of producing a directed, energy-variable, monoenergetic beam of *ortho*-Ps in vacuum.

While there exists in principle the possibility to look for doubly excited resonances in the e^- -Ps scattering cross-section, most of the calculated widths are too narrow (of the order of $10^{-5} - 10^{-3}$ eV) to be resolved with an experimentally available electron beam. Laser spectroscopy, on the other hand, provides the necessary resolution, but from the $^1\text{S}^e$ ground state only resonances of $^1\text{P}^o$ symmetry are accessible by one-photon transitions due to the selection rules for optical transitions. States of $^1\text{S}^e$ symmetry might be excited by two-photon absorption (as in the Doppler-free two-photon spectroscopy of the hydrogen 1S-2S transition, for example), but this requires high intensities and experiments which are not easy to realize. Looking at the energy scale, the most interesting resonances are those around the $n = 2$ threshold, but even they require rather short wavelengths (~ 230 nm for a positronium ion at rest).

In the non-resonant case, the positronium ion beam, produced by the standard beam-foil method, is crossed with a high power laser beam from a Nd:YAG laser (see Fig. 8). In order to enhance the detachment probability, a multipass configuration can be employed which maximizes the geometrical overlap of the laser beam and the particle beam. According to spin statistics, one expects 3/4 of the detached positronium atoms to be in the $^3\text{S}_1$ state and 1/4 in the $^1\text{S}_0$ state. Due to its much shorter lifetime, the *para*-Ps component quickly decays, and further downstream an effectively pure beam of ground-state *ortho*-Ps can be obtained. Assuming a laser power of 1 kW (cw) for the Nd:YAG laser, an estimated intensity of about 150 Ps/s can be reached. With a pulsed laser and appropriate bunching of the positron beam, an intensity of 4×10^4 Ps/s seems feasible.

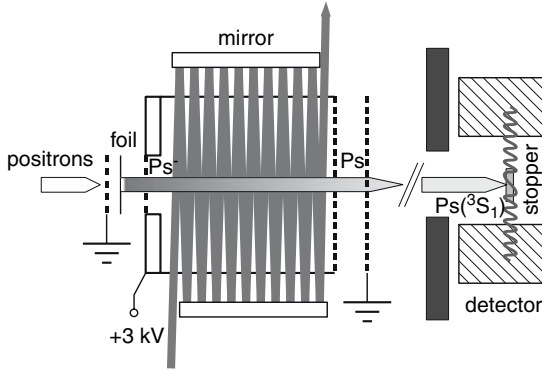


Fig. 8. Photodetachment experiments with positronium ions: a multipass geometry is used to achieve a large overlap of the positronium ion beam with the laser beam. For detection of the photodetachment events, a stopper foil is placed sufficiently far downstream from the interaction region and a shielded gamma detector setup is used to register the 2γ decays due to the quenching of *ortho*-Ps atoms in the foil

The resonant photodetachment experiment might use in a first approach the same general setup, with the Nd:YAG being exchanged for a suitable UV laser. As the doubly excited states predominantly decay by autodetachment (see Sect. 2.3), the detection of the excited ions can be achieved by counting the resulting Ps atoms: a stopper foil, placed sufficiently far downstream from the interaction region, and a shielded gamma detector setup can be used to register the 2γ decays due to the quenching of the *ortho*-Ps atoms in the foil.

Another interesting parameter of the negative positronium ion is the $3\gamma/2\gamma$ branching ratio. This quantity essentially reflects the ratio of the decay rates of *ortho*- and *para*-Ps, multiplied by a factor of three to take into account the spin statistics. It could be measured using a setup as shown schematically in Fig. 9. Again this is based on the standard Ps⁻ production technique. The positronium ions are accelerated to a relatively high energy, e.g. 50 keV, and are then allowed to decay in flight inside a long, field-free drift tube. Around the drift tube, separated from the production foil region by several centimetres of lead (or a tungsten alloy) shielding, a ring of HPGe detectors (for example MINIBALL modules, see 5.1) is mounted. The acceleration of the ions to a few tens of keV is necessary in order to make the distance travelled within the Ps⁻ lifetime long enough to leave room for the detector shielding and to distinguish the positronium ions decaying in flight from the ambient background due to positron annihilations at rest via the higher photon sum energy. Under optimal conditions, count rates of up to 0.1 detected 3γ events per second can be expected.

It would be very interesting to study the predicted 1γ decay of Ps⁻. Although this process has a distinct signature concerning the energy and the angular correlation of the photon and the electron in its final state, the extremely

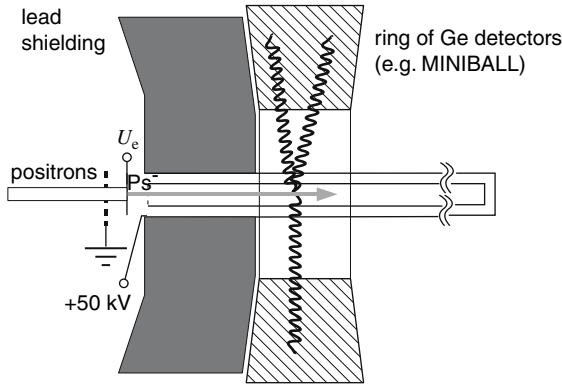


Fig. 9. Possible experimental setup to measure the $3\gamma/2\gamma$ branching ratio in Ps^- decays. Coming from the standard beam-foil Ps^- production setup, the positronium ions are accelerated to a relatively high energy, e.g. 50 keV, and are then allowed to decay in flight inside a long, field-free drift tube. Around the drift tube, separated from the production foil region by several centimetres of lead (or tungsten alloy) shielding, a ring of HPGe detectors is mounted

small branching ratio of about 4×10^{-11} of this exotic decay channel is still out of reach even at the NEPOMUC source.

4 Conclusion

Quite a few properties of the positronium negative ion have been investigated theoretically, but experimental data are largely unavailable; so far only the decay rate has been measured. More than 20 years after the experiments by Mills [2, 3], we have reported on a new measurement of the decay rate of the negative positronium ion. Our result, $\Gamma = 2.089(15) \text{ ns}^{-1}$, is in excellent agreement both with the theoretical value of $\Gamma = 2.086(6) \text{ ns}^{-1}$ [5] and the only previous experimental result of $\Gamma = 2.09(9) \text{ ns}^{-1}$, and with an error of 0.8%, it is a factor of six more precise than the latter.

With the very intense positron facility NEPOMUC at the FRM-II research reactor in Munich now being available, we are currently working on an improved decay rate measurement with better statistics. According to the analysis of the systematic error budget, a further improvement in precision by a factor of 4–5 seems feasible without major modifications to the present setup. Additionally, the high positron flux of NEPOMUC makes new experiments on the properties of the exotic Ps^- ion possible, thus presenting new opportunities for testing our understanding of the quantum-mechanical three-body system.

Acknowledgement

The author would like to thank D. Schwalm for stimulating discussions on the physics with Ps^- ions.

References

1. J.A. Wheeler: Ann. N.Y. Acad. Sci. **XLVIII**, 219 (1946). [261](#) [263](#)
2. A.P. Mills: Phys. Rev. Lett. **46**, 717 (1981). [262](#) [268](#) [269](#) [279](#)
3. A.P. Mills: Phys. Rev. Lett. **50**, 671 (1983). [262](#) [268](#) [269](#) [270](#) [279](#)
4. S.G. Karshenboim: Appl. Surf. Sci. **194**, 307 (2002). [262](#)
5. A.M. Frolov: Phys. Rev. A **60**, 2834 (1999). [263](#) [265](#) [276](#) [279](#)
6. Y.K. Ho: Phys. Rep. **99**, 1 (1983). [263](#)
7. A.K. Bhatia, R.J. Drachman: Phys. Rev. A **28**, 2523 (1983). [263](#) [264](#) [265](#)
8. P. Petelenz, V.H. Smith: Phys. Rev. A **36**, 5125 (1987). [263](#)
9. Y.K. Ho: Phys. Lett. A **144**, 237 (1990). [263](#)
10. Y.K. Ho: Phys. Rev. A **48**, 4780 (1993). [263](#)
11. A.M. Frolov: J. Phys. B **26**, 1031 (1993). [263](#)
12. A.M. Frolov: Phys. Rev. A **57**, 2436 (1998). [263](#) [265](#)
13. G.W.F. Drake, M.M. Cassar, R.A. Nistor: Phys. Rev. A **65**, 54501 (2002). [263](#)
14. M.I. Haftel, V.B. Mandelzweig: Phys. Rev. A **39**, 2813 (1989). [263](#)
15. R. Krivec, M.I. Haftel, V.B. Mandelzweig: Phys. Rev. A **47**, 911 (1993). [263](#)
16. A.K. Bhatia, R.J. Drachman: Nucl. Instrum. Methods Phys. Res., Sect. B **143**, 195 (1998). [263](#)
17. G.W.F. Drake, M. Grigorescu: J. Phys. B: At. Mol. Opt. Phys. **38**, 3377 (2005). [263](#)
18. A.H. Al-Ramadhan, D.W. Gidley: Phys. Rev. Lett. **72**, 1632 (1994). [264](#)
19. R.S. Vallery, P.W. Zitzewitz, D.W. Gidley: Phys. Rev. Lett. **90**, 203402 (2003). [264](#)
20. G. Ferrante: Phys. Rev. **170**, 76 (1968). [264](#)
21. J.M. Jauch, F. Rohrlich: *The Theory of Photons and Electrons*, 2nd edn. (Springer, New York 1976), pp. 263. [264](#)
22. A. Ore, J.L. Powell: Phys. Rev. **75**, 1696 (1949). [265](#)
23. I. Harris, L.M. Brown: Phys. Rev. **105**, 1656 (1957). [265](#)
24. S.I. Kryuchkov: J. Phys. B **27**, L61 (1994). [265](#)
25. M.C. Chu, V. Poenisch: Phys. Rev. C **33**, 2222 (1986). [265](#)
26. Y.K. Ho: J. Phys. B **16**, 1503 (1983). [265](#)
27. Y.K. Ho: Phys. Rev. A **32**, 2501 (1985). [266](#)
28. Y.K. Ho: Phys. Rev. A **19**, 2347 (1979). [267](#)
29. Y.K. Ho: Phys. Lett. **102A**, 348 (1984). [267](#)
30. A.K. Bhatia, Y.K. Ho: Phys. Rev. A **42**, 1119 (1990). [267](#)
31. Y.K. Ho, A.K. Bhatia: Phys. Rev. A **44**, 2890 (1991). [267](#)
32. Y.K. Ho, A.K. Bhatia: Phys. Rev. A **45**, 6268 (1992). [267](#)
33. A.K. Bhatia, Y.K. Ho: Phys. Rev. A **48**, 264 (1993). [267](#)
34. Y.K. Ho, A.K. Bhatia: Phys. Rev. A **47**, 1497 (1993). [267](#)
35. Y.K. Ho, A.K. Bhatia: Phys. Rev. A **50**, 2155 (1994). [267](#)
36. I.A. Ivanov, Y.K. Ho: Phys. Rev. A **60**, 1015 (1999). [267](#)
37. I.A. Ivanov, Y.K. Ho: Phys. Rev. A **61**, 032501 (2000). [267](#)

38. J. Usukura, Y. Suzuki: Phys. Rev. A **66**, 010502 (2002). [267](#)
39. A. Igarashi, I. Shimamura, N. Toshima: New J. Phys. **2**, 17 (2000). [267](#)
40. A.K. Bhatia, R.J. Drachman: Phys. Rev. A **32**, 3745 (1985). [267](#)
41. S.J. Ward, J.W. Humberston, M.R.C. McDowell: J. Phys. B **20**, 127 (1987). [267](#)
42. A. Igarashi, S. Nakazaki, A. Ohsaki: Phys. Rev. A **61**, 032710 (2000). [267](#)
43. A.P. Mills: Phys. Rev. A **24**, 3242 (1981). [268](#)
44. J. Botero: Phys. Rev. A **35**, 36 (1987). [268](#)
45. F. Fleischer, K. Degreif, G. Gwinner, M. Lestinsky, V. Liechtenstein, F. Plenge, D. Schwalm: Phys. Rev. Lett. **96**, 063401 (2006). [268](#) [275](#) [276](#)
46. Y. Nagashima: private communication, 2006. [268](#)
47. V.K. Liechtenstein, T. M. Ivkova, E. D. Olshanski, I. Feigenbaum, R. DiNardo, M. Doebeli: Nucl. Instrum. Methods, Sect. A **397**, 140 (1997). [268](#)
48. D. Schwalm, F. Fleischer, M. Lestinsky, K. Degreif, G. Gwinner, V. Liechtenstein, F. Plenge, H. Scheit: Nucl. Instrum. Methods, Sect. B **221**, 185 (2004). [268](#) [272](#)
49. F. Fleischer, K. Degreif, G. Gwinner, M. Lestinsky, V. Liechtenstein, F. Plenge, H. Scheit, D. Schwalm: Can. J. Phys. **83**, 413 (2005). [272](#)
50. K. Hagiwara *et al.*: Phys. Rev. D **66**, 010001 (2002). [275](#)
51. J. Eberth *et al.*: Prog. in Part. Nucl. Phys. **46**, 389 (2001). [278](#)

**Savely G. Karshenboim: Guide for Atomic
and Particle Physicists to CODATA's Recommended
Values of the Fundamental Physical Constants
DOI 10.1007/978-3-540-75479-4_3**

in

Lect. Notes Phys. 745

Savely G. Karshenboim, Precision Physics of Simple Atoms and Molecules

DOI 10.1007/978-3-540-75479-4

© Springer-Verlag Berlin Heidelberg 2008

Publisher's Erratum

The original version of this chapter unfortunately contained a mistake. The author name and affiliation was incorrect in the HTML version of this chapter. The correct author name and affiliation is given below.

S. G. Karshenboim^{23,24}

(23) D. I. Mendeleev Institute for Metrology (VNIIM), 190005 St., Petersburg, Russia

(24) Max-Planck-Institut für Quantenoptik Hans-Kopfermann-Str. 1, D-85748 Garching,
Germany

The publisher apologizes for the errors.

Index

- Absolute shielding constant, [236](#)
- Ab initio methods
 - shielding constant, [236](#)
- AD, [188](#)
- a_e , [42](#) [115](#)
 - experimental value, [18](#)
 - theoretical prediction, [18](#)
- α , *see* Fine structure constant
- a_μ , [50](#)
 - analytic results, [16](#) [19](#)
 - experimental value, [28](#)
 - QED prediction, [19](#)
 - theoretical prediction, [28](#)
- Anomalous magnetic moment, [10](#) [11](#)
 - of electron, *see* a_e
 - of muon, *see* a_μ
- Antiproton-to-electron mass ratio, [187](#)
- Antiprotonic helium atom, *see* $\bar{p}\text{He}^+$
- Antiproton decelerator, *see* AD
- ASACUSA, [188](#)

- Bohr magneton, [10](#)
- Born-Oppenheimer approximation, [3](#) [215](#)
- Bound-state QED, [262](#)

- CERN, [188](#)
- Charge-coupled devices, [175](#)
- Charge screening, [17](#)
- Chiral perturbation theory, [166](#)
- CODATA, [35](#) [36](#) [187](#) [188](#)
- Contribution to a_μ
 - hadronic, [22](#)
 - leading, [23](#)
 - subleading, [24](#)
 - universal, [16](#)
 - weak
 - leading, [20](#)
 - subleading, [21](#)
- Contribution to a_μ
 - weak, [22](#)
- Corrections
 - mass dependent, [17](#)
 - universal, [17](#)
- Coupled cluster methods, [244](#)
- CPT symmetry, [30](#)
- CPT theorem, [13](#) [187](#)
- Crystal spectrometer, [174](#)
- Current
 - axial, [20](#)
 - electromagnetic, [10](#)
- Cyclotron trap, [174](#)
 - ECRIT, [177](#)

- Decoupling of heavy states, [12](#)
- Deser formula, [169](#)
- Determination of fundamental constants via rovibrational spectroscopy of MHIs
 - m_e/m_p , [206](#)
 - m_p/m_d , [206](#)
- Dirac–Hartree–Fock calculations, [246](#)
- Dispersion integral, [22](#)
- Dispersion relations, [103](#)
- Doppler-free spectroscopy, [206](#) [214](#) [217](#)

- Effective field theory, [21](#) [25](#)
- Electro-optic modulator, [119](#)

Electron-positron annihilation, *see*
 e^+e^- -annihilation

Electron anomaly, *see* a_e

Electron $g - 2$, *see* a_e

Electron scattering, [111](#)

e^+e^- -annihilation, [22](#)

e^+e^- -data, [22](#), [31](#)

Exotic atoms, [2](#), [187](#)

Exotic atom cascade, [171](#)

 Coulomb de-excitation, [172](#), [178](#)

 molecular formation, [172](#)

 muonic hydrogen, [178](#)

 pionic hydrogen, [172](#)

 Stark mixing, [172](#)

Fabry Perot etalon, [113](#)

Femtosecond frequency comb, *see*
 Optical frequency comb

Fermion loops, [17](#)

 triangle loop, [20](#)

Fine structure, [111](#)

Fine structure constant, [15](#), [17](#), [31](#), [38](#),
[41-43](#), [112](#)

Form factor, [26](#)

 dipole, [80](#)

G_{EM} , [88](#)

G_{EN} , [85](#), [88](#)

G_{EP} , [82-84](#), [88](#)

G_{MN} , [85](#)

Fundamental constants, [3](#), [35-52](#)

 adjustment of, [36-38](#)

 auxiliary data, [38](#)

 CODATA recommended values,
[35-52](#)

g -factor, [10](#)

Goldstone bosons, [21](#), [25](#)

Gravitation constant, [44-45](#)

Gyromagnetic ratio, [10](#)

H-like ions, [2](#), [157-162](#)

H_2^+ ions, [211](#)

H_2^+ ions, [215](#)

 intensities of HFS lines, [215](#)

 ion trap, [219](#)

 laser system, [220](#)

 photodissociation, [216](#)

Hadrons, [17](#)

Halo nuclei, [2](#), [131-152](#)

He, [133](#)

 atomic spectroscopy, [141-144](#)

Li, [131-133](#)

 atomic spectroscopy, [144](#)

Harmonic Double Sided Microtron, [87](#)

HD^+ ions, [211](#), [225](#)

HD^+ ions

 Doppler broadening, [228](#)

 effective spin Hamiltonian, [227](#)

 Lamb-Dicke regime, [228](#)

 photodissociation, [224](#)

 population of ro-vibrational states,
[224](#)

 sympathetic cooling, [222](#)

HDSM, *see* Harmonic Double Sided Mi-
 crotron

Helium, [2](#)

HFS, *see* Hyperfine splitting

Hydrogen atoms, [1-2](#)

Hydrogen molecular ions, *see also* H_2^+
and HD^+ , [3](#), [205](#)

 hyperfine structure, [211](#), [227](#)

 intensities of transition lines, [213](#), [215](#)

 level structure, [215](#)

 ro-vibrational spectroscopy, [206](#)

 theory, [207](#)

Hylleraas Variational method, [111](#),
[133-136](#)

Hyperfine splitting

 in hydrogen, [93](#)

 polarizability correction, [98](#)

 recoil corrections, [96](#)

 in muonic hydrogen, [103](#)

Hyperfine structure, [111](#)

Isospin violations, [24](#)

Isotope shift, [111](#), [138](#), [141](#), [150](#)

KEK, [189](#)

Lagrangian

 effective, [24](#)

 Wess-Zumino-Witten, [24](#)

Lamb shift, [59](#), [66](#), [69](#), [80](#), [105](#), [112](#)

Larmor precession, [13](#)

Laser atomic beam measurement, [124](#)

Laser heterodyne, [115](#)

Laser spectroscopy, [111](#)

LEAR, [191](#)

- Leptons, [20](#), [21](#)
- Level crossing spectroscopy, [124](#)
- Light-by-light scattering, [13](#)
 - electron, [18](#)
 - hadronic, [16](#), [24](#)
- Lithium, [2](#), [111](#)
- Magic energy, [12](#), [13](#)
- Magnetic moment, [10](#)
 - anomalous, *see* Anomalous magnetic moment
 - of lepton, [9](#)
- Mainz accelerator
 - energy compressing system, [81](#)
 - LINAC, [81](#)
 - Mainz Microtron MAMI A/B, [84](#)
 - Mainz Microtron MAMI C, [87](#)
- Mainz experiments
 - Anklin et al., [85](#)
 - Becker et al., [85](#)
 - Bermuth et al., [85](#)
 - Bernauer et al., [88](#)
 - Borkowski et al., [82](#)
 - Glazier et al., [86](#)
 - Herberg et al., [86](#)
 - Kubon et al., [85](#)
 - Ostrick et al., [86](#)
 - Pospischil et al., [84](#)
 - Rohe et al., [85](#), [88](#)
 - Simon et al., [83](#)
- Mass radii, [126](#)
- MHIs, *see* Hydrogen molecular ions
- Micromotion of ions in an ion crystal, [228](#)
- Microwave, [115](#)
- Muon
 - decay, [11](#)
 - life time, [14](#)
 - magnetic moment, [50](#)
 - mass, [50](#)
 - polarization, [13](#)
 - storage ring, [13](#)
- Muon $g - 2$, *see* a_μ
- Muon anomaly, *see* a_μ
- Natural linewidth, [119](#)
- NEPOMUC positron source, [276](#)
- New physics scale, [31](#)
- New physics search, [11](#)
- NMR
 - absolute shielding, [236](#)
 - ab initio shielding constant, [236](#)
 - chemical shift, [238](#)
 - effective spin Hamiltonian, [235](#)
 - gas phase experiment, [240](#)
 - Non-perturbative effects, [21](#), [26](#)
 - NRM spectroscopy, [3](#)
 - Nuclear magnetic dipole moment, [233](#), [249](#)
- Optical double resonance, [124](#)
- Optical frequency comb, [113](#), [194](#)
- Optical theorem, [22](#)
- Parity violation, [12](#), [20](#)
- $\bar{p}\text{He}^+$, [187](#)-[200](#)
- Penning trap, [187](#)
- Perturbation theory
 - chiral, [25](#)
 - extended, [25](#)
- Pion, [21](#), [25](#), [26](#)
- Pion-nucleon interaction, [167](#)
 - chiral perturbation theory, [168](#)
 - coupling constant, [167](#), [181](#)
 - scattering length, [167](#), [181](#)
- Pionic atoms, [167](#)
 - pionic deuterium, [169](#)
 - pionic hydrogen, [169](#)
- Planck constant, [43](#)-[44](#)
- Poly-logarithms, [16](#)
- Polyelectrons, [261](#)
- Positronium
 - decay rate, [264](#)
 - production of a beam, [277](#)
- Positronium ion, [3](#)
 - binding energy, [263](#)
 - decay rate, [261](#)-[279](#)
 - angular correlation, [265](#)
 - branching, [264](#), [278](#)
 - measurement, [269](#)-[276](#)
 - one-gamma decay, [265](#), [278](#)
 - doubly excited states, [266](#)-[268](#)
 - meta-stable state, [268](#)
 - observation, [269](#)
 - photodetachment
 - cross section, [267](#)
 - experiments, [277](#)
 - production, [268](#)

- size, [263](#)
- Positronium molecular ion, *see* Positronium ion
- Positronium ion
- Proton-to-electron magnetic moment ratio, [50](#)
- Proton-to-electron mass ratio, [187](#)
- Proton structure, [2](#)
- Pseudo-scalars, [21](#)
 - exchange, [26](#)
- QCD, [21](#) [23](#)
 - large N_c , [25](#)
- QED, [11-3](#) [9](#) [19](#) [111](#) [137](#) [262-264](#)
 - scalar, [25](#)
- Quantum chemistry
 - ab initio methods, [237](#)
- Quantum chromodynamics, *see* QCD
- Quantum electrodynamics, *see* QED
- Quantum fluctuations, [11](#)
- Quark-hadron duality, [24](#) [25](#)
- Quarks, [17](#) [20](#) [21](#)
- Racetrack Microtron, [84](#)
- Radiative corrections, [10](#)
- Radioactive lithium isotopes, [126](#)
- Radiofrequency quadrupole decelerator, *see* RFQD
- Relativistic correction, [112](#) [136-137](#)
- REMPD, *see* Resonance enhanced multiphoton dissociation method
- Renormalization group, [17](#)
- Resonances, [23](#)
- Resonance enhanced multiphoton dissociation method, [218](#) [224](#)
- RFQD, [192](#)
- ρ -meson, [23](#) [25](#)
- RMS radii
 - of neutron, [79-80](#)
 - of proton, [48-50](#) [57-65](#) [79-84](#)
 - of deuteron, [69-71](#)
 - $A = 3$ nuclei, [71](#)
 - $A = 4$, [72](#)
 - $A > 4$, [73](#)
 - of ${}^6\text{He}$, [144](#)
 - of ${}^6\text{Li}$, [151](#)
 - of ${}^7\text{Li}$, [111](#)
 - of ${}^{8,9,11}\text{Li}$, [151](#)
- RTM, *see* Racetrack Microtron
- Rydberg Energy, [124](#)
- Scaling relation, [83](#)
- Short distance constraints, [26](#)
- Simple atoms, [1-3](#)
- Spin-rotation constant, [239](#)
- Standard Model, [11](#) [19](#)
- Stark collisions, [190](#)
- Strong interactions, [22](#)
- Super-symmetric SM, [30](#)
- Super symmetry, [30](#)
- Symmetry breaking
 - chiral, [21](#)
- Systematic shifts, [207](#) [229](#)
- τ -data, [24](#)
- τ spectral-functions, [24](#)
- Three-body systems, [262](#)
- Time dilatation, [14](#)
- Triangle anomaly, [21](#) [24](#) [27](#)
- Two photon exchange
 - in e-d scattering, [70](#)
 - in e-p scattering, [68](#)
 - in HFS, [67](#)
- Vacuum polarization, [17](#)
 - hadronic, [16](#) [22](#)
- Vector-meson, [25](#)
 - dominance, [25](#)
- Weak gauge bosons, [20](#)
- Weak interactions, [11](#) [20](#)
- Yang-Mills structure, [20](#)
- Zemach moment
 - of deuteron, [71](#)
 - of proton, [66-68](#) [95-96](#)
 - third, [69](#)
- Zemach radius, *see* Zemach moment